Title	Electric Field Gradients of Impurities in Solids
Author(s)	Sato, Kazunori
Citation	大阪大学, 1999, 博士論文
Version Type	VoR
URL	https://doi.org/10.11501/3155121
rights	
Note	

①

Electric Field Gradients of Impurities in Solids

K. Sato

Dissertation in Physics, 1999.

The Osaka University
Graduate School of Science
Toyonaka, Osaka.

Abstract

The electric field gradient (EFG) is one of the most important clues to investigate the electronic structure of solids. The EFG reflects a non-spherical charge distribution around the nucleus, therefore, it provides us precise information on interactions of the probe atom with the host matrix, *i.e.*, the EFG is a unique probe to investigate a chemical bonding in solids. In particular, a systematic study on the EFGs at impurities in solids is a candidate for a study on the electronic structure of impurities, because recent developments of *ab initio* methods for the band structure calculation of solids provide us a sound basis to discuss about origin of EFGs of impurities. Such a method will give insight not only for the electronic structure of impurities but also for the lattice location of impurities implanted into a solids by comparing theoretical predictions of EFGs with experimental measurements. In spite of its importance, the determination of the implantation site of impurities has been a difficult problem because of rather complicated experimental procedures. The present approach has possibility to be a new transparent way to work on the lattice location problem.

On the other hand, once such first principle method of the EFG calculations are established and its precision is guaranteed, it becomes possible to determine a nuclear quadrupole moment directly from its electric quadrupole coupling constant in solids by using a calculated EFG. In the *ab initio* method, all substances are treated in the same framework. This universality make such procedure to determine the quadrupole moment to be a very flexible one.

One of the purpose of the present study is to develop a method of *ab initio* EFG calculation of impurities and to elucidate the origin of the EFGs at impurity sites. To achieve it, first the EFGs in pure HCP metals were investigated. The electronic structure of the system was calculated self consistently by the Korringa-Kohn-Rostoker (KKR) method based on the local density approximation (LDA) of the spin-density functional theory and the EFG was calculated directly from the electron density distribution without further approximations except the muffin tin approximation for the shape of the respective atomic potentials. As a result, it was found that the present method could reproduce the experimental EFGs in pure HCP metals within the error of 20%. Next, the EFGs at impurities of the typical elements in Zn and Cd were studied systematically. Simulating the impurity system by the super cell method, the EFGs were calculated within the same procedure. As a result, the systematic variation of the EFGs at impurity sites was explained from the view points of the hybridyzation of the *p*-orbitals between impurities and the host atoms.

To establish reliability of the present method for all kinds of substances, it is indispensable to investigate the EFGs of impurities in ionic crystals. In the present study, we focussed on a TiO_2 in the rutile structure. In order to make up for a lack of the systematic experimental measurements, we measured the quadrupole coupling constants of several transition metals such as ^{45}Sc, ^{49}Ti and ^{93}Nb in a TiO_2 single crystal by the Pulsed Fourier-transformed NMR (FT-NMR) technique. Besides the present results of the EFGs at Sc, Ti and Nb, the EFGs at Cd and Ta impurities were known. For these systems, the present method were also applied. Taking advantage of the super cell method, local lattice relaxations were included when the EFGs were calculated. However, the essential point to reproduce the experimental EFGs at impurity sites was to simulate the charge states of impurities, *i.e.*, the diamagnetic situation of the impurities, which was observable in experiments, must be

reproduced. Taking into these points into account, finally the EFGs were predicted within the error of 20%.

Also, in order to enforce such systematic understanding, the hyperfine interactions of ^{12}N ($I^{\pi} = 1^{+}, T_{1/2} = 11$ ms) and ^{19}O ($I^{\pi} = 5/2^{+}, T_{1/2} = 27$ sec) in TiO_2 were precisely measured by utilizing the β-NMR (NQR) technique. It was found that there were two distinct implantation sites for both of ^{12}N and ^{19}O. These experimental results give us a good opportunity to apply our method to investigate lattice locations of light impurities. For ^{12}N, the oxygen substitutional site and the octahedral like interstitial site were suggested by comparing the experimental EFGs with the theoretical predictions. On the other hand, it was found that the main fraction of ^{19}O was implanted into the oxygen substitutional site, however, the other implantation site was left unknown. The substitutional implantation site of ^{19}O was also confirmed experimentally. From the present knowledge of the implantation site of the oxygen isotope, the nuclear quadrupole moments of ^{19}O and ^{13}O ($I^{\pi} = 3/2^{-}, T_{1/2} = 8.6$ ms) were determined.

The other purpose of the present study is to apply the present method for a nuclear study, *i.e.*, the determination of the nuclear quadrupole moments. First, it is tried to determine the nuclear quadrupole moment of the 247 keV exited state of ^{111}Cd from its quadrupole coupling constants in various HCP metals by referring to calculated EFGs. The two different quadrupole moments were reported for $^{111}Cd^{*}$ ($I^{\pi} = 5/2^{+}, T_{1/2} = 84$ ns) in spite of its importance as a PAC probe. By the present study, its quadrupole moment is determined reliably to be 0.78 ± 0.16 mb. This approach was also employed to determine the quadrupole moments of β-emitting ^{27}Si ($I^{\pi} = 5/2^{+}, T_{1/2} = 4.1s$) and ^{39}Ca ($I^{\pi} = 3/2^{+}, T_{1/2} = 0.86s$) which are of importance from the view points of the study on the nuclear shell structure. Recently the electric quadrupole coupling constants of ^{27}Si and ^{39}Ca in Al_2O_3 single crystal and $CaCO_3$ single crystal, respectively, were measured. By comparing the theoretical predictions on the EFGs, the quadrupole moment of ^{27}Si and ^{39}Ca were derived to be 61 ± 14 mb and 36 ± 4 mb, respectively, which were comparable with the OXBASH predictions of 60 mb and 26 mb, respectively. Since in the present study the quadrupole moments of ^{27}Si and ^{39}Ca were determined, it becomes possible to use these nuclei as probes to investigate hyperfine interactions.

Contents

Acknowledgments

The author wishes to extend his thanks to all of those who have helped to make this work successful.

Professor T. Minamisono for his proposing the present work, providing earnest guidance and discussions.

Professor H. Akai for his continued guidance on the electronic structure calculation and providing the KKR package.

Associated Professor K. Matsuta for his constant collaboration, discussions and encouragement.

Research Associate M. Fukuda for his constant collaboration, discussions and encouragement.

Research Associate M. Mihara for his constant collaboration, discussions and encouragement.

Professor Y. Nojiri for his constant collaboration, discussions and encouragement.

Associate Professor S. Takeda for the managements of FT-NMR measurements.

Mr. M. Sakamoto and Mr. Y. Takahashi for their constant technical supports on Van de Graaff Accelerator and encouragement.

Mr. K. Higa for his technical supports and encouragement.

Mr. K. Onishi for his computing supports during this work. The most of electronic structure calculations in this work were performed on the machines at Osaka University Laboratory of Nuclear Studies.

Dr. T. Ohtsubo, Dr. Tanigaki and Mr. Izumikawa for their discussions and encouragement.

Dr. T. Yamaguchi, Mr. T. Miyake, Mr. T. Onishi, Mr. M. Sasaki for their supports in the experiments.

Mr. Y. Matsumoto, Mr. T. Fukao and Dr. K. Minamisono for their encouragement.

Ms. Y. Maruyama and Mr. A. Morishita for their supports in the experiments.

Ms. K. Ohsawa for her business managements.

1 Introduction

The knowledge of the charge distribution is one of the most important points to obtain basic understandings for the properties of solids. The electric field gradient (EFG) sensitively reflects a non-spherical charge distribution around a nucleus, so we can investigate local electronic structures of solids through the EFGs. In particular, the EFGs at impurities provide us a unique tool to study on the nature of chemical bonding between impurities and host atoms.

To reach the detailed understandings of the electronic structure of an impurity, the EFG have been measured by various techniques, and large amount of data on electric quadrupole interactions of impurities were collected [1]–[3]. There are several experimental techniques to observe a quadrupole interaction [1, 3, 4]. In addition to the usual nuclear magnetic resonance (NMR) and nuclear quadrupole resonance (NQR) techniques, the methods with utilizing an unstable nucleus as a probe have been developed and form a field of nuclear solid state physics. The noble techniques for nuclear physics allow us to get information on the hyperfine interactions through observing nuclear radiations, for examples Mössbauer effect, perturbed angular correlation (PAC) techniques and so on. However, the lack of the proper probes prevent us from systematic investigations of the hyperfine interactions especially of light impurities. Owing to the recent development of the experiments utilizing radioactive nuclear beams, it becomes possible to use short-lived β-emitting nuclei as a probe to study the electronic structure of solids. In our laboratory, such light β-NMR probes have been developed and applied to study the internal fields of Fe, Ni, Pt, and so on [5]–[10]. However, a study on an ionic substance is at its starting point [11].

In the present study, to understand the EFGs of impurities in ionic crystals, the hyperfine interactions of ^{17}O, ^{45}Sc, ^{49}Ti and ^{93}Nb in a TiO_2 single crystal were measured by the Pulsed Fourier-Transformed NMR (FT-NMR) technique, and the EFGs at the substitutional site were precisely investigated. The EFGs at Ti and O site in pure TiO_2 were consistent with the previous measurements of by Gabathler *et al.* [12] and Kanert *et al.* [13]. With the previous data by Wenzel *et al.* [14] and Adams *et al.* [15] on the EFGs at Cd and Ta sites in TiO_2 by the PAC technique, we can discuss the EFGs of impurities in TiO_2 systematically. Also, the hyperfine interactions of ^{12}N ($I^\pi = 1^+, T_{1/2} = 11$ ms) and ^{19}O (^{19}O ($I^\pi = 5/2^+, T_{1/2} = 27$ sec) in TiO_2 single crystal were investigated. For both of them, two distinct implantation sites were discovered. For these two implantation sites, the electric quadrupole coupling constants of ^{12}N and ^{19}O were determined. The main fraction of ^{19}O in TiO_2 was determined to be the oxygen substitutional site. With this knowledge on the implantation sites of ^{19}O, we derived the quadrupole moment of ^{19}O for the first time by referring to the coupling constant of ^{17}O in TiO_2. This study of the implantation sites for the oxygen isotope in TiO_2 also allows us to derive the quadrupole moment of ^{13}O, which is of particular interest from the view point of the nuclear shell structure.

On the other hand, in spite of large amount of experimental data, the origin of the EFGs is not so clear, because discussions were based on rather ambiguous model calculations. For example, the model calculation such as the Sternheimer theory is usually used to obtain and analyze EFG values [1, 3, 16, 17]. In this model the EFG is originated from the array of ions which are regarded as point charges ($q_{lattice}$). The EFG will be created also by the non-spherical unfilled orbitals of the electrons as in the rare-earths (q_{local}). These EFGs polarize valence electrons and generate an additional EFGs which are described by Sternheimer factors γ_∞ and R respectively. Usually γ_∞ and R are about in the ranges of $10 < -\gamma_\infty < 80, -0.2 < R < 0.2$. Thus the resulting EFG in this model is written as,

$$q = (1 - \gamma_\infty) q_{lattice} + (1 - R) q_{local}.$$

This model has two ambiguous parameters. One of them is a value of a point charge at a lattice point. We do not know any rigorous definitions or criteria to decide the charge state of the atom in solids. It can be taken arbitrarily by choosing its atomic sphere as you like. The other is the Sternheimer factors. It is usually evaluated from the atomic calculations by the perturbation theory. However, the atomic potential will be modified in solids and the changes of the potential depend also on the host materials. Although the Sternheimer theory is useful to get rough estimations of EFG values, it does not have sufficient prediction power for the precise EFG. For a reliable prediction of the EFG, we must calculate the charge distribution in solids from the first principles without relying on any models, though it is a difficult many body problem.

In the last two decades, such first principles calculation becomes realistic for the electronic structure of solids, partly because of the development of computers and computing techniques, but mainly because of the success of the local density approximation (LDA) in the framework of the density functional theory [18]. The density functional prescription for a many body system was proposed by Kohn and Sham [19] based on the Hohenberg-Kohn theorem [20]. For a ground state, this theory reduces the many body problem to the one electron equations in an effective potential determined self consistently. It can be dealt with the ordinary band structure calculation techniques if the exchange correlation term is evaluated by the LDA. As was described in the book by Moruzzi, Janak and Williams [21], it was found that the LDA calculation gave the values in good agreement with experimental values in the lattice constant and so on for the most of elements in the periodic table.

The band calculation based on the LDA was applied to the calculation of the hyperfine fields by Akai *et al.* [22]–[29] and independently by Jülich group [30]–[35]. Akai *et al.* calculated self consistently the hyperfine field and spin-lattice relaxation time of impurity nuclei in ferro magnetic Fe, and explained the systematic variation of the hyperfine field from the view point of the theory proposed by Katayama, Terakura and Kanamori [36]–[44] in which the sd hybridyzation between the impurity and host atom had an important role.

According to the EFGs, recently Blaha and Schwarz gave a discussion on EFGs through the first principles calculations, and succeeded in explaining the EFGs in various pure systems [45]–[67]. They applied the LDA to the EFG calculation with using the FLAPW (full-potential linearized-augmented-plane-wave) method. They calculated EFGs in various metals and compounds, some of which have magnetic properties, and obtained good agreement with experiments. By analyzing calculated results, they found out followings.

- The main contribution for the total EFG is anisotropy of the density distribution in the *p*-orbitals.

- The contributions from the array of ions are small.

- The contributions from deeply bound states are negligible.

It was shown that the semi-empirical model calculations, which tried to calculate EFGs from the lattice summations and additional shielding factors, had the wrong starting point. Now the calculation for a more complex system with impurities is not only interesting but also realistic [68]–[84]. However, on a system with impurities, few calculations have been performed, and only impurities in metals were discussed [4, 69, 78, 79].

In the present study, to elucidate the origin of the EFGs of impurities in solids and to provide a systematic understanding on it, an *ab initio* method to calculate the electric field gradients (EFGs) were developed. Working not only on pure substances but also on systems with impurities, more advanced knowledge and standard view points will be given. The outline of the present calculation is as followings. The electronic structure of the system was calculated by the Korringa-Kohn-Rostoker (KKR) method [21], [80]–[83] with the LDA in the muffin tin approximation. We utilized the band structure calculation package developed by Akai [84, 85]. The system with impurities were simulated by the super-cell method [68]–[71], [79]. Once a self consistent charge distribution is obtained for a super-cell, it is straight forward to derive an EFG from a charge distribution. A detailed explanation will be given in the latter section.

We calculated the EFGs in several substances including the impurity systems. Here we clarify our aims of the present calculations. The most simple crystal structure with well defined EFG is the hexagonal closed packed (HCP) structure. For almost all the HCP metals, EFGs at the host atomic site were measured. So, we calculated EFGs in all of pure HCP metals except for the lanthanoides and predicted values were compared with the experimental data to check the reliability of the present method. The cases of impurity systems in the HCP metals are interesting to observe clear systematics of variations of EFGs. For such a purpose, EFGs at sp-impurity sites in Zn and Cd are calculated and was compared with the experimental data. For typical examples on the EFG calculations in compounds, we picked up an ionic substance TiO_2. Not only the EFGs in pure TiO_2 but also the EFGs at several transition metal impurities *i.e.*, Sc, Nb, Cd and Ta in TiO_2 were calculated. There was no reliable calculation on the EFG at an impurity site in an ionic crystal until now. By comparing theoretical predictions with the experimental measurements, predictability of the present method is discussed.

The present method of the EFG calculation was also applied to determine the lattice locations of the implanted nuclei. Generally, the lattice location of impurities is not obvious, so it has been an important problem to decide where it is. However, it is not so easy and needs complicated experimental procedures [7, 86]. In the super cell calculation, it is also possible to calculate the EFG at an interstitial impurity site [69]. Therefore, if the EFG at the impurity nucleus was known, the present EFG calculation can be used to determine the location of the impurity. This procedure was employed to the determination of the locations of light impurities O and N in a TiO_2 whose hyperfine interactions were investigated experimentally in the present study. For both of them two different implantation sites were discovered in TiO_2. By comparing the experimental EFGs with the theoretical ones, we tried to determine which sites they were implanted in. One of them was proposed to be the substitutional site of O, and the other to be the octahedral like interstitial site.

Another application is a determination of a nuclear quadrupole moment. We can deduce a nuclear quadrupole moment from its quadrupole coupling constant in a substance by referring to a calculated EFG. One of the recent topics on such a trial is the determination of the quadrupole moment of the 14 keV exited state of ^{57}Fe* ($I^\pi = 3/2^-, T_{1/2} = 98$ns) [87]. Two distinct values of quadrupole moment of 0.08 ± 8 b and 0.209 ± 5 b were reported for ^{57}Fe* in spite of its importance as a Mössbauer probe. Dufek *et al.* performed the first principles calculations based on the FLAPW method within the framework of the LDA, and calculated EFGs for a various compounds containing Fe. Comparing them with the experimental electric quadrupole coupling constants, they obtained $Q(^{57}\mathrm{Fe}^*) = 0.16$ b which is twice as large as the previously suggested value of $Q(^{57}\mathrm{Fe}^*) = 0.082$ b by Duff, Mishra and Das [88]. Recently Hagelberg and Das re-examined the Hartree-Fock calculations by Duff *et al.* and derived the quadrupole moment of ^{57}Fe* to be 0.11 b, which got somewhat closer to the FLAPW result [89]. The calculations by Dufek *et al.* were on the pure systems. If we can go with the impurity system along the same procedure, experiments to determine nuclear quadrupole moments, in particular for unstable nuclei, will have great possibilities. To examine whether it is realistic or not, we try to determine the quadrupole moment of the 247 keV exited state of ^{111}Cd ($I^\pi = 5/2^+, T_{1/2} = 84$ns), which is a well known PAC probe. Also for ^{111}Cd*, three different Q moments were reported. $Q(^{111}\mathrm{Cd}^*)$ was derived to be $+1.5 \pm 0.4$ b by Rosenblum and Steyert [90]. On the other hand Ernst *et al.* [91] and Herzog *et al.* [92] reported it to be $+0.83 \pm 0.13$ b and $|Q| = 0.77 \pm 0.12$ was given by Raghavan *et al.* [93, 94]. It is of particuar interest which quadrupole moment the present calculation support which quadrupole moment. Also, the quadrupole moments of short-lived β-emitting nuclei ^{27}Si ($I^\pi = 5/2^+, T_{1/2} = 4.1$s) and ^{39}Ca ($I^\pi = 3/2^+, T_{1/2} = 0.86$s) were determined by the same procedure. Recently, the electric quadrupole coupling constants of ^{27}Si and ^{39}Ca respectively in Al_2O_3 and $CaCO_3$ were determined by the β-NMR technique. In these cases, it is impossible or too difficult to determine experimentally the EFGs at their implanted sites, so the present procedure is almost only way.

This thesis is organized as follows. In section 2, the theory of hyperfine interactions are summarized. The details of the EFG calculation based on the *ab initio* band structure calculation are described in section 3. The NMR measurements of the quadrupole effects are explained in section 4 and 5. The results of the calculations are shown and compared with the experiments, and the systematics are discussed in section 6 and 7. A discussion on the lattice location is given in section 8 and a topic on the determination of the quadrupole moment is in section 9. In section 10, reliability of the present method is discussed. Lastly, a brief summary of the present study is given in section 11.

2 Hyperfine Interactions

The hyperfine interaction describes the interaction between electrons and the nuclear multipole moments.

In atoms, molecules and solids, electrons interact with nuclei and with the other electrons through the electromagnetic interaction. However, the electronic structures in them are mainly determined by the electromagnetic interactions between a point spinless nucleus and electrons, here the electronic structure means the density distributions of electrons in space, energy or momentum. Actually there are higher rank of the interaction because of finite extent of the nucleus and because of the nuclear spin and the electron spin. For example, in atoms the coupling of electron spin with its orbital angular momentum leads to the fine structure in electronic energy levels. In solids, where the orbital momentum is frozen, the interaction of nuclear dipole moment with the (external or local) magnetic field and the interaction of nuclear quadrupole moment with the electric field gradient become important. These lead to the hyperfine structure in nuclear energy levels. Typically the magnitude of the magnetic dipole term and the electric quadrupole term is in the region of the radio frequency and can be detected by the nuclear magnetic resonance (NMR) technique [95, 96].

Generally, the interaction energy W between the electronic system and the nuclear system is written in the form of

$$\begin{aligned} W &= W_M + W_E \\ &= -\frac{1}{c^2}\int \frac{\boldsymbol{j}_n \boldsymbol{j}_e}{r} dv_n dv_e + \int \frac{\rho_n \rho_e}{r} dv_n dv_e. \end{aligned}$$

$\boldsymbol{j}_{n,e}$ are the current density distributions, and $\rho_{n,e}$ are the charge density distributions of nucleons and electrons, respectively. Schwartz put the interaction Hamiltonian in the form of the scalar product of two tensor operators by the multipole expansion [97] as,

$$H = \sum_{k=0} T_n^{(k)} \cdot T_e^{(k)},$$

here $T_{n,e}^{(k)}$ are the spherical tensor operators for a nuclear and an electronic subsystems, respectively. There exist electric multipoles for even k and magnetic ones for odd k because of the inversion symmetry of the nuclear wave functions. For the nuclear subsystem, $T_n^{(k)}$ usually written in terms of nuclear spin operator I. The angular momentum algebra shows that $k \leq 2I$, because $\langle T_n^{(k)} \rangle \propto \langle Im | Y_k^q | Im \rangle \propto \langle kI; qm | kI; Im \rangle$, *i.e.*, I, I, k must make a triangle. Here Y_k^q is the spherical harmonic of rank k, and m, q are the magnetic quantum numbers and $\langle kI; qm | kI; Im \rangle$ is the Clebsh-Gordon coefficient. Therefore, a nucleus with $I \geq 1$ has a quadrupole moment. For the electronic subsystem, the energy of the hyperfine interactions is so small that they are calculated by the first order perturbation theory, *i.e.*,

$$\langle T_e^k \rangle = \langle \Psi_0 | T_e^k | \Psi_0 \rangle,$$

where Ψ_0 is the unperturbed wave function of the electronic system. Ψ_0 will be calculated in the framework of the local density approximation in the density functional theory. In the following section, the energy of the hyperfine interaction is derived. In the present study we do not deal with the hyperfine field (internal magnetic field), but it is also mentioned for complete knowledge on the hyperfine interaction.

2.1 Hyperfine Field

Intuitively it is recognized that the magnetic dipole moments caused by the spin and orbital angular momentum of electron produce a magnetic field at the nucleus, so the nuclear magnetic dipole moment interacts with it. The term of $k = 1$ represents such a magnetic interaction. It is decomposed to three contributions according to its origin, *i.e.*, the Fermi contact term, the dipolar term and the orbital term. They are obtained from the explicit expression of $T_e^{(1)}$ as was given in the paper of Schwarz, but in rather complicated way because of the vector nature of the currents $\boldsymbol{j}$. So we take the easier way in which the motion of electron in the nuclear dipole field is considered.

The vector potential $\boldsymbol{A}$ generated by the nuclear magnetic moment $\boldsymbol{\mu}_n$ is,

$$\begin{aligned} \boldsymbol{A} &= \frac{\boldsymbol{\mu}_n \times \boldsymbol{r}}{r^3} \\ &= \boldsymbol{\nabla} \times \frac{\boldsymbol{\mu}_n}{r^3}. \end{aligned}$$

The vector potential $\boldsymbol{A}$ satisfies the condition; $\boldsymbol{\nabla A} = 0$. The magnetic field $\boldsymbol{H}$ due to the nuclear magnetic moment is obtained by $\boldsymbol{H} = \boldsymbol{\nabla} \times \boldsymbol{A}$. The interaction of the electron with this magnetic field is described by the Hamiltonian H,

$$\begin{aligned} H &= \frac{1}{2m}(\boldsymbol{p} + \frac{e}{c}\boldsymbol{A})^2 + g_e\mu_B\boldsymbol{\sigma\nabla} \times \boldsymbol{A} \\ &\cong \frac{1}{2m}p^2 + \frac{e}{2mc}(\boldsymbol{pA} + \boldsymbol{Ap}) + g_e\mu_B\boldsymbol{\sigma\nabla} \times \boldsymbol{A}, \end{aligned}$$

here $\boldsymbol{\sigma}$ is the angular momentum of the electron and g_e, μ_B are the electron g-factor and the Bohr magneton. The perturbation term H' by the nuclear field is written as

$$H' = \frac{e}{2mc}(\boldsymbol{pA} + \boldsymbol{Ap}) + g_e\mu_B\boldsymbol{\sigma\nabla} \times \boldsymbol{A}.$$

Here, the relation $\hbar\boldsymbol{l} = \boldsymbol{r} \times \boldsymbol{p}, \mu_B = e\hbar/2mc$ leads the first term to

$$\frac{e}{2mc}(\boldsymbol{pA} + \boldsymbol{Ap}) = g_e\mu_B\frac{\boldsymbol{\mu}_n\boldsymbol{l}}{r^3}.$$

With the relation of $\boldsymbol{\nabla} \times (\boldsymbol{\nabla} \times \boldsymbol{B}) = \boldsymbol{\nabla}(\boldsymbol{\nabla B}) - \boldsymbol{\nabla}^2\boldsymbol{B}$, the second term is transformed to

$$\begin{aligned} \boldsymbol{\sigma\nabla} \times \boldsymbol{A} &= \boldsymbol{\sigma\nabla} \times \boldsymbol{\nabla} \times \frac{\boldsymbol{\mu}_n}{r} \\ &= \left[(\boldsymbol{\sigma\nabla})(\boldsymbol{\mu}_n\boldsymbol{\nabla}) - \frac{1}{3}(\boldsymbol{\sigma\nu}_n)\boldsymbol{\nabla}^2\right]\frac{1}{r} - \frac{2}{3}(\boldsymbol{\sigma\nu}_n)\boldsymbol{\nabla}^2\frac{1}{r} \\ &= -\frac{1}{r^3}(\boldsymbol{\sigma\mu}_n) + \frac{3}{r^5}(\boldsymbol{\sigma r})(\boldsymbol{\mu}_n\boldsymbol{r}) + \frac{8\pi}{3}(\boldsymbol{\sigma\mu}_n)\delta(r), \end{aligned}$$

where the Poisson equation $\boldsymbol{\nabla}^2(1/r) = -4\pi\delta(r)$ is used. Finally, the hyperfine field $\boldsymbol{H}_{hf}$, which is defined by

$$H' = -\boldsymbol{\mu}_N\boldsymbol{H}_{hf},$$

is obtained to be

$$\boldsymbol{H}_{hf} = -\frac{4\pi}{3}g_e\mu_B\boldsymbol{\sigma}\delta(\boldsymbol{r}) + \frac{1}{2}g_e\mu_B\left[\frac{\boldsymbol{\sigma}}{r^3} - \frac{3(\boldsymbol{\sigma r})\boldsymbol{r}}{r^5}\right] - \frac{1}{2}g_e\mu_B\frac{\boldsymbol{l}}{r^3}.$$

The first term is the Fermi contact field, the second one is the dipolar field and the last one is the orbital field.

If the system has cubic symmetry and the magnetic field is along the z-axis, the Fermi contact term is only finite contribution to the hyperfine field. Calculating the expectation value of the Fermi contact field for the ground state, the hyperfine field is,

$$\langle H_{hf} \rangle = \frac{4\pi}{3} g_e \mu_B \int^{\epsilon_f} \left(\rho_\uparrow(0;E) - \rho_\downarrow(0;E)\right) dE,$$

here, $\rho_\sigma(r;E)$ is the electron density distribution.

2.2 Electric Field Gradient

In the case of the electric interaction, the multipole expansion of the charge density distributions ρ_n, ρ_e is effective. The expansion of the Green's function is written as

$$\frac{1}{|\boldsymbol{r}-\boldsymbol{r}'|} = 4\pi \sum_{l,m} \frac{1}{2l+1} \frac{r_<^l}{r_>^{l+1}} Y_l^{m*}(\boldsymbol{r}') Y_l^m(\boldsymbol{r}),$$

where $r_<(r_>)$ denotes the smaller (the larger) value of $r = |\boldsymbol{r}|$ and $r' = |\boldsymbol{r}'|$.

This expression leads to the expression of W_E immediately in terms of the multipoles as

$$\begin{aligned} W_E &= \int \frac{\rho_n(\boldsymbol{r}_n)\rho_e(\boldsymbol{r}_e)}{|\boldsymbol{r}_n - \boldsymbol{r}_e|} dv_n dv_e \\ &= Q_L \cdot V_L \\ &= \sum (-)^m Q_l^m V_l^{-m}, \end{aligned}$$

where,

$$\begin{aligned} Q_l^m &= \sqrt{\frac{4\pi}{2l+1}} \int \rho_n(\boldsymbol{r}_n) r_n^l Y_l^m(\boldsymbol{r}_n) dv_n, \\ V_l^m &= \sqrt{\frac{4\pi}{2l+1}} \int \rho_e(\boldsymbol{r}_e) r_e^{-(l+1)} Y_l^m(\boldsymbol{r}_e) dv_e. \end{aligned}$$

Usually the electric field gradient tensor is defined by the second derivatives of the Coulomb potential at the nucleus in the Cartesian coordinate.

$$V_{ij} = \left. \frac{\partial^2 V(\boldsymbol{r}_n)}{\partial r_i \partial r_j} \right|_{r_n=0}, \ (i,j = x,y,z)$$

It is more appropriate to define the EFG as a traceless tensor because a potential caused by s-electron does not interact with the nuclear quadrupole moment. Therefore, the standard definition of the EFG is

$$V_{ij} = \left. \left(\frac{\partial^2 V(\boldsymbol{r}_n)}{\partial r_i \partial r_j} - \frac{1}{3} \delta_{ij} \boldsymbol{\nabla}_n^2 V(\boldsymbol{r}_n) \right) \right|_{r_n=0}.$$

$V(\boldsymbol{r}_n)$ is produced by the electron distribution. To calculate the EFG directly, first the $1/\boldsymbol{r}$ term is expanded.

$$\begin{aligned}
V(\boldsymbol{r}_n) &= \int \frac{\rho_e(\boldsymbol{r}_e)}{|\boldsymbol{r}_n - \boldsymbol{r}_e|} dv_e \\
&= \int \sum_{l,m} \frac{4\pi}{2l+1} \frac{r_n^l}{r_e^{l+1}} Y_l^m(\boldsymbol{r}_n) Y_l^{m*}(\boldsymbol{r}_e) \rho_e(\boldsymbol{r}_e) dv_e \\
&= \sum_{l,m} \sqrt{\frac{4\pi}{2l+1}} V_l^m r_n^l Y_l^m(\boldsymbol{r}_n), \\
\text{where } V_l^m &= \sqrt{\frac{4\pi}{2l+1}} \int \frac{\rho_e(\boldsymbol{r}_e)}{r_e^{l+1}} Y_l^{m*}(\boldsymbol{r}_e) dv_e.
\end{aligned}$$

Then calculating the second derivative and $r_n \to 0$,

$$\left.\frac{\partial^2 V(\boldsymbol{r}_n)}{\partial r_{ni} \partial r_{nj}}\right|_{r_n=0} = \sum_m \sqrt{\frac{4\pi}{5}} V_2^m \frac{\partial^2}{\partial r_{ni} \partial r_{nj}} r_n^2 Y_2^m(\boldsymbol{r}_n),$$

so,

$$\begin{aligned}
V_{ZZ} &= 2V_2^0, \\
V_{YY} &= -\sqrt{\frac{3}{2}} V_2^{-2} - V_2^0, -\sqrt{\frac{3}{2}} V_2^2, \\
V_{XX} &= \sqrt{\frac{3}{2}} V_2^{-2} - V_2^0, -\sqrt{\frac{3}{2}} V_2^2, \\
V_{XY} &= -\sqrt{\frac{3}{2}} i V_2^{-2} + \sqrt{\frac{3}{2}} i V_2^2, \\
V_{YZ} &= -\sqrt{\frac{3}{2}} i V_2^{-1} - \sqrt{\frac{3}{2}} i V_2^1, \\
V_{ZX} &= \sqrt{\frac{3}{2}} V_2^{-1} - \sqrt{\frac{3}{2}} V_2^1,
\end{aligned}$$

are obtained.

On the other hand, the nuclear moment are defined as

$$Q_{ij} = \int \rho_n (3r_i rj - \delta_{ij} r^2) dv_n.$$

As the same manner with the EFG, Q_{ij} is written as

$$\begin{aligned}
Q_{ZZ} &= 2Q_2^0, \\
Q_{YY} &= -\sqrt{\frac{3}{2}} Q_2^{-2} - Q_2^0, -\sqrt{\frac{3}{2}} Q_2^2, \\
Q_{XX} &= \sqrt{\frac{3}{2}} Q_2^{-2} - Q_2^0, -\sqrt{\frac{3}{2}} Q_2^2, \\
Q_{XY} &= -\sqrt{\frac{3}{2}} i Q_2^{-2} + \sqrt{\frac{3}{2}} i Q_2^2,
\end{aligned}$$

$$
\begin{aligned}
Q_{YZ} &= -\sqrt{\frac{3}{2}} i Q_2^{-1} - \sqrt{\frac{3}{2}} i Q_2^{1}, \\
Q_{ZX} &= \sqrt{\frac{3}{2}} Q_2^{-1} - \sqrt{\frac{3}{2}} Q_2^{1},
\end{aligned}
$$

and the relation with the nuclear quadrupole moment Q is

$$
\begin{aligned}
eQ &= \int \rho_n(\boldsymbol{r}_n)(3z^2 - r^2) dv_n \\
&= Q_{ZZ}.
\end{aligned}
$$

In the principal coordinate in which the EFG tensor is diagonalized, the electric quadrupole interaction energy is calculated as

$$
\begin{aligned}
W_E &= Q_2^2 V_2^{-2} + Q_2^0 V_2^0 + Q_2^{-2} V_2^2 \\
&= \frac{1}{4} V_{ZZ} Q_{ZZ} + \frac{1}{12}(V_{XX} - V_{YY})(Q_{XX} - Q_{YY}).
\end{aligned}
$$

Using the identical operator of Q_{ij},

$$
Q_{ij} = \frac{eQ}{I(2I-1)} \left[\frac{3}{2}(I_i I_j + I_j I_i) - \delta_{ij} I(I+1) \right],
$$

we get

$$
W_E = \frac{eQ}{4I(2I-1)} \left[V_{ZZ}(3I_Z^2 - I^2) + \frac{1}{2}(V_{XX} - V_{YY})(I_+^2 - I_-^2) \right].
$$

In the conventional notation, the coordinate axis is defined so that

$$
|V_{ZZ}| \geq |V_{YY}| \geq |V_{XX}|,
$$

are satisfied. Because of the Laplace equation $\sum_i V_{ii} = 0$, we can describe the EFG tensor by the electric field gradient q and the asymmetry parameter η as [98],

$$
\begin{aligned}
q &= V_{ZZ}, \\
\eta &= \frac{V_{XX} - V_{YY}}{V_{ZZ}}.
\end{aligned}
$$

Using this notation the interaction energy is given as,

$$
W_E = \frac{eqQ}{4I(2I-1)} \left[3I_Z^2 - I^2 + \frac{1}{2}\eta(I_+^2 - I_-^2) \right].
$$

2.3 High Field Limit

Now, the the hyperfine interaction is expressed in terms of the nuclear multipole moments and the magnetic field and the electric field gradient. The Hamiltonian of the system under the external field H_0, which is parallel to the z axis of the (xyz) coordinate fixed in space, is

$$
\begin{aligned}
H &= H_M + H_E \\
&= -g\mu_N H_0 I_z + \frac{eqQ}{4I(2I-1)} \left[3I_Z^2 - I^2 + \frac{1}{2}\eta(I_+^2 - I_-^2) \right],
\end{aligned}
$$

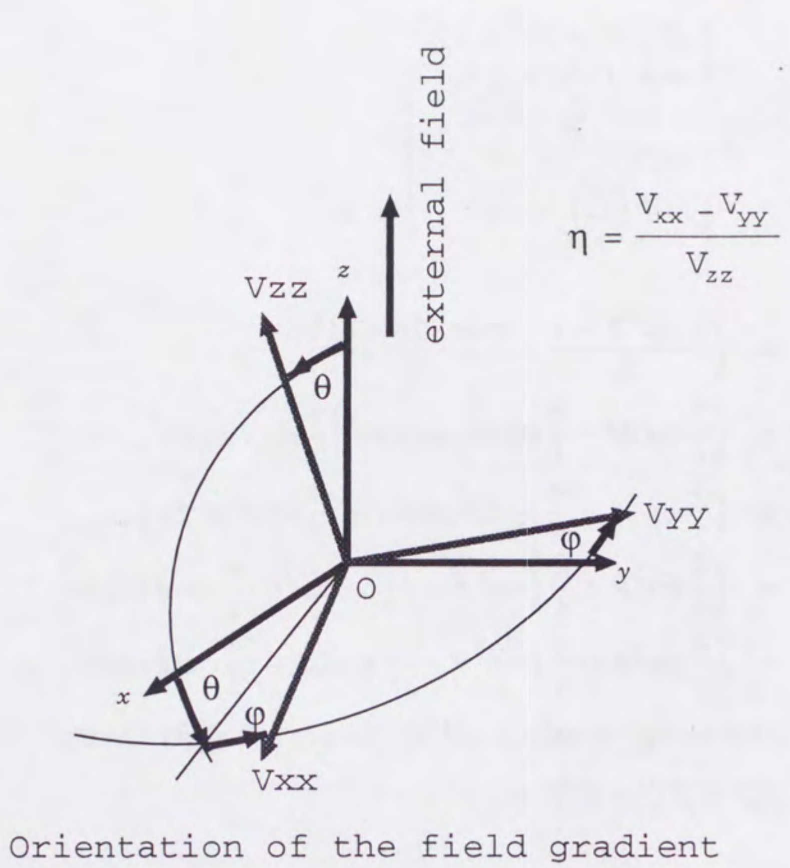

Figure 1: The Euler angles which describes the principal coordinate of the EFG.

where the principal coordinate of the EFG tensor is (XYZ). Under a high magnetic field, the electric quadrupole interaction is treated as a perturbation to the magnetic interaction. Here, the nuclear magnetic sub levels are calculated by the perturbation theory.

In general, (xyz) does not coincide with (XYZ) and the relation of them are described by the Euler angles (θ, ϕ) as shown in fig. 1. Rotating the angular momentum operator $I_{X,Y,Z}$ defined in the (XYZ) coordinate to the (xyz) coordinate, the electric quadrupole interaction Hamiltonian is written in the terms of $I_{x,y,z}$ as

$$H_E \;=\; \frac{eqQ}{4I\,(2I-1)} \left[\begin{array}{l} \left(\dfrac{3\cos^2\theta - 1}{2} + \dfrac{\eta\sin^2\theta\cos 2\phi}{2}\right)\left(3I_Z^2 - I\,(I+1)\right) \\ +\left(\dfrac{3}{4}\sin 2\theta - \dfrac{\eta}{4}\sin 2\theta\cos 2\phi + i\dfrac{\eta}{2}\sin\theta\sin 2\phi\right)\left(I_+ I_Z + I_Z I_+\right) \\ +\left(\dfrac{3}{4}\sin 2\theta - \dfrac{\eta}{4}\sin 2\theta\cos 2\phi - i\dfrac{\eta}{2}\sin\theta\sin 2\phi\right)\left(I_- I_Z + I_Z I_-\right) \\ +\left(\dfrac{3}{4}\sin^2\theta + \dfrac{\eta}{4}\left(\cos^2\theta + 1\right)\cos 2\phi - i\dfrac{\eta}{2}\cos\theta\sin 2\phi\right) I_+^2 \\ +\left(\dfrac{3}{4}\sin^2\theta + \dfrac{\eta}{4}\left(\cos^2\theta + 1\right)\cos 2\phi + i\dfrac{\eta}{2}\cos\theta\sin 2\phi\right) I_-^2 \end{array} \right]$$

$$= \frac{eqQ}{4I(2I-1)} \left[\begin{array}{l} \mathcal{F}\left(3I_Z^2 - I(I+1)\right) \\ +\mathcal{A}\left(I_+ I_Z + I_Z I_+\right) \\ +\mathcal{B}\left(I_- I_Z + I_Z I_-\right) \\ +\mathcal{C}\left(I_+^2\right) \\ +\mathcal{D}\left(I_-^2\right) \end{array} \right],$$

where,

$$\begin{aligned}
\mathcal{F} &= \left(\frac{3\cos^2\theta - 1}{2} + \frac{\eta \sin^2\theta \cos 2\phi}{2}\right) \\
\mathcal{A} &= \left(\frac{3}{4}\sin 2\theta - \frac{\eta}{4}\sin 2\theta \cos 2\phi + i\frac{\eta}{2}\sin\theta \sin 2\phi\right) \\
\mathcal{B} &= \left(\frac{3}{4}\sin 2\theta - \frac{\eta}{4}\sin 2\theta \cos 2\phi - i\frac{\eta}{2}\sin\theta \sin 2\phi\right) \\
\mathcal{C} &= \left(\frac{3}{4}\sin^2\theta + \frac{\eta}{4}\left(\cos^2\theta + 1\right)\cos 2\phi - i\frac{\eta}{2}\cos\theta \sin 2\phi\right) \\
\mathcal{D} &= \left(\frac{3}{4}\sin^2\theta + \frac{\eta}{4}\left(\cos^2\theta + 1\right)\cos 2\phi + i\frac{\eta}{2}\cos\theta \sin 2\phi\right).
\end{aligned}$$

Then, the interaction energy is calculated by the perturbation theory.

$$E_m = E_m^{(0)} + E_m^{(1)} + E_m^{(2)} + \cdots$$

$$\begin{aligned}
E_m^{(0)} &= \langle m|H|m\rangle \\
&= \langle m|H_M|m\rangle \\
&= -g\mu_N H_0 m \\
E_m^{(1)} &= \langle m|H_Q|m\rangle \\
&= \frac{eqQ}{4I(2I-1)}\left(\frac{3\cos^2\theta - 1}{2} + \frac{\eta\sin^2\theta\cos 2\phi}{2}\right)\left(3m^2 - I(I+1)\right) \\
E_m^{(2)} &= \sum_{n\neq m} \frac{\langle m|H_Q|n\rangle\langle n|H_Q|m\rangle}{E_m - E_n} =
\end{aligned}$$

$$\frac{1}{g\mu_N H_0}\left(\frac{eqQ}{4I(2I-1)}\right)^2 \left[\begin{array}{l} -|\mathcal{A}|^2((2m-1)^2(I-m+1)(I+m)) \\ +|\mathcal{B}|^2((2m+1)^2(I+m+1)(I-m)) \\ -\frac{1}{2}|\mathcal{C}|^2((I-m+2)(I+m-1)(I-m+1)(I+m)) \\ +\frac{1}{2}|\mathcal{D}|^2((I+m+2)(I-m-1)(I+m+1)(I-m)) \end{array} \right]$$

The intervals between the neighboring energy levels are equal under the magnetic field only, but are uneven under the perturbation by the electric quadrupole interaction. The energy shift by the quadrupole interaction depends only on the absolute values of the magnetic quantum number $|m|$ at the first order perturbation. The interval between the neighboring energy levels, or the transition frequencies are,

$$\begin{aligned}
\nu_{m\leftrightarrow m+1} &= (E_m - E_{m+1})/h \\
&= \nu_L - \frac{3eqQ}{4I(2I-1)h}\mathcal{F}(2m+1) \\
&\quad + \frac{2}{\nu_L}\left(\frac{eqQ}{4I(2I-1)h}\right)^2 \left[\begin{array}{l} (-4(I^2 - 6m^2) - 4(I - 6m) + 9)|\mathcal{A}|^2 \\ +(2(I^2 - 3m^2) + 2(I - 3m) - 3)|\mathcal{C}|^2 \end{array} \right]
\end{aligned}$$

Therefore, the NMR resonance appears only at the Larmor frequency $\nu_L = g\mu_N H_0/h$ if there is no quadrupole interaction. The quadrupole interaction causes split of the NMR resonance line. According to the nuclear spin I, we obtain $2I$ resonances in the NMR spectrum under the quadrupole interaction. It is noted that the frequency separations between the resonance lines are equal at the first order perturbation calculation. When I is half integer, the transition frequency between $m = -1/2$ and $m = 1/2$ is not affected at the first order, because $E_m^{(1)}$ depends only on $|m|$.

To understand the quadrupole effect on the nuclear energy levels, let us consider the most simple case, the nuclear spin $I = 1$ in the symmetric field gradient ($\eta = 0$) whose V_{ZZ} axis is along the external field H_0. The energy levels are then given by the first order calculation as

$$E_m \ = \ -g\mu_N H_0 m + \frac{eqQ}{8}\left(3m^2 - 2\right).$$

Suppose $Q > 0$ and $q > 0$, then $eqQ/h > 0$. So, the energy of $m = 0$ state shifts downwards and the energy of $|m| = 1$ states shifts upwards from the perturbation calculations as shown in fig. 2. The definition of Q shows that $Q > 0$ ($Q < 0$) means a prolate (oblate) deformation of the nucleus. And as will be shown in Section 5, $q > 0$ ($q < 0$) means that the electrons around the nucleus distribute densely in the xy-plane (z-axis). Now, the energy shifts of the levels is reasonable, because $m = 0$ means that the positive nuclear charge distribution get closer to the negative electron distribution and $|m| = 1$ means the positive charge get away from the negative charge distribution as shown in fig.2. So, comparing with the case of uniform electron distribution, the quadrupole interaction lowers the energy of the $m = 0$ state and raises those of the $|m| = 1$ states. In the cases of the other combinations of the sign of Q and q, the respective energy shift is understood in the same manner.

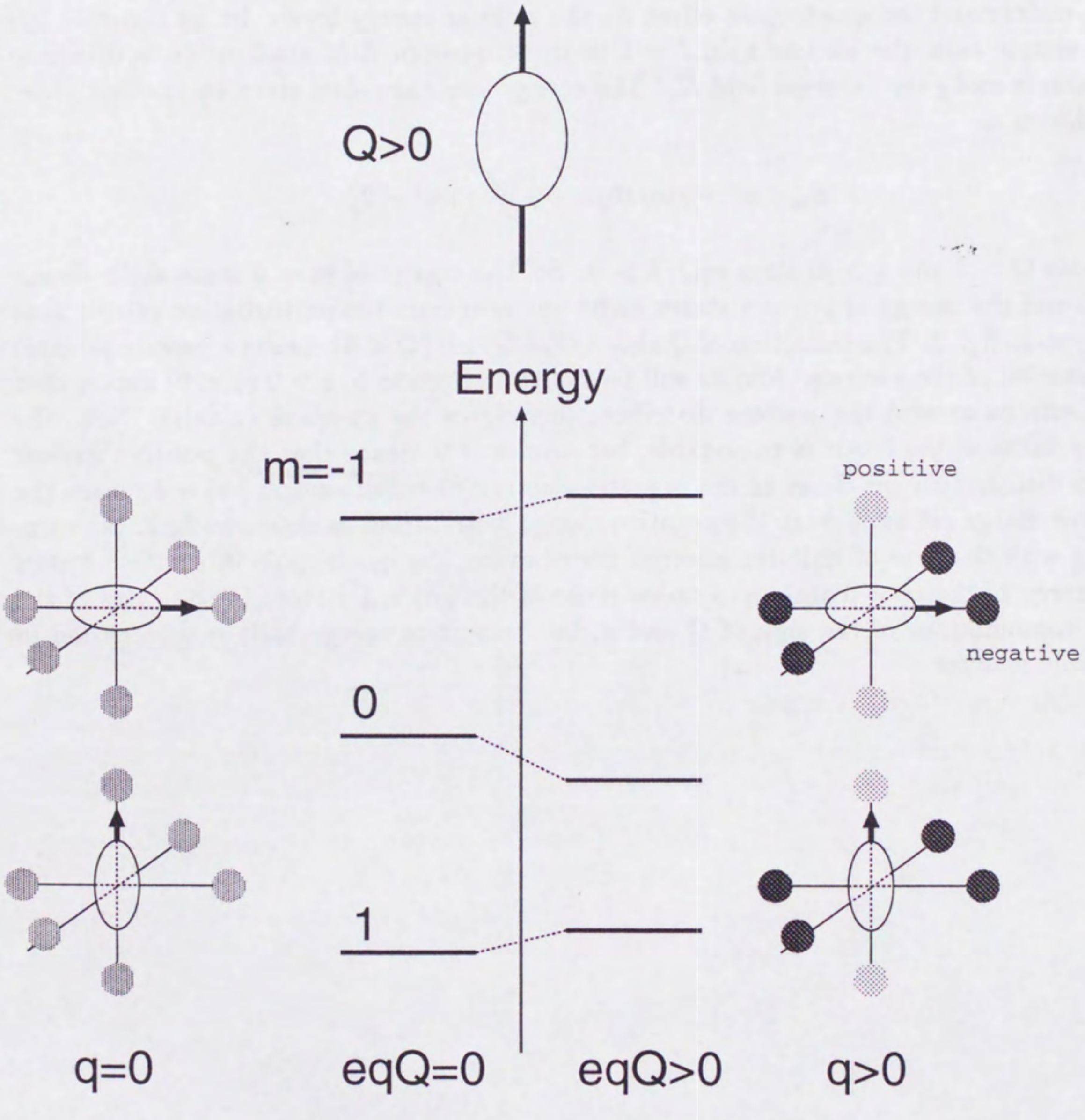

Figure 2: The energy shifts by the electric quadrupole interaction.

3 Calculation Principles and Methods

The overview of the band structure calculation used in the present study and the derivation of the EFG from the charge distribution are given. More detailed explanation on the density functional theory and the local density approximation will be given in appendix.

3.1 Band Structure Calculation

To deal with a system which consists of $N \sim 10^{23}$ scatterer, we have to introduce some approximations. Usually, the coordinates of nuclei are fixed at lattice points by the adiabatic approximation. For a periodic system such as a crystal, the Bloch's theorem tells us that we can get full information about an electronic structure of a whole crystal by solving a problem only about a unit cell [99]. In spite of these facts, it seems to be impossible to get N−electron wave function $\Psi(r_1, r_2, ..., r_N), N \sim 100$. To go ahead we need a prescription to reduce a many-body problem to a one-electron problem.

In the well known Hartree-Fock procedure, the N-body wave function is approximated to the Slater's determinant of one-electron orbitals. This leads to the N differential equations that are related each other through the exchange term (Fock term). The configuration mixing permits us to take the correlation effect into account. However, it is difficult to execute this scheme rigorously for a solid state.

In 1965, Kohn and Sham presented an effective scheme to treat a many electron system [19]. Their prescription is based on the Hohenberg-Kohn theorem [20]. This theorem tells us that we can regard a density of electron as a basic variable. Introducing a non-interacting many electron system K.-S. derived the self-consistent equations which described interacting many electrons. With the local density approximation for the exchange-correlation potential, it became possible to calculate the electronic structure of solids from the first principles [18].

In the density functional theory, the electron density is given as,

$$\rho(\boldsymbol{r}) = \sum_i |\psi_i(\boldsymbol{r})|^2,$$

in terms of the one electron wave functions ψ_i. ψ_i satisfies the one electron Schrödinger equation in an effective potential $V_{eff}(\boldsymbol{r})$.

$$-\boldsymbol{\nabla}_i^2 \psi_i(\boldsymbol{r}) + V_{eff}(\boldsymbol{r})\psi_i(\boldsymbol{r}) = \epsilon_i \psi_i(\boldsymbol{r}).$$

The effective potential describes the interactions with nuclei, the electron-electron interactions in the Hartree approximation and the rest, *i.e.*, the exchange-correlation potential.

$$V_{eff}(\boldsymbol{r}) = -2\sum_n \frac{Z^n}{|\boldsymbol{r} - \boldsymbol{R}^n|} + 2\int \frac{\rho(\boldsymbol{r}')}{|\boldsymbol{r} - \boldsymbol{r}'|} dv' + V_{XC}(\boldsymbol{r}).$$

If the exchange correlation potential V_{XC} is given exactly in a explicit form, the Kohn-Sham equations are solved strictly by an iteration procedure and the entire knowledge for a many body system is obtained. Several approximations to V_{XC} were proposed up to now. Most of them are based on the local density approximation (LDA) which was proposed by Kohn and Sham. In the LDA, we regard an inhomogeneous electron as a homogeneous one in local, *i.e.*,

$$
\begin{aligned}
E_{XC}[\rho] &\approx \int \rho\epsilon_{XC}(\rho)dv, \text{ so,} \\
V_{XC}[\rho] &\approx \epsilon_{XC}(\rho) + \rho\frac{\delta\epsilon_{XC}(\rho)}{\delta\rho}.
\end{aligned}
$$

We can get the exchange correlation energy per electron $\epsilon_{XC}(\rho)$ for an interacting homogeneous electron gas. Various approximations of $\epsilon_{XC}(\rho)$ were suggested, *e.g.*, the explicit form for spin-less case were given by Hedin and Lundqvist [100]. For a spin polarized case, von Barth and Hedin [101] developed the local spin density approximation (LSD) and proposed the spin polarized exchange correlation energy function $\epsilon_{XC}(\rho^+, \rho^-)$, where ρ^+ and ρ^- are the spin up and down components of the total electron density ρ, i.e., $\rho = \rho^+ + \rho^-$. Recently, Vosko, Wilk and Nusair [102] proposed new formula with referring to the Monte Carlo results by Ceperley and Adler [103]. Here the expression by von Barth and Hedin is given. We employ this expression with the parameterization after Moruzzi, Janak and Williams (MJW) [21]in our present calculations. The form by von Barth *et al.* is as,

$$
\begin{aligned}
\epsilon_{XC}(\rho^+, \rho^-) &= \epsilon^p_{XC}(r_s) + [\epsilon^f_{XC}(r_s) - \epsilon^p_{XC}(r_s)]f(\rho^+, \rho^-), \text{ where} \\
f(\rho^+, \rho^-) &= \left[\left(2\frac{\rho^+}{\rho}\right)^{4/3} + \left(2\frac{\rho^-}{\rho}\right)^{4/3} - 2\right]/(2^{4/3} - 2), \text{and} \\
\frac{4}{3}\pi r_s^3 &= 1/\rho.
\end{aligned}
$$

The paramagnetic and the ferromagnetic parts of energy functionals are given by

$$
\begin{aligned}
\epsilon^i_{XC} &= \epsilon^i_X(r_s) - c_i G(r_s/r_i), (i = p, f), \\
\epsilon^p_X &= -0.91633/r_s, \\
\epsilon^f_X &= 2^{1/3}\epsilon^p_X, \text{and} \\
G(x) &= (1 + x^3)\ln(1 + 1/x) - x^2 + \frac{x}{2} - \frac{1}{3}.
\end{aligned}
$$

The constants $c_p, c_f, r_p andr_f$ are chosen to fit ϵ_{XC} to that of the homogeneous electron gas. We use

$$
\begin{aligned}
c_p = 0.045, &\qquad c_f = c_p/2, \\
r_p = 21, &\qquad r_f = 2^{4/3}r_p
\end{aligned}
$$

after Moruzzi *et al.* [21].

One of the focus of the band structure calculation is to solve a one-electron Schrödinger equation. Under the periodic boundary condition, the electron states $\psi(\boldsymbol{r})$ satisfy the Bloch's theorem,

$$
\psi_k(\boldsymbol{r} + \boldsymbol{a}) = e^{i\boldsymbol{ka}}\psi_{\boldsymbol{k}}(\boldsymbol{r}),
$$

where $\boldsymbol{a}$ is any translation vector and $\boldsymbol{k}$ is the wave number of the electron. The eigenvalue problem for these states are efficiently solved by Korringa, Kohn and Rostoker [80]-[83].

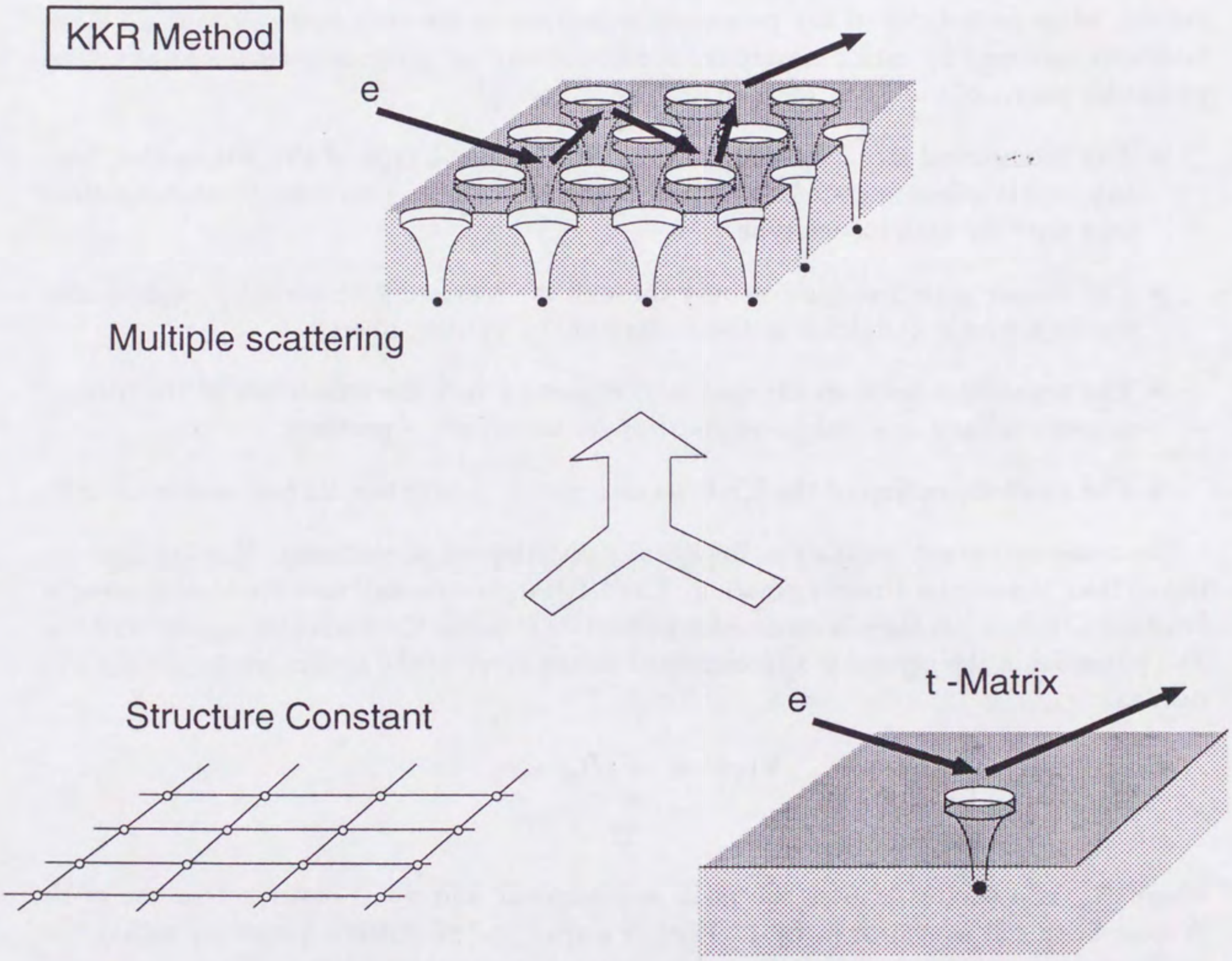

Figure 3: KKR method.

This method is called the KKR method after their names. They derived the secular equation of

$$\det|1 - t_L(E)g_{LL'}(E;\boldsymbol{k})| = 0,$$

where g is geometrical structure constants and t is a scattering t-matrix and L denotes (l,m). Roots of this equation determine a dispersion relation $E = E(\boldsymbol{k})$, *i.e.*, the band structure. Intuitively, the KKR method constructs wave functions by superposition as illustrated in fig. 3 [99]. In solid, electrons are scattered multiply by the array of the muffin tin potentials. Scattering by each potential is completely described by the t-matrix, while periodicity of the potentials is written in the structure constant g. Wave functions scattered by each t matrix are superposed by using the structure constant. The particular points of the KKR method are the followings.

- The geometrical structure constant which describe a type of the lattice (fcc, bcc, hcp, $\cdots$) is independent of a potential at the lattice site. Therefore, it must calculate only once for each lattice type.
- The atomic potential appears only through the scattering t-matrix (or equivalently the logarithmic derivative at the surface of the atomic sphere).
- The separation between the geometrical factors and the characters of the atomic potentials leads to a unique application for an impurity problem.
- The small dimension of the KKR secular matrix guarantees its fast computation.

The most important quantity is the density distribution of electrons. It is directly obtained from the crystal Green's function. The KKR method constructs the crystal Green's function $G(r,r';E)$ in the cell centered representation under the muffin tin approximation. The potential in the crystal is approximated to the array of the muffin tin potentials [99] such as

$$\begin{aligned} V(\boldsymbol{r}) &\approx V(\boldsymbol{R}_m + \boldsymbol{r}_m) \\ &= \sum_m v(\boldsymbol{r}_m), \end{aligned}$$

where $\boldsymbol{R}_m$ is a vector denotes the m-th lattice point and $\boldsymbol{r}_m$ is restricted in the m-th Wigner-Seitz cell as shown in fig.4. $V(\boldsymbol{r})$ is a spherical symmetric potential within the muffin tin sphere with radius R_{MT} and is constant in the interstitial region.

$$\begin{aligned} V(\boldsymbol{r}) &= V(r) \text{ for } r < R_{MT}, \\ &= 0. \quad \text{ for } r > R_{MT}. \end{aligned}$$

The cell centered representation [22, 31, 104, 105] of G is given as

$$\begin{aligned} G(\boldsymbol{r},\boldsymbol{r}';E) &= G(\boldsymbol{r}_m + \boldsymbol{R}_m, \boldsymbol{r}'_n + \boldsymbol{R}_n) \\ &= -i\sqrt{E}\delta_{mn}\sum_L Y_L(\boldsymbol{r})H_l^m(r_>;E)R_l^n(r_<;E)Y_L(\boldsymbol{r}') \\ &\quad + \sum_{L,L'} Y_L(\boldsymbol{r})R_l^m(r;E)G_{LL'}^{mn}R_{l'}^n(r';E)Y_{L'}(\boldsymbol{r}'), \end{aligned}$$

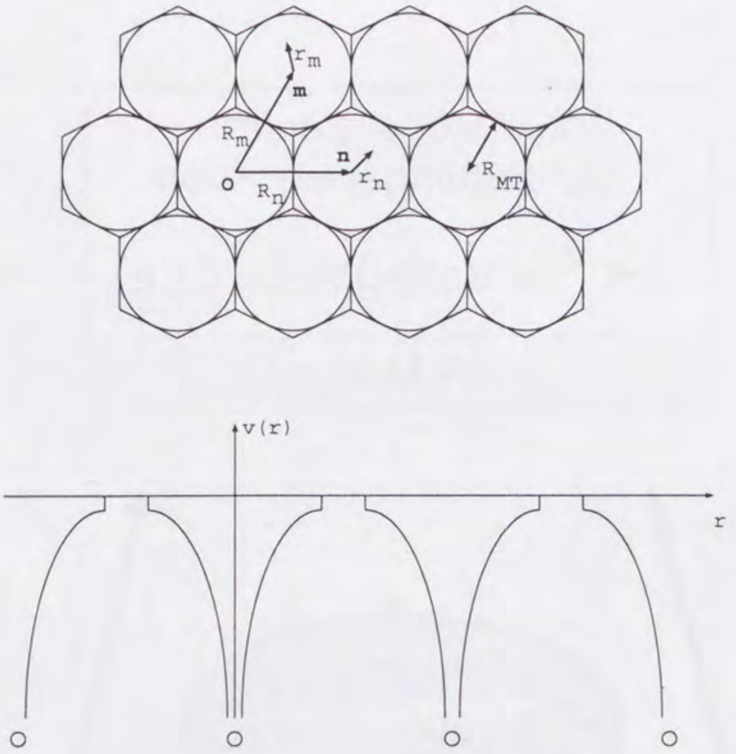

Figure 4: The muffin-tin potential.

where Y_L are the real spherical harmonics, $L = (l, m)$ denotes the angular momentum quantum number and R_l^n, H_l^n are the regular and irregular solutions of the radial Schrödinger equation at the n-th site. R_l^n and H_l^n are defined as the linear combinations of the spherical Bessel and spherical Hankel functions.

$$\begin{aligned} R_l^n(r;E) &= j_l(\sqrt{E}r) + \sqrt{E}t_l^n(E)h_l^{(1)}(\sqrt{E}r) \\ H_l^n(r;E) &= h_l^{(1)}(\sqrt{E}r), \end{aligned}$$

here, t_l^n is the scattering t-matrix which describes the single site scattering at the n-th site. The charge density $\rho = \sum_i \psi_i^* \psi_i$ is obtained from the imaginary part of the crystal Green's function as

$$\rho = -\frac{1}{\pi} \int ImG(\boldsymbol{r}, \boldsymbol{r}; E)dE.$$

The self consistent Kohn-Sham equations are solved by an iteration procedure as illustrated in fig. 5. Starting from a proper charge distribution, which is produced by superposing atomic charge densities for instance, we can reach to a self consistent solution finally independent of the starting condition. A given input charge density leads to an effective one electron potential which is given already. Under this effective potential, the new charge density ρ' is calculated by the KKR method. Generally, the obtained ρ' is different from ρ (from which the potential is constructed), therefore, the whole procedure is repeated until the difference becomes small enough. Practically, it is important to construct a new input from previous outputs by an efficient way to attain a self-consistency

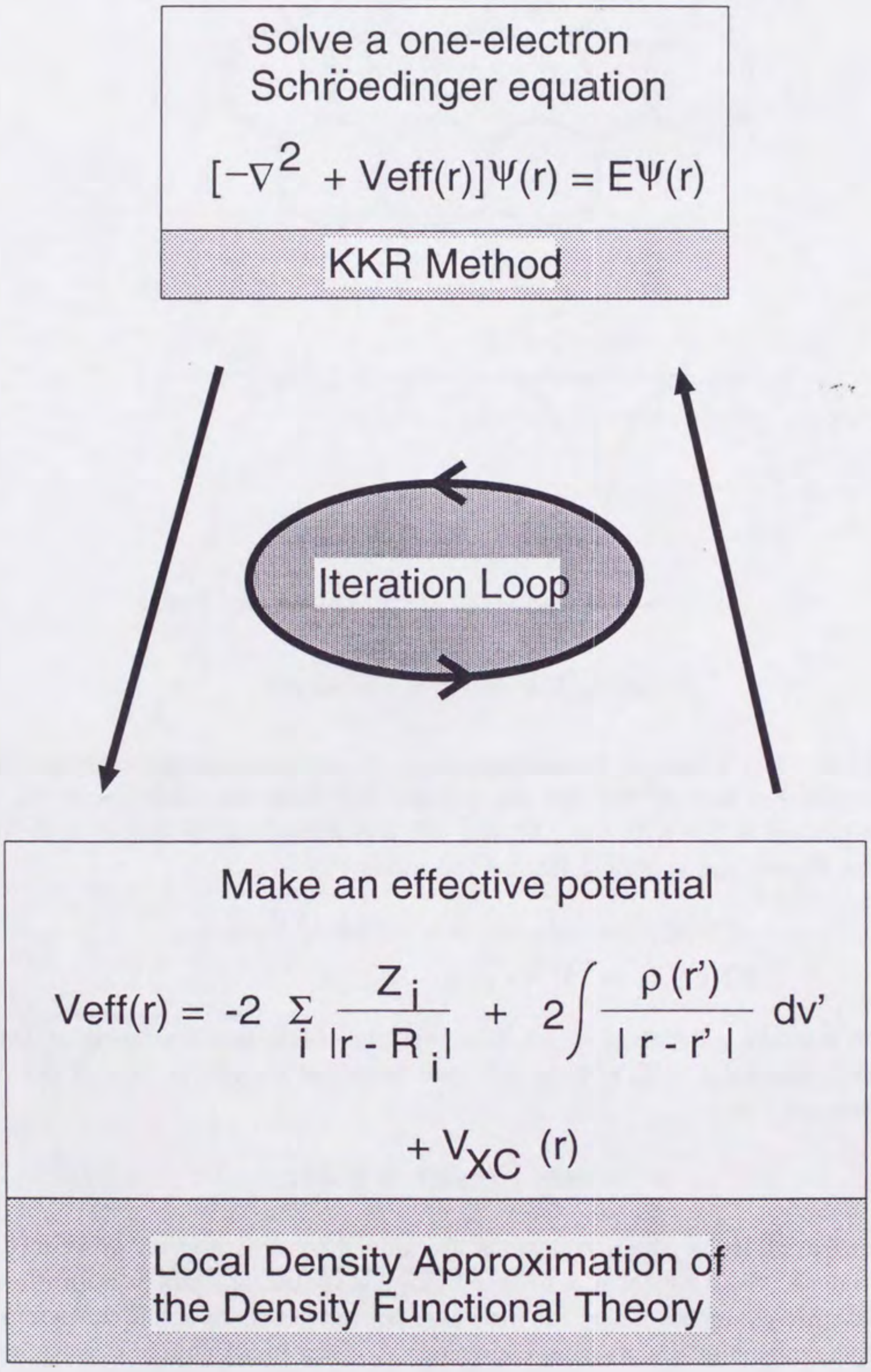

Figure 5: The schematic flowchart of the band structure calculation.

as fast as possible. A simple minded construction such as

$$\rho_{N+1}^{in} = \rho_N^{out}$$

usually leads to a divergence behavior because of severe charge oscillation. A contracted charge density leads to a rather repulsive potential and then this repulsive potential pushes out the charge density too much. This causes a too attractive potential and electrons rushes inward. The following simple mixing scheme is one of the solutions,

$$\rho_{N+1}^{in} = \alpha\rho_N^{out} + (1-\alpha)\rho_N^{in}.$$

The more efficient scheme, which applied the Chebychev acceleration technique to the self consistent iteration, was proposed by Akai and Dederichs [106]. The detail of this scheme is given in appendix.

3.2 EFG Calculation

In the muffin tin approximation, the Coulomb potential is divided into two parts [107, 108], *i.e.* the contribution from the charge density in the muffin tin sphere and the contribution from the assembly of ions at the lattice points as illustrated in fig. 6.

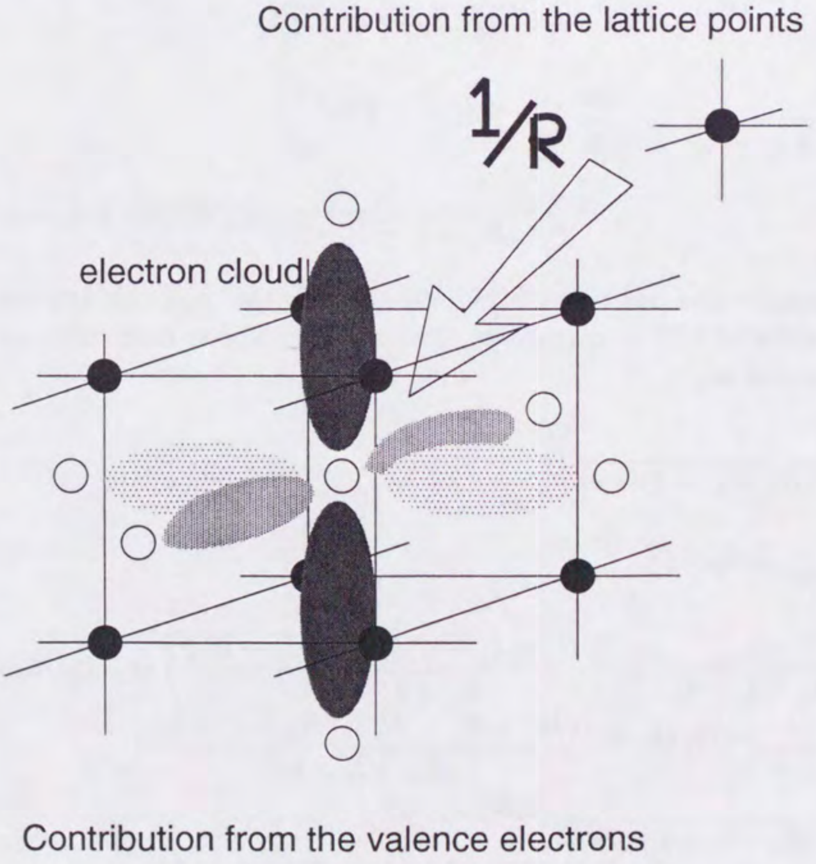

Figure 6: Origin of the electric field gradients.

$$\begin{aligned} V(\boldsymbol{r}_n) &= \int \frac{\rho_e(\boldsymbol{r}_e)}{|\boldsymbol{r}_n - \boldsymbol{r}_e|} dv_e + \sum_i \frac{Z_i}{|\boldsymbol{r}_n - \boldsymbol{R}_i|} \\ &= V^{MT} + V^{lat}, \end{aligned}$$

where Z_i is the total charge in the respective spheres.

The contribution of V^{lat} to the EFG is calculated straightforwardly by the Ewalt's method [99], which enables to converge a following summation fast.

$$\sum_i \frac{1}{|\boldsymbol{r}_n - \boldsymbol{R}_i|} = \frac{\pi}{v_c}\frac{1}{\eta^2} \sum_{\boldsymbol{g}} e^{i\boldsymbol{g}\boldsymbol{r}_n} \frac{e^{-g^2/4\eta^2}}{g^2/4\eta^2} + \sum_i \frac{1}{|\boldsymbol{R}_i - \boldsymbol{r}_n|} erfc(\eta|\boldsymbol{R}_i - \boldsymbol{r}_n|),$$

where v_c is a volume of a unit cell, η is an arbitrary constant and $erfc$ is the error function defined as

$$erfc(x) = \frac{2}{\sqrt{\pi}} \int_x^\infty e^{-s^2} ds.$$

When the unit cell has atoms more than one, contributions from respective atoms are summed up at the j-th site as,

$$\begin{aligned} V_j^{lat}(\boldsymbol{r}_n) &= \sum_i \sum_k \frac{Z_i}{|\boldsymbol{R}_k - \boldsymbol{r}_n + \boldsymbol{l}_j - \boldsymbol{l}_i|} \\ \sum_k \frac{1}{|\boldsymbol{R}_k - \boldsymbol{r}_n + \boldsymbol{l}_j - \boldsymbol{l}_i|} &= \frac{4\pi}{v_c} \sum_{\boldsymbol{g}} e^{i\boldsymbol{g}(\boldsymbol{l}_j - \boldsymbol{l}_i)} e^{i\boldsymbol{g}\boldsymbol{r}_n} \frac{e^{\frac{-g^2}{4\eta^2}}}{g^2} \\ &\quad + \sum_k \frac{1}{|\boldsymbol{R}_k + \boldsymbol{l}_j - \boldsymbol{l}_i - \boldsymbol{r}_n|} erfc(\eta|\boldsymbol{R}_k + \boldsymbol{l}_j - \boldsymbol{l}_i - \boldsymbol{r}_n|), \end{aligned}$$

where vector $\boldsymbol{l}_i$ denotes the position of the i-th atom in the unit cell as shown in fig. 7. The second derivative of V^{lat} is calculated directly from above expression of the sum of the Coulomb potential as,

$$\begin{aligned} &\frac{\partial^2}{\partial x_n \partial x_m} \left(\sum_i \sum_k \frac{1}{|\boldsymbol{R}_k + \boldsymbol{l}_j - \boldsymbol{l}_i - \boldsymbol{r}|} \right)\Bigg|_{\boldsymbol{r}=0} \\ &= -\frac{4\pi}{v_c} \sum_{\boldsymbol{g}} g_n g_m e^{i\boldsymbol{g}(\boldsymbol{l}_j - \boldsymbol{l}_i)} \frac{e^{-\frac{g^2}{4\eta 2}}}{g^2} \\ &+ \sum_k \left[\begin{array}{l} \left(\dfrac{-\delta_{nm}}{|\boldsymbol{R}_k + \boldsymbol{l}_j - \boldsymbol{l}_i|^3} + \dfrac{3(\boldsymbol{R}_k + \boldsymbol{l}_j - \boldsymbol{l}_i)_m (\boldsymbol{R}_k + \boldsymbol{l}_j - \boldsymbol{l}_i)_n}{|\boldsymbol{R}_k + \boldsymbol{l}_j - \boldsymbol{l}_i|^5} \right) erfc(\eta|\boldsymbol{R}_k + \boldsymbol{l}_j - \boldsymbol{l}_i|) \\ \quad + \dfrac{4\eta}{\sqrt{\pi}} e^{-\eta|\boldsymbol{R}_k + \boldsymbol{l}_j - \boldsymbol{l}_i|^2} \dfrac{(\boldsymbol{R}_k + \boldsymbol{R}_j - \boldsymbol{R}_i)_m (\boldsymbol{R}_k + \boldsymbol{l}_j - \boldsymbol{l}_i)_n}{|\boldsymbol{R}_k + \boldsymbol{l}_j - \boldsymbol{l}_i|^4} \\ \quad + \dfrac{1}{|\boldsymbol{R}_k + \boldsymbol{l}_j - \boldsymbol{l}_i|} \dfrac{2}{\sqrt{\pi}} \eta e^{-\eta|\boldsymbol{R}_k + \boldsymbol{l}_j - \boldsymbol{l}_i|^2} \times \\ \quad \left(\begin{array}{l} \dfrac{-\delta_{nm}}{|\boldsymbol{R}_k + \boldsymbol{l}_j - \boldsymbol{l}_i|} + \dfrac{2\eta(\boldsymbol{R}_k + \boldsymbol{l}_j - \boldsymbol{l}_i)_m (\boldsymbol{R}_k + \boldsymbol{l}_j - \boldsymbol{l}_i)_n}{|\boldsymbol{R}_k + \boldsymbol{l}_j - \boldsymbol{l}_i|} \\ \quad + \dfrac{(\boldsymbol{R}_k + \boldsymbol{l}_j - \boldsymbol{l}_i)_m (\boldsymbol{R}_k + \boldsymbol{l}_j - \boldsymbol{l}_i)_n}{|\boldsymbol{R}_k + \boldsymbol{l}_j - \boldsymbol{l}_i|^3} \end{array} \right) \end{array} \right] \end{aligned}$$

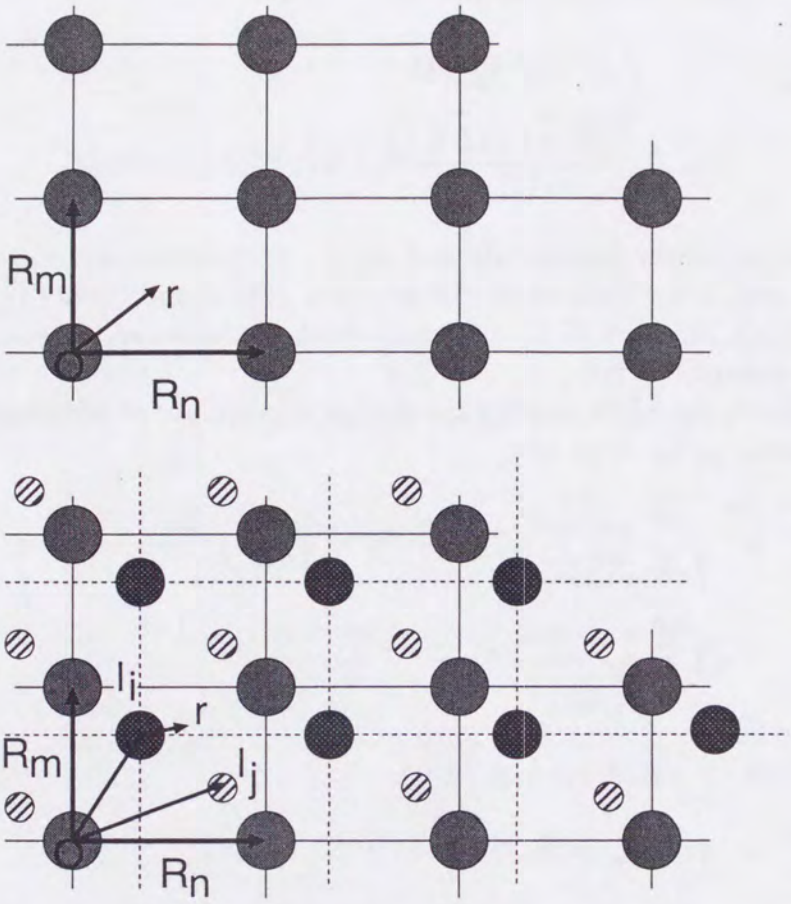

Figure 7: The lattice contributions to the EFG.

The electron density distribution in each muffin tin sphere is calculated from the imaginary part of the Crystal Green's function [22].

$$\rho_e(r) \;=\; -\frac{1}{\pi}\mathrm{Im}\int^{\epsilon_f} G(r,r;E)dE.$$

In the KKR-Green's function formalism, the crystal Green's function is doubly expanded by the eigenfunctions in each cell as shown in the previous section. Including the single site contribution [85],

$$\rho_e^n(r) \;=\; -\frac{1}{\pi}\mathrm{Im}\sum_{L,L'}\int^{\epsilon_f} R_l^{n*}(r,E)Y_L^*(r)\widetilde{G_{LL'}^{nn}}(E)R_{l'}^n(r,E)Y_{L'}(r)dE.$$

Consequently, the diagonal elements of $\int \widetilde{G_{LL'}^{nn}}dE$ are the population of the respective orbitals. As shown in section 2, the Coulomb potential is expanded into the multipoles, and the EFG is determined by the $l=2$ term.

$$\begin{aligned} V_2^M &= \sqrt{\frac{4\pi}{5}}\int \frac{\rho_e(r)}{r^3}Y_2^{M*}dv \\ &= \sqrt{\frac{4\pi}{5}}\sum_{l,l'} C_{ll'2}^{mm'M}\int dE\widetilde{G_{ll'}^{mm'}}(E)\int \frac{R_l^*(r;E)R_{l'}(r;E)}{r^3}r^2dr, \end{aligned}$$

here, $C_{ll'L}^{mm'M}$ is the Gaunt coefficient defined by

$$\begin{aligned} C_{ll'L}^{mm'M} &= \int Y_l^{m*} Y_{l'}^{m'} Y_L^M d\Omega \\ &= \sqrt{\frac{(2l'+1)(2L+1)}{4\pi(2l+1)}} \langle LMl', m'|lm\rangle \langle L0l'0|l0\rangle . \end{aligned}$$

These integrals are performed numerically and the V_{ij} components are calculated by the formulae given in section 2. Because of the selection rule of the Clebsh-Gordon coefficients, $(l, l') = (1,1), (2,2), (2,0), (0,2) \cdots$ terms, which are called pp, dd, sd contributions respectively, are remained [48, 54].

To show the origin of the EFG, now let the energy dependence of $R(r)$ neglected, then the pp, dd contribution to V_{2^0} term are

$$\begin{aligned} V_2^0 &= \sqrt{\frac{4\pi}{5}} \sum_{l=1,2} \sum_{mm'} C_{2ll}^{0mm'} \int \widetilde{G_{ll}^{mm'}}(E) dE \int \frac{|R_l(r)|^2}{r^3} r^2 dr \\ &= \sqrt{\frac{4\pi}{5}} \sum_m C_{211}^{0mm} p_m \langle \frac{1}{r^3} \rangle_p + \sum_m C_{222}^{0mm} d_m \langle \frac{1}{r^3} \rangle_d \\ &= V^{pp} + V^{dd} \\ V^{pp} &\propto \left(\frac{1}{2}(p_x + p_y) - p_z \right) \langle \frac{1}{r^3} \rangle_p \\ V^{dd} &\propto \left((d_{x^2-y^2} + d_{xy}) - \frac{1}{2}(d_{yz} + d_{xz}) - d_{z^2} \right). \end{aligned}$$

Now, it is clear that the anisotropic charge distribution around the nucleus creates the EFG, and the relation between the sign of the EFG and the population difference is also evident.

4 β-NMR Detection of ^{12}N and ^{19}O in TiO$_2$

For the study of the EFGs of light impurities in TiO_2, the quadrupole coupling constants of ^{12}N ($I^\pi = 1^+, T_{1/2} = 11$ ms) and ^{19}O ($I^\pi = 5/2^+, T_{1/2} = 27$ sec) in a TiO_2 single crystal (rutile structure, see fig. 8). The conventional β-NMR method was utilized for the experiments on ^{12}N [11], while the β-NQR [109] method were used for ^{19}O, which is a modified β-NMR technique to observe a quadrupole splitting of a resonance line efficiently. The quadrupole moment of ^{12}N has already determined to be 9.8± 0.9 mb by Minamisono *et al.* [109], however, the quadrupole moment of ^{19}O has not been determined. So, at the first stage the quadrupole moment of ^{19}O was determined, then information on the field gradient is derived. In Section 8 their implantation sites in TiO_2 are discussed by comparing the experimental EFGs with EFG calculations for plausible sites.

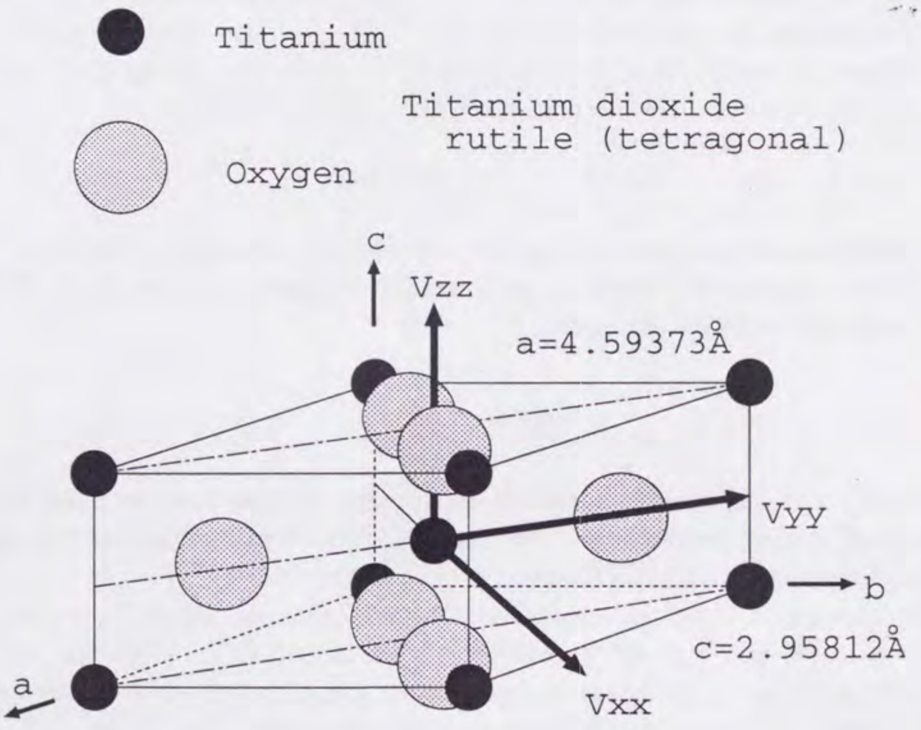

Figure 8: The crystal structure of TiO_2 (Rutile). The definition of the principal axis of the EFG is also given.

The rutile (TiO_2) structure [110, 57] is tetragonal with metal atoms (Ti) located at $(0,0,0), (1/2,1/2,1/2)$ and anions (O) located at $(1 \pm u, 1 \pm u, 0), (1/2 \pm u, 1/2 \mp u, 1/2)$ with the internal coordinate parameter u=0.3053. The Ti atoms are surrounded by a slightly distorted octahedron of oxygen atoms. The metal positions are identical by a 90° rotation around the crystal c axis followed by the $(1/2, 1/2, 1/2)$ translation. Considering this crystal symmetry, the principal axes of the EFG tensor are such as shown in fig.8 for pure TiO_2. In the figure, the directions of V_{ZZ}, V_{YY}, V_{XX} are shown for Ti site. The direction of V_{ZZ} was determined from the NMR experiment on Ti explained later, however, there is no way to distinguish $\langle 110 \rangle$ from $\langle 1\bar{1}0 \rangle$ experimentally. So, the direction of V_{YY}

and V_{XX} are assumed to be the same as the theoretical predictions presented later.

4.1 ^{12}N in TiO$_2$

The ^{12}N nuclei were produced via the ^{10}B(^{3}He, n)^{12}N reaction. The incident ^{3}He beam of 3.0 MeV was extracted from the Van de Graaff accelerator. The ^{12}N nuclei ejected at the recoil angle of $20 \pm 8°$ relative to the incident beam were selected to obtain the optimum nuclear polarization along the reaction normal. The polarized ^{12}N nuclei were implanted into a catcher of a single crystal TiO_2 placed under a strong external field of 7.3 kOe parallel to the polarization. The β-ray asymmetry was detected by two plastic scintillation counter telescopes placed above and below the catcher relative to the polarization. After a beam-on production time of 10 ms, the β-rays were detected during 20 ms. During 5 ms between the beam time and the counting time, an rf magnetic field was applied perpendicular to the polarization for a spin manipulation. The present experimental set up for β-NMR detection is schematically shown in fig. 9. The angular distribution of β-rays emitted from an ensemble of polarized nuclei as a function of the electron ejection angle θ defined relative to the direction of the polarization P is given as,

$$W(\theta) \;=\; 1 + AP\cos\theta,$$

where A is the asymmetry parameter. The ratio of the β-ray counts in the upper counter to that in the lower counter for the rf-on cycle was normalized by that of the rf-off cycle to obtain the β-ray asymmetry change as,

$$\Delta \;=\; \frac{(u/d)_{on}}{(u/d)_{off}} - 1 \sim 2A(P_{on} - P_{off}),$$

where P_{on} and P_{off} are the nuclear polarization detected during the counting sections in the rf-on and rf-off cycles, respectively. By mapping the β-ray asymmetry change as a function of the rf frequency, the NMR spectra were observed.

The β-NMR spectra of ^{12}N were obtained for two cases as shown in fig.10. In the first step, the crystal c-axis was set parallel to the external field. With this set up, we found two sets of quadrupole splittings in the spectrum as denoted by the closed triangles in fig.10. This result suggests two different implantation sites for ^{12}N in TiO_2. In the second step, we observed the β-NMR spectrum with the crystal $\langle 110 \rangle$ axis set parallel to the external field to obtain complete knowledge on these EFG tensors. Considering the crystal symmetry of the TiO_2, two sets of quadrupole splittings have to be observed for each site in this set up. They are shown in fig.10 for respective sites by the open circles. In the figures, the dotted curves and the solid curves are the best fitted Gaussians. From these analyses, the quadrupole coupling constants for site 1 and site 2 were deduced to be $+469 \pm 5$ kHz and $+2888 \pm 12$ kHz, respectively. The asymmetry parameters, $\eta = 0.37 \pm 0.02$ and $\eta = 0.038 \pm 0.005$ were determined for site 1 and site 2, respectively. For each site, the splitting width in the case of $H_0 // c$-axis was middle. This means that the V_{YY} component for each site is along the c-axis. The results are summarized in table 1 with the experimental EFGs deduced based on the quadrupole moment of ^{12}N of $+9.8 \pm 0.9$ mb [109].

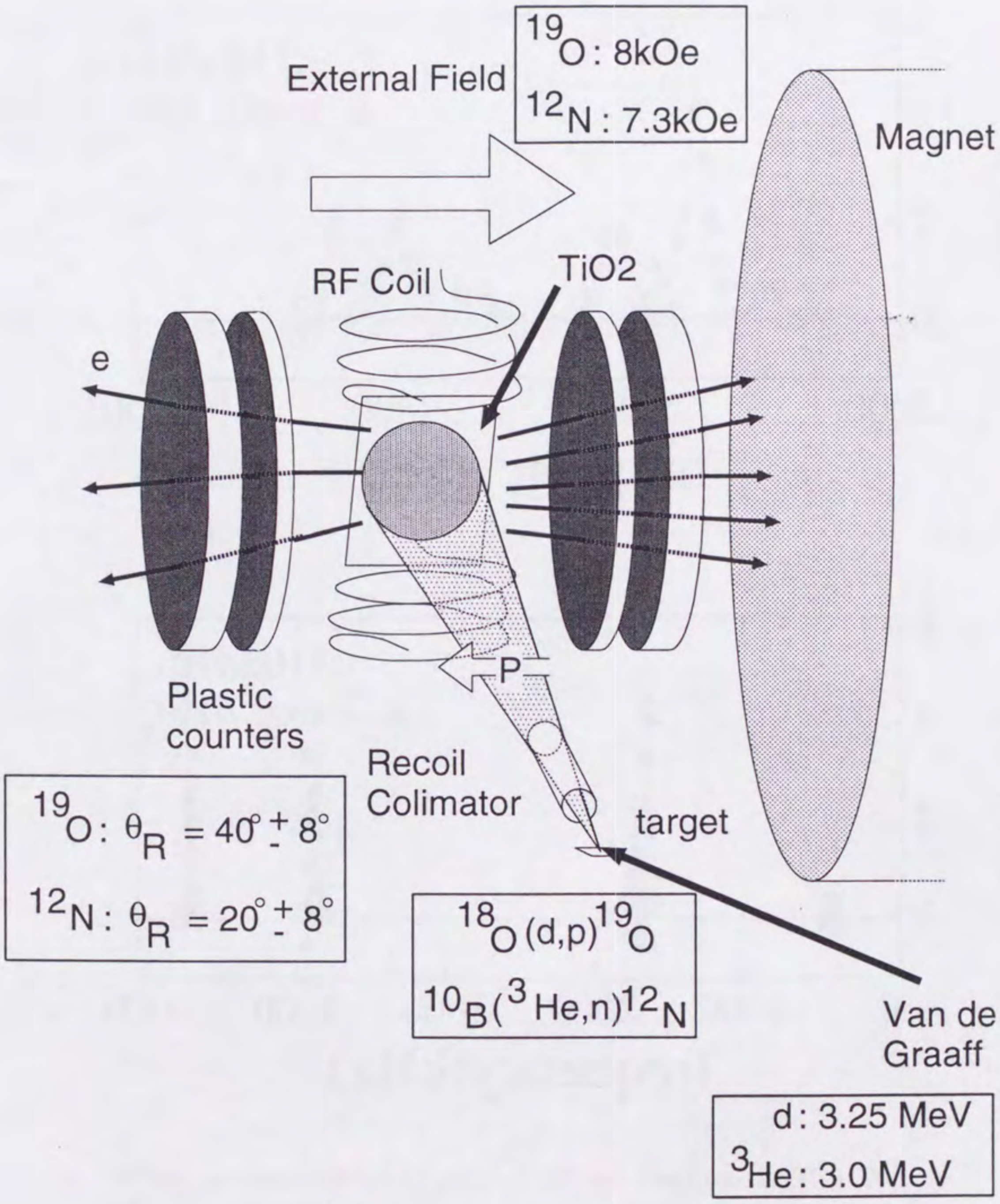

Figure 9: Sketch of the experimental set up for the *beta*-NMR detection.

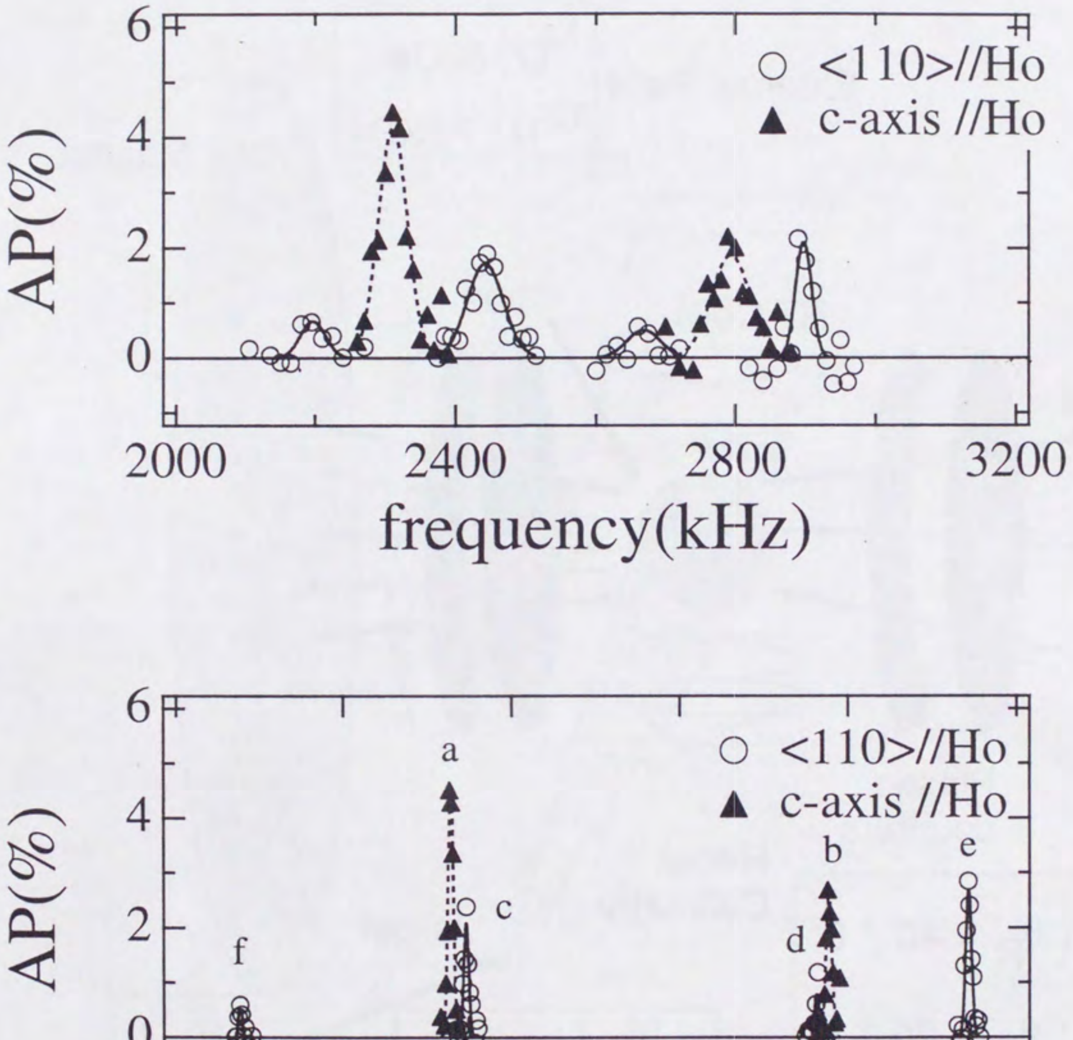

Figure 10: β-NMR spectrum for ^{12}N in TiO_2 under the external field of 0.73 T for respective implantation sites. (Up: site 1, Down: site 2) The closed triangles mean that the c-axis was set parallel to the external field and the open circles mean that the $\langle 110 \rangle$ axis was parallel to the external field.

Table 1: The electric coupling constants of ^{12}N and the electric field gradients at N site in TiO_2. The EFGs was derived with the $Q(^{12}\mathrm{N})=+9.8\pm0.9$ mb .

	site 1	site 2
eqQ/h (MHz)	+469±5	+2888±12
η	0.37±0.02	0.038±0.005
$q(10^{19}\mathrm{V/m^2})$	+198±14	+1220±85
	$V_{YY}//$c	$V_{YY}//$c

4.2 ^{19}O in TiO_2

The production of polarized ^{19}O nuclei was carried out by use of the $^{18}\mathrm{O(d, p)}^{19}\mathrm{O}$ nuclear reaction. An incident beam of deuteron with an energy of 3.25 MeV extracted from the Van de Graaff accelerator at the Osaka University was used for the production. The deuteron beam was used to bombard a TiO_2^{18} target which was produced by oxidizing a 0.5 mm thick titanium foil with ^{18}O [111]. The recoil angle of ^{19}O was selected to be $40 \pm 8°$. A TiO_2 crystal was used as an implantation medium and was placed in an external magnetic field of 8 kOe to maintain the polarization and to detect β-NQR of ^{19}O. The experimental set up is schematically shown in fig. 9. Under the electric quadrupole interactions, $2I$ resonance lines are observed as explained in section 2. For $I = 5/2$ case, their frequencies ν_m are

$$\begin{aligned}\nu_m &= \nu_L - \nu_Q\left(m - \frac{1}{2}\right)\left(3\cos^2\theta - 1 + \eta\sin^2\theta\cos 2\phi\right)/2,\\ \nu_Q &= \frac{3eqQ}{2I(2I-1)h}\\ &= \frac{3eqQ}{20h}.\end{aligned}$$

The polarization change induced by one of the resonance lines ν_m in the conventional β-NMR detection is about 1/44 of the initial polarization, which is estimated with the assumption of a negligible initial spin alignment. Therefore, for the efficient detection of the resonance lines perturbed under the electric quadrupole interactions, the β-NQR technique were employed. The β-NQR technique is illustrated in fig. 11. In this technique, magnetic resonances were observed as a function of ν_s, which is the separation of the transition frequencies between the magnetic sub-states m and $m \pm 1$. The five ν_m calculated from ν_s are applied simultaneously during one rf time. At the right coupling frequency the initial polarization is completely destroyed and the full NMR effect of $-2P_{off}$ is observed. Therefore, a β-NQR spectrum is directly detected with the maximum efficiency as a function of the coupling frequency. For a more effective measurement, we can utilize the AFP technique. The sequential application of five modulated rf with a proper intensity in a correct order makes it possible to achieve the inverted population of the initial one. So, we can get the NMR effect of $8AP_{off}$ at the maximum. We determined the Larmor frequency ν_L in TiO_2 by observing the transition between $m = 1/2$ and $m = -1/2$ which was free from the electric quadrupole interaction at the first order perturbation theory. With the measured ν_L, we calculated the five frequencies corresponding to a trial ν_s.

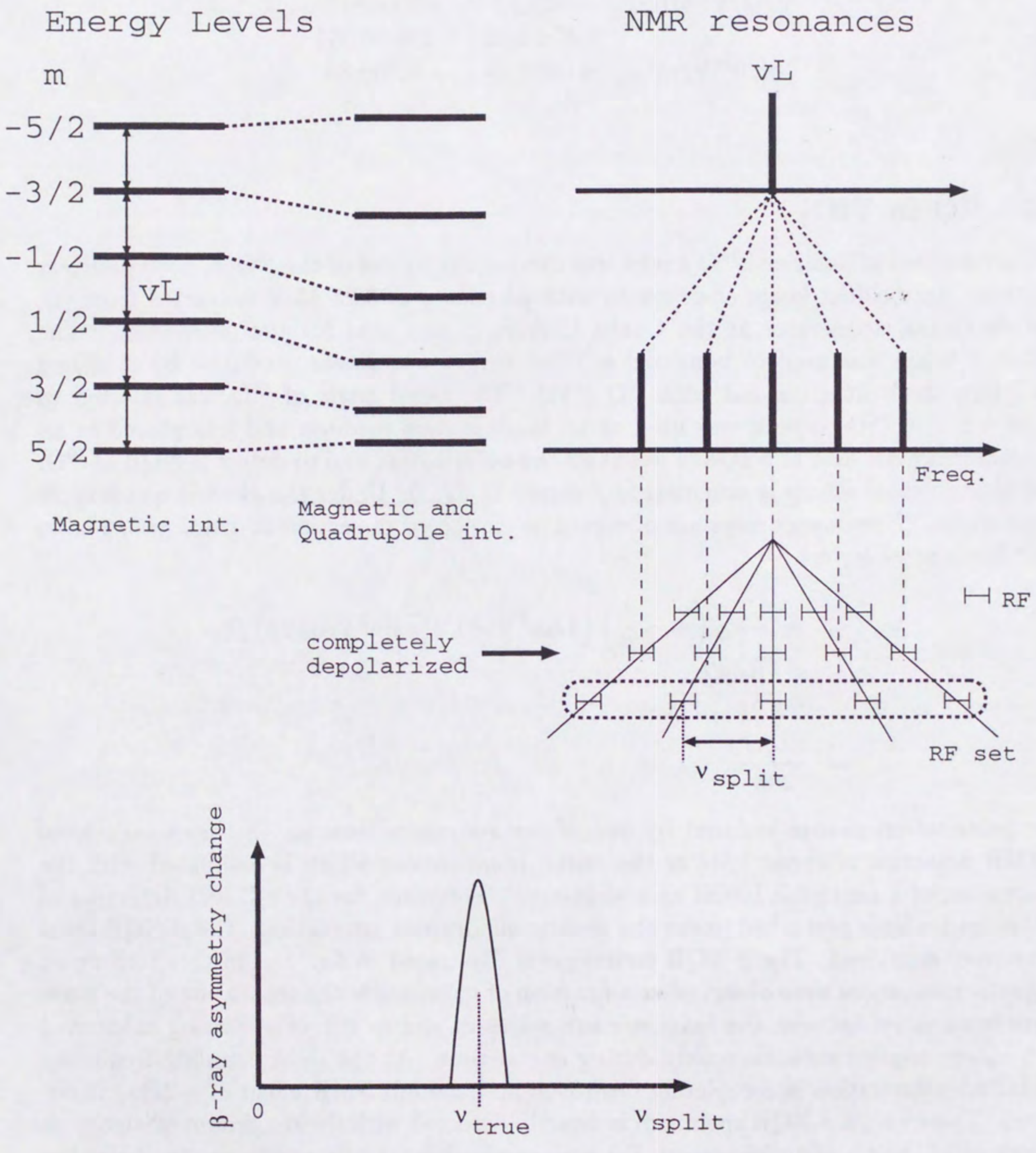

Figure 11: Schematic explanation on the β-NQR technique.

The ν_s is a function of not only the coupling constant eqQ/h but also the asymmetry parameter η, all of which must be determined experimentally. It depends also on the orientation of the principal axes of the EFG relative to the external field. So, to get a complete knowledge on the EFG, we have to measure the β-NQR spectra at least at two different crystal orientations. For the first trial, the c axis of the crystal was set parallel to the magnetic field. Under this set up, two EFGs for the two identical oxygen sites is equivalent. We performed β-NQR with monochromatic RF fields with their amplitude H_1 of 0.3 Oe and the duration time of 30 msec. The obtained spectrum is shown in fig.12. Two peaks were found corresponding to two implantation sites for oxygen atoms. We analyzed the spectrum assuming Gaussian type line shapes. The solid line is the best fit to the data. We derived two split frequencies $\nu_s^{(1)} = 2.64 \pm 0.19$ kHz (site 1) and $\nu_s^{(2)} = 6.31 \pm 0.12$ kHz (site 2) for these two resonances.

In the next step, the crystal $\langle 110 \rangle$ axis was set parallel to the external field. In this setup, two resonance lines are observed for each oxygen site. Considering that the main component of EFG (q) is in the direction of the $\langle 110 \rangle$ axis, two resonances in the β-NQR spectrum for an implantation site will be observed at ν_Q and $\nu_Q - \nu_s$. Therefore, we will have four resonances in the β-NQR spectrum for the two different sites. We employed the AFP technique for the β-NQR measurement. RF fields with H_1 of 3 Oe and the duration time of 100 ms, and the frequency modulation width of ± 10 kHz were applied. Fig.12 shows the obtained β-NQR spectrum. Because of the small $\nu_s^{(1)}$ and $\nu_s^{(2)}$, each resonance peak at ν_Q could not be resolved from that at $\nu_Q - \nu_s$ to form one broad line. The Gaussian type line shape was assumed for each resonances and used to fit the data. The solid line in fig.12 is the best fit. Contributions from each resonances are shown by the dashed lines. $\nu_Q^{(1)} = 31.9 \pm 0.5$ kHz and $\nu_Q^{(2)} = 52 \pm 1$ kHz were extracted for each resonances from the spectrum.

The η for the first peak at lower frequency is calculated to be 0.836 ± 0.008 from $\nu_s^{(1)}$ and $\nu_Q^{(1)}$. This is in good agreement with the $\eta = 0.831 \pm 0.007$ derived from the FT-NMR experiment for the substitutional site of O [112]. Therefore, we assign $\nu_s^{(1)}$ and $\nu_Q^{(1)}$ to the signals from oxygen atoms in the oxygen substitutional sites. The electric quadrupole coupling constant $|eqQ/h|$ of ^{19}O in the TiO$_2$ at the oxygen substitutional site was thus obtained to be 213 ± 2 kHz. For the other implantation site, $|eqQ/h|$ and η were determined to be 350 ± 9 kHz and 0.760 ± 0.009, respectively. It is suggested that the second implantation site is an interstitial site in TiO$_2$ from the analogy of the experimental results on ^{12}N in TiO$_2$.

Now, we can derive the quadrupole moment of ^{19}O. Using the known quadrupole moment of ^{17}O [113], we extracted EFG at the oxygen substitutional site from the coupling constant, which had been measured by the FT-NMR on ^{17}O. Therefore, we can derive the quadrupole moment of ^{19}O nuclei from $|eqQ/h|$ at the oxygen substitutional site. As a result, the quadrupole moment of ^{19}O is determined to be 3.7 ± 0.4 mb. Using the obtained quadrupole moment of ^{19}O, the EFG at the interstitial site was derived to be $390 \pm 40 \times 10^{19}$ V/m^2.

The present results on the implantation site of O isotope are also important to determine the quadrupole moment of ^{13}O ($I^\pi = 3/2^-, T_{1/2} = 8.6$ ms). The β-NQR spectrum had already been measured for ^{13}O in TiO$_2$ by Tanigaki *et al.* [114]. The β-NQR was detected as a function of Δf which was defined as a half of the quadrupole splitting or the deviation from the Larmor frequency. Typical spectrum is shown in fig.13. As shown in the figure, the obtained spectrum is similar to that for ^{19}O. Unfortunately, the peak

Table 2: The electric coupling constants of O isotopes and the electric field gradients at O site in TiO_2. The EFGs was derived with the $|Q(^{17}O)|=26\pm3$ mb , and $|Q(^{19}O)|=3.7\pm0.4$ mb

	site 1 O substitutional	site 2
^{17}O		
eqQ/h (kHz)	1512±4	—
η	0.831±0.007	—
$\lvert Q\rvert$ (mb)	26±3	
$\lvert q\rvert(10^{19}\mathrm{V/m^2})$	240±30	—
	$V_{XX}//c$	—
^{19}O		
eqQ/h (kHz)	213±2	350±9
η	0.836±0.008	0.760±0.009
$\lvert Q\rvert$ (mb)	3.7±0.4	
$\lvert q\rvert(10^{19}\mathrm{V/m^2})$	(240±30)	390±40
	$V_{XX}//c$	$V_{XX}//c$
^{13}O		
eqQ/h (kHz)	—	1070±60
η	—	(390±40)
$\lvert Q\rvert$ (mb)	11±1	

at the lower frequency side of the spectrum which corresponds to the substitutional site was not complete, and the experiment was not performed in the different direction of the crystal. However, we could derive the electric quadrupole coupling constant at site 2 by using the η measured by the ^{19}O. From the analysis of the spectrum, $|eqQ/h|$ was obtained to be 1070 ± 60 kHz. Then, comparing the coupling constants of ^{19}O and ^{13}O at site 2, we can derive the quadrupole moment of ^{13}O to be 11±1 mb with using the presently determined $Q(^{19}O)=3.7\pm0.4$ mb.

The results are summarized in table. 2

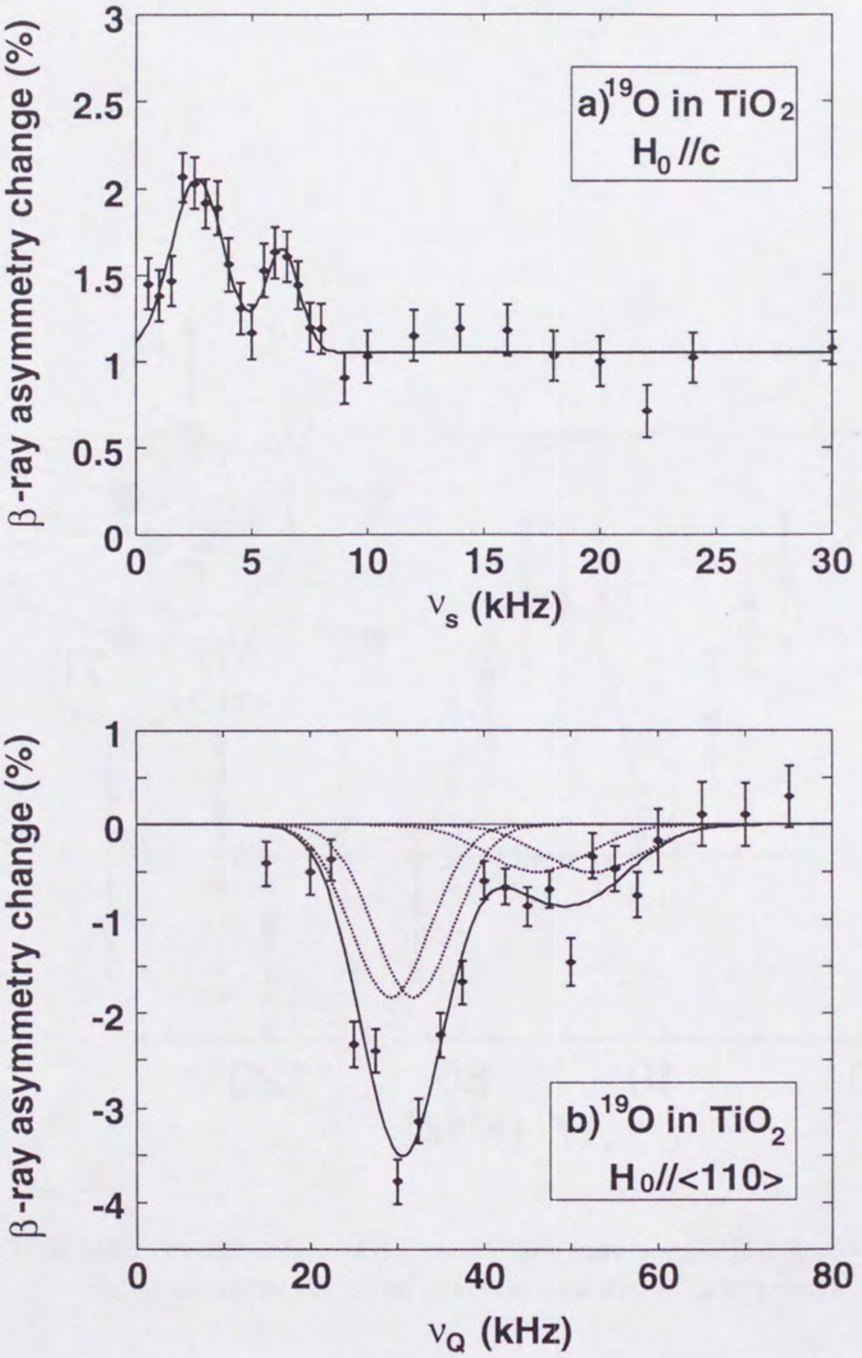

Figure 12: β-NQR spectrum for ^{19}O in TiO$_2$ under the external field of 8 kOe. (a) The crystal c-axis was set parallel to the external field. (b) The crystal $\langle 110 \rangle$ axis was set parallel to the external field. Each resonance consists of two adjacent peaks as shown by two broken curves for each site.

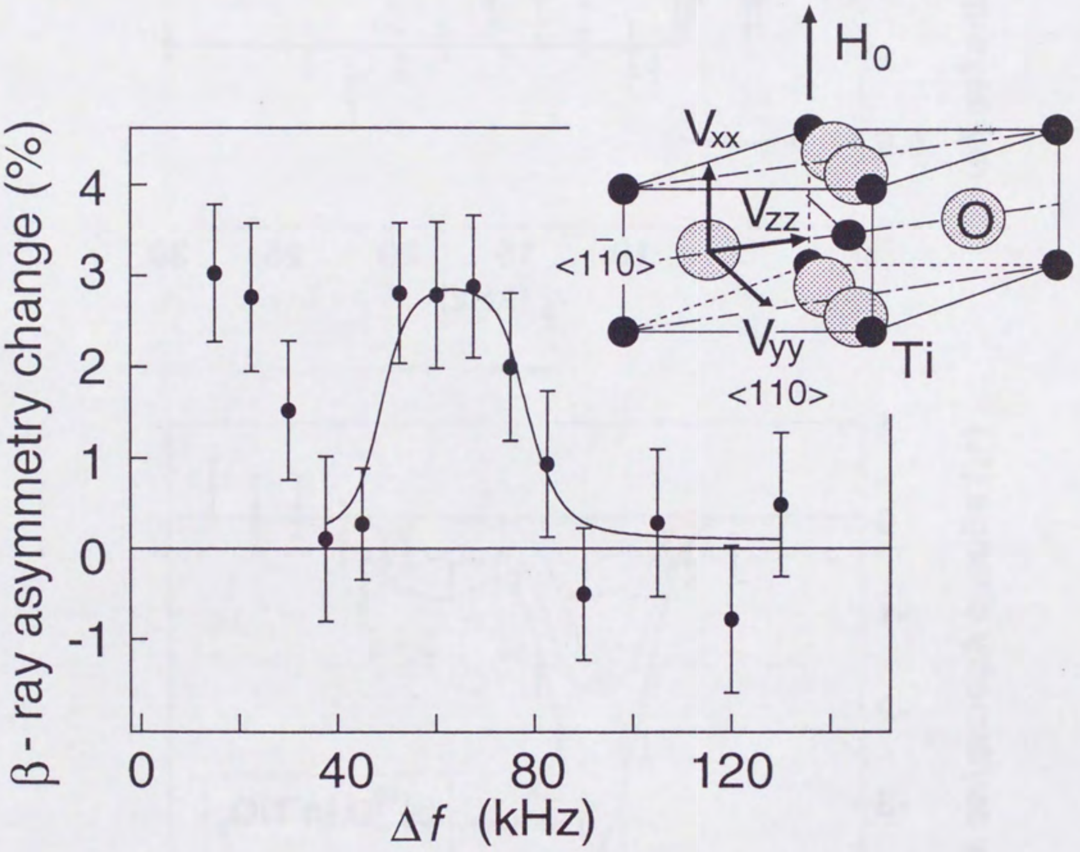

Figure 13: β-NQR spectrum for ^{13}O in TiO_2 under the external field of 8 kOe . The crystal c-axis was set parallel to the external field.

5 FT-NMR of ^{45}Sc, ^{49}Ti, ^{93}Nb and ^{17}O in TiO_2

For further systematic investigation of EFG in TiO_2, we have measured EFGs for ^{45}Sc, ^{49}Ti, ^{93}Nb and ^{17}O in TiO_2 by the Pulsed FT-NMR technique [95, 96]. In this section, experimental results are summarized.

First, the principle of the FT-NMR is explained (fig.14). In the FT-NMR method, a pulse magnetic field is used. In the thermal equilibrium under a high external magnetic field, a small magnetization is induced in a nuclear spin ensemble by the consequence of the nuclear para-magnetism. This magnetization is fallen down by the pulse field and reach to the xy-plane which is perpendicular to the external field. Then, the magnetization precesses around the external field. So, during a relaxation time of the magnetization we can detect the nuclear induction by a pickup coil which is often the same one used to apply the pulse magnetic field. This nuclear induction is recorded and compiled to the NMR spectrum by the Fourier transformation.

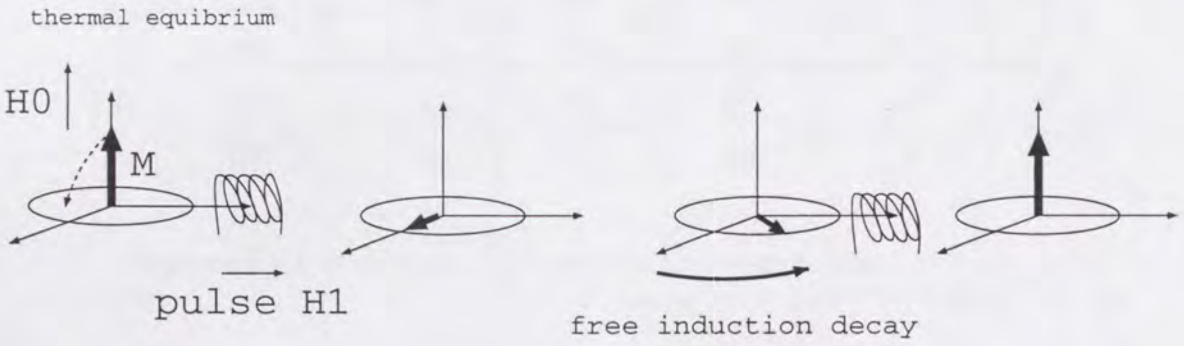

Figure 14: The principle of the FT-NMR.

The TiO_2 sample containing ^{45}Sc was prepared by mixing a proper amount of $^{45}Sc_2O3$ powder and TiO_2 material before single crystal was synthesized [115]. The sample with ^{93}Nb was commercially available [115]. The concentration of ^{45}Sc and ^{93}Nb in TiO_2 were 0.5 atomic % and 0.05 atomic %, respectively. The signals from ^{49}Ti whose natural abundance was 5.5 % were detected without enrichment of the isotope. ^{17}O is the only stable oxygen isotope which has a finite electric quadrupole moment, however its natural abundance is only 0.04% so the NMR signals of ^{17}O is almost undetectable. Therefore, we synthesized a TiO_2 single crystal which was enriched in ^{17}O up to 5 atomic %.

The $m = \pm\frac{1}{2} \leftrightarrow \mp\frac{1}{2}$ transition frequencies were observed for ^{45}Sc($I = 7/2$), ^{49}Ti($I = 7/2$), 93Nb($I = 9/2$) and ^{17}O. These transition frequencies are not changed by the quadrupole interaction in the first order. However, the second order perturbation calculation shows a sizable shifts in the transition frequencies as shown in section 2. This shifts depends on the orientation of the crystal relative to the external magnetic field H_0. So by observing the transition frequencies as a function of the rotating angle of the crystal around the axis vertical to the external field, we can determine the quadrupole coupling constant eqQ/h and the asymmetry parameter η.

For the pure TiO_2 crystal and Nb doped crystal the $\langle 110 \rangle$ axis was placed close to the rotation axis. For the Sc doped TiO_2 crystal and for the ^{17}O enriched crystal the

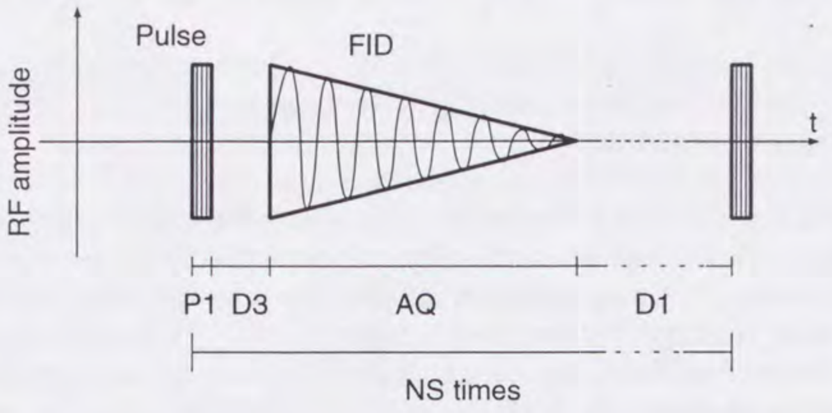

	P1(μsec)	D3(μsec)	AQ(msec)	D1(sec)	NS(times)
^{45}Sc	1	18	12	5	360
^{49}Ti	2.5	30	16	1	600
^{93}Nb	1	30	5	2	1800
^{17}O	2	50	33	20	1500

Figure 15: Summary of experimental parameters of the pulse sequence for the present FT-NMR measurements.

crystallographic *a*-axis and *c*-axis were set so, respectively. The crystals were rotated around the axis perpendicular to H_0. FT-NMR measurements were performed by a simple one pulse sequence. Parameters of the pulse sequence is summarized in fig.15. From the analyses, we extracted the quadrupole coupling constant eqQ/h and the asymmetry parameter η, as well as the exact direction of the crystal axes.

For Sc in the TiO_2, the experiments were performed under two different external magnetic field of 70 kOe and 94 kOe to separate out the effect of the anisotropic chemical shift [96]. The observed transition frequencies are shown in fig.16 as a function of crystal orientation. Two signals were observed because the unit cell had two geometrically different sites for the metal atoms. The shape of the rotation pattern at the two different external magnetic field slightly differs from each other. It is because of an anisotropic chemical shift. The solid curves are the theoretical one best fitted to the data in which the anisotropic chemical shift was taken into account. As a result, the electric quadrupole coupling constant $|eqQ/h| = 11.02 \pm 0.01$ (MHz) and the asymmetry parameter $\eta = 0.983 \pm 0.003$ were derived. It was found that the V_{YY} component of EFGs was along the c-axis.

For ^{93}Nb, the NMR was detected under the external field of 70 kOe. However, we can separate out the anisotropic chemical shift effects from the angular dependence of the frequency shift. The observed NMR frequencies are shown in fig.17 with the theoretical curves best fitted to the data. For ^{93}Nb, $|eqQ/h| = 49.83 \pm 0.13$ (MHz) and $\eta = 0.463 \pm 0.007$ were derived. It was found that the V_{ZZ} component of EFGs was along the c-axis.

For ^{49}Ti, the NMR was detected under the external field of 94 kOe. Because of the low Larmor frequency, the perturbation due to the anisotropy of the chemical shift was negligible. In fig.17, the NMR frequencies of ^{49}Ti are shown as a function of the rotation angle. $|eqQ/h| = 14.00 \pm 0.03$ (MHz) and $\eta = 0.192 \pm 0.008$ were derived. They are consistent with the previous measurements by Kanert *et al.* [13] and Gabathuler *et al.* [12].

For ^{17}O, the NMR was measured at the external fields of 70 kOe and 94 kOe. As shown in fig. 18, it was found that the effect of the anisotropic chemical shift dominated the electric quadrupole effect in this case, so it was impossible to extract a precise electric quadrupole coupling constant from these spectra. Therefore, we measured the transition frequencies between $m = \pm 1/2$ and $m = \pm 3/2$ as a function of the rotation angle of the crystal under the external field of 70 kOe as shown in fig. 18. These transitions are subjected to the electric quadrupole effect at the first order of the perturbation theory, so it is possible to derive the quadrupole effect precisely. However, a rather wide line width of these resonances makes a measurement itself difficult. It is why that this transitions were not measured in the other cases. In the analysis, first the chemical shift anisotropy was extracted from the rotation patterns of $m = \pm 1/2 \leftrightarrow \mp 1/2$ transitions at the fields of 70 and 94 kOe. Next, taking it into account, the quadrupole coupling constant and the asymmetry parameter were determined to be 1.512 ± 0.004 MHz and 0.831 ± 0.007, respectively. They are comparable with the previous results by Gabathuler *et al.* [12]. In the Gabathuler's experiments, a certain amount of Cr was doped in a TiO_2 crystal to enhance the signal of ^{17}O in spite of a enrichment of it. The present result is free from any perturbations by artificially doped impurities.

Since the electric quadrupole moments of ^{45}Sc, ^{49}Ti, ^{93}Nb and ^{17}O are known [113], the electric field gradients at their sites were derived from the experimental values of eqQ/h. The results of analyses are summarized in table 5 with some experimental parameters.

Table 3: Experimental results of electric field gradients ($\times 10^{19}$V/m^2) at the Sc, Ti, Nb and O sites in TiO_2(rutile).

	^{45}Sc	^{49}Ti	^{93}Nb	^{17}O
nuclear spin	7/2	7/2	9/2	5/2
Q(fm^2)	-23.6(2)	+24(1)	-32(2)	-2.6±0.3
sample shape(mm)	$5 \times 7 \times 20$	$10 \times 10 \times 2$	$8 \times 8 \times 12$	
rotation axis	$\langle 100 \rangle$	$\langle 110 \rangle$	$\langle 110 \rangle$	$\langle 001 \rangle$
external field H_0 (kOe)	70, 94	94	70	70, 94
$\lvert eqQ/h \rvert$ (MHz)	11.02(1)	14.00(3)	49.83(13)	1.512±0.004
η	0.983(3)	0.192(8)	0.463(7)	0.831±0.007
$\lvert q \rvert$	193(2)	241(11)	644(40)	240±30
	$V_{YY}//$c	$V_{ZZ}//$c	$V_{ZZ}//$c	$V_{XX}//$c

At last, influences of the anisotropic chemical shift to the rotation pattern of the NMR transitions are discussed. The orbital motion of electrons are perturbed by an external field and a net magnetization is induced in a substance. This gives rise to the so called chemical shifts, *i.e.*, a NMR frequency of a nucleus is shifted from that of a bare nucleus [95, 96]. Generally, chemicals shifts are differ from each other for different substances, because they depend on the electronic structures. Moreover, even if in a same substance, it is expected that the chemical shifts are different according to which direction an external field is put on. Such anisotropic chemical shift coexists with the quadrupole interaction. In order to extract a precise quadrupole coupling constant from a dependence of a NMR transition on a rotation angle of a crystal, effects of anisotropic chemical shift were included in the magnetic term of the interaction Hamiltonian H_M as,

$$H_M \;=\; -g\mu_N \boldsymbol{H}_\circ (\boldsymbol{1} - \boldsymbol{\sigma})\, \boldsymbol{I},$$

where $\boldsymbol{\sigma}$ is the anisotropic chemical shift tensor such as,

$$\boldsymbol{\sigma} \;=\; \begin{pmatrix} \sigma_{XX} & \sigma_{XY} & \sigma_{XZ} \\ \sigma_{YX} & \sigma_{YY} & \sigma_{YZ} \\ \sigma_{ZX} & \sigma_{ZY} & \sigma_{ZZ} \end{pmatrix},$$

where $\mathrm{Tr}(\boldsymbol{\sigma}) = 0$. Assume that $\boldsymbol{\sigma}$ is diagonal in the principal coordinate system of the EFG as shown in fig. 1, we get H_M as

$$H_M \;=\; -g\mu_N H_0 I_z \left[1 - \left(\sigma_{XX}\cos^2\phi\sin^2\theta + \sigma_{YY}\sin^2\phi\sin^2\theta + \sigma_{ZZ}\cos^2\theta\right)\right].$$

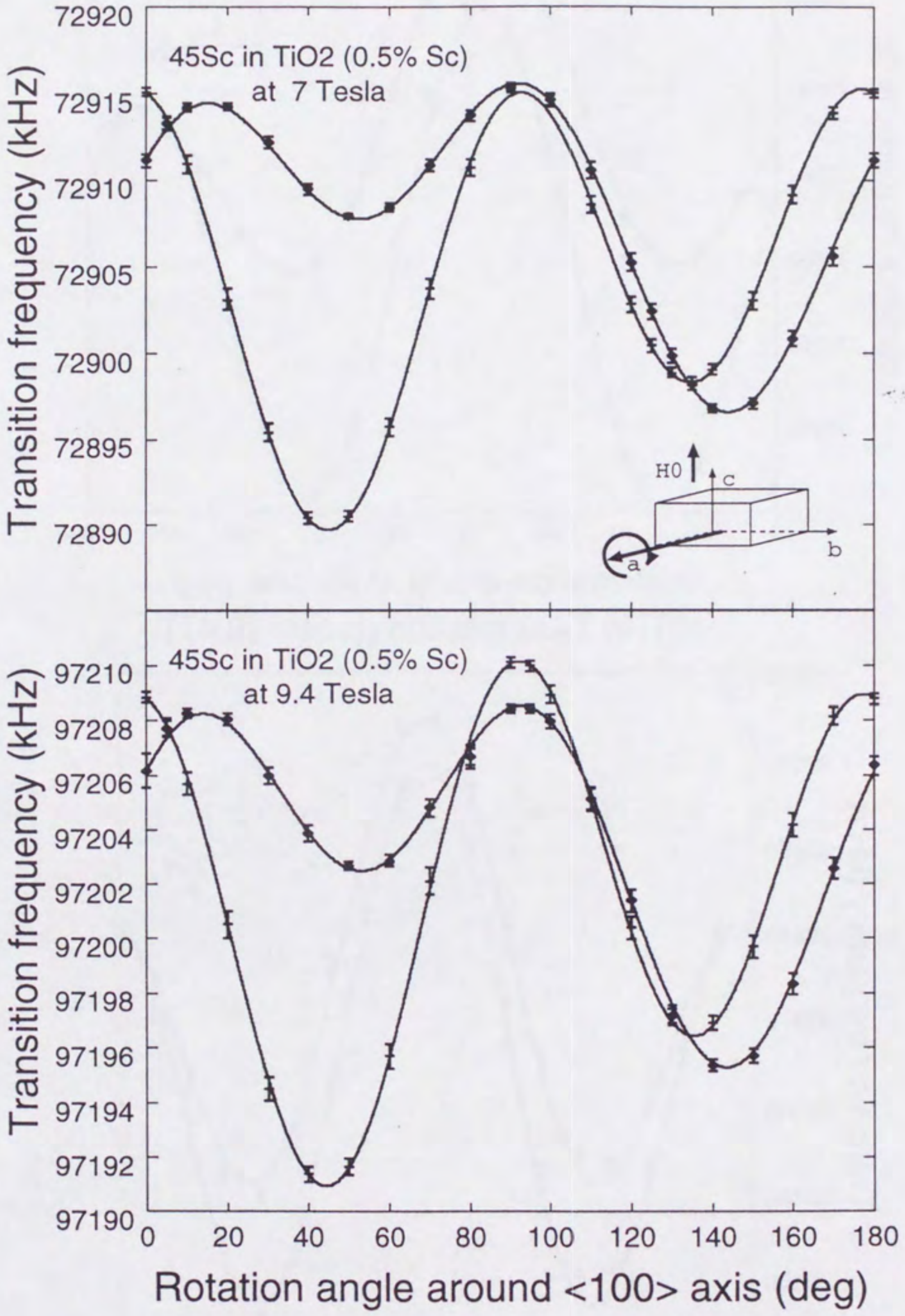

Figure 16: Resonance frequencies of ^{45}Sc as a function of crystal orientation. The m=$\pm\frac{1}{2} \leftrightarrow \mp\frac{1}{2}$ transition frequencies were observed under the external fields of 70 kOe and 94 kOe. The crystal was rotated about the axis near ⟨100⟩.

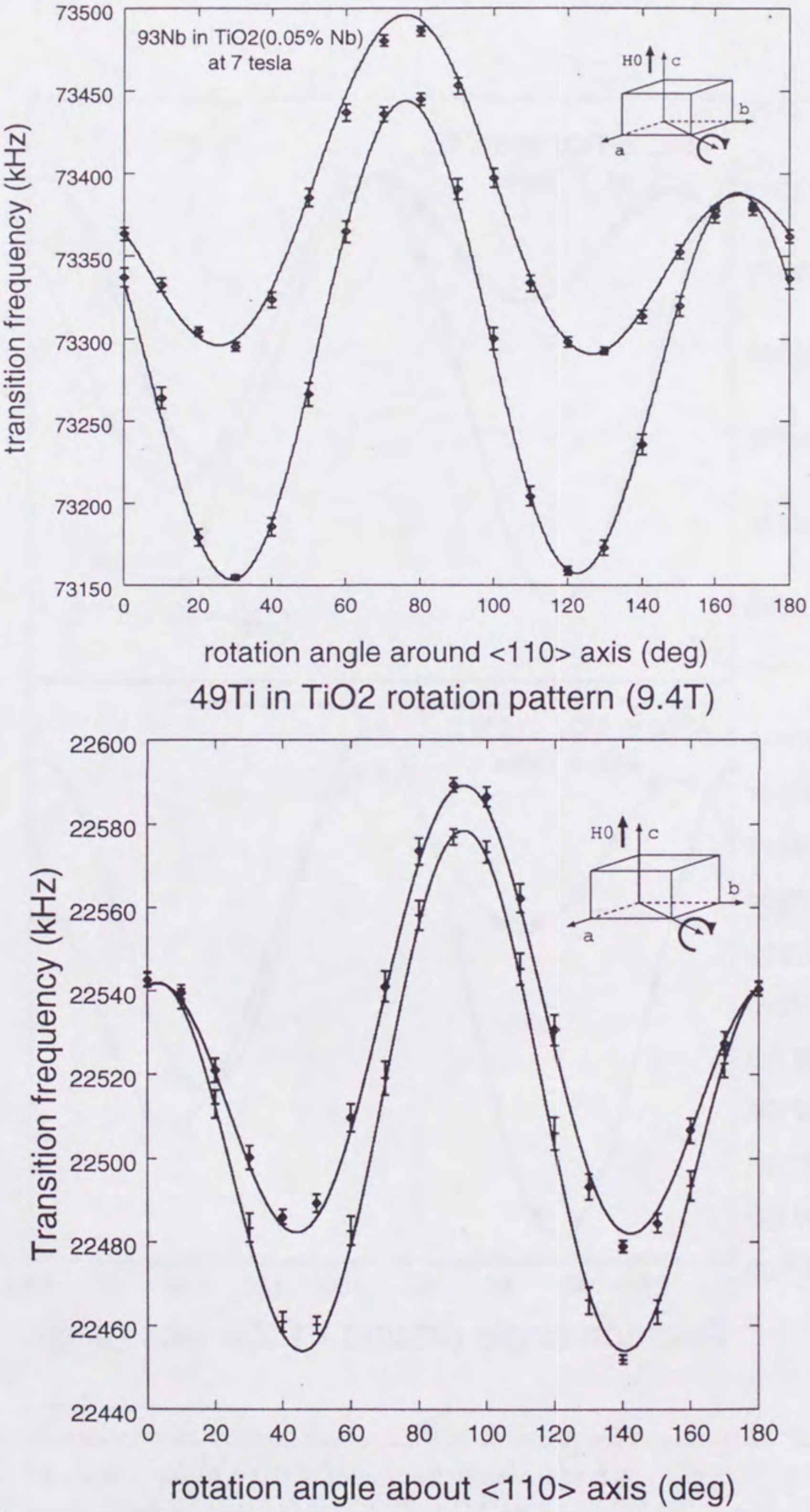

Figure 17: Resonance frequencies of ^{93}Nb (Up) and ^{49}Ti (Down) as a function of crystal orientation. The $m=\pm\frac{1}{2} \leftrightarrow \mp\frac{1}{2}$ transition frequencies were observed under the external field of 70 kOe and 94 kOe for ^{93}Nb and ^{49}Ti, respectively. The crystal was rotated about the axis near $\langle 110 \rangle$.

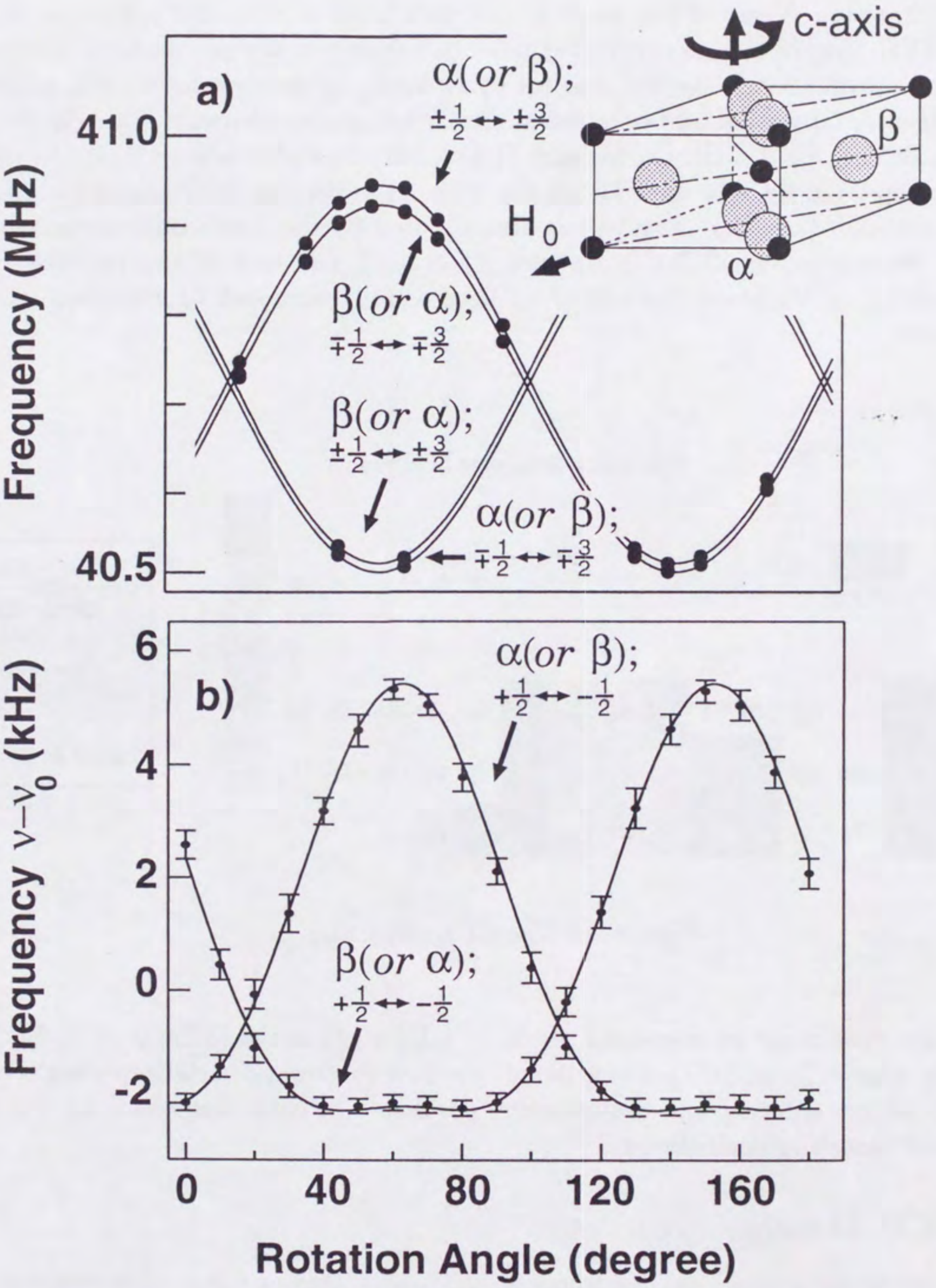

Figure 18: Resonance frequencies of ^{17}O as a function of crystal orientation at the external field of 70 kOe. a) The m=$\pm\frac{1}{2} \leftrightarrow \pm\frac{3}{2}$ transitions. b) The m=$\pm\frac{1}{2} \leftrightarrow \mp\frac{1}{2}$ transitions. The crystal was rotated about the axis near $\langle 001 \rangle$. Assignments of the respective resonances are also shown.

6 EFGs in HCP Metals

The HCP structure is one of the most simple structures of elements which has a non vanishing EFG. Considering the crystal symmetry, the asymmetry parameter η is zero not only for the substitutional site but also for other highly symmetric interstitial positions such as trigonal, tetragonal and octahedral sites. Among the elements, Be, Mg, Sc, Ti, Co, Zn, Y, Zr, Tc, Ru, Cd Hf, Re, Os and Tl have this crystal structure [110]. As shown in fig.19, except for Be, Mg and Tl, all the elements with the HCP structure are the transition metals. The HCP structure is also adopted by the Lanthanide series with 4f electrons. Because of the difficulty to treat $4f$ orbitals and lack of experimental data, only La and Lu, which has either empty $4f$ shell or fully occupied $4f$ shell respectively, are concerned.

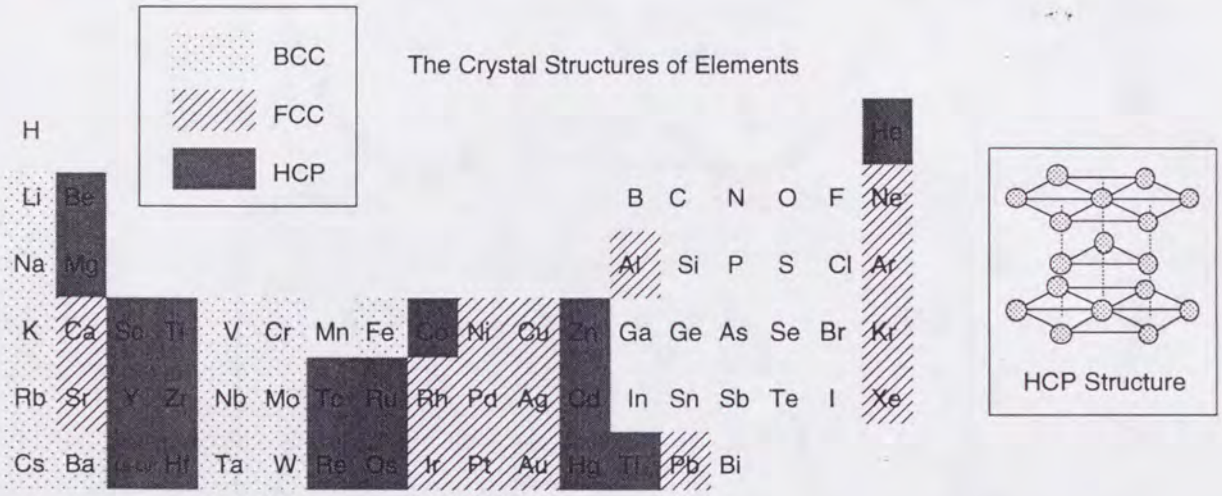

Figure 19: The HCP elements.

Since there exist many experimental results [1]–[3] for impurities in Zn and Cd, EFGs at sp-impurity sites in Zn and Cd are calculated and their systematic variations are discussed [4, 78, 79]. Before entering into the impurity problems, EFGs at respective atomic sites in pure HCP metals are calculated.

6.1 HCP Metals

The purpose to treat these pure systems is two folds. One of them is to examine the reliability of present procedure for the EFG calculation. As explained in the section 3, we restrict a shape of an atomic potential to the muffin tin type. It might cause a severe error to a resulting EFG. By the way, Blaha *et al.* performed the first principle EFG calculations on these systems by the FLAPW method based on the LDA and obtained good agreements with experimental EFGs [48]. The FLAPW method needs no shape approximation for an atomic potential. Therefore, we can compare our results not only with the experiments but also with their calculations to confirm validity of the muffin tin approximation in the EFG calculation. The other is to obtain some clues to understand

Table 4: Lattice Constants of HCP metals

Element	a (Å)	c (Å)	c/a	
Be	2.2866	3.5833	1.5671	at 22°C
Mg	3.20927	5.21033	1.62352	at 25°C
Sc	3.3090	5.2733	1.5936	at 20°C
Ti	2.950	4.686	1.588	at 25°C
Co	2.5071	4.0686	1.6228	at 20°C
Zn	2.6648	4.9467	1.8563	at 25°C
Y	3.6474	5.7306	1.5711	at 20°C
Zr	3.232	5.147	1.593	at 25°C
Tc	2.743	4.400	1.604	
Ru	2.70389	4.28168	1.58353	at 20°C
Cd	2.97887	5.61765	1.88583	at 26°C
La	3.75	6.07	1.62	
Lu	3.5031	5.5509	1.5846	at 20°C
Hf	3.1967	5.0578	1.5822	at 26°C
Re	2.7608	4.4582	1.6148	at 25°C
Os	2.7352	4.3190	1.5790	at 20°C
Tl	3.456	5.525	1.599	

the systematics for the variation of EFGs of impurities. Though only limited elements crystallize into the HCP structure, it seems that a certain systematic trend exists *i.e.* at both ends of the *d*-series the EFGs have positive sign, and they are negative at middle of the *d*-series. Our interest is to explain this behavior from a view point of electronic structures of the HCP metals. Of course, it is also a motivation to show the first principle EFG calculations for Hf, Re, Os, Tl, La and Lu, for which EFGs have not calculated by the FLAPW method.

Before showing results of EFG calculations, the conditions for the present calculations are summarized in brief. It is essentially common with the other calculations in this thesis. The electronic structure calculations were based on the LDA with the parameterization according to MJW which was explained in section 3. To examine the relativistic effect, the calculations were performed both in a non-relativistic (nrl) and in a scalar relativistic (sra) version of the KKR method [116, 117]. The potential and the charge density were approximated to the muffin tin form. The wave functions in the muffin tin spheres were expanded respectively into real harmonics up to l=2, where l is the angular momentum defined at the respective atomic sites. The 512 k points in the irreducible wedge of the 1st Brillouin zone were calculated. The energy spectrum in the region down to -1.2 Ry relative to the Fermi level was calculated for all elements except for La. In the case of La the energy window of -1.6 Ry was employed to include the rather shallow its 5p levels. The LDA procedure was iterated until the differences between the input (V_{in}) and the output (V_{out}) atomic potentials becomes small enough. We set the tolerance to be 10^{-3} in the root mean square difference of them, *i.e.*,

$$\sum_n \sqrt{\frac{1}{V_n} \int_{V_{C_n}} [V^n_{out} - V^n_{in}]^2 dv} \leq 10^{-3},$$

Table 5: Theoretical and Experimental EFGs in HCP Metals in 10^{19} V/m^2.

Host	Theory		Theory	Experiment
	nrl	sra	(Blaha*et al.*)	
Be	+1.3	+1.4	-4.2	4.41±0.04
Mg	+3.5	+3.3	+1.6	4.8
Sc	+79	+78	+96	38±2
Ti	+243	+242	+207	110±34
Co	-22	-24	-19	-30±3
Zn	+301	+315	+375	+314±31
Y	+243	+265	+279	—
Zr	+448	+461	+429	372±18
Tc	-89	-153	-147	183±9
Ru	-30	-77	-123	97±7
Cd	+609	+624	+762	+612±5
La	+163	+116		148±21
Lu	+427	+429		+373±16
Hf	+948	+1004		+732±172
Re	-213	-598		-512±12
Os	-127	-453		-433±15
Tl	-88	-105		226±39

here n runs through all types of atoms in the unit cell, and Vc means the volume of the sphere. We employed the experimental lattice constants and c/a values which are summarized in table 4. They are the only given parameters in the present calculations. This is the reason why the present method is called *ab initio* method.

The results are shown in table5 and fig.20 with the experimental values (see appendix) [2, 3]. In the figure, the sra results were referred as the theoretical predictions. The overall agreement with the experimental values is almost perfect. Note that the agreement with the FLAPW calculations is also satisfactory as shown in table5. It shows that the electronic structure is well described by the muffin tin approximation in these HCP metals. It is not obvious whether the present EFG calculation procedure is also reliable for the other systems *e.g.* for a covalent system, ionic system, impurity systems and so on.

As shown in table5, the relativistic effect is large for Tc, Ru, Re and Os which are located at the center of the d series. It is not so pronounced for Co. This maybe because of its small atomic number [116].

Here, it is appropriate to point out the systematic variation of the EFGs of HCP metals. The following were known from the experimental works.

- At the beginning of the *d*-series the EFG is positive, and they increases as the number of *d* electrons (Sc→Ti, Y→Zr and La→Lu→Hf).
- At the center of the *d* series the EFG turns to negative, and decreases in absolute value as the number of *d* electrons (Co, Tc→Ru and Re→Os).
- At the end of the *d* series the EFG turns to positive large value (Zn and Cd).

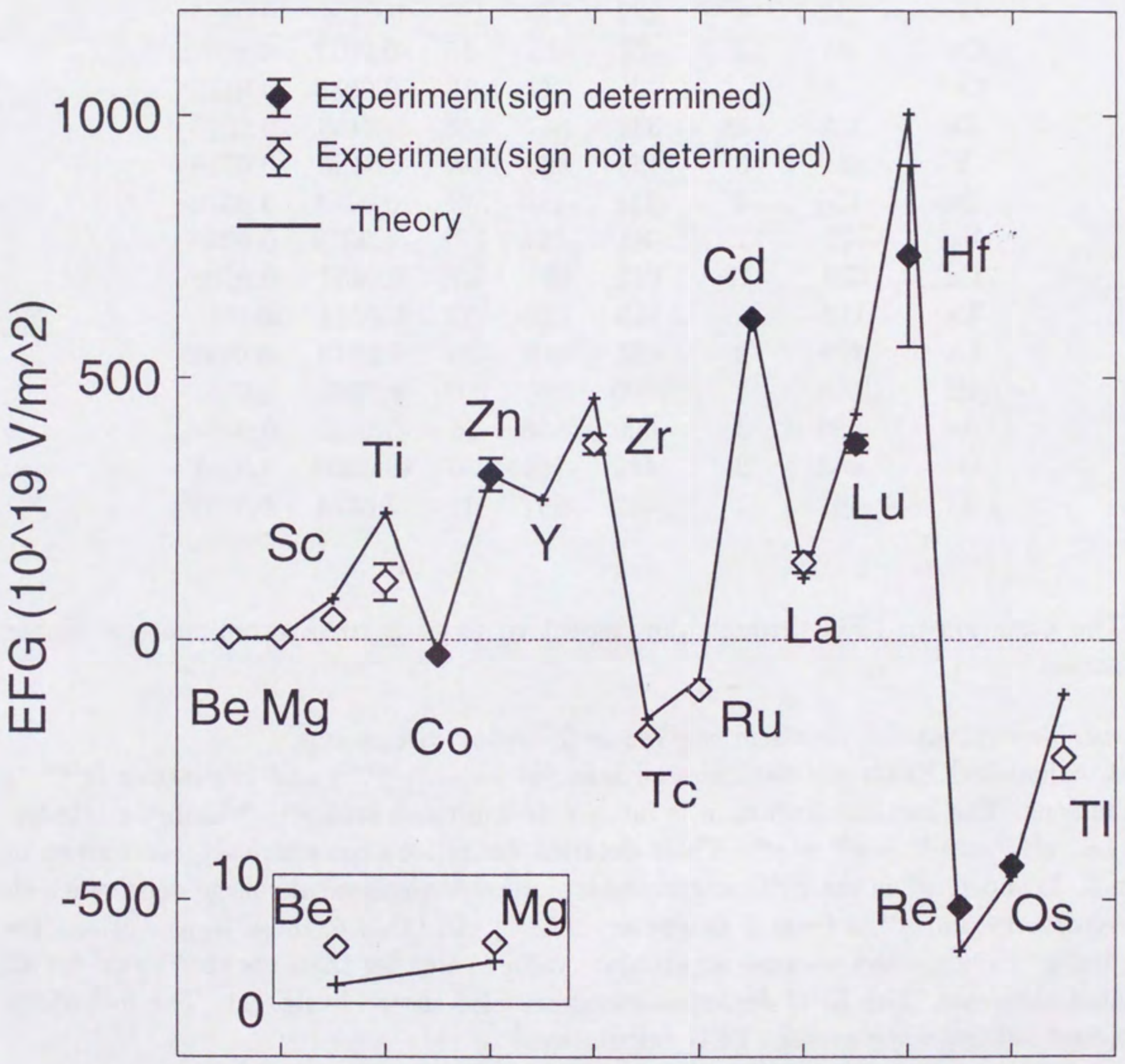

Figure 20: Theoretical predictions (sra) and experimental values of EFGs at the host atomic sites in HCP metals.

Table 6: Decompositions of EFGs in HCP Metals calculated by the sra. (in 10^{19} V/m^2 unit.)

Element	q^{total}	$q^{lattice}$	q^{local}	q^{pp}	q^{dd}	Δp	Δd
Be	1.4	7.1	-5.7	-4.1	0.0	-0.0076	0.0002
Mg	3.3	0.9	2.9	2.9	0.0	0.0014	-0.0008
Sc	78	2	76	87	-10	0.0142	-0.0179
Ti	242	4	239	139	100	0.0154	0.0985
$\mathrm{Co}^{\uparrow}$	-24	1	-24	-10	-15	-0.0017	-0.0082
$\mathrm{Co}^{\downarrow}$			-1	-22	21	-0.0038	0.0110
Zn	315	-18	332	347	-18	0.0456	0.0015
Y	461	3	458	360	98	0.0186	0.0719
Tc	-154	4	-158	-190	32	-0.0068	0.0072
Ru	-77	7	-84	-197	112	-0.0070	0.0246
Cd	624	-18	642	598	37	0.0457	0.0100
La	116	1	115	126	-12	0.0044	-0.0091
Lu	429	2	427	449	-24	0.0142	-0.0149
Hf	1004	4	1000	793	202	0.0180	0.0775
Re	-598	3	-600	-656	56	-0.0105	0.0064
Os	-453	9	-462	-704	237	-0.0109	0.0311
Tl	-401	2	-402	-391	-11	-0.0174	-0.0017

- The variation in EFG through the respective series is more prominent for higher period.

A reasonable explanation for them is given in following discussions.

First, calculated EFGs are decomposed into the local (q^{loccal}) and the lattice ($q^{lattice}$) contributions. The local contribution is further decomposed into q^{pp}, q^{dd}andq^{sd} contributions, i.e., $q^{local} = q^{pp} + q^{dd} + q^{sd}$. Their detailed definitions have already been given in section 5. In short, q^{pp} is the EFG originated from the non-spherical charge density which has *p* symmetry and q^{dd} is from *d* charge asymmetry. In table 6, these contributions are listed, but q^{sd} is neglected because its absolute value is smaller than 1×10^{19} V/m^2 for all calculated elements. The EFG decompositions are also shown in fig. 21. The followings are pointed out from the present EFG calculation.

- The dominant contribution to the total EFG is the q^{pp} contribution, therefore the q^{pp} decides the sign and the overall trend of the total EFG.
- The q^{dd} is also important to explain the experimental EFG, but the contribution is smaller than the q^{pp} even for *d*-valence elements where the asymmetry of individual *d* charge is expected to be large.
- The lattice contribution is even smaller and it can not be the main cause to contribute to the sign change of the total EFG.

These were basically the same as those already pointed out by Blaha [48]. In the present calculations, the same tendencies were also confirmed for heavier atoms (La - Tl) which were not calculated by FLAPW. At the same time, it was verified that the present method of the EFG calculations have an enough prediction power for almost all of the elements in the periodic table.

In order to get complete knowledge for the origin of the EFG, it is worth to examine the non-spherical charge density Δp and Δd. Δp and Δd are defined as the population differences,

$$\begin{aligned}\Delta p &= \frac{1}{2}(p_x + p_y) - p_z, \\ \Delta d &= (d_{xy} + d_{x^2-y^2}) - \frac{1}{2}(d_{xz} + d_{yz}) - d_{z^2},\end{aligned}$$

where $p_{x,y,z}$ and d_{xy,x^2-y^2,xz,yz,z^2} are the populations for respective orbitals. As shown in section 2, q^{pp} and q^{dd} are proportional to Δp and Δd with the coefficients of $\langle 1/r^3 \rangle_p$ and $\langle 1/r^3 \rangle_d$. In table6, calculated non-spherical charge Δp and Δd are shown for HCP elements. In fig.22, $q^{pp}, \Delta p$ and $q^{dd}, \Delta d$ are plotted. It is found that the sign change of q^{pp}, which determines the sign of q^{total}, reflects the sign change of Δp. The variations of Δp through the respective rows in the periodic table are very similar with each other, because of the similarity of c/a's of them in the same column. It is also found that the behavior of Δp and Δd is amplified with increasing the atomic number to result in similar behavior of q^{pp} and q^{dd}. This amplification is reasonable, because of the larger $\langle 1/r^3 \rangle$ factor for larger atomic number.

The local density of states (DOS) in the respective atomic spheres are shown to explain the origin of Δp. In fig.23, the local DOS of p-states are shown for HCP metals, about in the order of the periodic table. For the transition metals, the shape of the local DOS is very similar to each other. Therefore, it is recognized that the sign change of Δp in the respective rows is almost because of the band filling effect. For example, the peak of the local DOS of $p_{x,y}$ seen in fig.23 is half filled in case of Y and the excess of the occupation number of $p_{x,y}$ states gives the positive sign of its EFG. This peak is fully occupied for Zr. This leads to increase in the EFG. The peak of the local DOS of p_z is occupied for Tc and Ru and the occupation number of p_z state exceeds that of $p_{x,y}$. This leads to negative sign of the EFGs of them. In the case of Cd, $p_{x,y}$ are populated more than p_z and it has positive EFG. In the same sense, the behavior of EFGs are explained for the others. For the transition metal elements, the p-states in their spheres are originated from the tail of the d-orbitals at the neighboring spheres, *i.e.* what is called a hybridization. Because of the cylindrical symmetry of the HCP structure, overlap between orbitals in the neighboring spheres are larger in the x-y plane than in the z direction. This is the reason why the difference can occur in the local DOS between $p_{x,y}$ and p_z. A more detailed discussion will be given with examples of typical elements in Zn and Cd in the next section, since it is more clear.

As a summary of this section, it is concluded that the key points to understand the origin of the EFG are the non-spherical p-charge generated by the hybridization (overlap) of the orbitals in the neighboring spheres, and the atomic number dependence of $\langle 1/r^3 \rangle$ expectation value decorates it.

For the future, calculations for Lanthanoides are hoped. Because, it seems that the Lanthanoide series provide us a unique sample to test our calculations. It is supposed that the 4f electrons are highly localized at the atomic site and cause an isotropic atomic potential which is not dealt with in the muffin tin approximation. Therefore, we can know a limit of our EFG calculations through a result for the Lanthanoides.

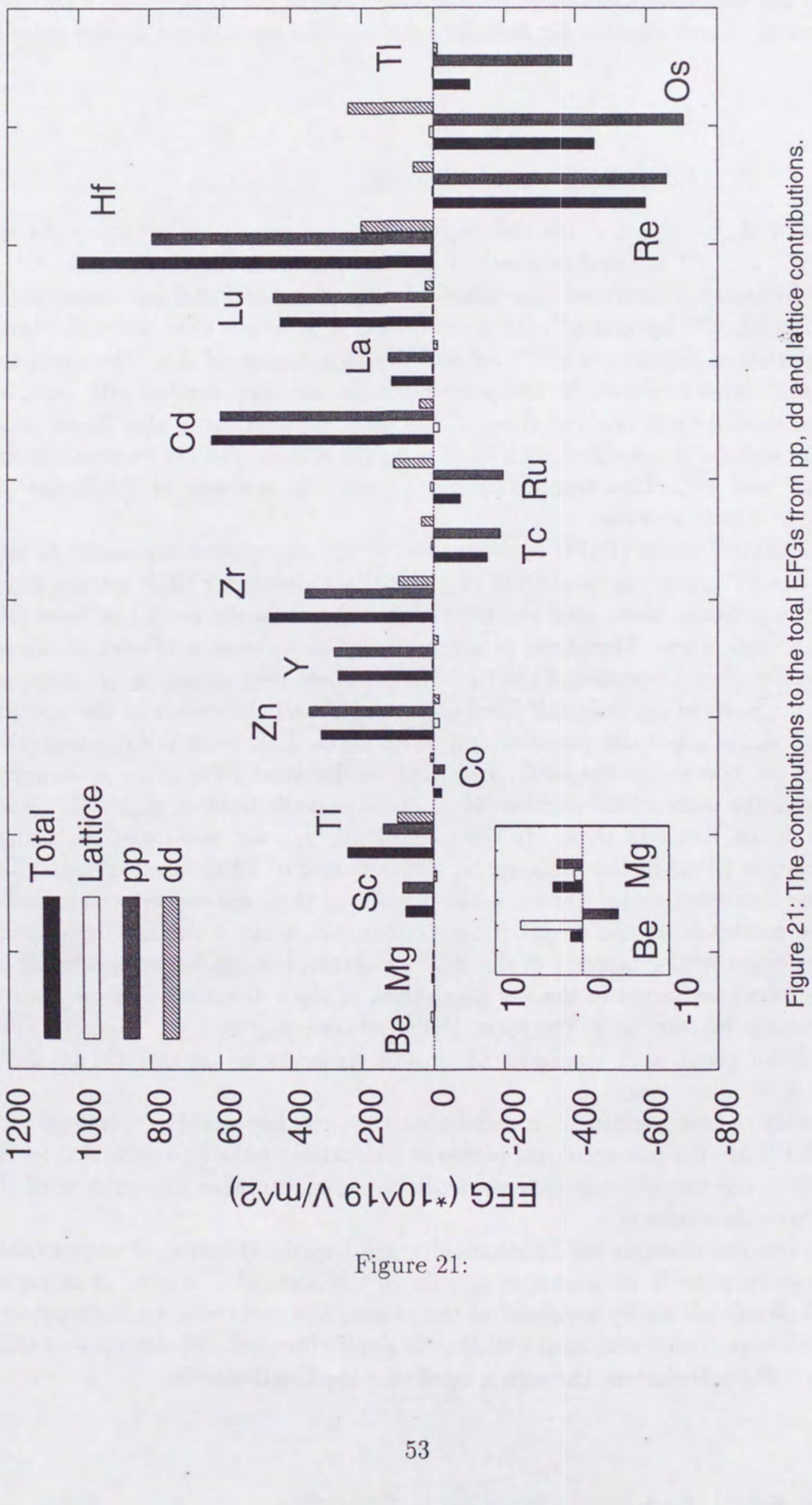

Figure 21: The contributions to the total EFGs from pp, dd and lattice contributions. The Definitions were given in the text.

Figure 21:

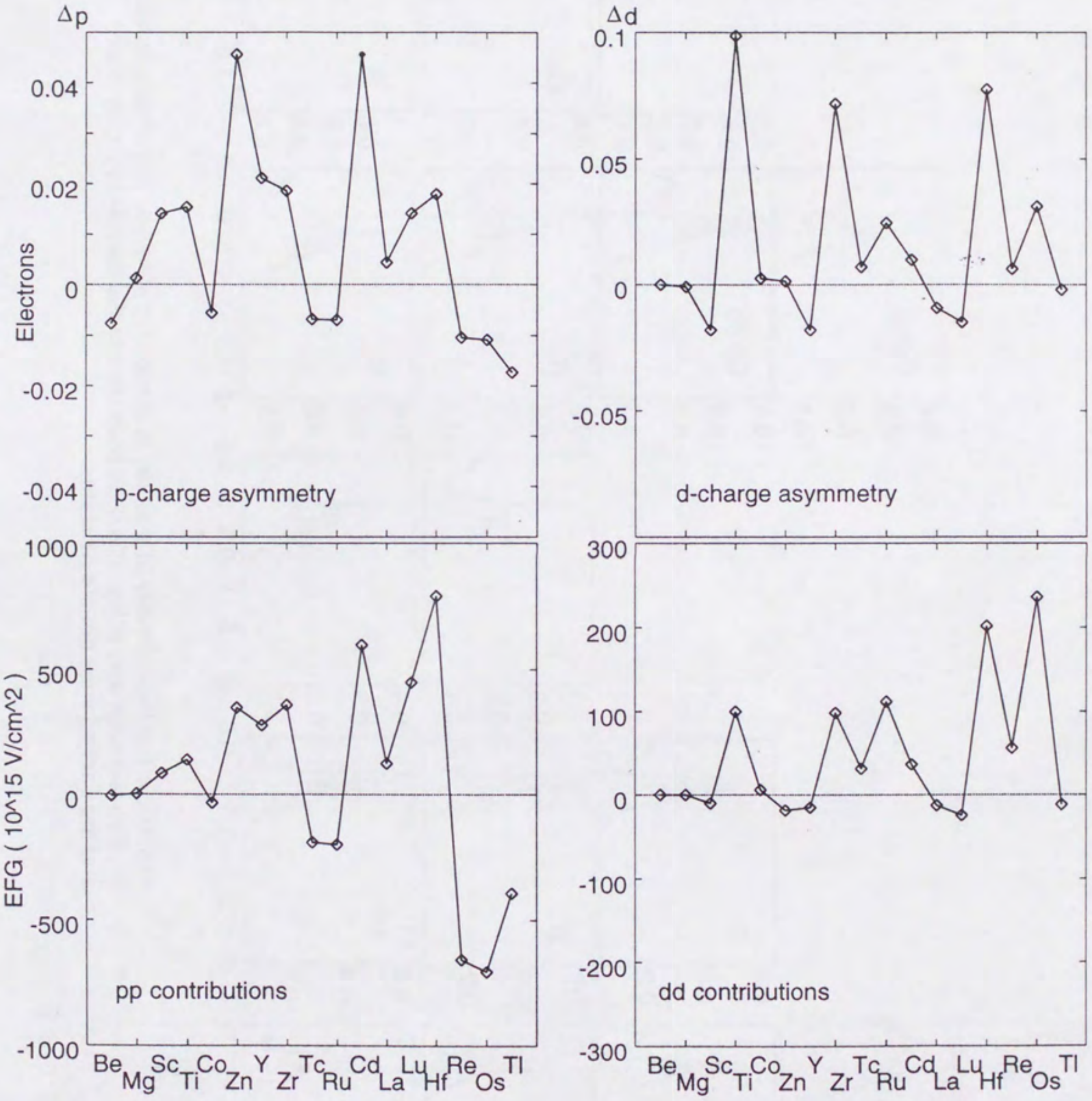

Figure 22: The contributions to the total EFGs from *pp*, *dd* and lattice contributions. The definitions were given in the text.

Figure 23:

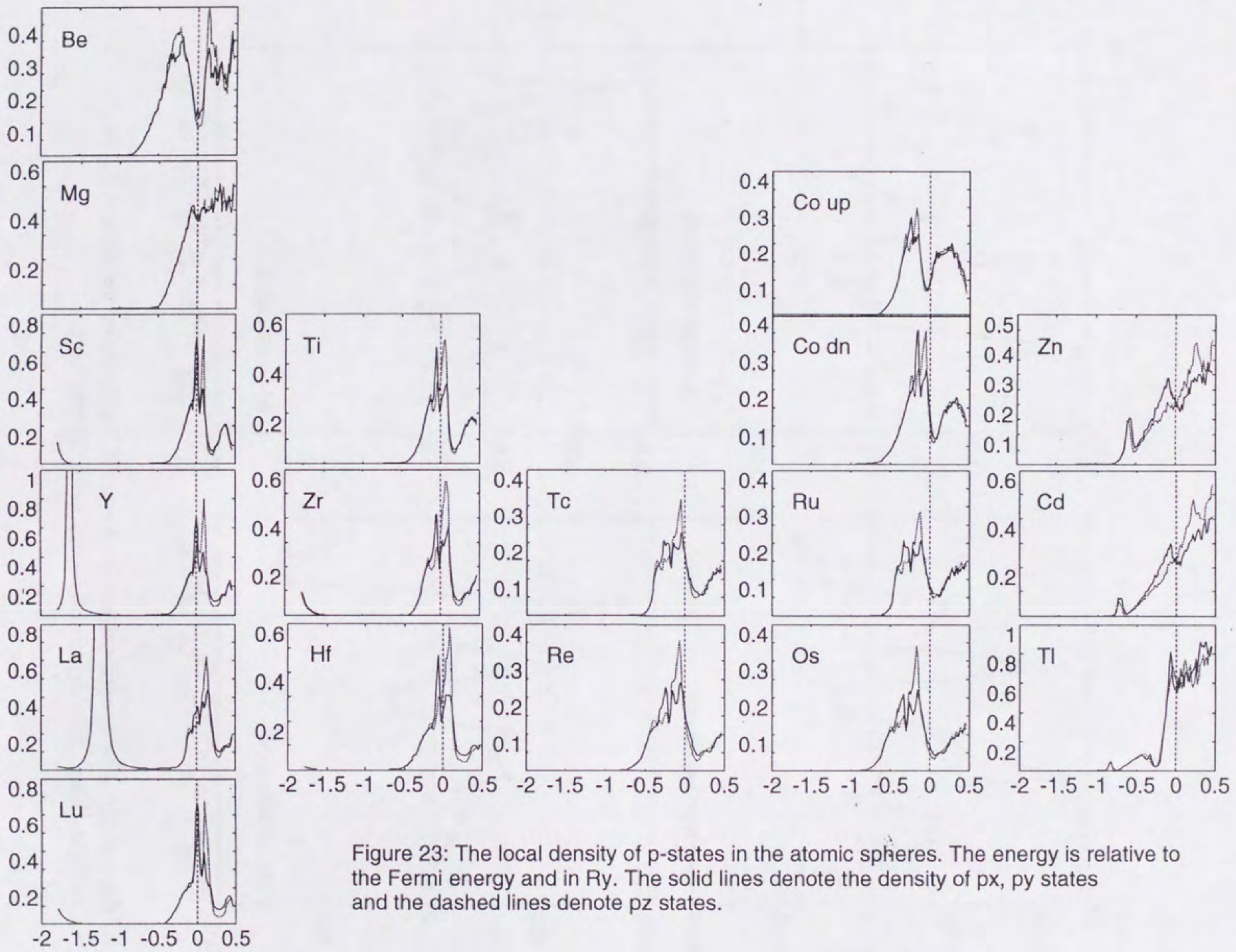

Figure 23: The local density of p-states in the atomic spheres. The energy is relative to the Fermi energy and in Ry. The solid lines denote the density of px, py states and the dashed lines denote pz states.

6.2 Typical Elements in Zn and Cd

In the previous section, the behavior of the EFGs in HCP metals were essentially understood from the view point of the band filling effect. However, someone may worry about the fact that the lattice constant a and c/a are different to each element [110]. (Of course this can not explain the sign change of EFGs, because only Zn and Cd have the c/a's bigger than the ideal value of $\sqrt{8/3} = 1.633$.) Moreover all elements does not have the HCP structure as shown in fig.19. A more clear evidence of a systematic variation is seen in the case of EFGs of impurities in a same host. In this section, the EFGs at impurities of typical elements in HCP Zn and Cd are calculated systematically. In particular, 4sp elements (K, Ca and Cu-Kr) and 5sp elements (Rb, Sr and Ag-Xe) are dealt with.

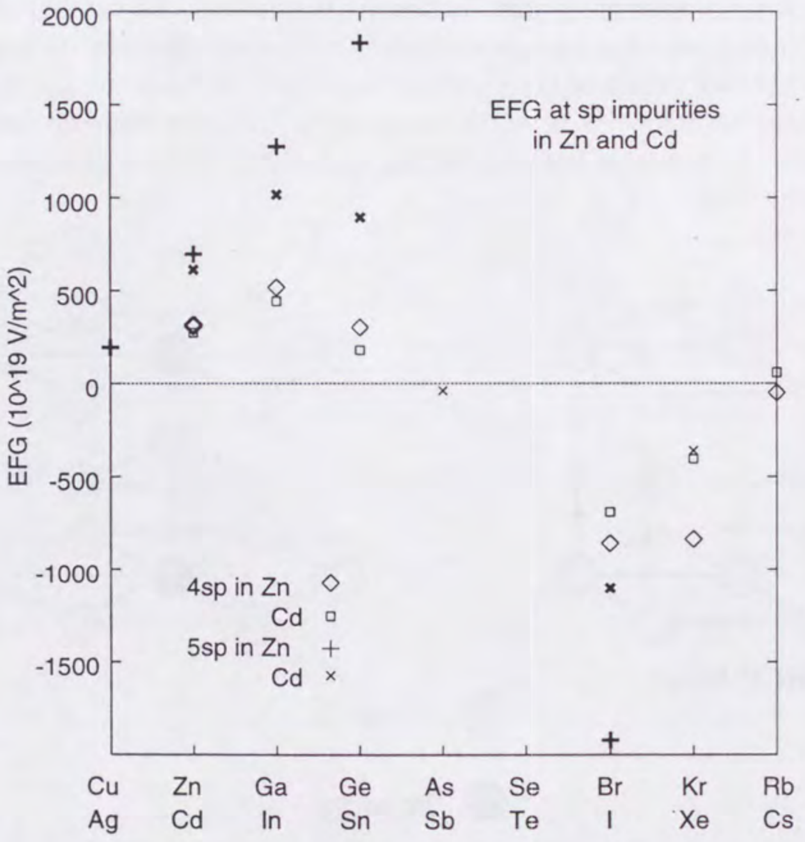

Figure 24: The systematics of experimental EFGs at sp-impurity sites in Zn and Cd . For the bold symbol, the sign of the EFG was experimentally determined.

The systematic trends of the EFGs at typical elements introduced as a dilute impurity had been pointed out by Haas [4]. As shown in fig.24, both for Zn and Cd hosts, the EFG for the first half of the sp valence series is positive and that for the last half is negative. In detail for the case of Cd host, from Cd to In the EFG increases gradually and reaches the maximum absolute value at In. Then, the EFG deceases and crosses zero at about Sb, and the EFG becomes the largest negative value at I. In turn from I to Xe, the EFG increases and closes to zero. The same tendency is seen in the case of Cd host.

This systematic behavior, in particular the change in the sign of the EFG, can not been explained by the Sternheimer model, because in that model the origin of the EFG is the lattice contribution which is common in the present cases.

There are some theoretical studies on this problem. By a simple tight binding approximation, Haas suggested that the origin of this systematic trend is a gradual change in population of the *p* orbit of impurity, however he did not give values of the EFGs actually [4]. Lindgren performed self-consistent molecular-cluster calculations of EFGs of 5sp impurities in Cd [78], and Schmidt *et al.* carried out self-consistent super-cell band-structure calculations by the augmented spherical wave (ASW) method for the same systems [79]. Both of them succeeded to reproduce the systematic trend. However, there is some doubt about their calculation procedure. In the cluster calculation, the band structure was simulated by empirical smearing technique of the discrete levels, and it is not clear whether the size of the cluster is large enough or not. In the ASW method the validity of permission of the overlapped region between atomic spheres is uncertain. Besides, to evaluate EFGs Schmidt used expectation values of $\langle 1/r^3 \rangle$ which were derived from the other calculations on atoms. Therefore, we believe it is worth to calculate EFGs in these systems by our *ab initio* procedure and to examine the mechanism underlying for the systematic behavior of EFGs at impurity sites.

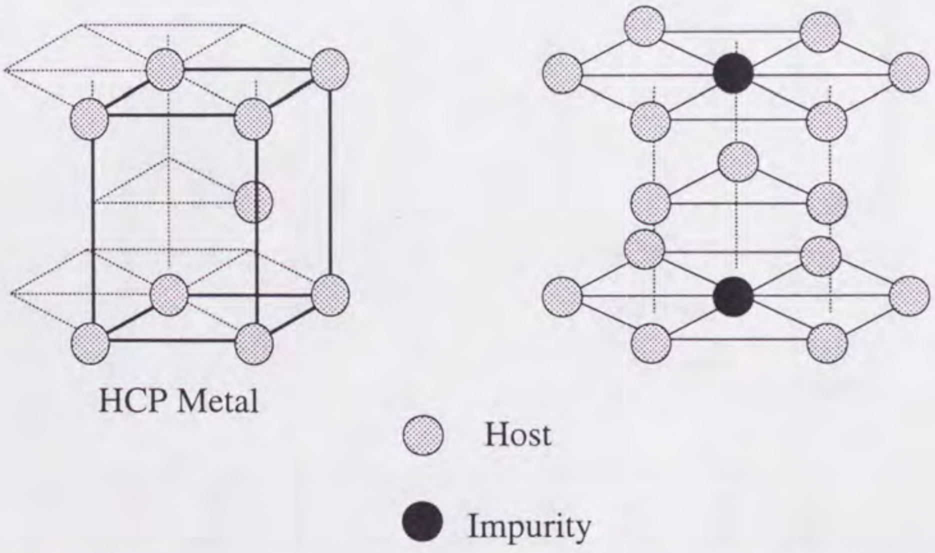

Figure 25: The super cell used for the present impurity calculations.

The calculational procedure is essentially similar to the cases of the pure HCP metals in the previous section. From the systematics of the lattice location of a heavy impurity, it is plausible that the probe nuclei sit at the substitutional site in the HCP crystal. The super cell method was employed to simulate the impurity system [68, 69]. In this method impurity atoms are placed periodically in a crystal. With an assumption that interactions between neighboring impurities are negligible, it is permitted to approximate the electronic structure of the impurity with that of such ordered alloy. In the present study, we defined the super cell so that it consisted of three primitive unit cells of the HCP structure and one of the host atoms was substituted with the impurity as shown in fig.25. As a result, the density of the impurity is about 17 atomic %. Since this concentration

Table 7: Theoretical and Experimental EFGs at sp-Impurities in Zn and Cd in 10^{19} V/m^2 unit.

	Zn Host		Cd Host	
Probe nucleus	Theory	Experiment	Theory	Experiment
K	+145	—	+83	—
Ca	+329	—	+231	—
Cu	+190	—	+93	—
Zn	+291	+314±31	+238	272±27
Ga	+402	514±41	+207	440±31
Ge	+307	301±69	+142	179±41
As	-331	—	-513	—
Se	-1376	—	-2460	—
Br	-2156	858	-1274	688
Kr	-705	836±56	-69	404±28
Rb	-145	—	+205	—
Sr	+654	—	+647	—
Ag	+597	+193±15	+397	—
Cd	+638	+697±62	+632	+612±5
In	+858	+1277±23	+600	+1015±17
Sn	+624	+1829±73	+343	+890±21
Sb	-252	—	-395	—
Te	-1360	—	-1828	—
I	-1488	-1923±753	-3480	-1099±553
Xe	-974	—	-795	360±38
Cs	-865	—	-364	—
Ba	+536	—	+869	—

of impurity is rather high, it is not obvious whether the electronic structure of the dilute impurity is described well by the present super cell method. To confirm the validity of the present method, it is necessary to try a bigger super cell, which is very time consuming. At the present stage, we leave this problem, and go ahead expecting at least that the trends of EFGs at impurities will be reproduced. The dependence of EFGs on the dimension of the super cell will be discussed in the later section. The LDA calculation was performed for this super cell by the KKR method in the sra version. The 216 k sampling points in the irreducible wedge of the 1st Brillouin zone were calculated. The substitution of the atom with the impurity does not reduces the symmetry of the HCP structure. The energy window of 1.6 ~ 1.8 Ry was employed. The local lattice expansion around the impurity was not considered, because it is supposed to be small for the substitutional impurity.

The results are shown in table 7 and fig.26 with the experimental data. The overall trend of the experimental EFGs are reproduced by the theoretical predictions rather well in spite of the small size of the present super cell. In detail, a discrepancy is seen. For 4sp impurities, the agreement is quite well except for the cases of the Br impurity. The theoretical values are almost two times bigger than the experimental values. The situation is similar to the case of I in Cd. However, the quadrupole moment of Br probe,

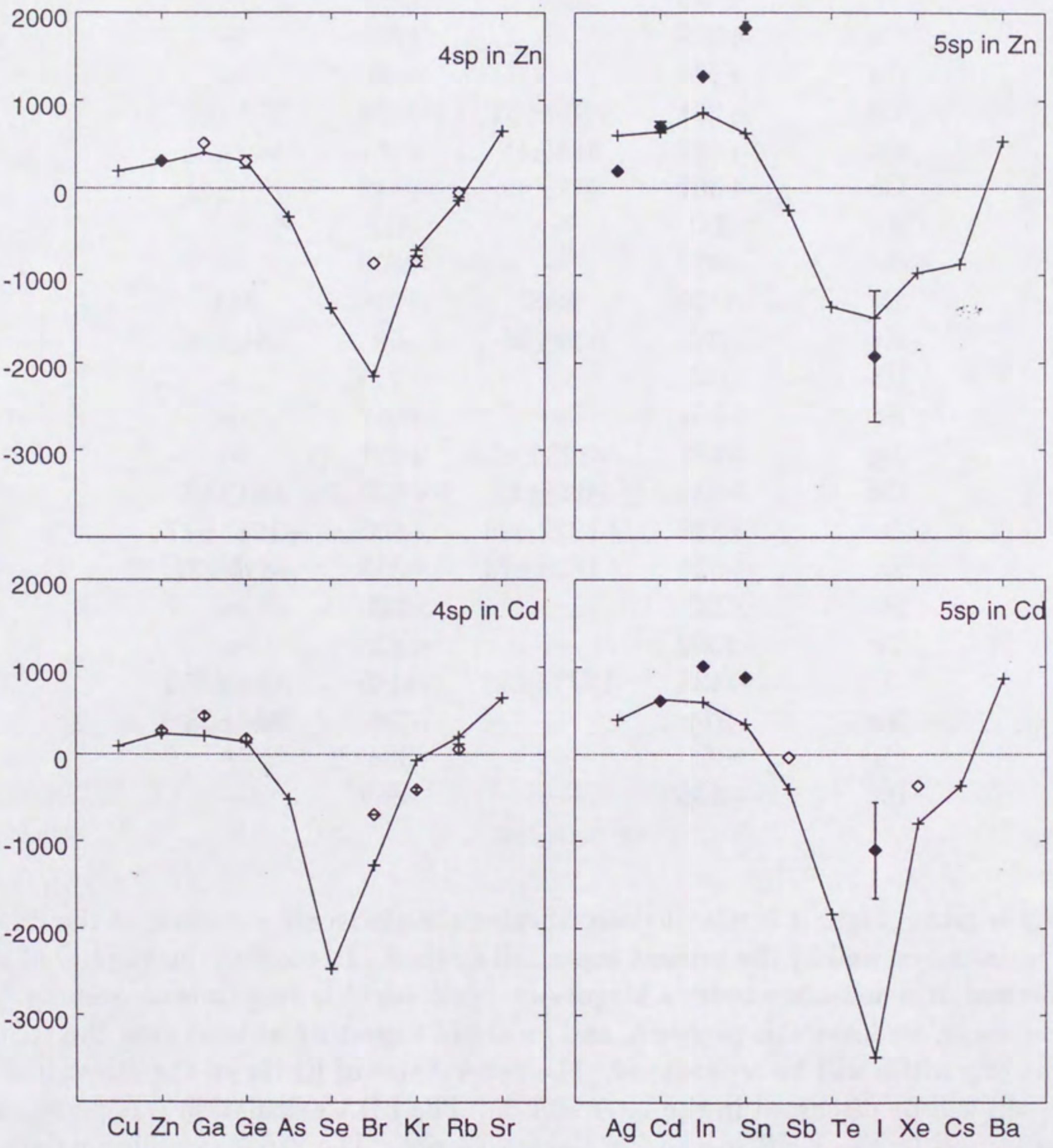

Figure 26: Theoretical and experimental EFGs at sp-impurity sites in Zn and Cd. For the closed symbol, the sign of the EFG was experimentally determined. For the open symbol the sign was not determined, so it was assumed to be the same as the theoretical one.

i.e. the 293 keV exited state of ^{77}Br, is very uncertain [113], and the experimental EFGs at I probes are scattered in a wide region of about -1000 to -7000 in 10^{19}V/m^2 depending which isotope is used as a probe [2]. For these cases, a more precise experiment is strongly encouraged to clarify reasons of the discrepancy. The linear increase of the experimental EFGs from Ag to Sn is not reproduced, too. This behavior is quite curious and not seen in the case of the Cd host. It is not obvious that the lattice relaxation causes for this behavior. The further calculations are needed.

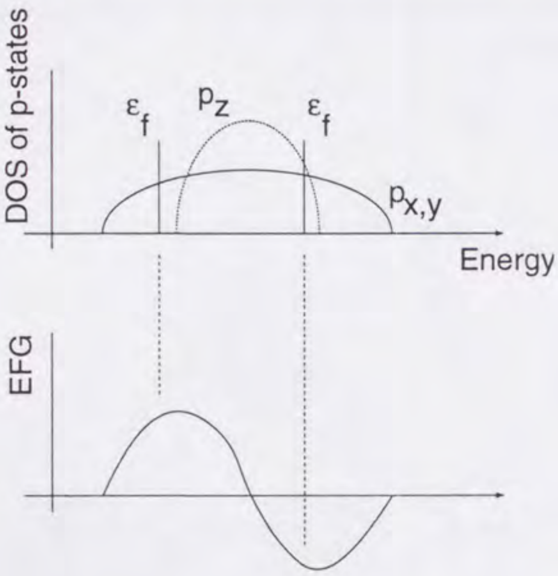

Figure 27: The schematic density of p-states in the HCP structure, and the behavior of the EFG with increasing the impurity valency.

The success in the explanation of the EFGs at impurity sites in Zn and Cd encourages a discussion on the electronic structures of the impurities. As shown in the previous section, mainly the non-spherical p-charge creates the EFG at the nuclear position, and the more occupation of $p_{x,y}$ than p_z leads to a positive EFG, and the less occupation leads to negative. It is expected that the successive occupation of the p-band explains the systematic behavior in fig.26. As noticed in the previous section, in the HCP symmetry the overlap of p_z orbitals between the neighboring atomic spheres is less than that of $p_{x,y}$ orbitals. This leads to narrower p_z band than the $p_{x,y}$ bands. Considering these facts, the local density of states of the p-orbitals in the impurity sphere is schematically shown in fig.27 exaggerated. At the both ends of the p-band $p_{x,y}$ components exceed p_z component, and around the center p_z component is major. Now, it is clear that the EFG shows a S-shaped behavior, with increasing the valency of the impurity atom. This simple model was first proposed by Haas.

Now, the DOS of p-states are shown. In fig.28 and 29, the local DOS of p-states in the impurity spheres are respectively shown for Zn and Cd hosts. The form of the DOS has very complicated structure and the splitting to the bonding and the anti-bonding states is also seen. The difference between p_z and $p_{x,y}$ in the DOS is small, but it is evident that at the end of the p-band $p_{x,y}$ component is larger than p_z and at the center p_z is larger than $p_{x,y}$. To make it clear, in fig. 30 the population of p_z and $p_{x,y}$ orbitals are shown as a function of the atomic number of the impurity in Zn and Cd hosts respectively. They are calculated by integrating the DOS up to the Fermi level. For all cases, in the first half of the period $p_{x,y}$ is more populated than p_z and in the latter half they are interchanged. The difference of population numbers between $p_{x,y}$ and p_z is also shown in fig.30. This is the origin of the S-shaped behavior of the EFGs. It is found that the previous simple minded consideration for the local DOS of p-states described the essential point to explain the systematic trend of the EFGs. It is because that the previous model calculation by Haas succeeded to reproduce the systematic behavior. The present calculation gives a more sound basis to the model.

Figure 28:

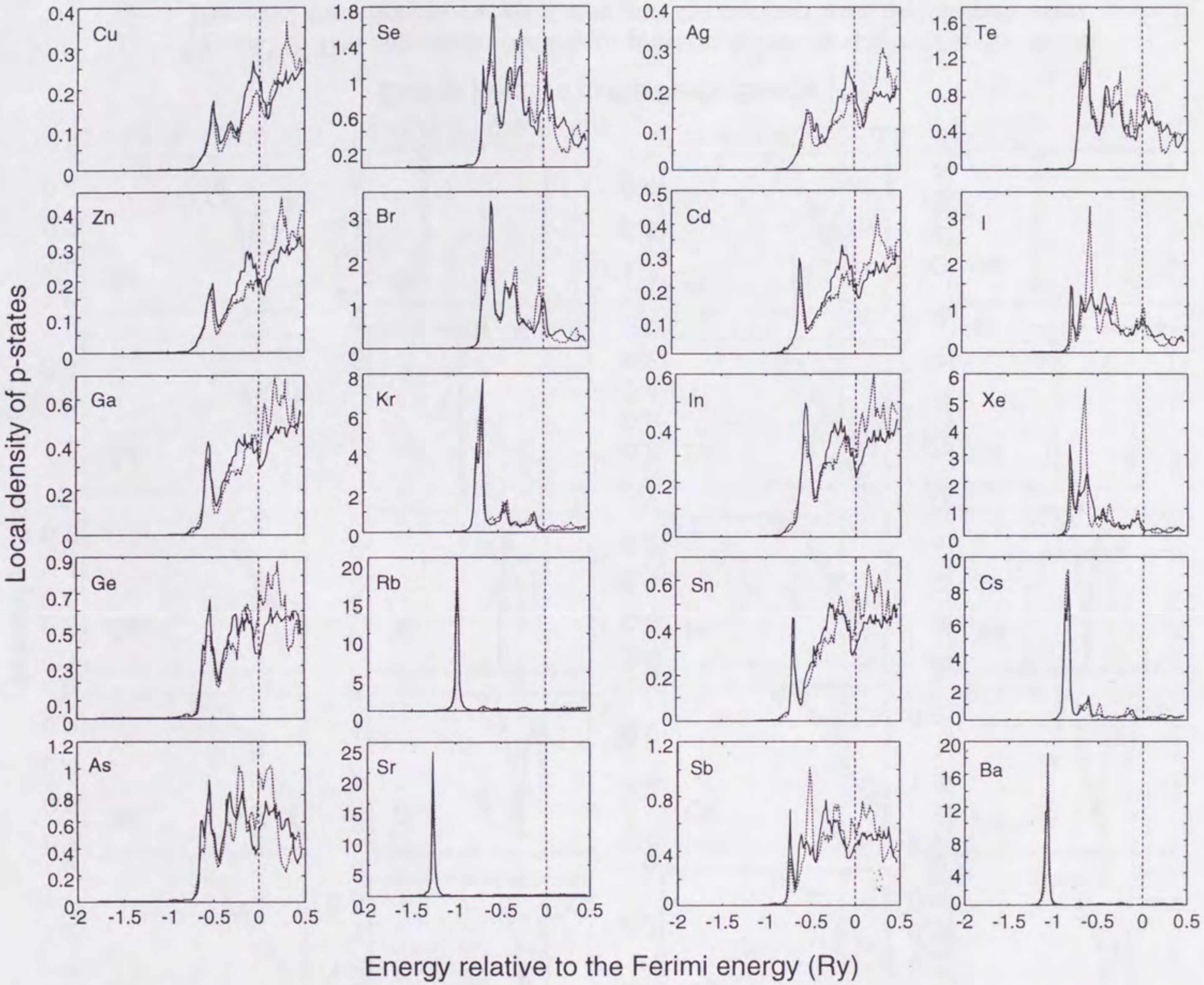

Figure 28: The calculated density of p-states at the sp-impurity sphere in Zn. The solid lines denote px, py states and the dashed lines denote pz states.

Figure 29:

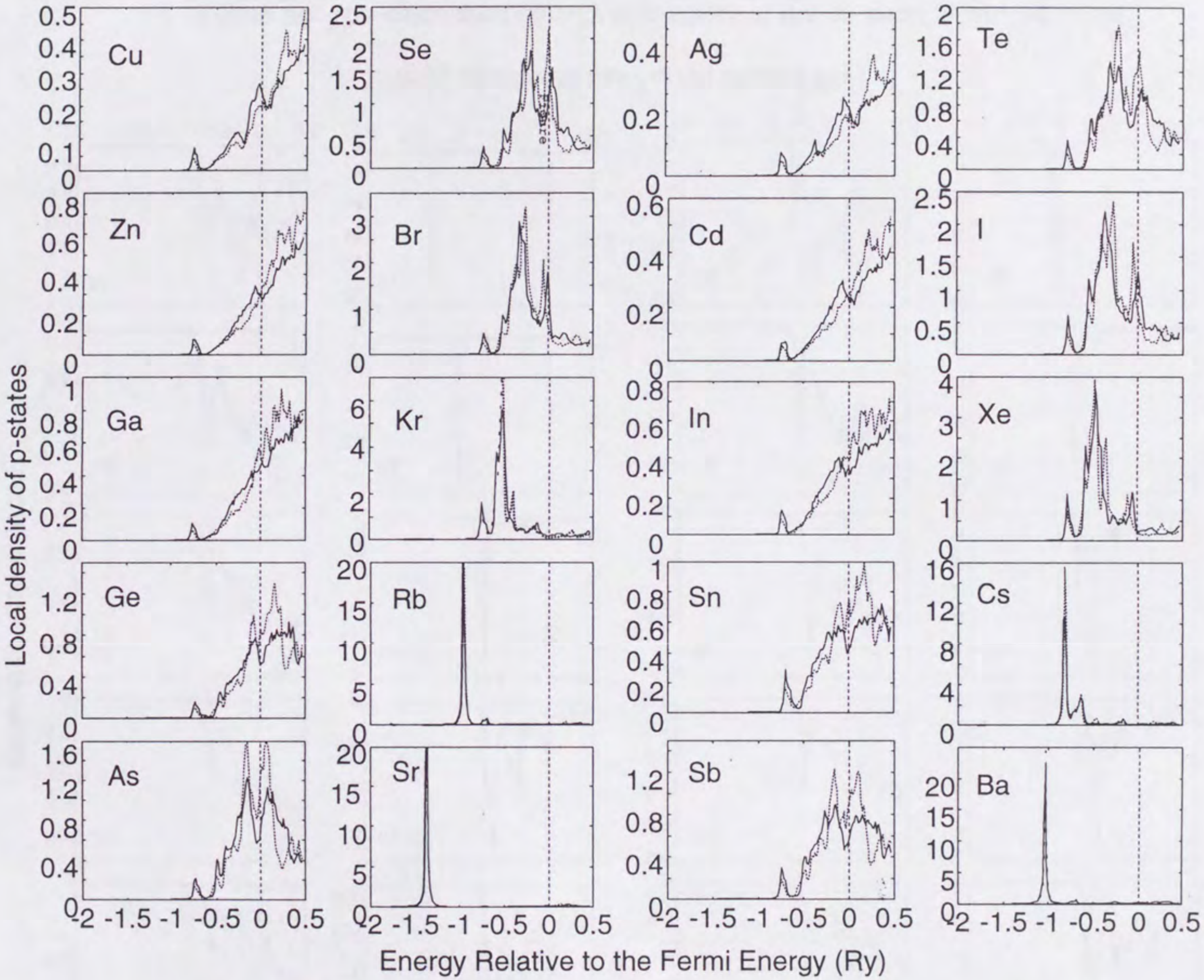

Figure 29: The calculated density of p-states at the sp-impurity spere in Cd. The solid lines denote px, py states and the dashed lines denote pz states.

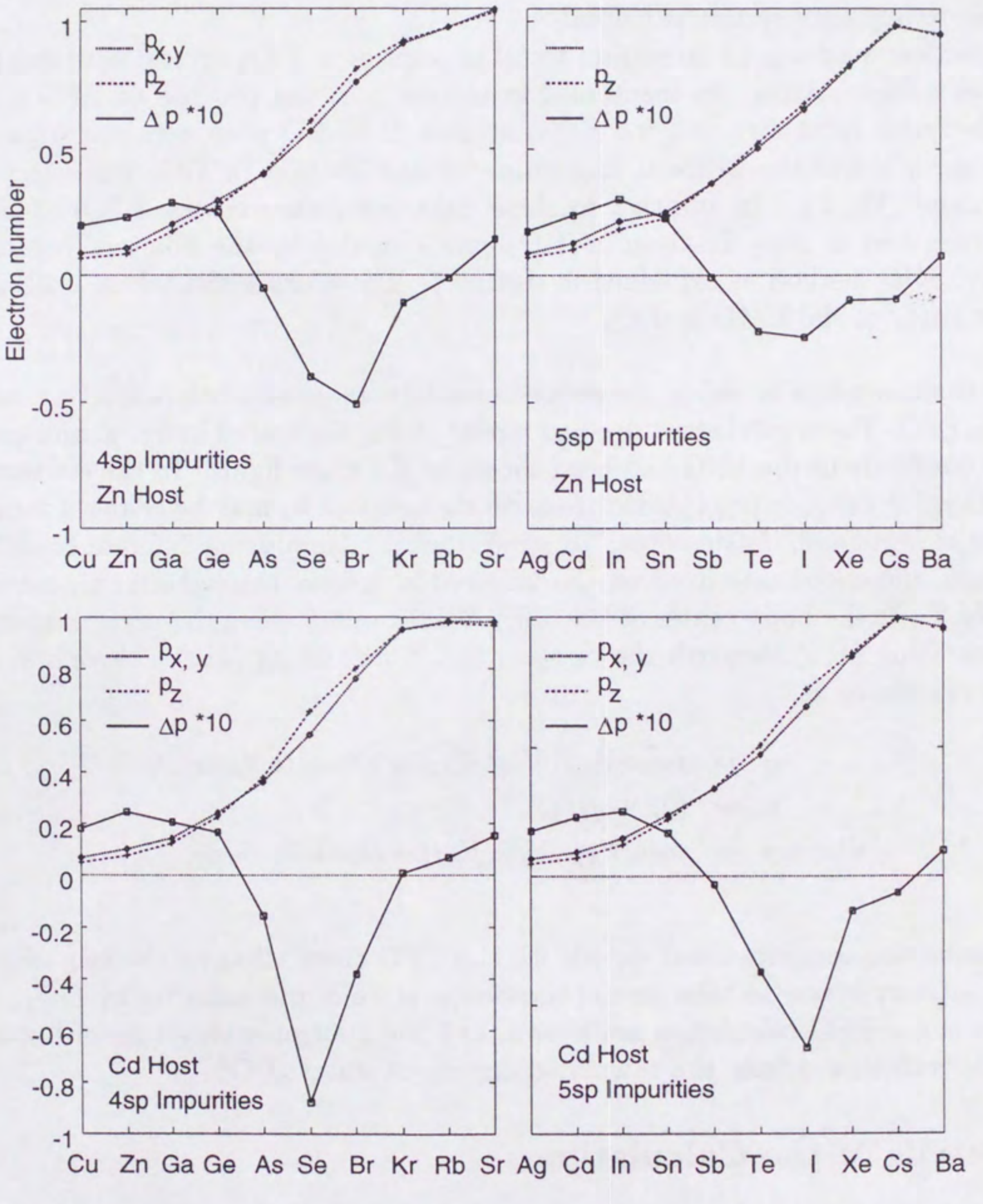

Figure 30: The populations of $p_{x,y}$ and p_z states and their differences. The differences are multiplied by 10. Up: Zn host, Down: Cd host.

7 Transition Metals in TiO_2

Because of variety in its structure, it is difficult to find out systematics of EFGs in various compounds, *i.e.* with changing number of valence electrons, not only their composition but also their spatial configuration changes generally. The EFG reflects the point symmetry at the nuclear position. Therefore, it is the case where a perspective discussion by use of a dilute impurity system is helpful.

In this section, we focus on transition metal impurities in TiO_2 crystal with the Rutile structure as a host matrix. As mentioned in section 1, it can provide an EFG with its tetragonal crystal symmetry and the EFGs at host Ti and O sites were investigated by the NMR method and the EFGs at impurities Cd and Ta sites in TiO_2 were studied by PAC technique [14, 15]. In addition to these data, we measured the EFGs at Sc and Nb impurities and at host Ti atom in TiO_2 single crystal by the Fourier-Transformed NMR (FT-NMR) method as explained in section 5. These experimental data allow us a systematic study of the EFGs in TiO_2.

Here, it is appropriate to define the common coordinate system before starting calculation on the EFG. The crystal structure had already been illustrated in fig. 8, and also the principal coordinate of the EFG had been shown in the same figure. In the conventional notation, $|V_{ZZ}| \geq |V_{YY}| \geq |V_{XX}|$ is satisfied. So the order of V_{ii} may be changed for different impurities or different lattice sites. To avoid trouble in employing different coordinates for each case, the coordinate fixed on the unit cell is defined throughout this section as shown in fig.8. At the body center of the cell, , Z axis points along the crystallographic c axis, Y axis along $\langle\bar{1}10\rangle$ (towards the oxygen) and X axis along $\langle 110\rangle$. Therefore, q and η must be calculated as,

$$\begin{aligned} q &= max[V_{XX}, V_{YY}, V_{ZZ}]\text{in absolute value}, \\ \eta &= (2p+q)/q, \\ \text{where } p &= min[V_{XX}, V_{YY}, V_{ZZ}]\text{in absolute value}. \end{aligned}$$

We describe the computational details for the EFG calculation at the impurity site. The main interest is how to take care of the charge state of the impurity in TiO_2. Next, the results of the EFG calculation are shown, and the electronic structure of impurities in the TiO_2 is discussed from the calculated density of states (DOS).

7.1 Details of the Calculation

The band structure calculations were performed essentially in the same procedure as for the sp impurities in Zn and Cd explained in the previous section. The muffin-tin sphere radii were 0.2085a and 0.21515a (a is the lattice constant) for the metal and oxygen atoms respectively [57]. The 3p states of Sc and Ti atom, the 4p state of Nb atom and the 5p state of Ta atom were included in the band-structure calculation. For Cd case, the 4p state is not included because it lies at -4 Ry relative to the Fermi level and supposed to be confined inside the sphere. The other states at lower energies are assumed as the core states and treated as an atomic problem. To evaluate integrals over the k-space, we used 8 k points in the irreducible wedge of the Brillouin zone. It seems too small. However,

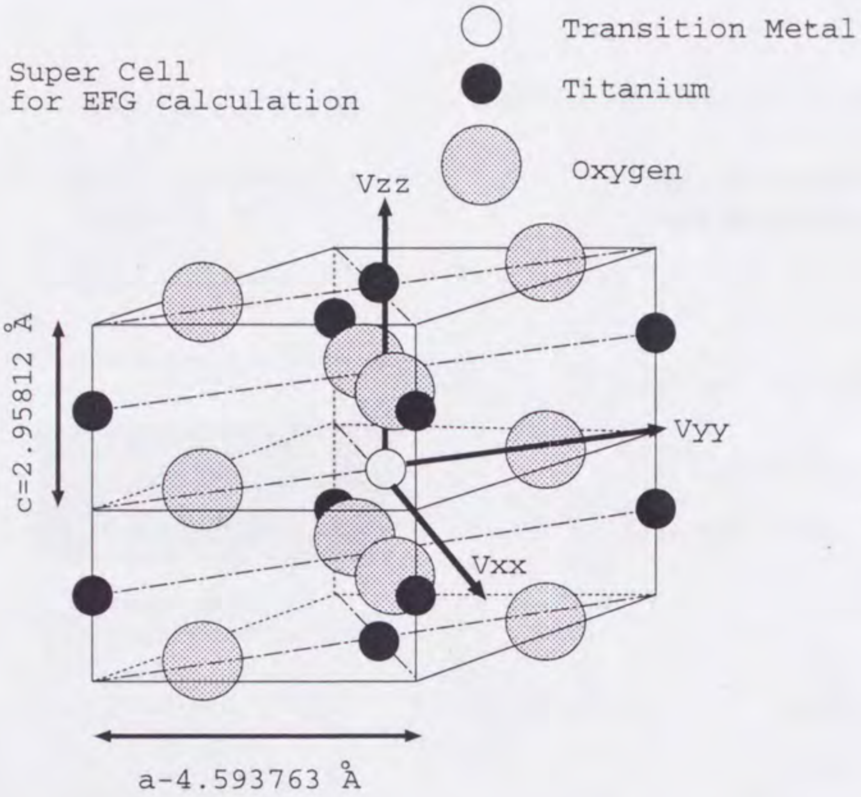

Figure 31: The super cell used in the present EFG calculations for the impurity systems. The definition of the principal axis of the EFG is also given.

it was confirmed in the typical case where the number of k points was varied up to 125 that the calculation was well converged even in 8 k points.

To simulate the system with impurities, the super cell shown in fig.31 was employed. It consists of two unit cells of TiO_2 stacked along the c-axis with the body centered Ti atom substituted by the respective impurity atom.

For the realistic calculation, we have to simulate the charge state of impurities in TiO_2. For the case of Nb, the NMR signals of the transitions between magnetic sub-states $m = \frac{1}{2}$and $-\frac{1}{2}$ of Nb were observed at about the Larmor frequency of Nb nucleus, so the Nb atom was in the diamagnetic electronic configuration. The neutral Nb atom has one more valence electron than the neutral Ti atom. In the TiO_2 matrix which consists of Ti^{4+} ion and two O^{2-} ions, it is reasonable that Ti^{4+} ions are substituted with Nb^{5+} ions, and the residual electron is compensated by a certain mechanism. In the dilute impurity limit, which is the real experimental situation, the charge neutrality must be kept only in the very broad region, so the charge neutrality can be broken when we focus on the same region with the super-cell around the impurity. It means that the super-cell must lose one electron, and is charged up to +1. For the case of Sc, Cd and Ta, it is plausible that Sc^{3+}, Cd^{2+} and Ta^{5+} are realized in TiO_2.

To make the situation more clear, we now consider the electronic structure of the TiO_2 matrix with impurities. The schematic band-structure of pure TiO_2 is shown in fig.32.

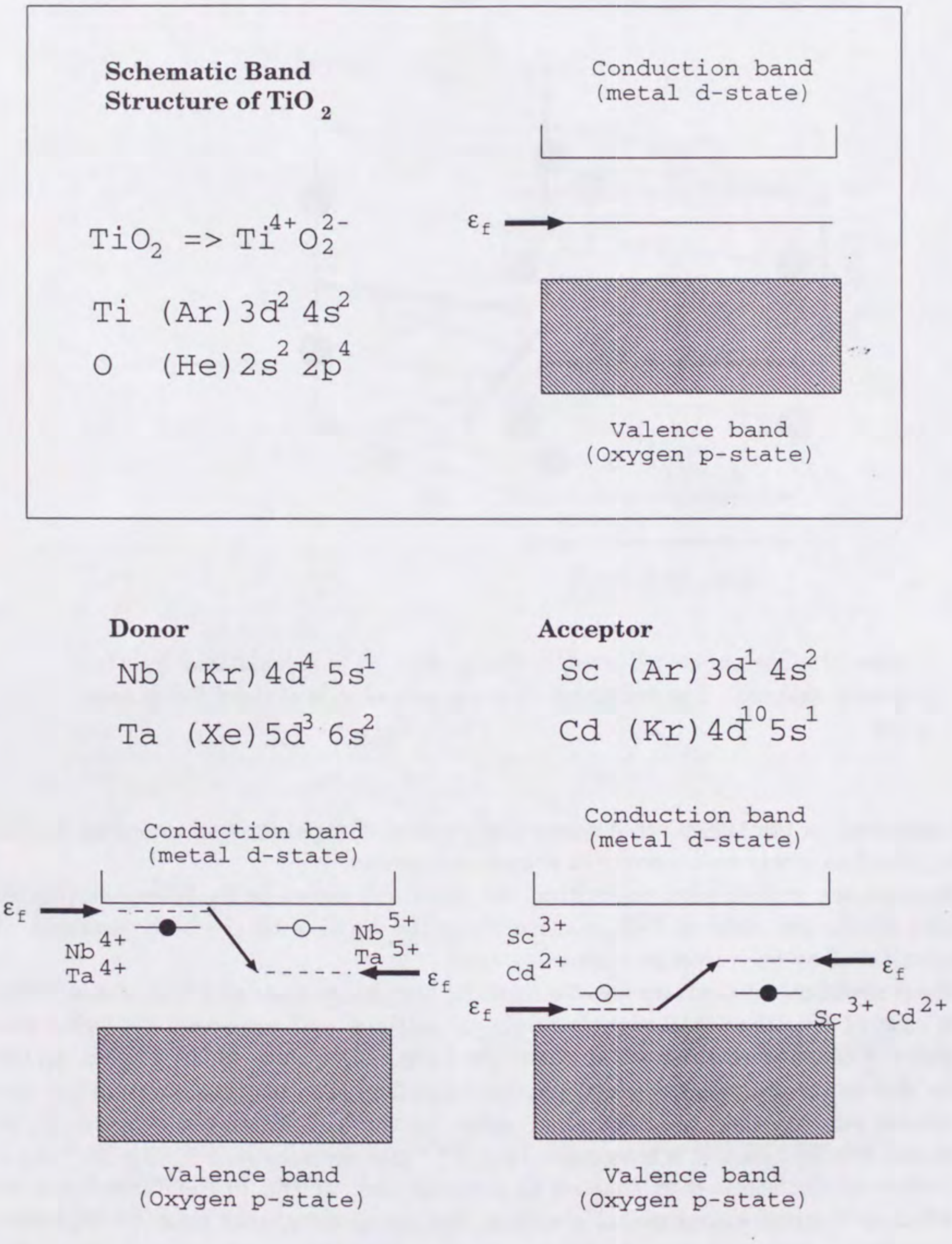

Figure 32: Schematic band structure of pure TiO_2 and TiO_2 with impurities.

The Fermi level (ϵ_f) of pure TiO_2 sits in the band gap. The valence band is mainly from the oxygen p-states and the conduction band is mainly from the metal d-states. Nb atom and Ta atom has one more valence electron than Ti atom. When such donor impurities are introduced in this matrix, donor levels are produced in the band gap (fig.32). Under the charge neutral condition the donor levels are populated, and paramagnetic Nb^{4+} and Ta^{4+} are realized. For the diamagnetic Nb^{5+} and Ta^{5+}, the donor level must release an electron. So, to simulate the diamagnetic situation, the ϵ_f must be shifted downward until the system loses one electron. The donor levels are from metal d-state, so calculated EFG is affected by this manipulation. On the contrary, when the acceptor impurities such as Sc and Cd are introduced, the ϵ_f must be shifted upward until the system get one or two electrons respectively. The acceptor level are mainly from oxygen p-state, so calculated EFG is not affected so much by shifting the ϵ_f. However, whether calculated EFG is affected or not depends on the covalency between the impurity atom and the oxygen atom.

In the band-structure calculation, the unit cell of the system must be charge neutral. We reproduce the realistic electronic structure of the impurity in the framework of the band-structure calculation with the super-cell method as follows: First, the self-consistent band-structure calculation is performed for the super-cell. Then, to simulate the realistic charge state of the impurity, the calculated ϵ_f is shifted. In the case of TiO_2(Nb), the super-cell is charged up to +1 under this manipulation. With thus obtained new ϵ_f, the charge density distribution is calculated to obtain EFGs at the impurity site in the realistic charge state for respective impurities. In this sense, the self-consistency is not achieved in the present calculations.

By the way, more or less the local lattice relaxation caused by the odd impurities is expected. In the super cell method we can handle rearrangements of atoms around the impurity, and we can also estimate the local relaxation by calculating the total energy of the system. The present band structure calculation was performed on the assumption of the charge neutral of the system and it is impossible to calculate the total energy without the charge neutral condition. So, after the estimation of the lattice relaxation under the charge neutral we calculated the EFG with shifting ϵ_f, and made it the theoretical prediction. It is not obvious that the relaxation estimated under the charge neutral condition is also true for the no charge neutral situation. It was investigated separately how much the lattice relaxation influenced to the resulting EFG under the diamagnetic situation. More realistic estimation on the local lattice relaxation is a problem for the future. Of course, the calculations for the pure TiO_2 are free from above discussed problems and straightforward.

7.2 Results and Discussions

First, the DOS of pure TiO_2 is shown in fig. 33 to show the reliability of the present muffin tin calculations. It is the DOS of typical insulator. By the XPS (X-ray photo emission spectroscopy) measurements, Kowalczyk *et al.* [118] found that the TiO_2 had a valence band width of 5.4 eV. It was well reproduced by the present calculations which gave the band width of about 5 eV. Kowalczyk *et al.* also reported that the two major features in the valence band whose energy separation is 1.9 eV. This structure is also seen in the calculated DOS and their separation is about 1.6 eV, which is in perfect agreement with the experiment. He also measured the energy separation of 15.0 eV between the oxygen 2s peak and the lower peak in the valence band. It is comparable to the present result of 13 eV. On the other hand, the experimental band gap of 3.0 eV is severely underestimated by the calculated band gap of 1.4 eV. However it is not so strange, because the LDA only predicts the ground state of the system so an error will occur in the exited states. The overall structure of the calculated DOS is also similar to the FLAPW calculation [119]. It is concluded that the electronic structure of TiO_2 is well described by the muffin tin approximation.

Next, the EFGs at the Ti and O sites were calculated. The results are summarized in table. 8 The predictions by the FLAPW method are also cited [57]. It is found that the both calculations reproduced the experimental EFGs at Ti and O sites well. In particular, they predicted correctly the experimental situations that the EFG along the crystal c-axis (V_{ZZ}) is the maximum (minimum) component for the Ti (O) site in an absolute value. Of course, the complete knowledge about the EFG tensor was not obtained experimentally. The experimental V_{XX} and V_{YY} are arranged in the same order as the theoretical predictions, because there is no way to distinguish V_{XX} from V_{YY} experimentally. According to the sign of them, only $q < 0$ for the O site was experimentally determined. For the others, it was assumed to be the same with the theoretical prediction. However, from the overall agreement in the absolute values and the previous experiences in the calculations of the HCP metals, we can believe the theoretical predictions. In other words, it is determined that the EFG along the c-axis is negative and the second largest component is along the O-Ti-O chain in the basal plane. For the O site, it is concluded that the EFG along the O-Ti-O chain is negative and has the largest absolute value. Regarding the η value, the agreement of the theoretical η value for the O substitutional site is almost perfect. However, for the Ti site the agreement of η by the present method is worse than that of the FLAPW. It is supposed that the error is originated from the muffin tin approximation. The rutile structure is rather open structure and its crystal symmetry is rather low, therefore a correct treatment of not only non-spherical components of atomic potentials but also interstitial regions must be important. Anyway, it is found that the present method can explain the trends of the EFGs in TiO_2, however the calculation precision of η is worse.

From now on, the results of the EFG calculations at the impurity sites are shown. First, it is appropriate to show that the EFG calculations without simulating the charge states of the impurities can not reproduce the experimental results, even if the local lattice relaxations are considered. The total energy of the system was calculated with replacing the 6 oxygen atoms around the impurity. The isotropic local lattice relaxation was assumed so that the local symmetry at the impurity atom was not changed. The calculations of the total energy are plotted as a function of a relaxation in fig. 34, 35, 36 and 37. The relaxation is defined as the ratio of the displacement of the oxygen atom against the distance between the impurity and the nearest neighboring O atom. The local lattice relaxations of about 6%, 7%, 4% and 5% were predicted for Nb, Ta, Sc and Cd impurities, respectively. In the same figures, the calculated EFGs and their decompositions to the *pp* and *dd* contributions were also shown with the respective experimental EFGs. At a glance of these figures, it is found that the EFGs at the Sc site are reproduced well but for the others the EFGs are not reproduced at all. In spite of the well reproduction of V_{ZZ} component of the Sc site, for the cases of the Nb, Ta and Cd impurities, even the direction of the largest component of the EFGs was not predicted correctly. Of course, the sign of the EFG was not determined for all cases and it is assumed to be the same with the EFG at host Ti

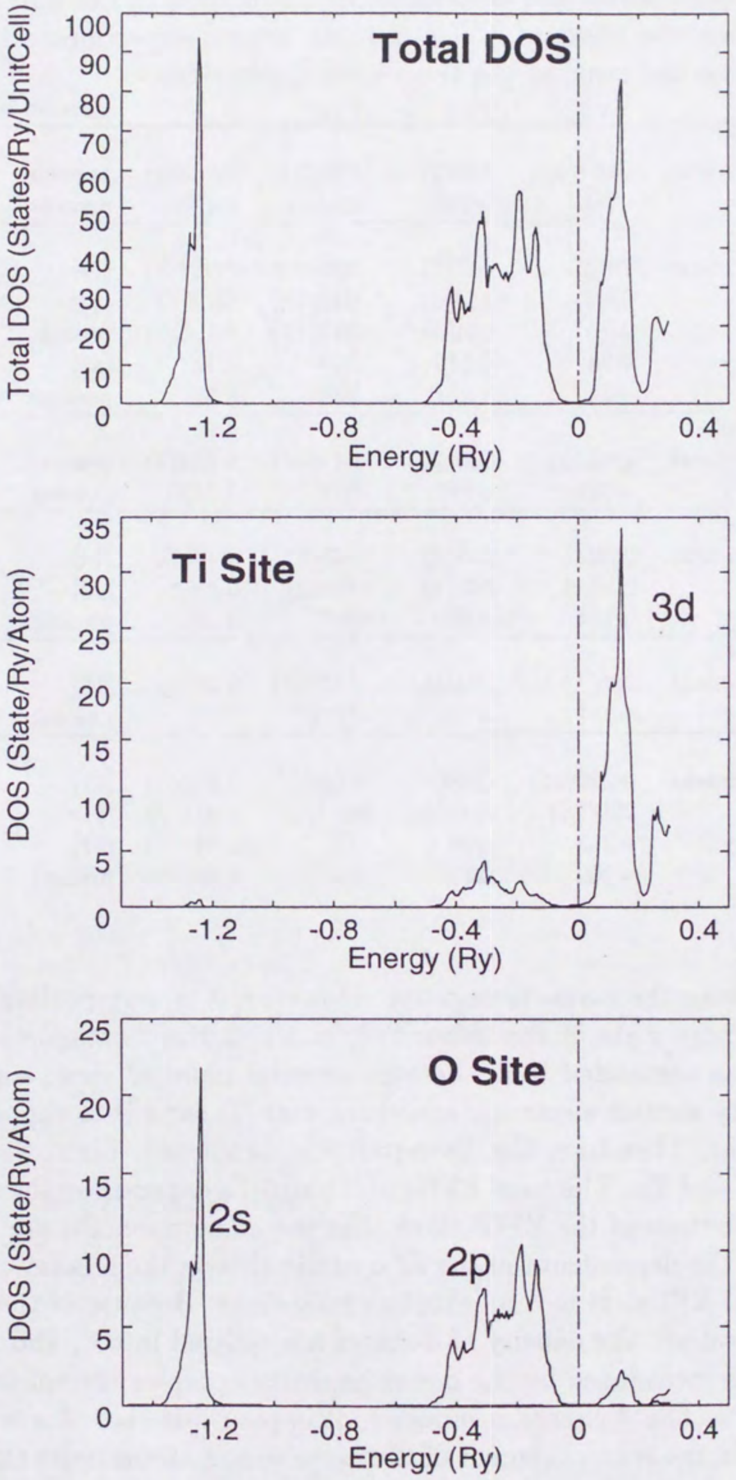

Figure 33: Calculated DOS of pure TiO_2. Total and local DOS are shown. The horizontal axis means the energy relative to the Fermi energy (1 Ry = 13.6 eV).

Table 8: Experimental and theoretical EFGs in TiO_2 in the unit of 10^{19} V/m^2. When the signs of EFGs are not known experimentally, it is assumed to be the same as the theoretical predictions.

	V_{XX}	V_{YY}	V_{ZZ}	η	Reference
Sc site					
Experiment	-1.64(2)	193(2)	-191(2)	0.983(3)	present
Theory	+50	+146	-196	0.490	present
Ti site					
Experiment	79(3)	147(6)	-226(9)	0.303(8)	[12]
	97(4)	143(6)	-240(10)	0.19(1)	[13]
	97(5)	144(8)	-241(11)	0.192(8)	present
Theory	+60	+149	-209	0.43	[57]
	+44	+222	-266	0.67	present
Nb site					
Experiment	174(11)	470(29)	-644(40)	0.463(7)	present
Theory	+189	+392	-581	0.349	present
Cd site					
Experiment	232(4)	333(4)	-565(8)	0.18(1)	[14]
	236(1)	340(1)	-576(2)	0.18(1)	[15]
Theory	+154	+356	-509	0.39	present
Ta site					
Experiment	286(1)	1044(5)	-1330(6)	0.57(1)	[15]
Theory	+391	+786	-1176	0.34	present
O site					
Experiment	+222(26)	-238(27)	+16(2)	0.868(5)	[12]
	220(25)	-240(28)	20(2)	0.831(7)	[114]
Theory	+213	-196	-17	0.84	[57]
	+209	-215	+6	0.94	present

site, *i.e.* the EFG along the c-axis is negative. However, it is very probable, because the discussion on the charge state of the impurities, in which the diamagnetic configuration for each impurity was demanded from the experimental point of view, suggests that the impurities are in very similar electronic structure with Ti, and it is supposed that their EFGs are very similar. Therefore, the discrepancy is significant. First, we discuss on the donor impurities Nb and Ta. The total EFGs of Nb and Ta depends on the relaxation very much. The decompositions of the EFGs show that the *dd* components are as much as the *pp* components, and the dependence of the *dd* contribution on the relaxation causes to the variation of the total EFGs. It is recognized as followings. Because of the crystal ligand field at the metal position, the density of d-states are splitted into e_g and t_{2g} states. The last electron which is introduced by the donor impurity occupies the splitted *d*-band and the large anisotropy of the *d* charge is induced. It is plausible that this weakly bounded electron is affected by the rearrangement of the neighboring atoms more than the inner *p*-orbitals. So, the *pp* contribution is not so sensitive to the relaxation, on the other hand *dd* contribution depends very much. Anyway, it is found that the last *d*-electron contributes to the resulting EFGs significantly. In the real experimental situation the last electron is compensated, therefore to reproduce the experimental EFGs it is indispensable to simulate such diamagnetic situation of the donor impurities. In the case of acceptor impurity Sc, the *pp* contribution is a main component to the total EFG, because the *d*-band is not occupied. The *pp* component is mainly from the deep $3p$ states of Sc, so the dependence on the lattice relaxation is not so pronounced. More over, the acceptor level is made from the oxygen $2p$ states, so the EFGs at the Sc site is reproduced whether the ϵ_f is shifted or not. In other words, the electronic structure of Sc^{3+} has already reproduced and the EFGs are also reproduced well. On the contrary, in the case of Cd acceptor the significant dependence of the EFGs on the lattice relaxation is shown, and the decompositions of the total EFGs tells us that the *dd* contribution is large and causes to the variation of the total EFGs. This is a consequence of the hybridization between $3d$ states of Cd and $2p$ states of O, *i.e.*, the rather large amplitude is contained in the acceptor states. In such case it is supposed that the simulation of the charge state is indispensable.

Now, the results of the EFG calculations with simulating the charge states of the impurities are shown. In fig. 38 and fig. 39, the calculated EFGs are shown as a function of the charge neutrality, where charge neutrality is defined as *(charge neutrality) = (electron number in the sphere) - (atomic number)*. As explained previously, the charge neutrality of -1, -1, +1 and +2 means Nb^{5+}, Ta^{5+}, Sc^{3+} and Cd^{2+}. It is clearly shown that the calculated EFGs are well reproduced by the theory if the charge neutralities are correctly taken into account.

In detail, the following must be pointed out. For the donor impurities, as shown in fig.38 in the case of Nb in TiO_2, the calculated EFGs depend on the charge neutrality so strongly to change the direction of the maximum component of the EFGs. This strong dependence of the EFG on the charge neutrality is a natural consequence of the fact that the donor level is mainly from the 4d-orbitals of Nb. In the case of TiO_2(Ta), the tendency was almost the same as shown in fig. 38. In the case of Sc as a typical acceptor in TiO_2, the dependence of the EFGs on the charge neutrality are shown in fig.39. The acceptor level mainly consists of the oxygen 2p-state, so shifting the ϵ_f does not influence on the EFG so much as shown in fig.39. On the other hand, as shown in the fig. 39 in the case of Cd, which is also an acceptor impurity, the calculated EFG at Cd site varies with the charge neutrality, and when the charge neutrality is equal to +2, the experimental values are well reproduced. This suggests the covalent bonding between cadmium and oxygen.

The final theoretical predictions and experimental results of EFGs in TiO_2 are summarized in table8 and shown in fig. 40. In these calculations, the local lattice relaxations and the charge states of the impurities were taken into account. It is also found that the agreement of η is not so good in spite of the good reproduction of V_{ZZ} and its direction relative to the unit cell. Besides the unsuitableness of the muffin tin approximation and the smallness of the super cell, the inaccurate estimation of the local lattice relaxation may cause these disagreements. Here, a discussion on the final results are given. We pay attention to the largest component V_{ZZ}. The characteristic behavior of the V_{ZZ} is a significant increase with increasing the atomic number of the impurity atom. In table 9, the respective contributions to V_{ZZ} are shown. To discuss on the origin of the EFG, the population differences Δp and Δd are also summarized in table 9. It is found that Δp and Δd are not depend so much on the atomic number of the impurity. So we reach to the picture in which the charge asymmetry is decided by the local symmetry and it is multiplied by the respective $\langle 1/r^3 \rangle$ factors.

To verify the discussions until now the density of states of these systems are shown. For examples of the donor impurities, DOS of TiO_2(Nb) and TiO_2(Ta) are shown in fig.41. The total DOS and the local DOS at the each atom site are shown. The structure of DOS is very similar to the schematically sketched one in fig. 32. At the dilute impurity

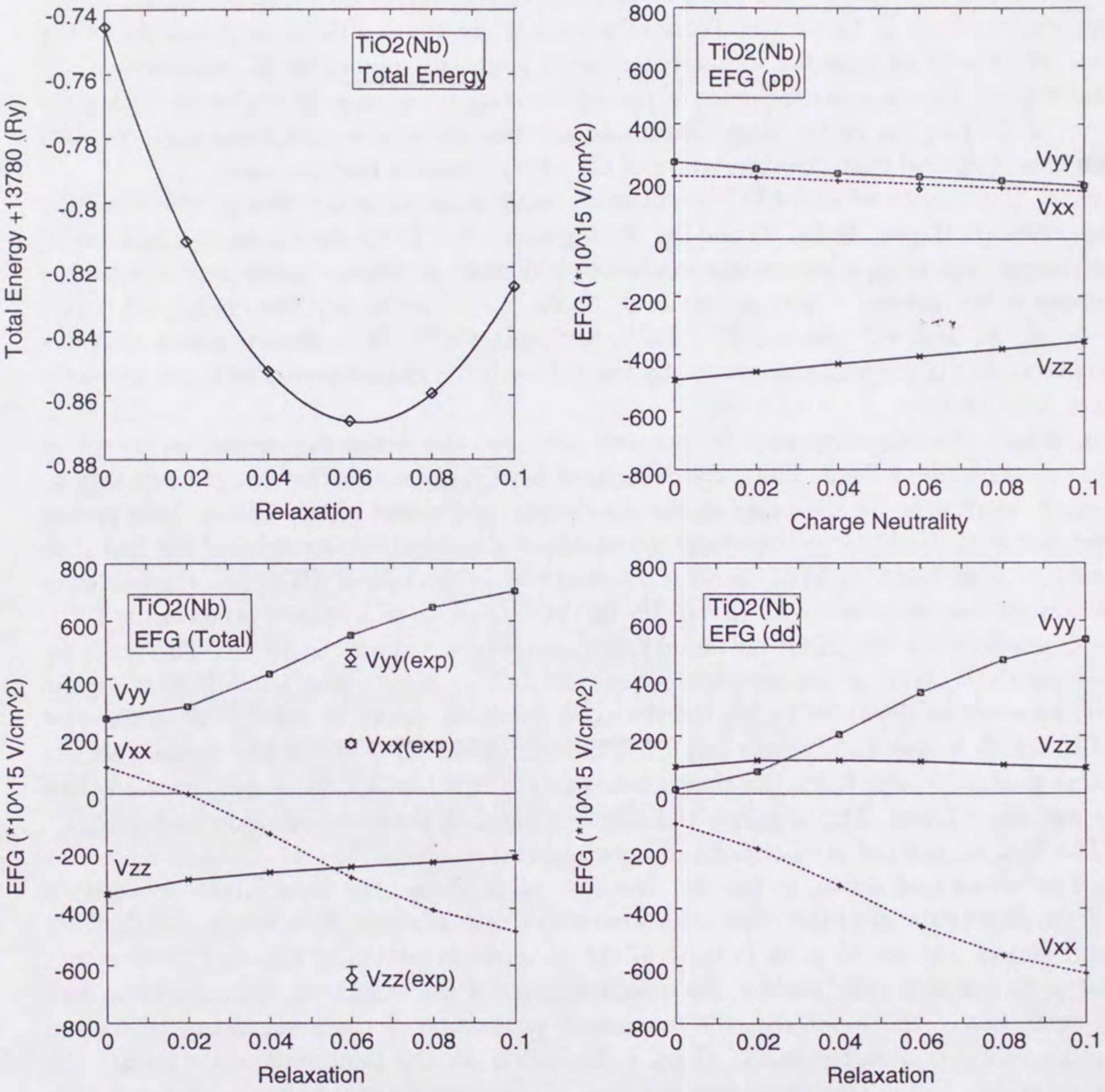

Figure 34: Up left: Total energy calculation for TiO_2(Nb) as a function of a lattice relaxation. Down left : EFG calculation at the Nb site as a function of the relaxation. The experimental results are also shown by the open diamond at the estimated relaxation. Right : The contributions from p (Up) and d (down) charge.

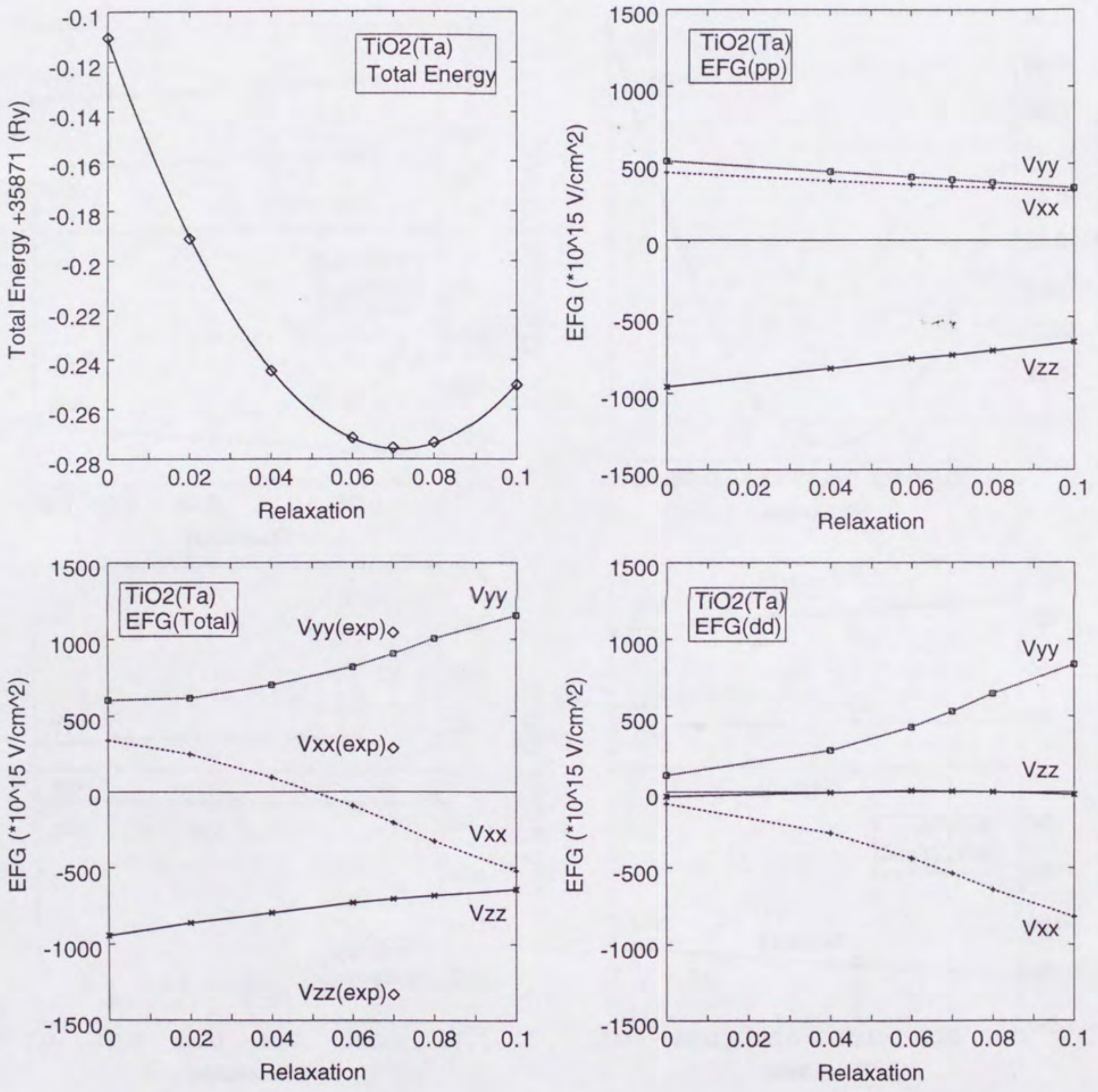

Figure 35: Up left: Total energy calculation for TiO_2(Ta) as a function of a lattice relaxation. Down left : EFG calculation at the Ta site as a function of the relaxation. The experimental results are also shown by the open diamond at the estimated relaxation. Right : The contributions from *p* (Up) and *d* (down) charge.

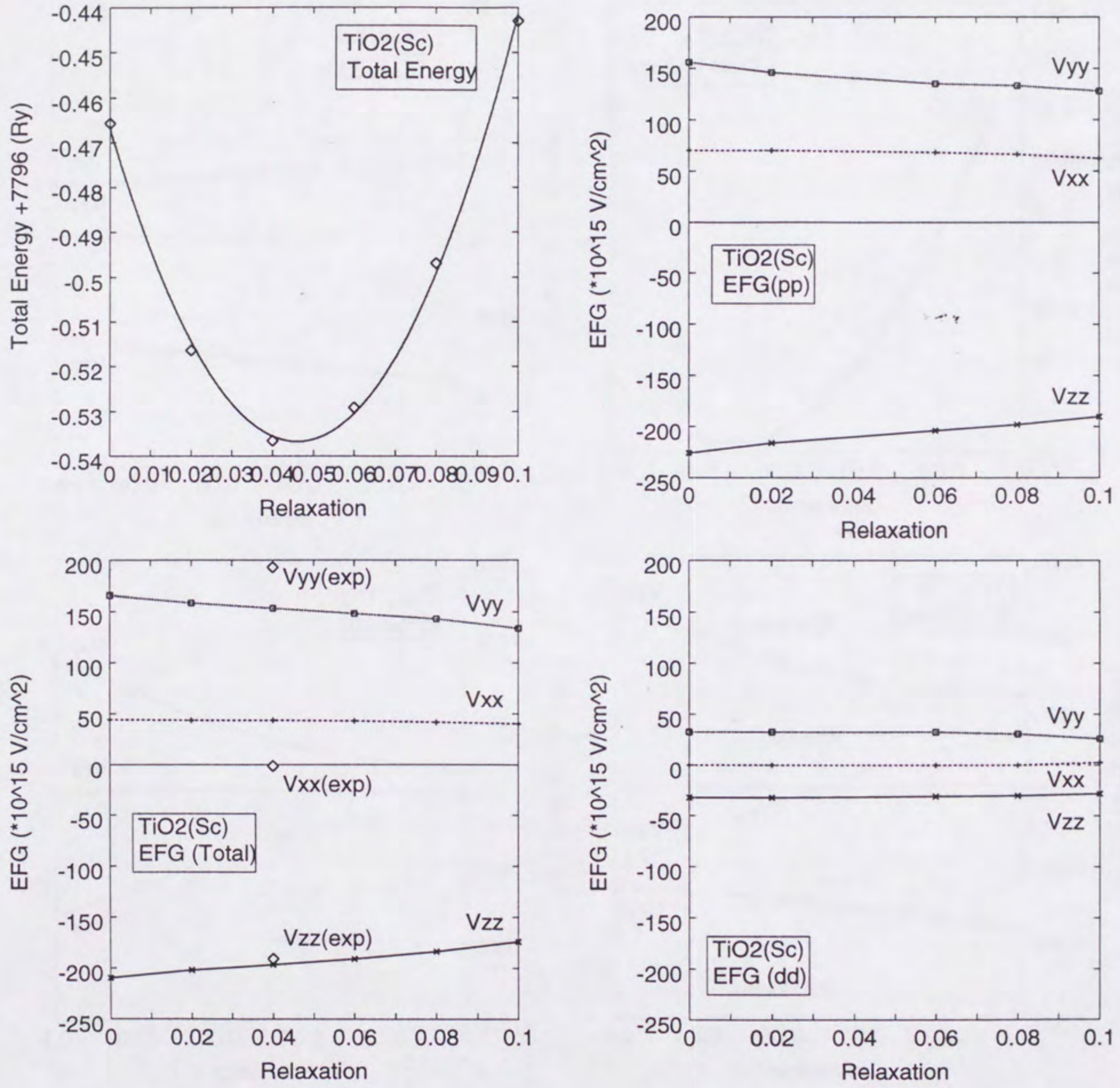

Figure 36: Up left: Total energy calculation for TiO_2(Sc) as a function of a lattice relaxation. Down left : EFG calculation at the Sc site as a function of the relaxation. The experimental results are also shown by the open diamond at the estimated relaxation. Right : The contributions from *p* (Up) and *d* (down) charge.

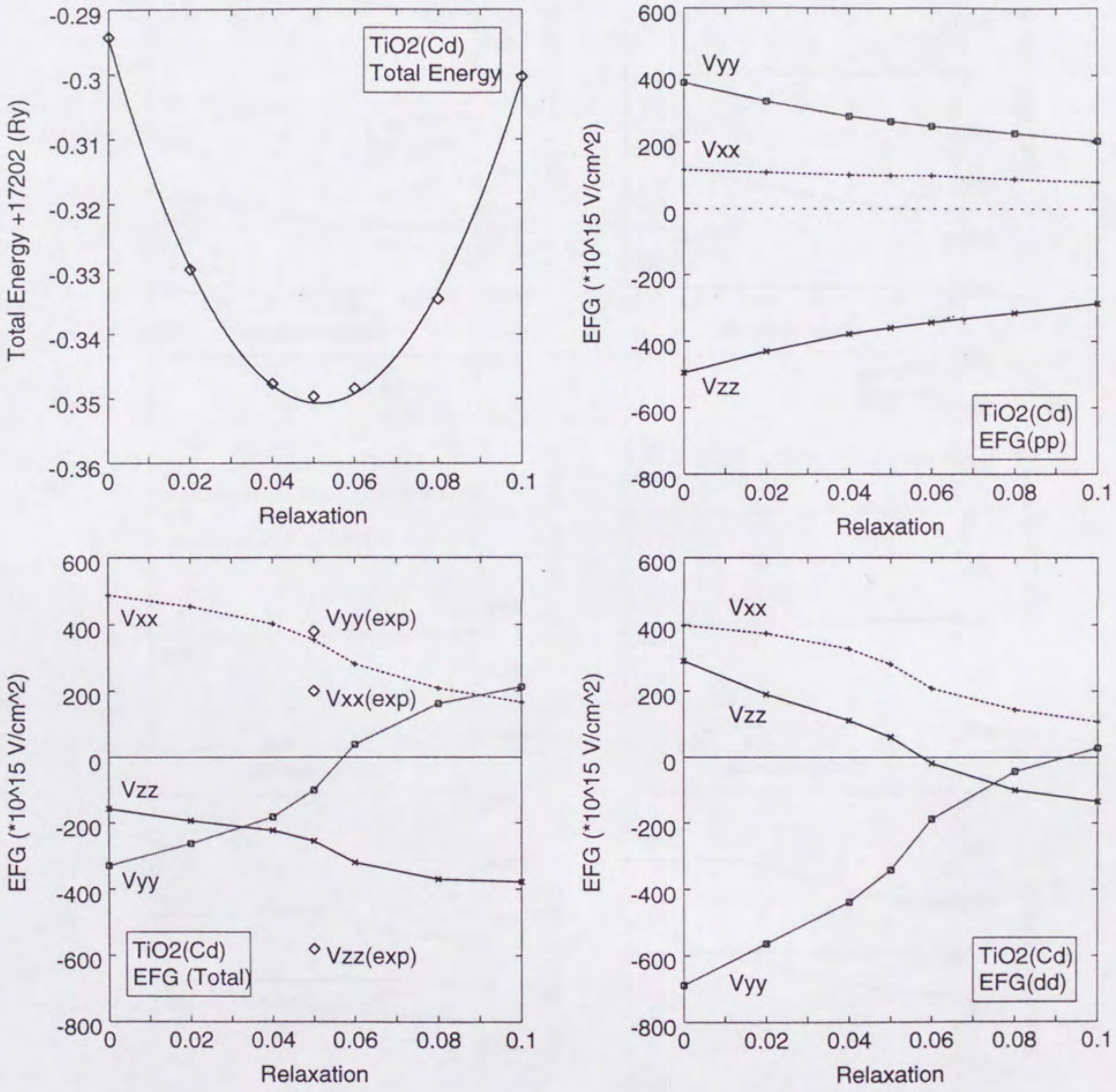

Figure 37: Up left: Total energy calculation for TiO_2(Cd) as a function of a lattice relaxation. Down left : EFG calculation at the Cd site as a function of the relaxation. The experimental results are also shown by the open diamond at the estimated relaxation. Right : The contributions from p (Up) and d (down) charge.

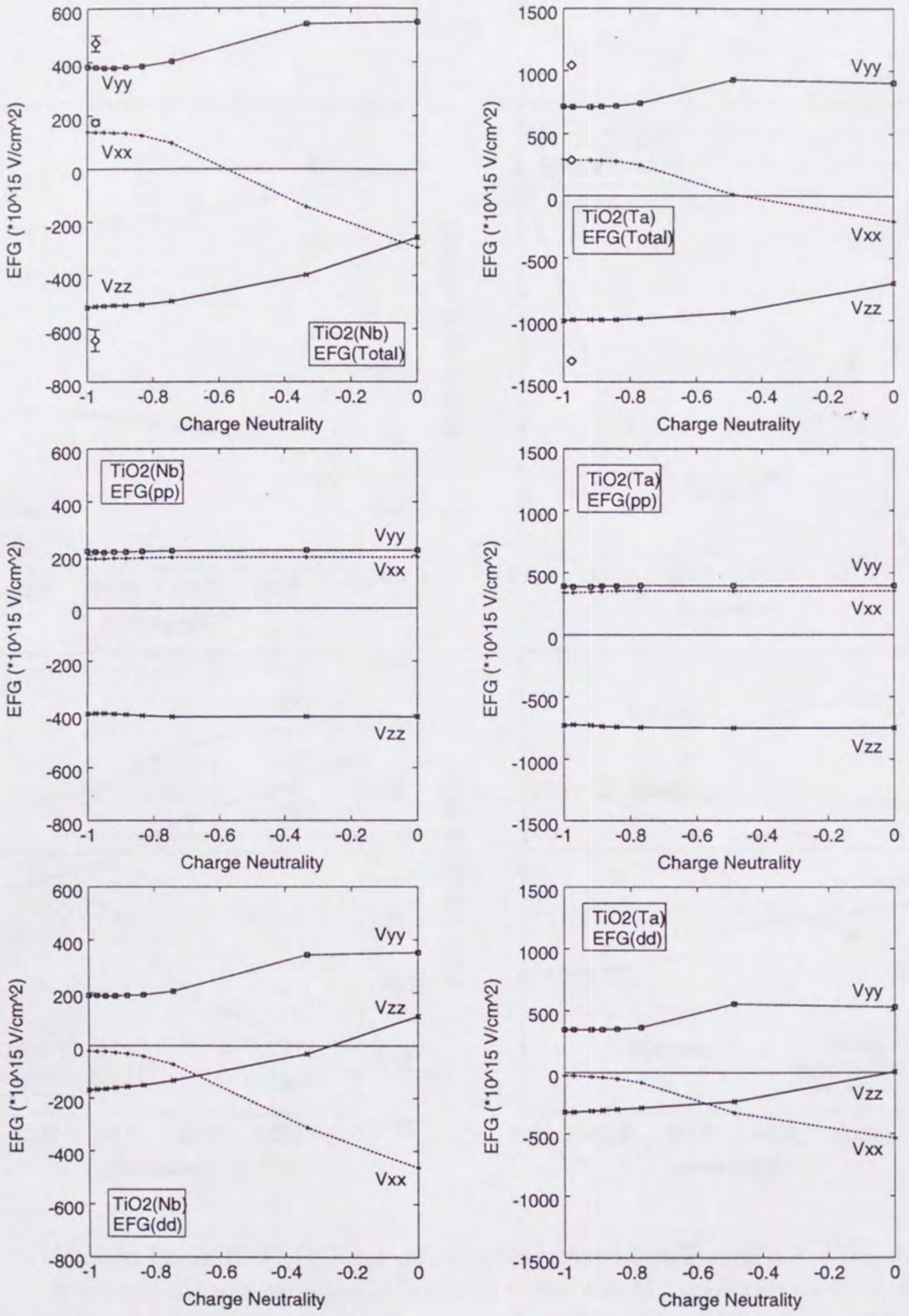

Figure 38: Total and decomposed EFGs at Nb (left hand side) and Ta (right) sites in TiO_2 as a function of the charge neutrality. The charge neutrality = -1 means that the Nb^{5+} and Ta^{5+} are simulated. The experimental EFGs are also indicated by the open diamonds.

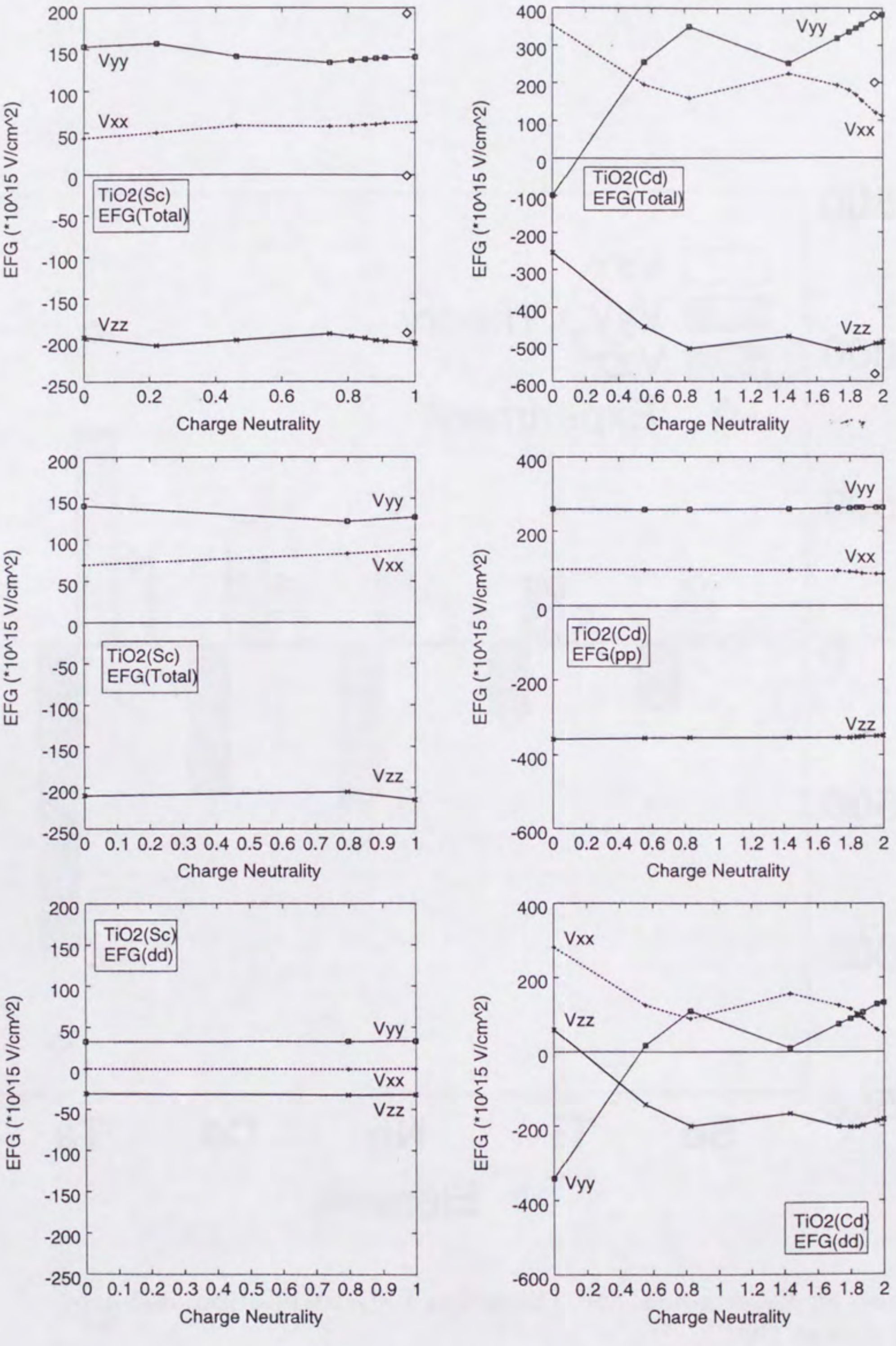

Figure 39: Total and decomposed EFGs at Sc (left hand side) and Cd (right) sites in TiO_2 as a function of the charge neutrality. The charge neutrality = +1 means that the Sc^{3+} is simulated and +2 means Cd^{2+}. The experimental EFGs are also indicated by the open diamonds.

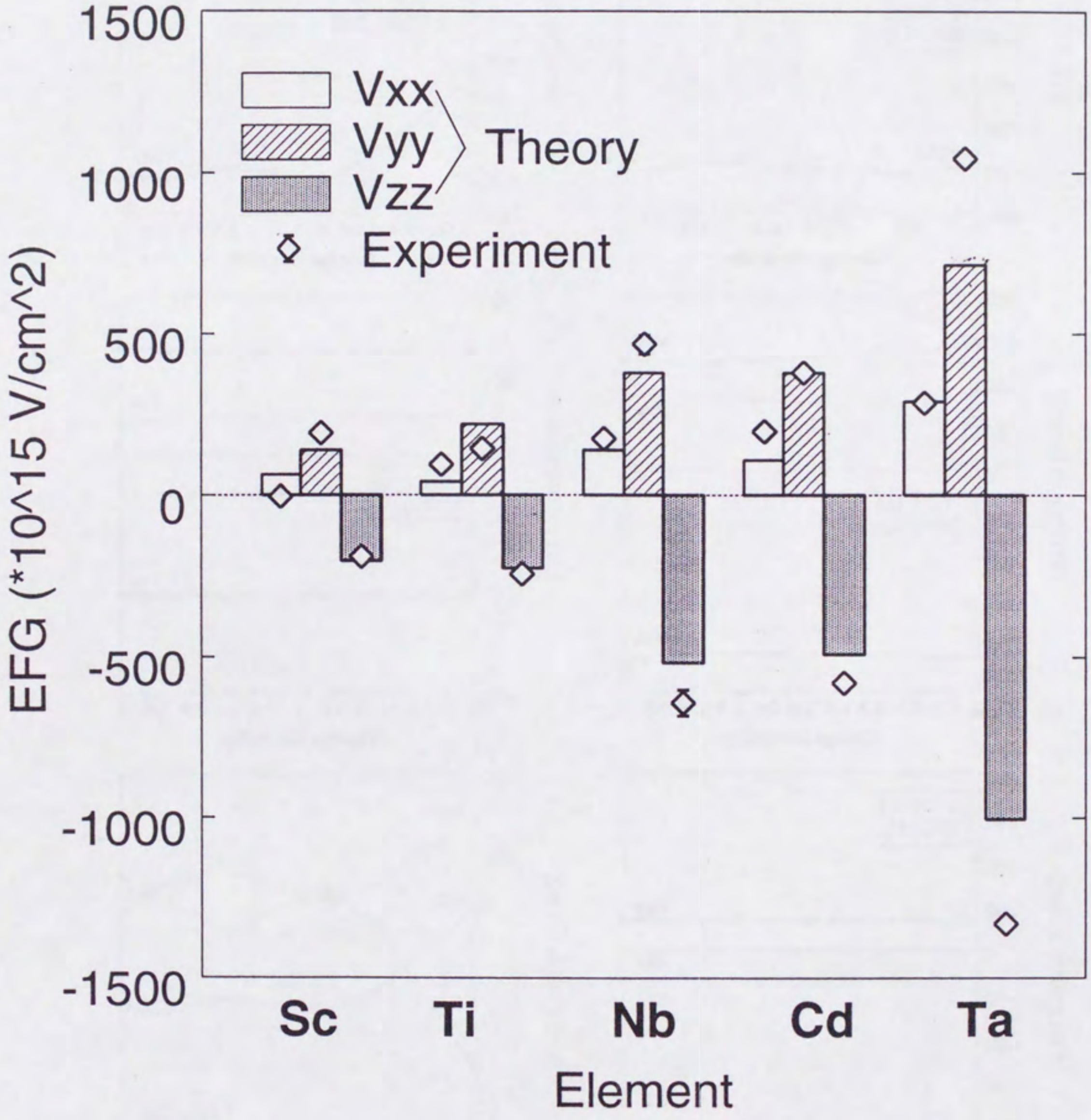

Figure 40: Experimental and Theoretical EFGs at substitutional impurity sites in TiO_2.

Table 9: V^{p}_{ZZ} and V^{d}_{ZZ} components and charge asymmetry Δp and Δd for Sc, Ti, Nb, Cd and Ta.

	V^{total}_{ZZ}	V^{pp}_{ZZ}	V^{dd}_{ZZ}	$V^{lattice}_{ZZ}$	Δp	Δd
Sc	-203	-215	-32	44	-0.00288	-0.01596
Ti	-311	-256	-57	45	-0.00328	-0.02300
Nb	-520	-398	-168	46	-0.00236	-0.02439
Cd	-494	-349	-183	38	-0.00188	-0.00857
Ta	-1004	-729	-321	46	-0.00231	-0.02275

limit, the donor level is formed in the band gap. However, because of the smallness of the super-cell we can not differ it from the conduction band. The occupied lowest states of the conduction band is localized on the metal atom and have negligible amplitude on the Oxygen atom. This electron is removed by shifting the ϵ_f. Therefore, shifting the ϵ_f affects to the calculated EFG for Nb and Ta in TiO_2. On the contrary, for the case of TiO_2(Sc) holes in the valence band are occupied by shifting the ϵ_f. These states are localized on the Oxygen atom as shown in fig. 42. So, shifting the ϵ_f does not affect to the calculated EFG so much. On the other hand, the acceptor level seen in the DOS of TiO_2 in fig.42 have amplitude in the Cd sphere. It means that the bonding between Cd and O is like a covalent bond. Because this covalency of the bonding between Cd and O, the calculated EFG at the Cd are affected by shifting the ϵ_f.

Next, the influence of the local lattice relaxation is examined. The dependence of the EFGs on the lattice relaxation was originated from the variation of the *dd* contribution. Therefore, only a slight dependence on the relaxation is expected under the diamagnetic condition. As shown in fig. 43, it is found that only 10 % difference occurs at most.

Lastly, the dependence on a super cell dimension is discussed. For the EFG of Nb in TiO_2, calculations were performed for the 5 kinds of the super cell as shown in fig. 44. Any lattice relaxation is not taken into account. Only a slight dependence of the calculated EFGs against the cell dimension is seen when the Nb^{5+} charge state was taken into account, on the other hand the calculations presented the severe errors for some of the cells without simulating the Nb^{5+} state (fig 44). It was already shown that the electrons in the *d* states of Nb produced a significant EFGs. It is reasonable that these shallow states influenced by the cell dimension. However, once the donor levels are made to be empty, the EFG is determined by quite local arrangement of atoms. So, the EFG was reproduced rather well by the smallest super cell in which Ti atoms and impurities are placed alternately.

As a summary of this section, it was shown that the present method reproduced experimental EFGs if the realistic charge states of the impurity ions in TiO_2 is considered. The charge state of the impurity ion is simulated by shifting ϵ_f. Considering the charge state of the impurity was indispensable in calculating the EFGs at impurity site in ionic crystals.

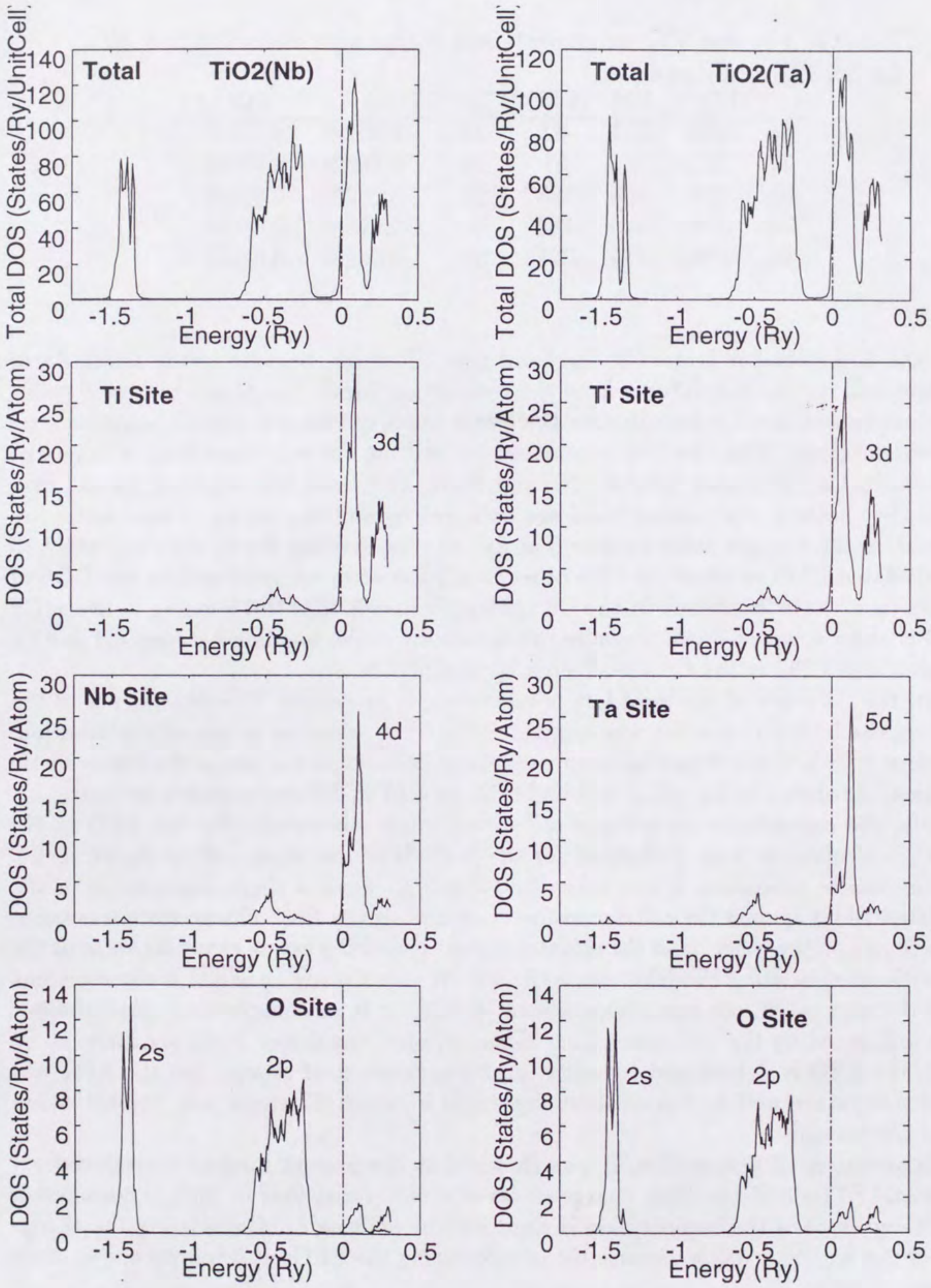

Figure 41: Calculated DOS of TiO_2 with Nb and Ta. Total and local DOS are shown. The horizontal axis means the energy relative to the Fermi energy.

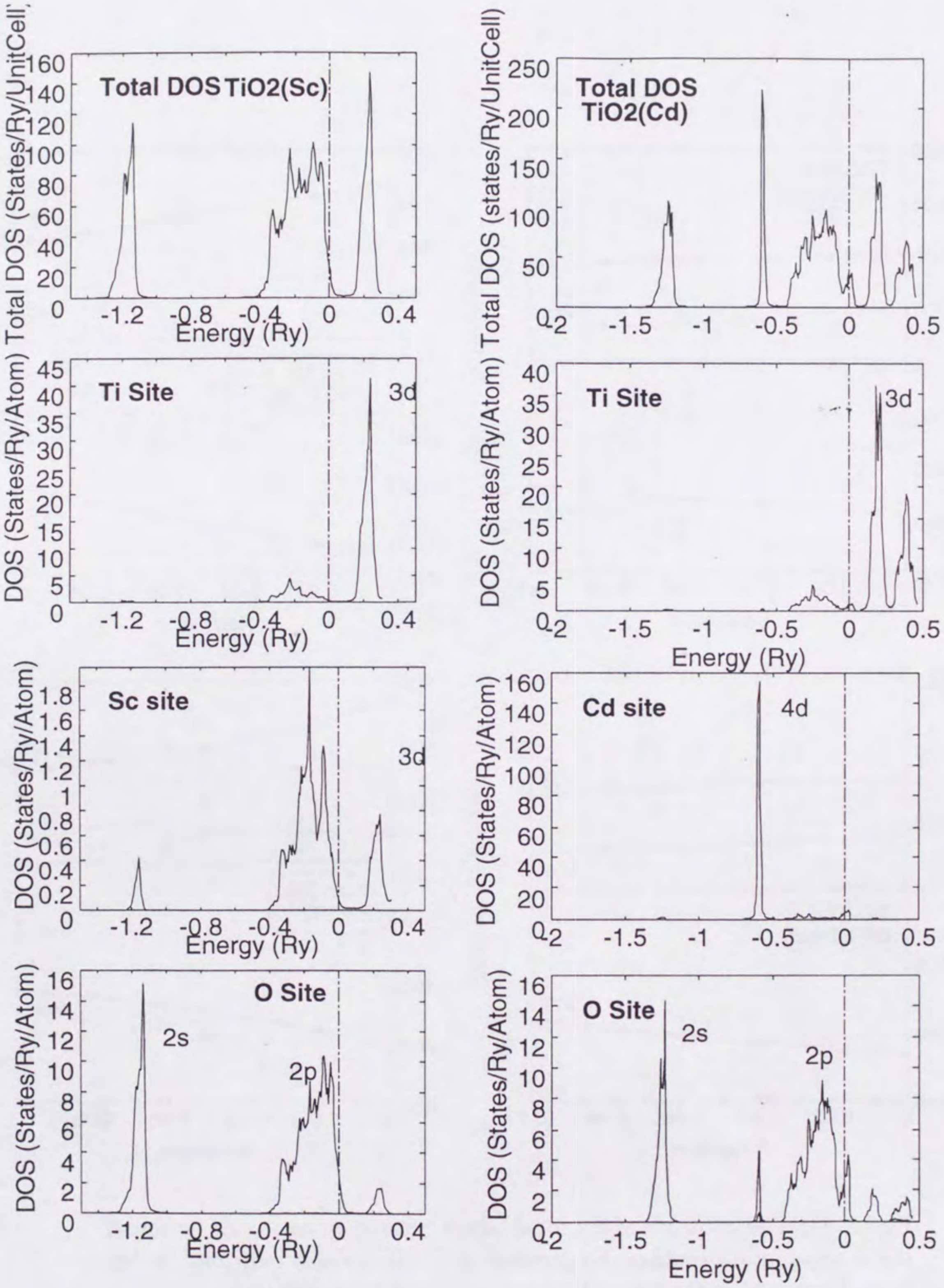

Figure 42: Calculated DOS of TiO_2 with Sc and Cd. Total and local DOS are shown. The horizontal axis means the energy relative to the Fermi energy.

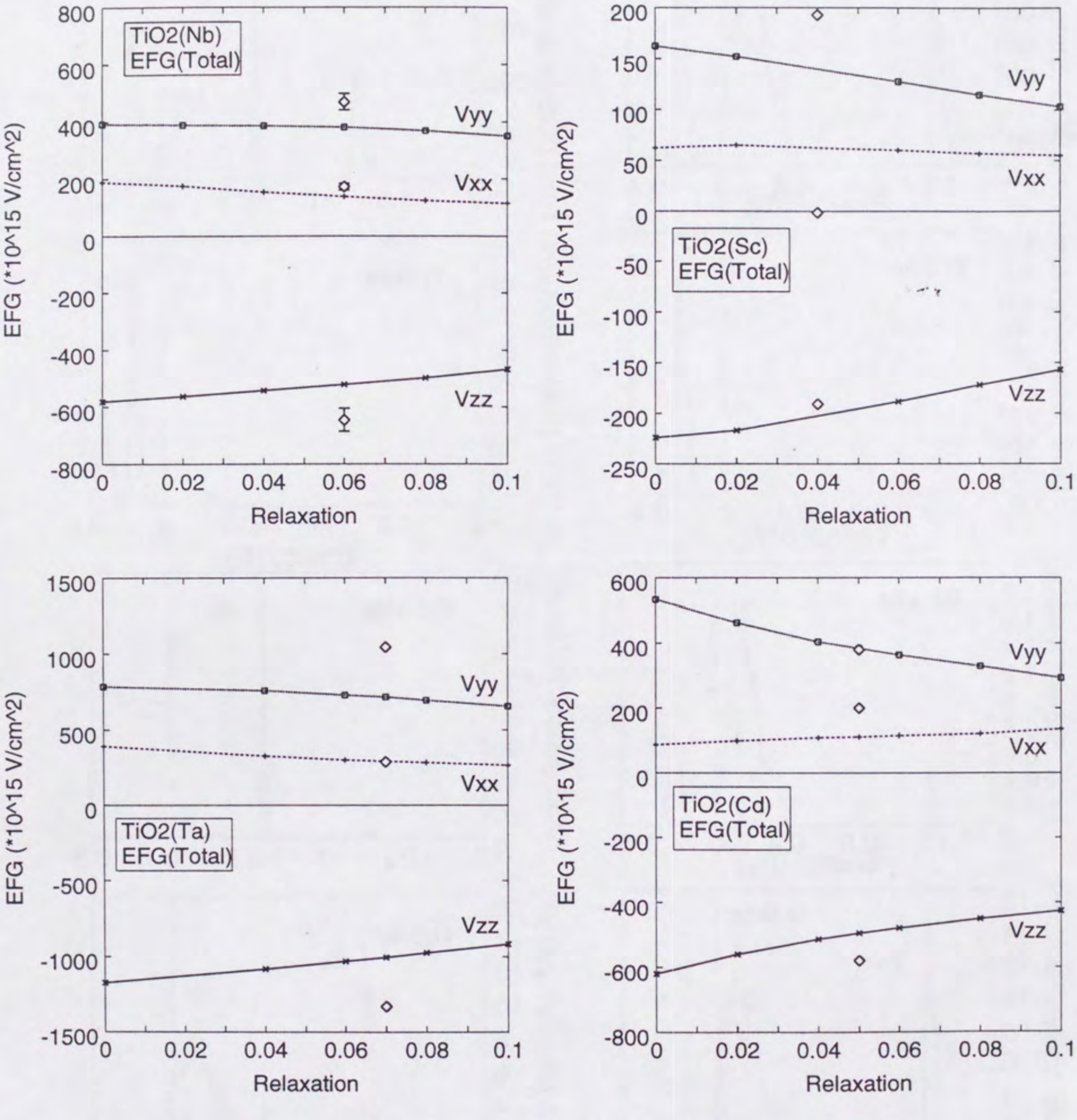

Figure 43: The influence of the local lattice relaxation on the EFGs under the diamagnetic situation. Experimental EFGs are also indicated by the open diamonds at the respective estimation of the relaxation.

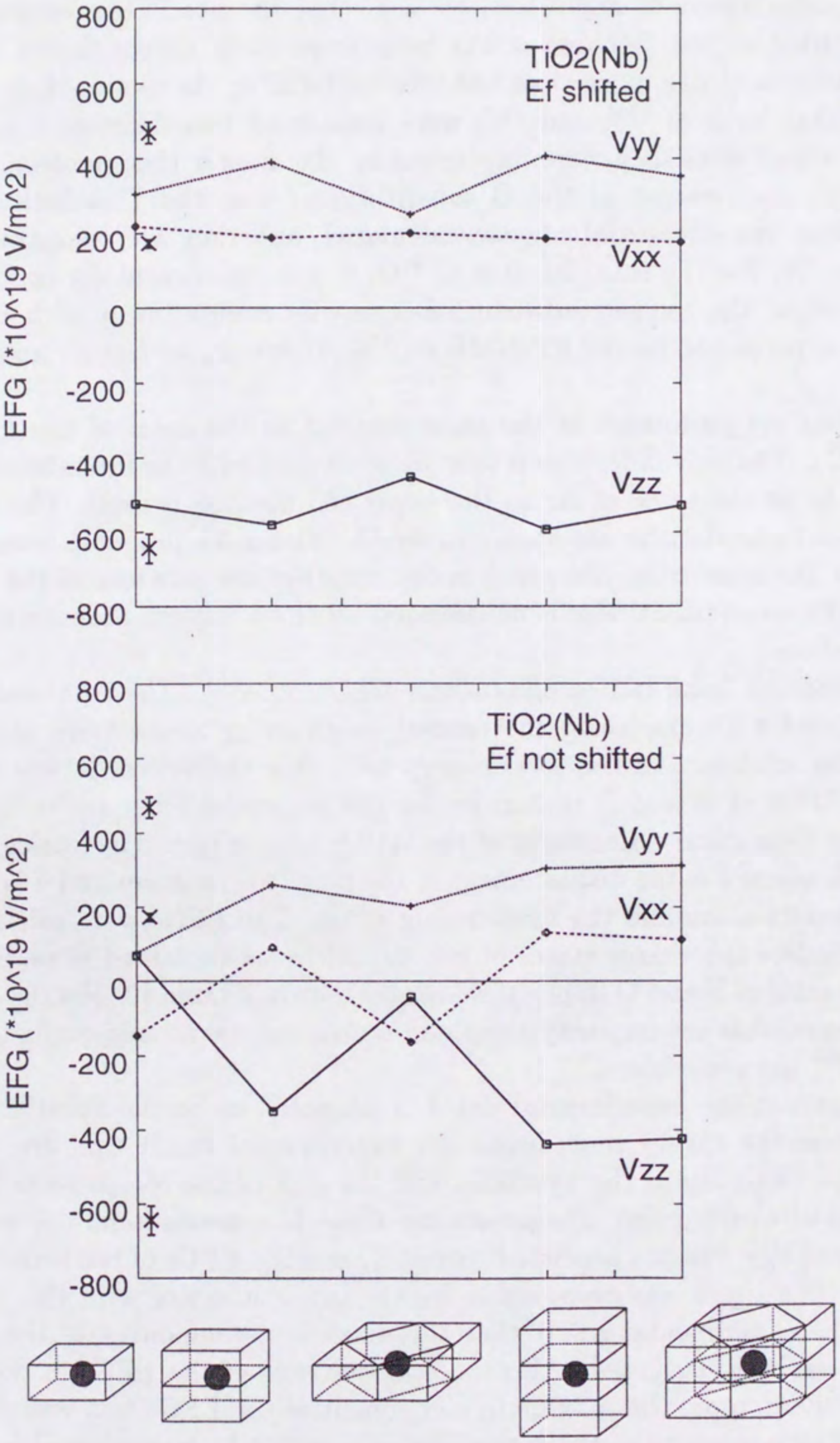

Figure 44: Dependence on the dimension of the super cell. The super cell dimensions are illustrated by the figures. Up: The charge state of Nb was taken into account. Down: The charge state of Nb was not simulated.

8 Lattice Locations of Light Impurities in TiO_2

In the previous calculations of impurities, we neglected the possibility for impurities to reside at an interstitial site, because it has been empirically shown that a heavy ions favors the substitutional site more than the interstitial sites. In section 4, it was found experimentally that both of ^{12}N and ^{19}O were implanted two different sites in TiO_2. The question is which sites they were implanted in. To answer this question, the EFGs of N and O impurities resided at the O substitutional site, the Ti substitutional site and the octahedral like interstitial site are calculated, and they are compared with the experimental results. For the main fraction of ^{19}O, it was experimentally concluded that they were located at the oxygen substitutional site by comparing η with that of the substitutional site measured by the FT-NMR on ^{17}O. However, we frankly go ahead with the plan.

The calculations are performed in the same manner as the cases of transition metal impurities in TiO_2. The only difference is that we must deal with the interstitials, however it is turned out to be the same as far as the super cell method is used. The super cells used in the present calculations are shown in fig.45. The most probable interstitial site is the octahedral like interstitial site which is the center of the side face of the tetragonal TiO_2 unit cell. This interstitial site is surrounded by the 6 oxygen atoms which form a distorted octahedron.

In these calculations, local lattice relaxations are considered. The total energy of the system is calculated with displacing the nearest neighboring atoms from their original positions, and the minimum of the total energy tells us a theoretical lattice relaxation. The calculated EFGs of N and O impurities for the respective sites are summarized in table 10 with the theoretical estimations of the lattice relaxations. The lattice relaxation is defined as δ/d, where δ is the displacement of the neighboring atom and d is a distance between the impurity atom and the neighboring atom. The EFGs were calculated with shifting ϵ_f to simulate the charge states of the impurities as explained in section 7. The supposed charge state of N and O impurities are also shown in table 10. For the interstitial site, it was supposed that the impurity atom had a diamagnetic atomic configuration, *i.e.* N^{1+}, N^{1-} and O^{0+} are plausible.

For the N impurity, the experimental site 1 is proposed to be the substitutional site of oxygen, because the theory reproduced the experimental result that the maximum component of the EFGs lay in the xy-plane, and the sign of the components laid in the xy-plane was opposite each other. The possibility of the Ti substitutional site was rejected because the sign of V_{ZZ} was not predicted correctly, and the EFGs of the interstitial sites were too much. The site 2 was proposed to be the interstitial site with the N^{1+} charge state, because the experimental result that the maximum component of the EFGs lay in the xy-plane was well predicted. Also the opposite sign of the EFGs in the xy-plane was reproduced. Even more the maximum component of the EFGs was well reproduced by the theory. The possibility of the interstitial site with N^{1-} was rejected because the calculated EFGs were too large. The results are summarized in fig. 46.

For the O impurity, the experimental site 1 was confirmed to be the oxygen substitutional site, because of their perfect agreement in η's. Besides, the EFG values were also well reproduced as shown in fig. 47. On the other hand, we could not find out a plausible lattice site for site 2. The theory did not predict any site which had slightly larger EFGs than the site 1 and the similar η with the oxygen substitutional site.

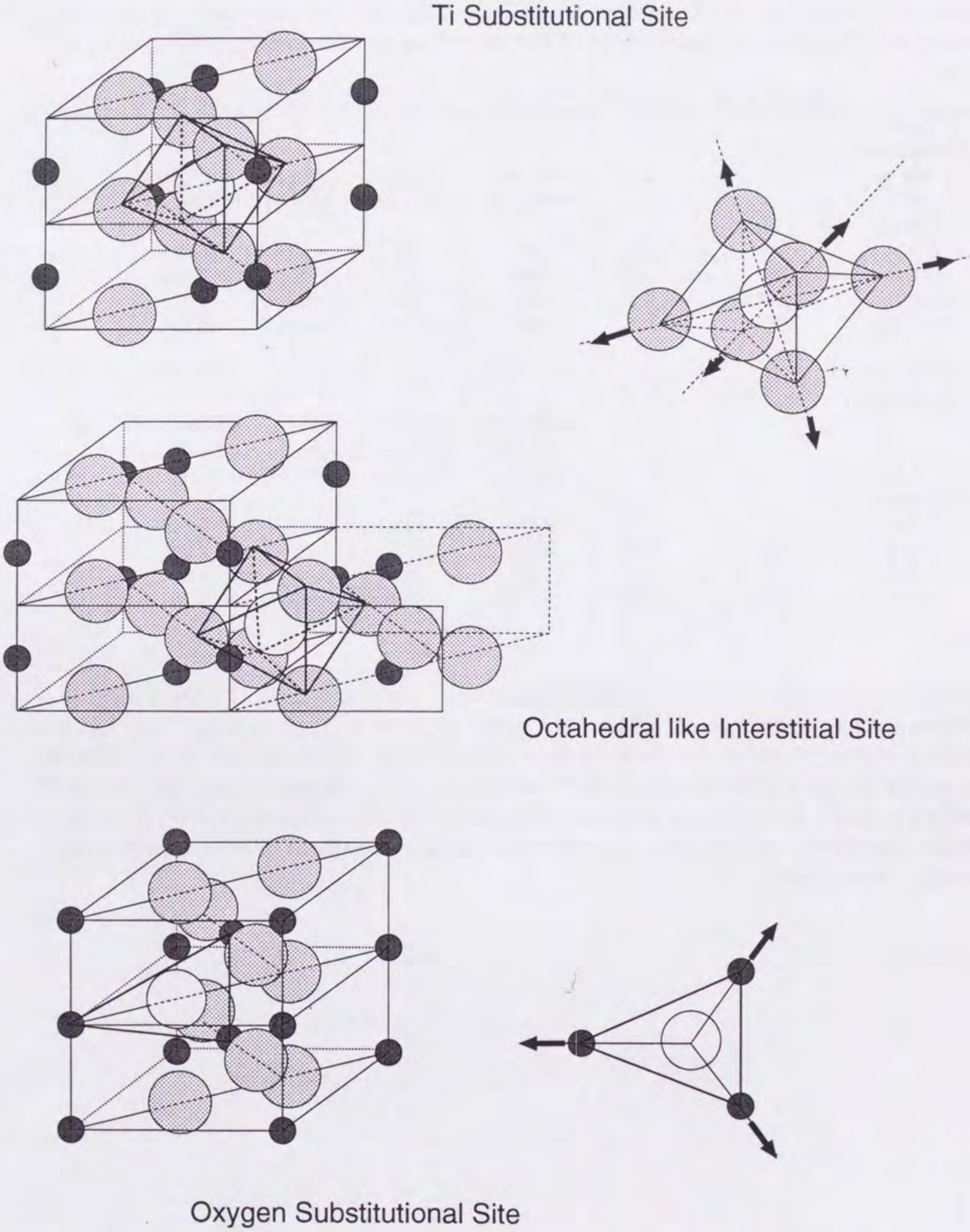

Figure 45: The super cell for the EFG calculations. The Ti substitutional, O substitutional and the octahedral interstitial sites are shown.

Table 10: Theoretical and Experimental EFGs in TiO_2 and the estimations of the lattice relaxation. The assumed charge state of the impurities are also shown. EFGs are in 10^{19} V/m^2.

Site	Charge state	relaxation	V_{XX}	V_{YY}	V_{ZZ}	η	Ref.
N impurity							
Experiment							
site 1			-62±4	+198±14	-135±10	0.37±0.02	
site 2			-586±73	+1220±85	-633±44	0.038±0.005	
Theory							
Ti Sub.	N^{5+}	-8%	-46	-192	+239	0.611	
O Sub.	N^{3-}	+0.3%	+185	-178	-6	0.930	
Oct. Int.	N^{1+}	+22%	-449	+1304	-855	0.311	
Oct. Int.	N^{1-}		-696	+2124	-1429	0.345	
O impurity							
Experiment							
			+222±26	-238±27	+16±2	0.868±0.005	[12]
site1			220±25	-240±28	20±2	0.831±0.007	
site2			343±35	390±40	47±5	0.760±0.009	
Theory							
O Sub.			+213	-196	-17	0.840	[57]
O Sub.	O^{2-}	±0%	+209	-215	+6	0.944	
Ti Sub.	O^{6-}	-9%	-185	-281	+466	0.206	
Oct. Int.	O^{0+}	+20%	+4358	-2284	-2074	0.048	

For both cases of N and O impurities, however, the agreement of the theoretical predictions with the experimental EFGs were still poor. It was already pointed out that the muffin tin approximation may cause to these discrepancies. In the case of the interstitials, not to conflict the muffin tin spheres with each other, it is inevitable to take a rather small muffin tin radius for the impurity atom. This makes the approximation worse. So, in particular with the interstitial impurity, the more realistic treatment of atomic potentials is strongly encouraged.

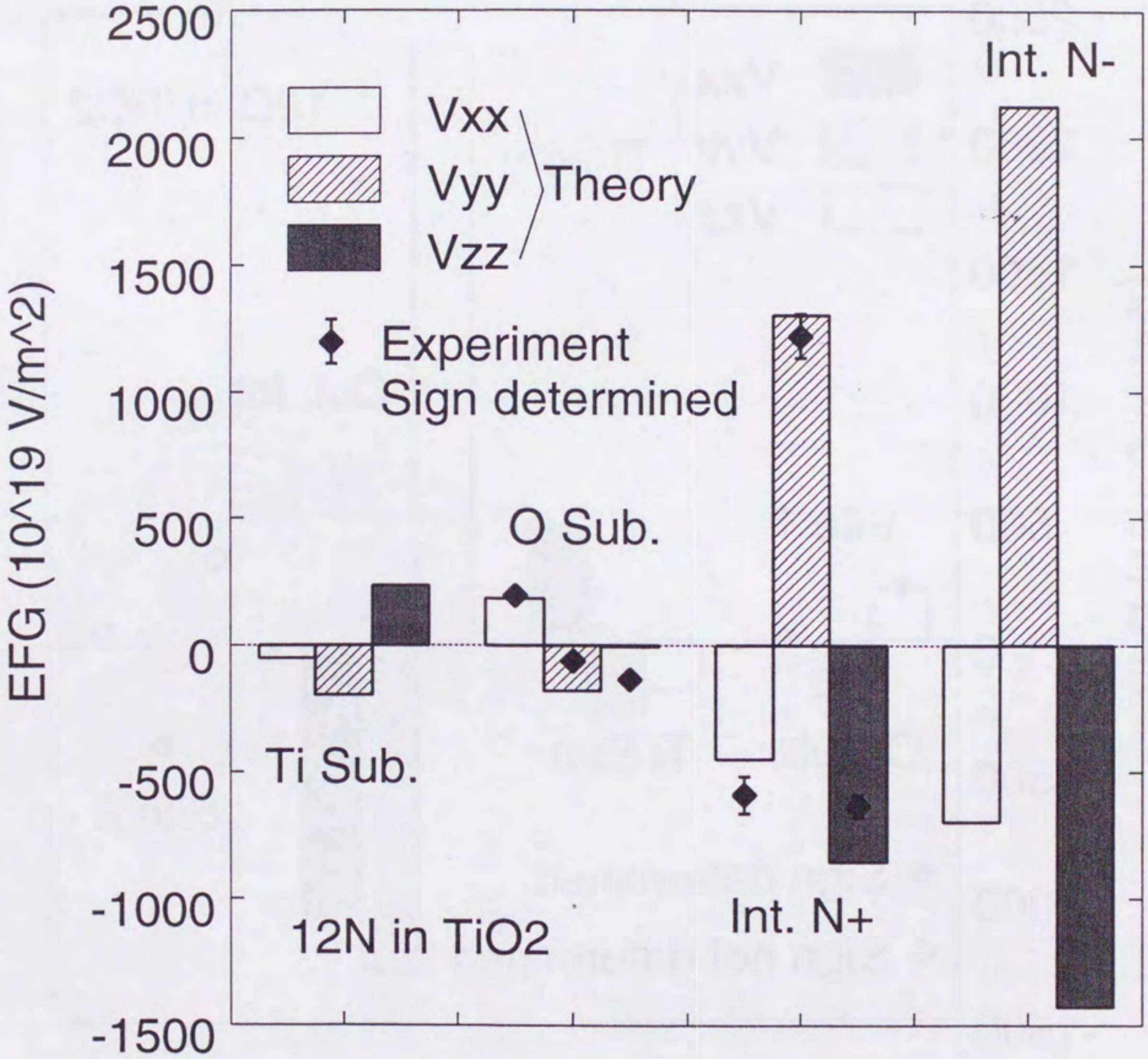

Figure 46: Site assignment for ^{12}N in TiO$_2$.

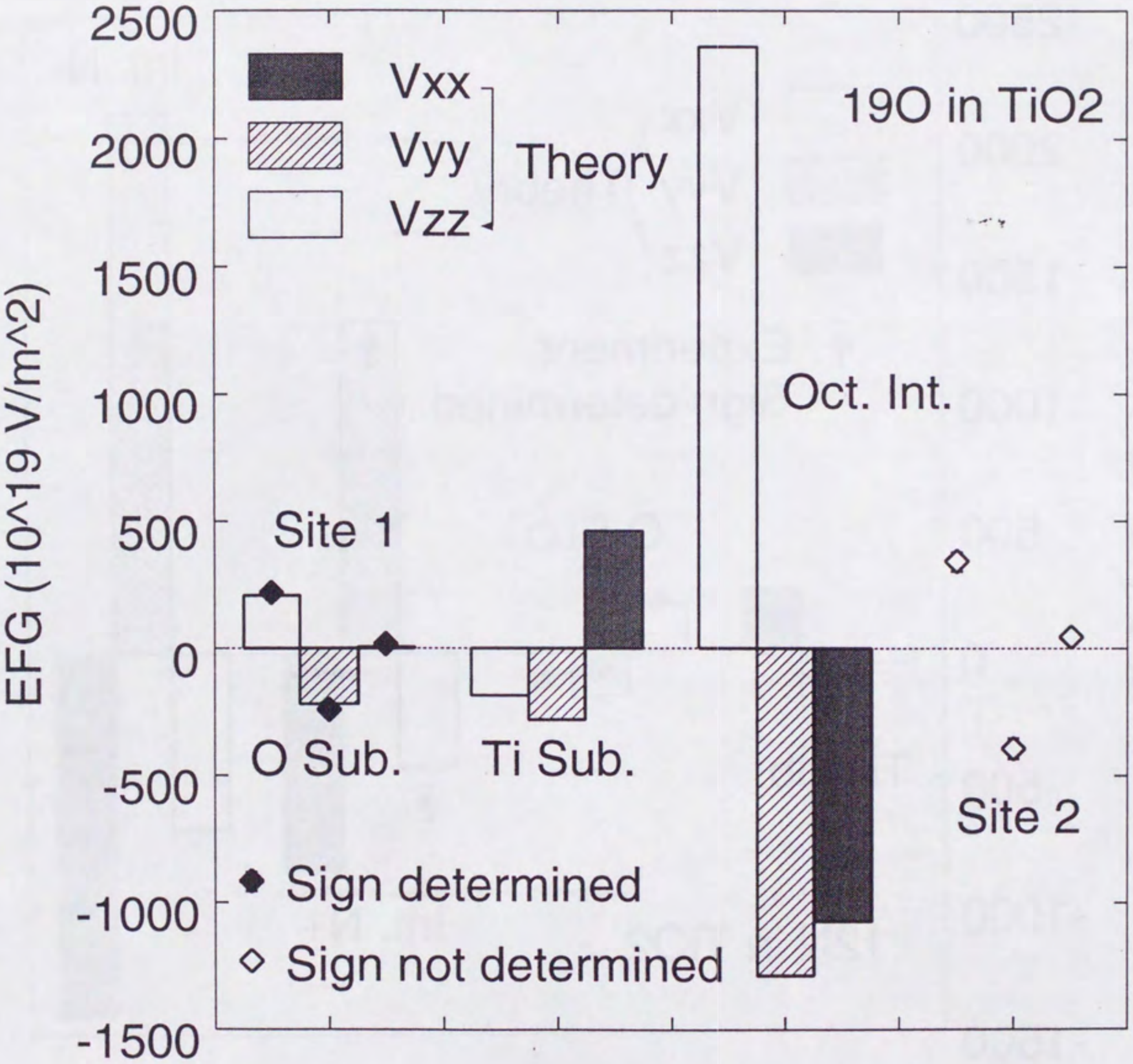

Figure 47: Site assignment for ^{19}O in TiO_2.

9 Determination of Nuclear Quadrupole Moments

The nuclear quadrupole moment is one of the most important clues to investigate the nuclear shell structure. In spite of a large effort to determine a nuclear quadrupole moment (Q-moment), experimental precision of a Q-moment is as high as about 10%. this difficulty comes from the fact that an enough electric field gradient is not produced in an artificial way. Artificially, only a field gradient of about 10^8 V/m^2 at most is available. It corresponds to 0.24×10^{-5} Hz in eqQ/h for a Q-moment of 1 b, which is unobservable. Therefore, a field gradient in an atom, molecule or crystal is utilized. Usually, a reference isotope, whose Q-moment is decided from a Rabi-type experiment for an atom with a calculation of a field gradient in the atom, is used to determine a field gradient. In short, we calculate the following with an assumption that a target isotope is in the same circumstance of a reference isotope,

$$Q = \frac{eqQ^{target}/h}{eqQ^{reference}/h} \times Q^{reference}.$$

Therefore, a total experimental error for a Q-moment is decided by the error of the reference Q-moment.

Owing to the development of the first principles calculation of solids, recently, Dufek *et al.* [87] determined the Q-moment of the most important Mössbauer nucleus ^{57}Fe by comparing experimental quadrupole splittings with calculated electric field gradients for a large number of different Fe compounds. Their calculations were only for the pure systems. If the same approach is possible in the case that a target isotope is introduced in a crystal as an impurity, it is a great improvement from an experimental point of view, because we are free from a selection of a host crystal. In this section, we try to determine the Q-moment of ^{111}Cd*, ^{27}Si, ^{39}Ca and ^{17}F. For ^{111}Cd* [90]-[94] and ^{17}F [113, 120, 121] several inconsistent Q-moments have been reported. The Q-moments of ^{27}Si and ^{39}Ca are not known. A comparison the respective Q-moments with the shell model calculations will be given in appendix.

9.1 ^{111}Cd*

The Q-moment of the 247 keV exited state of ^{111}Cd ($I^\pi = 5/2^+, T_{1/2} = 84$ ns) are determined by comparing its quadrupole coupling constants in HCP metals with calculated electric field gradients by the present method. As mentioned in the introduction, three different Q-moments were reported, *i.e.* $|Q| + 0.77 \pm 0.12$ b by Raghavan *et al.* [93, 94], $Q = +1.5 \pm 0.4$ b by Rosenblum *et al.* [90] and $Q = 0.83 \pm 0.13$ b by Herzog *et al.* [92].

The experimental quadrupole coupling constants are available for 14 HCP hosts such as Be, Mg, Ti, Co, Zn, Y, Zr, Ru, Cd, Lu, Hf, Re, Os and Tl [2, 3]. The computational procedure is essentially similar to the previous calculations. The super cell in the same dimension that was used in the cases of the sp-impurities in Zn and Cd was employed. However, for Co, Ru, Lu, Hf, Re and Os, it was found that the EFGs at their sites were rather sensitive to the dimension of the super cell, therefore the bigger one was used for them, *i.e.* the HCP primitive cell was doubled along the a, b and c directions to obtain the super cell which has 8 primitive units of the HCP structure. For such super cells, the LDA calculations were performed by the KKR method in the scalar relativistic version. The 216 k points were calculated for the smaller super cell, on the other hand for the bigger super cell the 64 k points were calculated. The energy window of 1.7 Ry down from the Fermi level was calculated. Any local lattice relaxations were not concerned and the experimental lattice parameters were used, and the substitutional site was supposed for the location of the impurity.

The results were summarized in table 11, and the experimental coupling constants are plotted against the calculated field gradients in fig.48. They shows a good liner correlation as expected [87]. The dependence of the coupling constant on the field gradient is written as

$$\begin{aligned} eqQ/h(\mathrm{MHz}) &= \frac{1.602177 \times 10^{-19} q(10^{19}\mathrm{V/m^2}) \times Q(\mathrm{b})}{6.626076 \times 10^{-34}} \\ &= 0.2417988 \times q(10^{19}\mathrm{V/m^2}) \times Q(\mathrm{b}), \end{aligned}$$

so the slope of the linear correlation between theoretical EFGs and the experimental coupling constants means the Q-moment of $^{111}\mathrm{Cd}^*$. The least-square analysis gives the Q of 0.78 $/pm$ 0.04 b. It supports the results by Raghavan and Herzog, and rejects the result by Rosenblum.

Table 11: The experimental coupling constant (MHz) and the theoretical EFGs in HCP Metals.

Host	Experimental eqQ/h (MHz)	Theoretical EFG (10^{19} V/m^2)
Be	-16.1 ± 0.7	-63
Mg	-7.4 ± 0.1	-39
Ti	+27.8 ± 0.2	+161
Co	0.96 ± 0.06	-52
Zn	+133.1 ± 0.7	+638
Y	14.2 ± 0.3	+43
Zr	+14.70 ± 0.07	+61
Ru	22.6 ± 0.3	-165
Cd	+124.94 ± 0.36	+632
Lu	14 ± 1	+183
Hf	+28.0 ± 0.4	+146
Re	-29.70 ± 0.14	-269
Os	33.4 ± 0.3	-212
Tl	7.8 ± 0.8	+24

9.2 Fluorine Isotopes

The reference of quadrupole moments of Fluorine isotopes is the quadrupole moment of the 197 keV exited state of $^{19}\mathrm{F}$ ($I^{\pi} = 5/2^{+}$). $Q(^{19}\mathrm{F})$ was determined by Sugimoto *et al.* by the PAD technique [122]. In their experiment, the electric quadrupole coupling constant of $^{19}\mathrm{F}^*$ in ClF molecule was measured to be 12.4 ± 0.6 MHz and Q was derived to be 0.120 b with the error of 20 %. by comparing the estimated EFG of 1.07 $\times 10^{16}$ esu/cm^3 at F site in ClF. The EFG was estimated by the empirical rule of Townes and Dailey [123]. Later, Mishra, Duff and Das performed self-consistent field calculations on

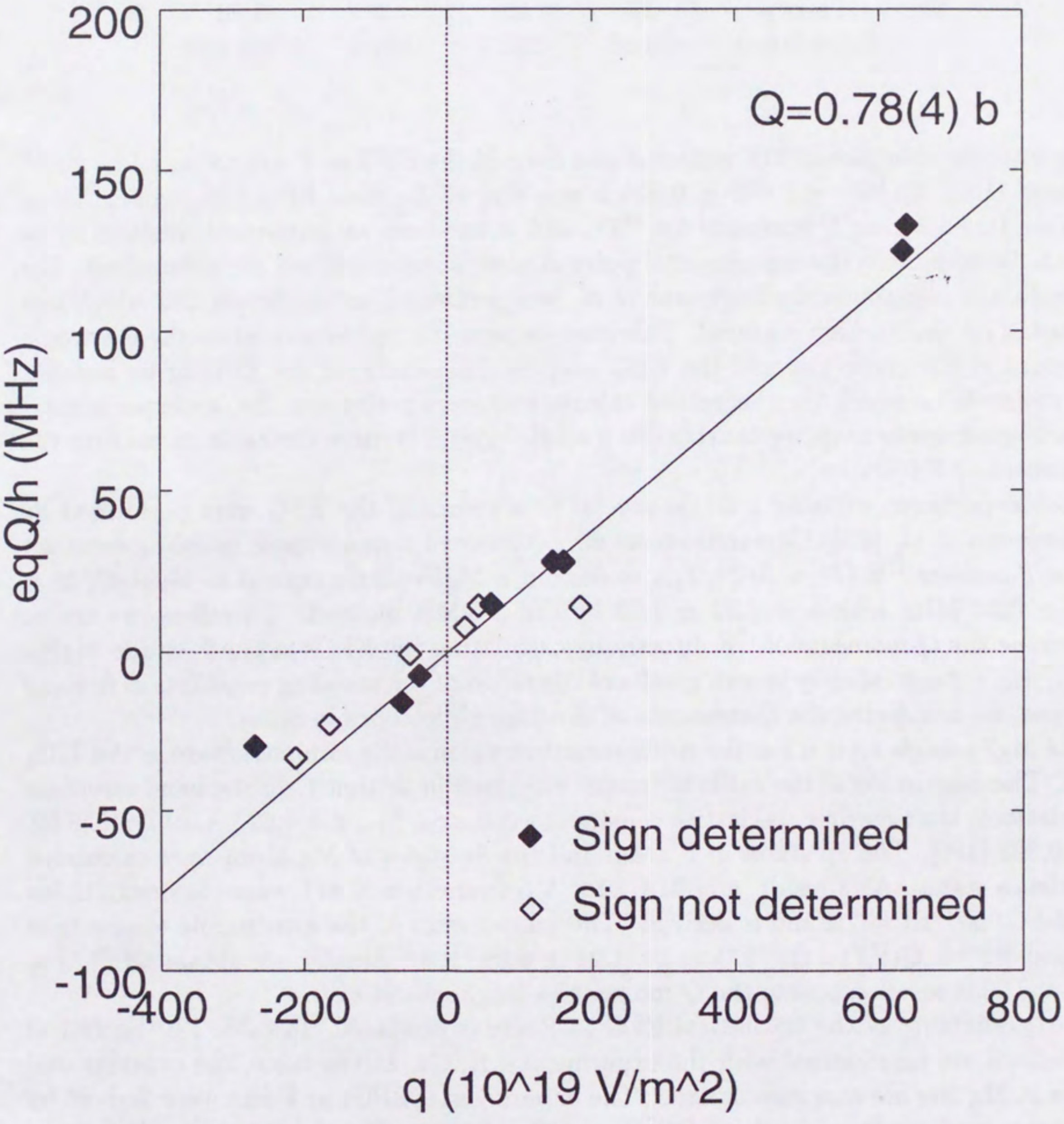

Figure 48: The experimental coupling constants are plotted against the calculated EFGs. The solid line corresponds $Q = +0.78$ b.

Table 12: Theoretical and experimental EFGs in $10^{19}\mathrm{V/m}^2$ at Mg and F sites in MgF_2. $Q(^{17}\mathrm{F})$=100±20 mb was used.

Site		V_{XX}	V_{YY}	V_{ZZ}	η
F	Theory	-298	318	-21	0.87
	Experiment	-230pm46	348±70	-111±22	0.32±0.02
Mg	Theory	-23	21	2	0.83
	Experiment	-66±6	21±2	45±4	0.36±0.04

the electronic structure of ClF molecule and derived the EFG at F site to be 1.591 $\times 10^{16}$ esu/cm^3 [121]. $Q(^{19}\mathrm{F}) = 0.072 \pm 0.004$ b was derived by their EFG calculation. Thus, we have two different Q moments for $^{19}\mathrm{F}^*$, and it has been an important problem to be solved. Besides, from the experimental point of view, some questions are pointed out. For example, the experiment by Sugimoto *et al.* was performed on the frozen ClF which was deposited on the backing material. This may cause some perturbations on the electronic structure of ClF molecule, and the EFG may be different from the EFG of an isolated ClF molecule on which the theoretical calculations were performed. So, an experimental electric quadrupole coupling constant in a single crystal is more desirable to confirm the Q-moment of F isotopes.

Such experiment utilizing a single crystal as a source of the EFG were performed by Minamisono *et al.* [120]. Minamisono *et al.* determined a quadrupole coupling constant of the β-emitter $^{17}\mathrm{F}$ ($I^\pi = 5/2^+, T_{1/2} = 66\mathrm{s}$) in a MgF_2 single crystal to be $|eqQ/h| = 8.41 \pm 0.24$ MHz with $\eta = 0.32 \pm 0.02$ by the β-NMR method. Therefore, we try to determine the Q-moments of $^{17}\mathrm{F}$ directly by calculating the EFGs at the F site in MgF_2. Then, using the previously known results of the ratios of the coupling constants of fluorine isotopes, we can derive the Q-moments of the fluorine isotopes in series.

The MgF_2 single crystal has the rutile structure which is the same structure as the TiO_2 [110]. The description of the rutile structure was given in section 4. In the band structure calculations, the experimental lattice constants were used, *i.e.*, $a = 4.623$ Å, $c/a = 0.6602$, $u = 0.303$ [110]. The $2p$ states of F atom and the $3s$ states of Mg atom were calculated as valence states. As a result, $q = 318 \times 10^{19}\mathrm{V/m}^2$ and $\eta = 0.871$ were obtained. Using this EFG, $Q(^{17}\mathrm{F}) = 110$ mb is derived. The known ratio of the quadrupole moments of $^{17}\mathrm{F}$ and $^{19}\mathrm{F}^*$ is $Q(^{17}\mathrm{F}) : Q(^{19}\mathrm{F}^*) = 1 : 1.24 \pm 0.06$ [120]. Finally, we obtain $Q(^{19}\mathrm{F}^*) = 136$ mb. This result supports the Q-moment by Sugimoto *et al.*.

Next, reliability of the theoretical EFG at F site is discussed. In table 12, theoretical predictions are summarized with the experimental EFGs. In the table, the experimental EFGs at Mg site are also summarized. The experimental EFGs at F site were derived by using the quadrupole moments of $Q(^{17}\mathrm{F}) = 100 \pm 20$ mb. The theoretical predictions of η at F and Mg [124, 125] sites do not reproduce the experimental η. Moreover, the theory did not reproduce that the second largest component of the EFGs at Mg site was along the c-axis [124, 125]. From a detailed study on the convergence of the present calculations, it was found that the calculated EFGs showed a severe dependence on the choice of the respective muffin tin radii. The origin of this curious behavior is not understood now. Besides, Dufek *et al.* performed *ab initio* EFG calculation at F site in NiF_2 and MnF_2 recently, and their results supported the smaller Q of 0.072 b [60]. Therefore, it is not possible to judge which Q moment is true now.

For the future, it is desirable to calculate the EFGs at F site in various fluorides besides MgF_2 to solve the problem. Because, the electric quadrupole coupling constants of $^{19}F^*$ were measured in various fluorides [126, 127]. Comparing the theoretical predictions with the experimental results, some insight not only on the Q-moments of F isotopes but also on the errors in the EFG calculations may be given.

9.3 ^{27}Si and ^{39}Ca

For Si and Ca isotopes, we do not have proper reference isotopes to determine their quadrupole moments. For example, the nuclear spin of ^{29}Si, which is the stable isotope of Si, is $I = 1/2^+$ [113]. Therefore, we have no way to measure the EFG by using this isotope. In the case of Ca, the quadrupole moment of ^{43}Ca ($I = 7/2^-$) is known [113], however its natural abundance is extremely small. Therefore, the NMR measurement on its is very difficult. In these cases, the present procedure to determine the quadrupole moment is one of the most promising ways.

Recently, in our laboratory the electric quadrupole coupling constants of ^{27}Si ($I^\pi = 5/2^+, T_{1/2} = 4.1$s) in a Al_2O_3 single crystal and ^{39}Ca ($I^\pi = 3/2^+, T_{1/2} = 0.86$s) in a $CaCO_3$ single crystals were measured to be 1.93 ± 0.12 MHz and 602 ± 41 kHz, respectively [128]. EFGs not only at Si site in Al_2O_3 but also Ca site in $CaCO_3$ were not measured. Therefore, we must derive the Q-moments by calculating the EFGs.

The crystal structure of Al_2O_3 and $CaCO_3$ is the Corundum structure in the rhombohedral symmetry [110]. Considering the point symmetry at the substitutional site of the metal ion, it is found that the maximum component of the EFG is along the c-axis and $\eta = 0$. ^{27}Si and ^{39}Ca were implanted into the respective catchers. Assuming that they were implanted at the substitutional site of the metal ion, the EFGs at the respective implantation sites were calculated. In the case of the Si impurity in Al_2O_3, we must take care not only of the local lattice relaxation but also of its charge state in the host crystal. The detailed explanation was given in section 7. The theoretical predictions are given in table 13. For Al_2O_3 host, the electric field gradient at the host Al [129, 130] site and the Cd [131] impurity site were known. They are also summarized in the table with theoretical predictions for them. The agreement of the theoretical prediction of the EFG at Al site in Al_2O_3 is perfect, so the calculated EFG at the Ca site in $CaCO_3$ may be reliable. On the other hand the theory reproduces only 60% of the experimental EFG for the Cd site in Al_2O_3. This error is serious from the view point of the determination of the quadrupole moment. Here, we suppose optimistically that the error of the calculated EFG of Si site in Al_2O_3 is not so large as the case of Cd, because the difference of the atomic numbers of Al and Si is only 1. Assuming the error of the theoretical predictions to be ± 20 %, the quadrupole moments of ^{27}Si and ^{39}Ca are derived to be 61 ± 14 mb and 36 ± 4 mb, respectively. On the error of the prediction on the EFG is discussed in the next section.

Table 13: Theoretical and experimental EFGs in Al_2O_3 and $CaCO_3$ in 10^{19}V/m^2.

Host	Site	Charge neutrality	Lattice relaxation	q^{Theory}	$q^{Experiment}$
Al_2O_3	Al	0	0	+69	+65.5 ± 1.7 [129, 130]
	Cd	+1	+9%	+650	1040 ± 170 [131]
	Si	-1	+6%	+130	—
$CaCO_3$	Ca	0	0	-70	—

9.4 Sign of $Q(^8B)$

One of the recent topics on the investigations of the nuclear structure is the observation of the halo structure in neutron-rich nuclei. In spite of the centrifugal and the Coulomb potential, it is expected that the proton drip-line nucleus ^{8}B ($I^\pi = 2^+, T_{1/2} = 0.77$s) has the proton halo structure because of its rather small one nucleon separation energy of the last proton. Minamisono *et al.* proposed a new approach to investigate the halo structure of the nucleus through its quadrupole moment Q and demonstrated that the quite large $Q(^8B)$ of 68.3 ± 2.1 mb was explained by taking the proton halo picture of ^{8}B into account [132, 133]. However, the sign of the quadrupole moment of ^{8}B has not been determined. For a complete knowledge on the quadrupole moment of ^{8}B, the determination of the sigh of $Q(^8B)$ has been urged.

By the way, the sign of the electric quadrupole coupling constant eqQ/h of ^{8}B in ZrB_2 single crystal had been determined to be positive through the β-delayed α-ray anisotropy measurement combined with the spin manipulation technique in the β-NMR method [134]. Therefore, it is possible to derive the sign of Q-moment by referring to a theoretical prediction on the EFG at B site in ZrB_2.

Table 14: Theoretical and Experimental EFGs at B sites in various diborides with the AlB_2 structure in unit of 10^{19} V/m^2.

	Theory		Experimental $\lvert q \rvert$
	KKR	FLAPW	
ScB_2	65		53±2
TiB_2	55	38	37±2
VB_2	49	39	43±1
CrB_2	66	60	63±1
MnB_2	93		115.8±0.5
YB_2	23		35±2
ZrB_2	22	10	12±1
NbB_2	18	10	<7
MoB_2	35	22	23±2
TaB_2	6	2	<5

Theoretical predictions of EFGs at B site in various diborides by the FLAPW method had been given by Schwarz *et al.* [65], however, the signs of them were not given in the literature explicitly. Therefore, we calculated the EFGs at B site in ZrB_2 and the other diborides and tried to determine the sign of $Q(^8B)$. Many of transition metal diborides have the AlB_2 structure [110]. The crystal symmetry of the AlB_2 structure leads that the asymmetry parameter at the B site is equal to 0. Silver *et al.* and Kopp *et al.* determined the electric quadrupole coupling constants of ^{11}B ($I^\pi = 3/2^-$) in them by measuring their NMR [135]. The EFG at each B site is derived as table 14 by using the $Q(^{11}B) = 40.65 \pm 0.26$ mb [113]. For all of them, the EFGs were calculated from the first principles by the KKR method. The experimental lattice constants were used in respective compounds. The 125 k-points were calculated in the irreducible wedge of the 1st Brillouin zone of the HCP structure. The energy window of 1.0 Ry was employed. The rather shallow p-states of metals were not included in the calculations, but it was confirmed that their influences on the EFGs at B sites were negligible. The present results were summarized in table 14 with the results by FLAPW and shown in fig. 49.

As shown in fig. 49, the experimental EFGs are well reproduced by the KKR predictions, and the sign of the EFG at B site in ZrB_2 is reliably determined to be positive, which was also predicted by the FLAPW [137]. This result leads to the positive Q-moment of ^{8}B. Also the positive eqQ/h of ^{12}B in ZrB_2 and TiB_2 [5] leads to the positive Q-moment of ^{12}B.

Discrepancies between the KKR results and the FLAPW results are rather large, and it seems that the muffin-tin approximation is not suitable for the present cases. In other words, a strong covalent nature of these compounds was shown. In these calculations only the contributions inside the respective muffin-tin spheres were estimated, because it was found that the simple estimations of the lattice contributions by an array of point charges gave unreliable results. It is not obvious whether the errors of the estimations of the lattice contributions are originated from the strong covalency or not. A more precise calculation and analysis beyond the muffin-tin approximation is encouraged.

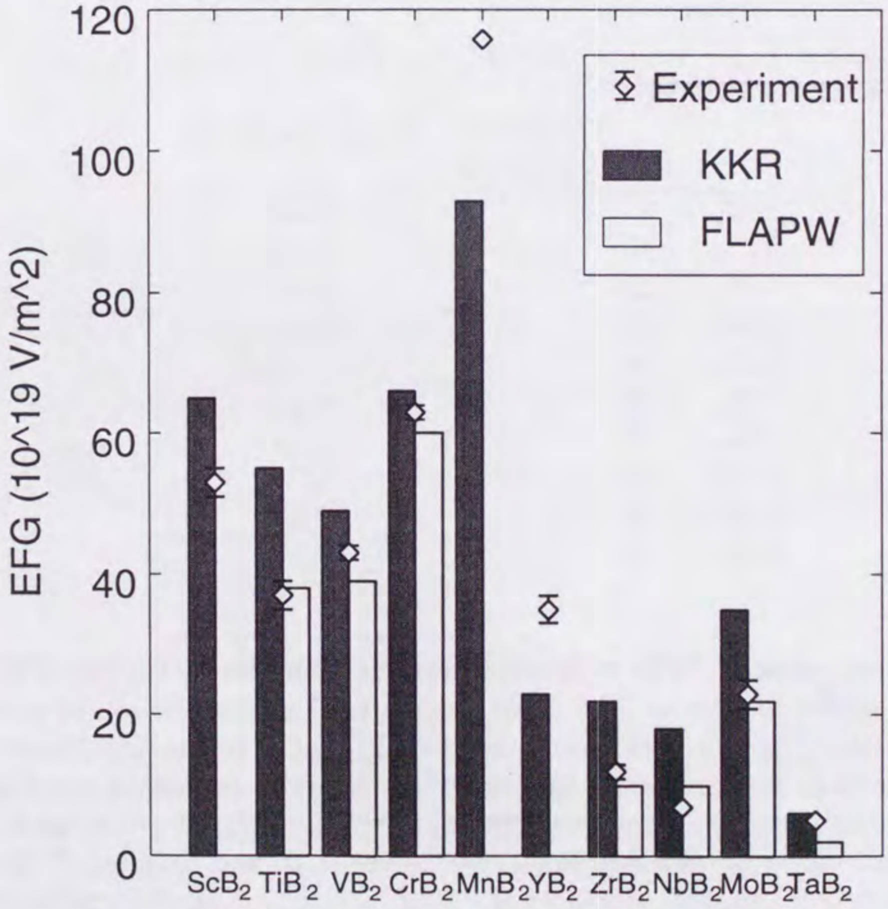

Figure 49: Theoretical predictions and experimental EFGs in diborides (10^{19}V/m^2).

10 Reliability

In this section, reliability of the present EFG calculation is discussed. The *ab initio* method has no adjustable parameter and gives a solution of the Schrödinger equation in an arbitrary precision. However, to make a problem solvable it stands on some approximation in principle [22]. The elements which may give a considerable error to a result is the followings.

- Error from the local density approximation.
- Error from the muffin-tin approximation.
- Error from the super cell method (for impurities).
- Inaccuracy from the finite k sampling points in the Brillouin zone.
- Inaccuracy from the l truncation.
- Inaccuracy from the finite energy mesh.
- Inaccuracy from the radial mesh.
- Inaccuracy from the truncation of the iteration cycle.

The last four points is not so serious, *i.e.*, less than 1% at most. Also it is possible to converge a calculation within 1%, if sufficient k-points are calculated. However, sometimes it becomes difficult to take many k-points according to computational power of a machine. In our case, it was difficult to converge calculations in cases of impurity systems, because a unit cell contained many atoms due to the super cell calculation. The error may be less than 10%. It is desirable to perform calculations on a vector array processor.

On the first three points, it is almost impossible to estimate an error quantitatively, because they affect a final result through a complicated way. Therefore, we get overall information about reliability of calculations by comparing theoretical calculations with experimental measurements. For example, calculations of lattice constants of HCP metals are performed. In these calculations, the experimental c/a values were used and the lattice constants were estimated from the total energy minimum as shown in fig. 50. As summarized in the same figure and table 15, the lattice constant is reproduced within the error of about 5% for metallic substances. Because the c/a was fixed at the experimental value, an error of a prediction of c/a affects on the prediction of a. Such effects maybe cause to rather large discrepancies for the cases of Sc, Y and Cd.

In the case of EFGs, we get information on reliability of EFG calculations from the results previously presented in this thesis. The ratio $1 - q^{Theory}/q^{Experiment}$ is calculated for all of them. However, the Rb probe is removed from the analysis because of its rather ambiguous experimental results. It seems appropriate to carry out comparison in these three categories, *i.e.*,

- EFGs at in pure HCP metals,
- EFGs at impurity sites in HCP metals,
- EFGs in ionic TiO_2 and Al_2O_3.

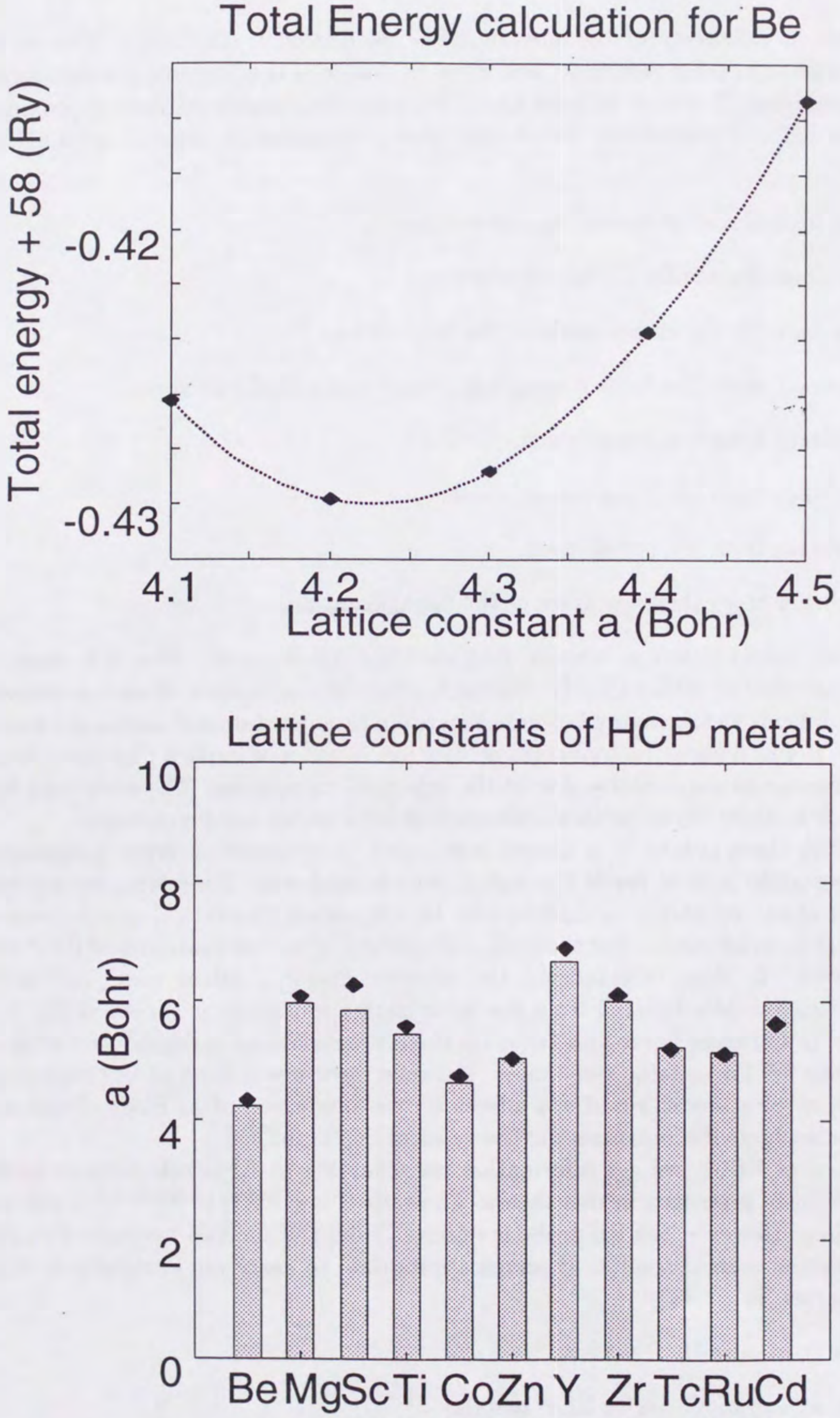

Figure 50: Theoretical predictions of lattice constants of HCP metals.

Table 15: Theoretical predictions of lattice constants of HCP metals. In the present calculations experimental c/a ratios were used.

Element	a^{Theory} (Å)	$a^{Experiment}$ (Å)	difference (%)
Be	2.236	2.2866	2.2
Mg	3.148	3.20927	1.9
Sc	3.082	3.3090	6.9
Ti	2.876	2.950	2.5
Co	2.452	2.5071	2.2
Zn	2.665	2.6648	0.0
Y	3.533	3.6474	3.1
Zr	3.177	3.232	1.7
Tc	2.785	2.743	-1.5
Ru	2.727	2.70389	-0.9
Cd	3.176	2.97887	-6.6

The results of the analyses are shown in fig. 51, 52, 53. The predictability of ~20%, ~50% and ~20% are guessed for the pure HCP metals, the impurities in HCP metals and the ionic systems, respectively. Considering that any local relaxations were not included in the calculations of impurities in HCP metals, for all systems the predictability of ~20% is suggested.

Lastly, dependences on a choice of the muffin tin radius and on a dimension of a super cell are mentioned. In section 7, the dependence on the super cell dimension was discussed, and it was found that the dependence was within ± 10%. For a metallic system, it was not studied. The above discussion on the discrepancies of the calculated EFGs from the experimental results also may be an evidence of the insufficient super cell. The KKR method can be applied to a calculation on an isolated impurity in an otherwise perfect crystal [22]. An estimation on efficiency for a super cell can be given, if such a calculation is carried out. In the series of the present study, it was found that sometimes calculated EFGs strongly depended on a choice of the muffin tin radius. When a unit cell has atoms of different types more than one, ratios of muffin tin radii between different atoms are arbitrary taken. The EFGs at F site in MgF_2 is such a case. The dependence was so large that the EFG changed its sign, so the result was not reliable at all. It seems that the muffin tin approximation is unsuitable for a rather open structure such as the rutile structure. A method beyond the muffin tin approximation is strongly encouraged [138]-[141].

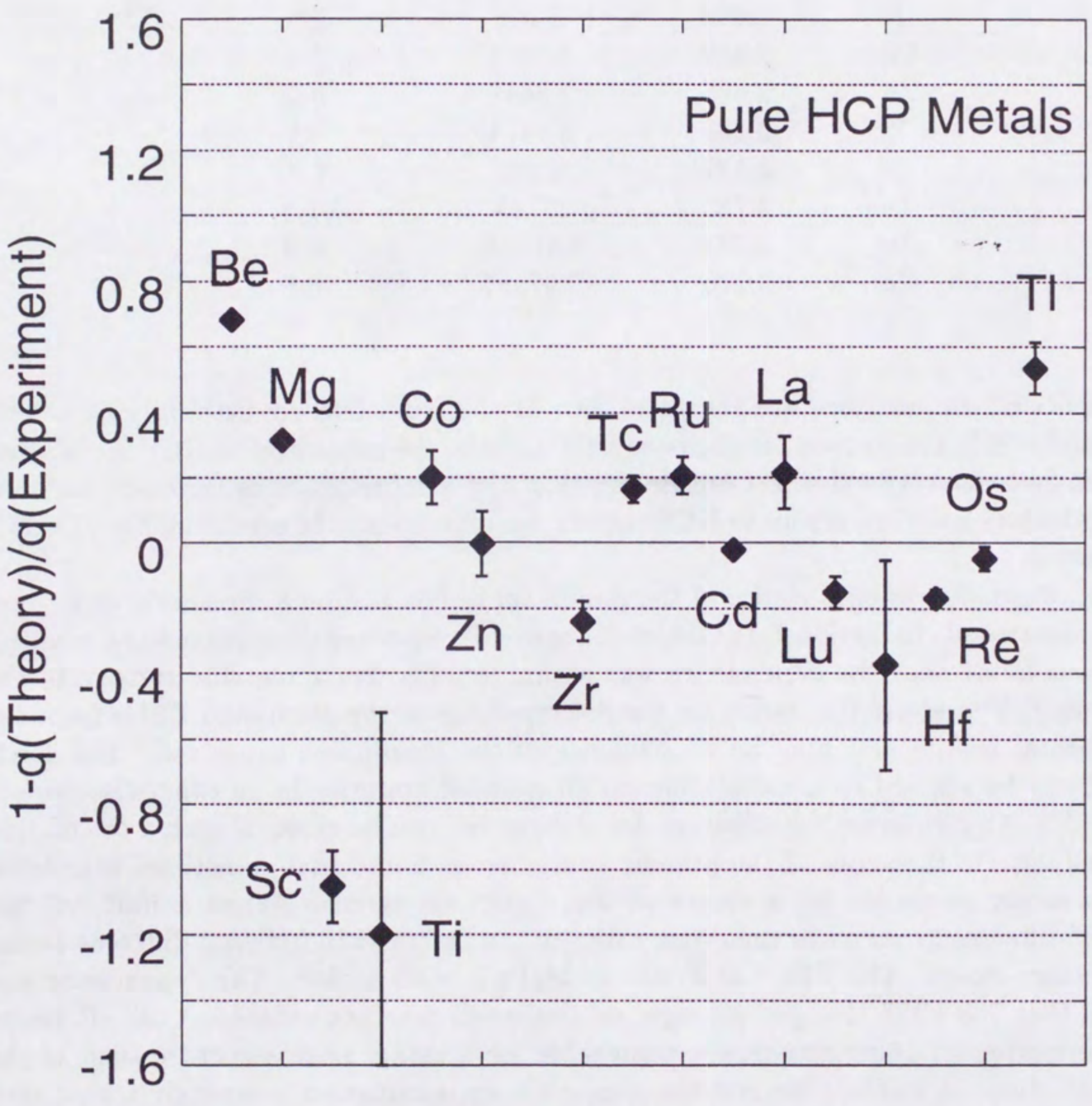

Figure 51: Deviations of the theoretical predictions from the experimental measurements of the EFGs in the HCP metals.

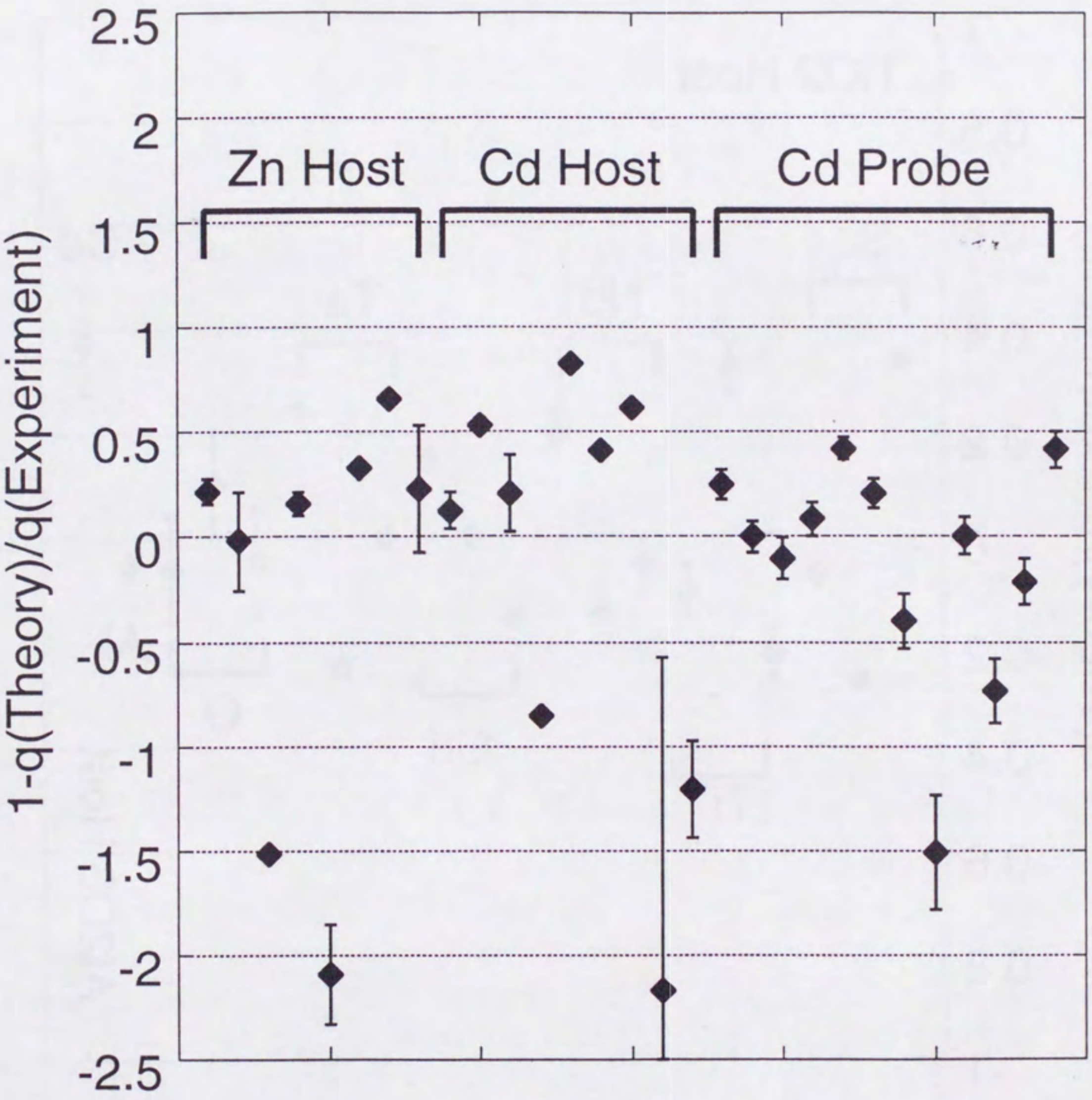

Figure 52: Deviations of the theoretical predictions from the experimental measurements of the EFGs at the impurity sites in the HCP metals.

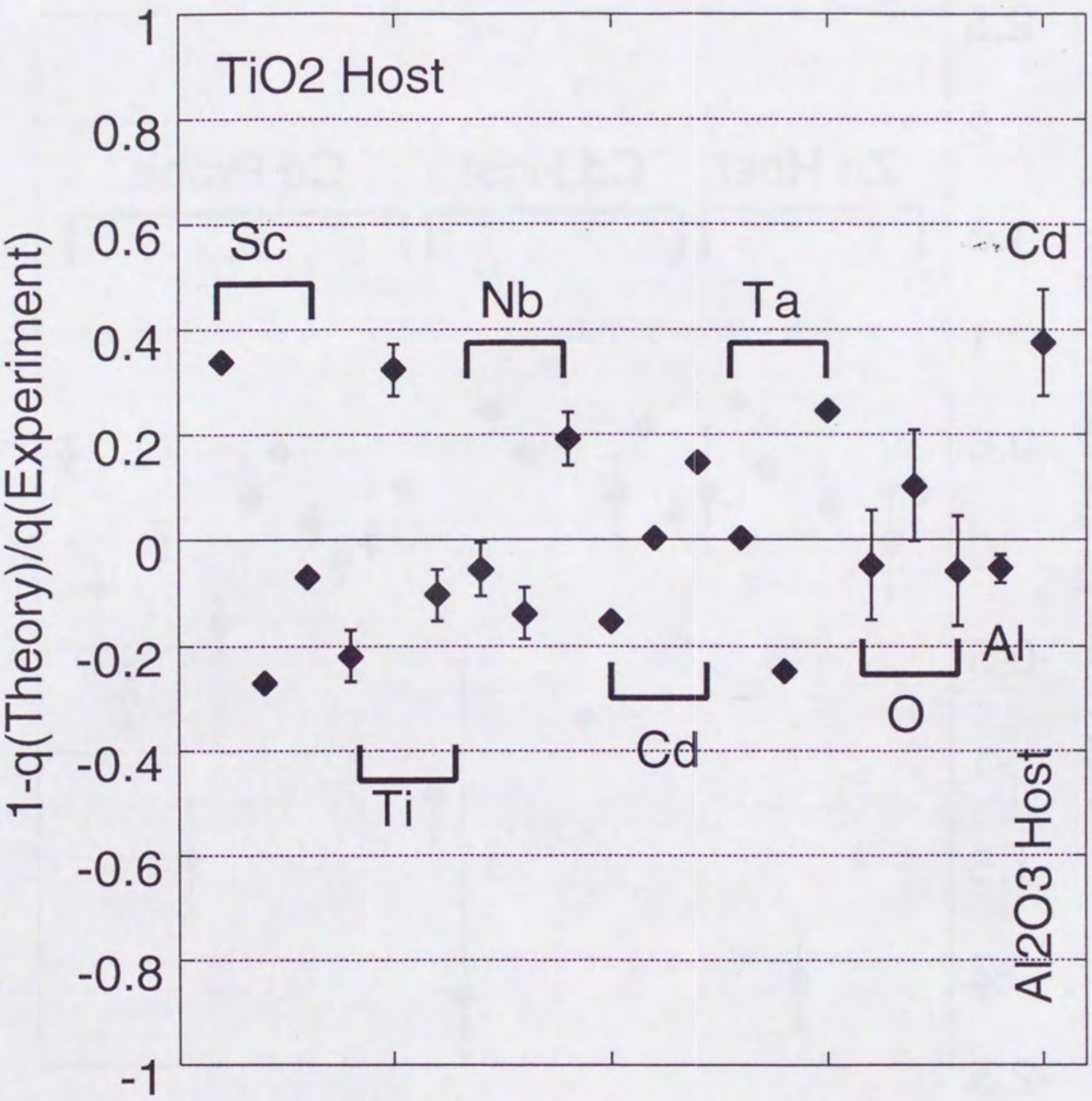

Figure 53: Deviations of the theoretical predictions from the experimental measurements of the EFGs in the ionic TiO_2 and Al_2O_3.

11 Summary

To investigate the electronic structure of impurities in solids, the *ab initio* method to calculate the EFGs at impurities sites was developed. Besides it, to enforce the systematic study of the EFGs of impurities in the ionic TiO_2 single crystal, the FT-NMR measurements on ^{45}Sc, ^{49}Ti and ^{93}Nb and the β-NMR measurements on ^{12}N and ^{19}O were performed.

The KKR method based on the LSD was applied to calculated the EFG, and the system with impurities were simulated by the super cell method. It was proved that the present method could predict the EFGs quite well not only in a pure system but also in a system with impurities for both of metallic and ionic substances. The predictability of about 20% was suggested.

With this method the EFGs in HCP metals were analyzed precisely, and it was found that the overall trend of the EFGs was controlled by the occupation of the p-orbitals and its $\langle 1/r^3 \rangle$. In the cases of EFGs in TiO_2, it was shown that it was indispensable to consider the charge states of impurities to reproduce the experimental EFGs. The systematic study of the EFG at the impurity site was performed for the first time both for metallic and non metallic systems within the same computational framework.

This method was applied to the determination of the lattice locations of ^{12}N and ^{19}O in TiO_2. For a N impurity, the O substitutional site and the octahedral like interstitial site were suggested by comparing theoretical predictions with the experimental results. For O impurity, it was found that its main fraction was implanted into the O substitutional site, which was experimentally confirmed also. However, where the rest was implanted in was not predicted.

This method was also applied to the determination of the quadrupole moment of the 247 keV exited state of ^{111}Cd, ^{27}Si and ^{39}Ca. This method simplifies the procedures and extends possibility of experiments to determine the quadrupole moment. It is the first attempt to apply the *ab initio* EFG calculations of impurity sites for the determination of the quadrupole moment. It seems that more effort to gain a high precision in EFG calculations is needed to make this approach a standard method to determine a nuclear quadrupole moment. A calculation at the single impurity limit for an impurity problem is strongly encouraged to check a convergence of the super cell method. Also the full potential calculation as a way beyond the muffin tin approximation is expected to improve a calculation in particular for an open structure.

References

[1] E. N. Kaufmann, R. J. Vianden Rev. Mod. Phys. 51 (1979) 161.

[2] R. Vianden Hyp. Int. 15/16 (1983) 1081.

[3] W. Witthuhn, W. Engel Hyperfine Interactions of Radioactive Nuclei ed. J. Christiansen (Springer, Berlin, 1983) p. 205.

[4] H. Haas Z. Naturforsch 41a (1986) 78.

[5] T. Minamisono, K. Matuda, A. Mizobuchi, K. Sugimoto J. Phys. Soc. Japan 30 (1971) 311.

[6] H. Hamagaki, Y. Nojiri, K. Sugimoto, K. Nakai J. Phys. Soc. Japan (1979) 1806.

[7] T. Minamisono Hyp. Int. 21 (1985) 103.

[8] T. Ohtsubo, Y. Nakayama, I. Minami, M. Tanigaki, S. Fukuda, A. Kitagawa, M. Fukuda, K. Matsuta, Y. Nojiri, H. Akai, T. Minamisono Hyp. Int. 80 (1993) 1051.

[9] K. Matsuta, M. Fukuda, M. Tanigaki, T. Minamisono, Y. Nojiri, H. Akai et al. Hyp. Int. 97/98 (1996) 501.

[10] T. Minamisono, K. Matsuta, M. Fukuda, M. Tanigaki, Y. Nojiri, H. Akai, M. Mihara, T. Yamaguchi, M. Sasaki, T. Miyake, T. Onishi, K. Minamisono, K. Sato, T. Ohtsubo, S. Fukuda, K. Yoshida, A. Ozawa, S. Momota, I. Tanihata RIKEN Rev. 16 (1997) 7.

[11] T. Minamisono, K. Sato, H. Akai, S. Takeda, Y. Maruyama, K. Matsuta, M. Fukuda, T. Miyake, A. Morishita, T. Izumikawa, Y. Nojiri Z. Naturforsch. 53a (1998) 293.

[12] C. Gabathuler, E. E. Hundt, E. Brun Magnetic Resonance and Related Phenomena, ed V. Hovi (North Holland, Amsterdam, 1973) p. 499.

[13] O. Kanert, H. Kolem J. Phys. C21 (1988) 3909.

[14] Th. Wenzel, A. Bartos, K. P. Lieb, M. Uhrmacher, D. Wiards Ann. Phys. 1 (1992) 155.

[15] J. M. Adams, G. L. Catchen Phys. Rev. B50 (1994) 1264.

[16] R. M. Sternheimer Z. Naturforsch. 41a (1986) 24.

[17] T. P. Das, P. C. Schmidt Z. Naturforsch. 41a (1986) 47.

[18] R. G. Parr, W. Yang Density-Functional Theory of Atoms and Molecules (Oxford, New York, 1989)

[19] W. Kohn, L. J. Sham Phys. Rev. 140 (1965) A1133.

[20] P. Hohenberg, W. Kohn Phys. Rev. 136 (1964) B864.

[21] V. L. Moruzzi, J. F. Janak, A. R. Williams Calculated Electronic Properties of Metals (Pergamon, U.S.A, 1978)

[22] H. Akai, M. Akai, S. Blügel, B. Drittler, H. Ebert, K. Terakura, R. Zeller, P. H. Dederichs Prog. Theo. Phys. Supplement 101 (1990) 11.

[23] M .Akai, H. Akai, J. Kanamori J. Phys. Soc. Japan 54 (1985) 4246.

[24] H. Akai, M. Akai, J. Kanamori J. Phys. Soc. Japan 54 (1985) 4257.

[25] M. Akai, H. Akai, J. Kanamori J. Phys. Soc. Japan 56 (1987) 1064.

[26] H. Akai J. Phys. Soc. Japan 51 (1982) 468.

[27] H. Akai, M. Akai, S. Blügel, R. Zeller, P. H. Dederichs J. Mag. Mag. Mat. 45 (1984) 291.

[28] H. Akai Hyp. Int. 68 (1991) 3.

[29] H. Akai P. H. Dederichs Phys. Rev. B47 (1992) 8739.

[30] R. Zeller, P. H. Dederichs Phys. Rev. Lett. 42 (1979) 1713.

[31] P. H. Dederichs, R. Zeller Festkörperprobleme XXI (1981) 243.

[32] S. Blügel, H. Akai, R. Zeeler, P. H. Dederichs Phys. Rev. B35 (1987) 3271.

[33] P. H. Dederichs, B. Drittler, R. Zeller, H. Ebert, W. Weinert Hyp. Int. 60 (1990) 547.

[34] M. Battocletti, H. Ebert, H. Akai Phys. Rev. B53 (1995) 9776.

[35] T. Huhne, C. Zecha, H. Ebert, P. H. Dederichs, R. Zeller Phys. Rev. B58 (1998) 10236.

[36] K. Terakura, J. Kanamori Prog. Theo. Phys. 46 (1971) 1007.

[37] K. Terakura Physica 91B (1977) 162.

[38] H. Katayama, K. Terakura, J. Kanamori J. Phys. Soc. Japan 46 (1979) 822.

[39] H. K. Yoshida, K. Terakura, J. Kanamori J. Phys. Soc. Japan 48 (1980) 1504.

[40] H. K. Yoshida, K. Terakura, J. Kanamori J. Phys. Soc. Japan 49 (1980) 972.

[41] J. Kanamori, H. Katayama-Yoshida, K. Terakura Hyp. Int. 8 (1981) 573.

[42] J. Kanamori, H. Katayama-Yoshida, K. Terakura Hyp. Int. 9 (1981) 363.

[43] J. Kanamori, H. Akai, M. Akai Proc. of the Yamada Conf. VII Muon Spin Rotation, Shimoda, 1983. Hyp. Int. 17-19 (1984) 287.

[44] J. Kanamori Hyp. Int. 21 (1985) 159.

[45] P. Blaha, J. Redinger, K. Schwarz Z. Phys. B57 (1984) 273.

[46] P. Blaha, K. Schwarz, P. Herzig Phys. Rev. Lett. 54 (1985) 1192.

[47] P. Blaha, K. Schwarz J. Phys. F17 (1987) 899.

[48] P. Blaha, K. Schwarz, P. H. Dederichs Phys. Rev. B37 (1988) 2792.

[49] P. Blaha, K. Schwarz, P. H. Dederichs Phys. Rev. B38 (1988) 9368.

[50] C. Ambrosch-Draxl, P. Blaha, K. Schwarz J. Phys. Condens. Matter 1 (1989) 4491.

[51] P. Blaha, P. Sorantin, C. Ambrosch, K. Schwarz Hyp. Int. 51 (1989) 917.

[52] P. Blaha, K. Schwarz Hyp. Int. 52 (1989) 153.

[53] P. Blaha Hyp. Int. 60 (1990) 773.

[54] K. Schwarz, C. Ambrosch-Draxl, P. Blaha Phys. Rev. B42 (1990) 2051.

[55] J. Yu, A. J. Freeman, R. Podloucky, P. Herzig, P. Weinberger Phys. Rev. B43 (1991) 532.

[56] P. Blaha J. Phys. Condens. Matter 3 (1991) 9381.

[57] P. Blaha, D. J. Singh, P. I. Sorantin, K. Schwarz Phys. Rev. B46 (1992) 1321.

[58] K. Schwarz, P. Blaha Z. Naturforsch. 47a (1992) 197.

[59] P. Blaha, K. Schwarz, P. Dufek Z. Naturforsch. 48a (1993) 129.

[60] P. Dufek, K. Schwarz, P. Blaha Phys. Rev. B48 (1993) 12672.

[61] W. Tröger, T. Butz, P. Blaha, K. Schwarz Hyp. Int. 80 (1993) 1109.

[62] C. Ambrosch-Draxl, P. Blaha, K. Schwarz J. Phys. Condens. Matter 6 (1994) 2347.

[63] P. Blaha, P. Dufek, K. Schwarz Hyp. Int. 95 (1995) 257.

[64] P. Dufek, P. Blaha, K. Schwarz Phys. Rev. B51 (1995) 4122.

[65] K. Schwarz, H. Ripplinger, P. Blaha Z. Naturforsch. 51a (1995) 527.

[66] P. Blaha, P. Dufek, K. Schwarz, H. Haas Hyp. Int. 97/98 (1996) 3.

[67] H. Petrilli, P. E. Blöchl, P. Blaha, K. Schwarz Phys. Rev. B57 (1998) 14690.

[68] M. Takeda, H. Akai, J. Kanamori Hyp. Int. 78 (1993) 383.

[69] H. Akai Interatomic Potential and Structural Stability, ed. K. Terakura and H. Akai (Springer-Verlag, 1993) p. 42.

[70] H. Akai Computational Physics as a New Frontier in Condensed Matter Research (1995) p. 96.

[71] H. Akai, M. Takeda, M. Takahashi, J. Kanamori Solid State Comm. 94 (1995) 509.

[72] J. Bogner, W. Steiner, M. Reissner, P. Mohn, P. Blaha, K. Schwarz, R. Krachler, H. Ipser, B. Sepiol Phys. Rev. B58 (1998) 14922.

[73] P. Schmidt, T. Soldner, W. Tröger, X. Ni, T. Butz, P. Blaha Z. Naturforsch. 53a (1998) 323.

[74] T. Soldner, W. Tröger, T. Butz, P. Blaha, K. Schwarz, the ISOLDE-Collaboration Z. Naturforsch. 53a (1998) 404.

[75] T. Soldner, W. Tröger, T. Butz, P. Blaha, K. Schwarz Z. Naturforsch. 53a (1998) 411.

[76] H. Akai Phys. Rev. Lett. 81 (1998) 3002.
[77] B. Drittler, M. Weinert, R. Zeller, P. H. Dederichs Phys. Rev. B42 (1990) 9336.
[78] B. Lindgren Phys. Rev. B34 (1986) 648.
[79] P. C. Schmidt, Al. Weiss, S. Cabus, J. Kübler Z. Naturforsch 42a (1987) 1321.
[80] W. Kohn, N. Rostoker Phys. Rev. 94 (1954) 1111.
[81] F. S. Ham, B. Segall Phys. Rev. 124 (1961) 1786.
[82] B. Segall Phys. Rev. 124 (1961) 1797.
[83] A. R. Williams, J. F. Janak, V. L. Moruzzi Phys. Rev. B6 (1972) 4509.
[84] H. Akai J. Phys. Condens. Matter 1 (1989) 8045.
[85] T. Kotani, H. Akai Phys. Rev. B54 (1996) 16502.
[86] T. Minamisono, Y. Nojiri, K. Matsuta Phys. Lett. 94A (1983) 312.
[87] P. Dufek, P. Blaha, K. Schawarz Phys. Rev. Lett. 75 (1995) 3545.
[88] K. J. Duff, K. C. Mishra, T. P. Das Phys. Rev. Lett. 46 (1981) 1611.
[89] F. Hagelberg, T. P. Das Z. Naturforsch. 53a (1998) 358.
[90] S. S. Rosenblum, W. A. Steyert Phys. Lett. 53A (1975) 34.
[91] H. Ernst, E. Hagn, E. Zech Phys. Lett. 93A (1983) 357.
[92] P. Herzog, K. Freitag, M. Reuschenbach, H. Walitzki Z. Phys. A294 (1980) 13.
[93] R. S. Raghavan, P. Raghavan, J. M. Friedt Phys. Rev. Lett. 30 (1975) 10.
[94] P. Raghavan, E. N. Kaufmann, R. S. Raghavan, E. J. Ansaldo, R. A. Naumann Phys. Rev. B13 (1976) 2835.
[95] A. Abragam, Principles of Nuclear Magnetism (Oxford, 1961).
[96] C. P. Slichter Principles of Magnetic Resonance (Springer-Verlag, 1989).
[97] C. Schwartz Phys. Rev. 97 (1955) 380.
[98] M. H. Cohen, F. Reif Solid State Physics 5 (1957) 321.
[99] J. M. Ziman Principles of the Theory of Solids 2nd ed. (Cambridge, 1972).
[100] L. Hedin, B. I. Lundqvist J. Phys. C4 (1971) 2064.
[101] U. von Barth, L. Hedin J. Phys. C5 (1972) 1629.
[102] S. H. Vosko, L. Wilk, M. Nusair Can. J. Phys. 58 (1980) 1200.
[103] D. M. Ceperley, B. J. Alder Phys. Rev. Lett. 45 (1980) 566.
[104] R. Podloucky, R. Zeller, P. H. Dederichs Phys. Rev. B22 (1980) 5777.
[105] P, J, Braspenning, R. Zeller, A. Lodder, P. H. Dederichs Phys. Rev. B29 (1984) 703.
[106] H. Akai, P. H. Dederichs J. Phys. C18 (1985) 2455.
[107] M. Weinert J. Math. Phys. 22 (1981) 2433.
[108] P. Herzig Theoret. Chim. Acta 67 (1985) 323.
[109] T. Minamisono, T. Ohtsubo, K. Sato , S. Takeda, S. Fukuda, T. Izumikawa, M. Tanigaki, T. Miyake, T. Yamaguchi, N. Nakamura, H. Tanji, K. Matsuta, M. Fukuda, Y. Nojiri Phys. Lett. B420 (1998) 31.
[110] R. W. G. Wyckoff Crystal Structures 2nd. Ed. (Krieger, 1986).
[111] Y. Matsumoto Master Thesis at Osaka University 1996.
[112] M. Tanigaki, S. Takeda, K. Matsuta, Y. Matsumoto, T. Minamisono, H. Akai, K. Sato, T. Miyake, Y. Maruyama, A. Morishita, M. Fukuda, Y. Nojiri Z. Naturforsch. 53a (1998) 305.
[113] Atomic Data and Nuclear Data Tables (Academic Press, 1989).

[114] M. Tanigaki Doctor Thesis at Osaka University 1998.

[115] Synthesized and offered by Earth Jewelry Company, Ikeda, Osaka, Japan.

[116] H. Ebert, H. Akai Hyp. Int. 78 (1993) 361.

[117] T. Takeda Z. Physik B32 (1978) 43.

[118] S. P. Kowalczyk, F. R. McFeely, L. Ley, V. T. Gritsyna, D. A. Shirley Solid State Commun. 23 (1977) 161.

[119] P. I. Sorantin, K. Schwarz Inorg. Chem. 31 (1992) 567.

[120] T. Minamisono, Y. Nojiri, A. Mizobuchi, K. Sugimoto Nucl. Phys. A236 (1974) 416.

[121] K. C. Mishra, K. J. Duff, T. P. Das Phys. Rev. B25 (1982) 3389.

[122] K. Sugimoto, A. Mizobuchi, K. Nakai Phys. Rev. 134 (1964) B539.

[123] C. H. Townes B. P. Dailey J. Chem. Phys. 17 (1949) 782.

[124] H. E. Bleich, A. G. Redfield J. Chem. Phys. 67 (1977) 5040.

[125] Y. Hiyama, P. M. Woyciesjes, T. L. Brown, D. A. Torchia J. Mag. Res. 72 (1987) 1.

[126] F. W. Richter D. Wiegandt Z. Phys. 217 (1968) 225.

[127] C. Bernhardt, F. W. Richter, D. Babel Z. Naturforsch. 32a (1977) 1119.

[128] T. Kawa Master Thesis at Osaka University 1999.

[129] R. V. Pound Phys. Rev. 79 (1950) 685.

[130] R. Kelley Nucl. Instr. Meth. 182/183 (1981) 351.

[131] J. Kesten Hyp. Int. 52 (1989) 17.

[132] T. Minamisono, T. Ohtsubo, I. Minami, S. Fukuda, A. Kitagawa, M. Fukuda, K. Matsuta, Y. Nojiri, S. Takeda, H. Sagawa, H. Kitagawa Phys. Rev. Lett. 69 (1992) 2058.

[133] H. Kitagawa, H. Sagawa Phys. Lett. 299 (1993) 1.

[134] T. Yamaguchi, K. Sato, C. Ha, A. Morishita, K. Tanaka, T. Miyake, M. Sasaki, K. Minamisono, H. Akai, M. Mihara, M. Fukuda, K. Matsuta, Y. Nojiri, T. Minamisono Hyp. Int. (C) Proc. of XIth Int. Conf. on Hyperfine Interactions, Durban, South-Africa, August 23-28, 1998. to be published.

[135] A. H. Silver, T. Kushida J. Chem. Phys. 38 (1963) 865.

[136] J. P. Kopp, R. G. Barnes J. Chem. Phys. 54 (1971) 1840.

[137] K. Schwarz, private communication.

[138] H. Akai, B. Drittler, P. H. Dederichs Full potential KKR.

[139] R. Zeller J. Phys. C20 (1987) 2347.

[140] B. Drittler. M. Weinert, R. Zeller, P. H. Dederichs Solid State Comm. 79 (1991) 31.

[141] B. Drittler, M. Weinert, R. Zeller, P. H. Dederichs Phys. Rev. B39 (1989) 930.

[142] B. A. Brown, A. Etchegoyen W. D. M. Rae MSUCL. Report 524 (1988).

[143] R. Zeller, J. Deutz, P. H. Dederichs Solid State Comm. 44 (1982) 993.

[144] W. H. Press, S. A. Teukolsky, A. T. Vetterling, B. P. Flannery Numerical Recipes in Fortran (Cambridge, 1988)

A Theoretical Predictions of Nuclear Quadrupole Moments

In this appendix, some theoretical predictions of nuclear quadrupole moments, which are determined in the present study, are given. It becomes easy to calculate nuclear magnetic dipole moments and electric quadrupole moments by using a widely distributed shell model calculation code OXBASH [142]. The results of the OXBASH are given. Besides, for ^{13}O and ^{19}O recent Hartree-Fock calculations by Sagawa and Kitagawa [114] are given. Their theoretical values were obtained by two methods with the same shell model structure factors of PW interaction. Firstly, they used the harmonic oscillator (HO) wave functions, while the modified Hartree-Fock (HF) wave functions were adopted in the second method with the halo effect (HF(Halo)). The modified HF calculation was carried out by solving self-consistently the HF equation for the core wave functions. Then the last halo orbit was obtained to reproduce the separation energy by adjusting the central part of the potential. The effective charges of $e_p^{eff} = 1.3e$ and $e_n^{eff} = 0.5e$ for protons and neutrons were used to derive the quadrupole moments [133]. The experimental and theoretical Q moments are summarized in table 16.

Table 16: Experimental and Theoretical quadrupole moments of ^{13}O and ^{19}O.

	Experiment (mb)	OXBASH (mb)	H.O. (mb)	H.F.(Halo) (mb)
^{13}O	11.0±1.3	+17	+15.7	+9.0
^{19}O	3.7±0.4	-7.1	-6.8	-6.0
^{27}Si	61±14	60	—	—
^{39}Ca	36±4	26	—	—

In the case of ^{13}O, HO calculation gives almost 50% larger value than the present experiment. If the halo effect is taken into account, HF(Halo) calculation is in perfect agreement with the experiment. The radial extension $\langle r^2\rangle^{1/2} = 3.3$ fm for the 2 protons in the $p_{1/2}$ orbit calculated by the wave functions in HF(Halo) method is larger than $\langle r^2\rangle^{1/2} = 2.6$ fm for the neutrons in the $p_{3/2}$ orbit. This indicates a thin proton halo effect in spite of the rather large separation energy of $S_p = 1.5$ MeV. In the case of ^{19}O, the prediction by the HF(Halo) is not in good agreement with the experiment. In order to obtain the experimental value, the effective charge should be e_n^{eff}(Halo)$= -(0.73 \pm 0.07)e$, which is somewhat larger than the systematic value. It suggests importance of higher configuration mixing in ^{19}O than the β-stable sd-shell nuclei.

B Density Functional Theory

B.1 Hohenberg-Kohn Theorem

The Hohenberg-Kohn theorem on which the density functional theory is established is explained according to the original paper [20].

An N-electron system under an external potential $v(r)$ is described with the following Hamiltonian H.

$$H = T + V + U,$$

where T is the kinematic energy, V is the potential energy and U is the Coulomb energy between electrons, *i.e.*,

$$\begin{aligned} T &= \sum_i^N -\nabla_i^2 \\ V &= \sum_i^N v(r_i) \\ U &= \sum_i^N \frac{2}{|r_i - r_j|}. \end{aligned}$$

The N-electron wave function Φ satisfies the Schrödinger equation written as

$$H\Phi = E\Phi.$$

In the framework of the quantum theory, the ground state of the system, Ψ, under the given external potential v is deduced by the variational principle as

$$\begin{aligned} H\Psi &= E_0\Psi, \\ E_0[\Psi] &= Min\langle\Psi|H|\Psi\rangle, \\ \langle\Psi|\Psi\rangle &= N. \end{aligned}$$

Once the N-electron wave function Ψ is obtained, the density distribution ρ and any expectation values are obtained from Ψ.

$$\begin{aligned} \rho &= \Psi^\dagger\Psi, \\ \langle A\rangle &= \langle\Psi|A|\Psi\rangle. \end{aligned}$$

That is Ψ, ρ and $\langle A\rangle$ are the functionals of v.

$$\begin{aligned} \Psi &= \Psi[v] \\ \rho &= \rho[v] \\ \langle A\rangle &= A[v] \end{aligned}$$

In this procedure, we must deal with Ψ which has 3N degrees of freedom and must take the variation of the total energy functional by Ψ.

If we can regard the density distribution ρ as a basic function in spite of Ψ, it will make the problem easy because ρ has only 3 degrees of freedom. It is shown that v is a functional of ρ by the *reductio ad absurdum*. If the same ρ gives two different v and v', we get the different wave functions Ψ, Ψ' and the ground state energy $E; E'$ according to the two different Hamiltonians H, H' associated to v, v' respectively. This leads following two inequalities.

$$\begin{aligned} E &= \langle \Psi | H | \Psi \rangle \leq \langle \Psi' | H | \Psi' \rangle = E' + \int (v - v') \rho dv, \\ E' &= \langle \Psi' | H' | \Psi' \rangle \leq \langle \Psi | H' | \Psi \rangle = E + \int (v' - v) \rho dv. \end{aligned}$$

The sum of these two inequalities gives the inconsistent result $E + E' \leq E' + E$. Therefore, v is a unique functional of ρ. So, in turn the N-electron ground state wave function Ψ and all ground state properties are functionals of ρ.

$$\begin{aligned} v &= v[\rho] \\ \Psi &= \Psi[\rho] \\ \langle A \rangle &= \langle \Psi[\rho] | A | \Psi[\rho] \rangle \\ &= A[\rho] \end{aligned}$$

Next, the variational principle for $E_v[\rho]$ is derived. When Ψ and Ψ' are the ground states for given v and v' respectively, the following inequality is satisfied because of the variational principle of $E_v[\Psi]$ for Ψ.

$$E_v[\Psi] \leq E_v[\Psi']$$

Now, we know that the ground state energy E_v for a given potential v is a functional of ρ.

$$\begin{aligned} E_v &= E_v[\rho] \\ &= \int \rho v dv + F[\rho], \text{where} \\ F[\rho] &= T[\rho] + U[\rho] \end{aligned}$$

Therefore, the variational principle for $E_v[\rho]$ for ρ is derived as

$$E_v[\rho] \leq E_v[\rho'].$$

Because of the universality of the functional $F[\rho]$, if the functional $F[\rho]$ is given the ground state properties are determined.

B.2 Kohn-Sham Equations

Kohn and Sham developed an approximated way to treat an inhomogeneous electron system [19] from the theory of Hohenberg and Kohn. It has already shown that the total energy E_v of ground state under the external field v was the functional of the density ρ and written down as,

$$\begin{aligned} E_v &= E_v[\rho] \\ &= \int v \rho dv + \frac{1}{2} \int \frac{\rho(r)\rho(r')}{|r - r'|} dr dr' + G[\rho], \end{aligned}$$

where $G[\rho]$ was the universal functional of the density. They wrote G as

$$G[\rho] = T_s[\rho] + E_{XC}[\rho],$$

where T_s is the kinetic energy of a non-interacting system of electrons. All of the many body effects are included into E_{XC}. To make a discussion clear, an effective potential V_{eff} is introduced, and E_v is divided into two terms such as

$$\begin{aligned} E_v[\rho] &= E_B[\rho] + E_D[\rho], \\ E_B[\rho] &= T_s + \int V_{eff}\rho dv, \\ E_D[\rho] &= -\int V_{eff}\rho dv + \int v\rho dv + E_H + E_{XC}. \end{aligned}$$

Therefore, the variational equation given by Hohenberg and Kohn, *i.e.*

$$\frac{\delta E_v}{\delta \rho} = 0,$$

is divided and the simultaneous equations are derived as

$$\frac{\delta E_B}{\delta \rho} = 0, \quad \text{and} \quad \frac{\delta E_D}{\delta \rho} = 0.$$

In the one electron approximation, the density is written with the one electron wave functions ψ_i as

$$\rho = \sum_i \psi_i^* \psi_i,$$

and $T_s[\rho]$ is written as

$$T_s = -\sum_i \int \psi_i^* \nabla_i^2 \psi_i dv.$$

So, the variational equation leads to the Kohn-Sham equations .

$$\begin{aligned} -\nabla_i^2 \psi_i(r) + V_{eff}(r)\psi_i(r) &= \epsilon_i \psi_i(r) \\ V_{eff}(r) &= v(r) + \int \frac{\rho(r')}{|r-r'|} dv' + V_{XC}(r) \\ \rho(r) &= \sum_i |\psi_i|^2 \\ V_{XC}(r) &= \frac{\delta \tilde{E}_{XC}[\rho]}{\delta \rho} \end{aligned}$$

C KKR-Green's Function Method

To solve the one electron Shoröeinger equation and to get the eigenvalues and the Bloch functions ψ_i is a task for a band structure calculation. The Korringa-Kohn-Rostoker (KKR) method is one of the methods of the band structure calculation.

In this section, the traditional KKR method [21], [80]–[83] and the general Green's function method [22] are reviewed in brief.

C.1 Traditional KKR

Usually, the KKR method is formulated based on the muffin tin approximation. Under this approximation, the Schrödinger equation can be solved exactly.

The Schrödinger equation in atomic unit is

$$(-\nabla^2 + V(r))\psi(r) \ = \ E\psi(r).$$

This differential equation is transformed to the integral form with the free space Green's function $g(r, r')$, which is defined as

$$(\nabla^2 + E)g(r, r') \ = \ \delta(r - r').$$

The simple substitution shows that

$$\psi(r) \ = \ \int g(r, r')V(r')\psi(r')dv.$$

With the cell centered representation,

$$\begin{aligned}
\psi(r) &= \int g(R_m + r_m, R_n + r'_n)\sum_n v(R_n + r'_n)\psi(R_n + r'_n)dv'_n \\
&= \sum_n \int g(r_m, R_n - R_m + r'_n)v(r'_n)\psi(r'_n)dv'_n.
\end{aligned}$$

Here, $\psi(r)$ is expanded by the atomic wave functions in the m-th sphere ψ_L^m as

$$\psi(r) \ = \ \sum_L C_L^m \phi_L^m(r_m).$$

ϕ_L^m satisfies the Shcrödinger equation in the m-th sphere and written down with g,

$$\begin{aligned}
(-\nabla^2 + v(r))\phi_L^m(r) &= E\phi_L^m(r) \\
\phi_L^m(r) &= \phi_L^0(r) + \int g(r, r')v(r')\phi_L^m(r')dv'.
\end{aligned}$$

Substituting these expressions we get

$$\begin{aligned}
& \sum_L C_L^m[\phi_L^0(r_m) + \int g(r_m, r'_m)v(r'_m)\phi_L^m(r'_m)dv'_m] \\
= & \sum_n \int g(r_m, R_n - R_m + r'_n)v(r'_n)\sum_L C_L^n \phi_L^n(r'_n)dv'_n.
\end{aligned}$$

The free space Green's function $g(r,r')$ is expanded with the partial waves as

$$g(r,r') \;=\; -i\sqrt{E}\sum_L j_l(\sqrt{E}r_<)Y_L(r_<)h_l^{(1)}(\sqrt{E}r_>)Y_L(r_>).$$

In the cell centered expression, by using the additional theorem of

$$h_l^{(1)}(r)Y_L(r) \;=\; 4\pi\sum_{L,L''} i^{l-l'+l''}C_{LL'L''}j_{l'}(r_<)Y_L(r_<)h_{l''}(r_>)Y_{L''}(r_>),$$

for $m \neq n$, it is shown that

$$\begin{aligned}
g(r_m, R_n - R_m + r_n') &= -i\sqrt{E}\sum_L j_l(\sqrt{E}r_m)Y_L(r_m)h_l^{(1)}(\sqrt{E}|r_n' + R_n - R_m)Y_L(r_n' + R_n - R_m) \\
&= -i\sqrt{E}\sum_L j_l(\sqrt{E}r_m)Y_L(r_m) \\
&\quad \times 4\pi\sum_{L',L''} i^{l-l'+l''}C_{LL'L''}h_{l''}^{(1)}(\sqrt{E}|R_n - R_m|) \\
&\quad \times Y_{L''}(R_n - R_m)j_{l'}(\sqrt{E}r_n')Y_{L'}(r_n') \\
&= \sum_{LL'}\phi_L^0(r_m)g_{LL'}^{mn}\phi_{L'}^0(r_n'),
\end{aligned}$$

where,

$$g_{LL'}^{mn} \;=\; -i4\pi\sqrt{E}\sum_{L''} i^{l-l'+l''}C_{LL'L''}h_{l''}^{(1)}(\sqrt{E}|R_n - R_m|)Y_{L''}(R_n - R_m)$$

Finally we get

$$\begin{aligned}
\sum_L C_L^m[\phi_L^0(r_m) \;&+\; \int g(r_m, r_m')v(r_m')\phi_L^m(r_m')dv_m'] \\
&= \sum_{n\neq m}\int\sum_{LL'}\phi_L^0(r_m)g_{LL'}^{mn}\phi_{L'}^0(r_n')v(r_n')\sum_L C_L^n\phi_L^n(r_n')dv_n' \\
&\quad + \int g(r_m, r_m')v(r_m')\phi_L^m(r_m')dv_m' \\
\sum_L C_L^m Z_L^m(E)\phi_L^0(r_m) &= \sum_L\phi_L^0(r_m)\sum_{n\neq m}\sum_{L'}g_{LL'}^{mn}\int\phi_{L'}^0(r_n')v(r_n')\phi_L^n(r_n')dv_n'C_{L'}^n \\
&= \sum_L\phi_L^0(r_m)\sum_{n\neq m}\sum_{L'}g_{LL'}^{mn}Y_{L'}^n(E)C_{L'}^n
\end{aligned}$$

This leads to the secular equation of

$$\sum_{L'n}\left[\delta_{LL'}\delta_{mn}Z_L^m(E) - g_{LL'}^{mn}Y_{L'}^n(E)\right]C_{L'}^n = 0,$$

i.e.,

$$\det\left[\delta_{LL'}\delta_{mn} - g_{LL'}^{mn}t_{L'}^n(E)\right] = 0$$

must be satisfied.

C.2 Crystal Green's Function

The electron density distribution is directly obtained from the Green's function of the system. It is shown evidently from the eigen function expansion of the Green's function.

The eigenfunction ϕ_n of the Schrödinger equation $H\phi = E\phi$ which associated to the eigenvalue E_n and the Green function of the system satisfy

$$\begin{aligned} H\phi_n &= E_n, \\ (E-H)G(r,r') &= \delta(r-r'). \end{aligned}$$

Expanding $G(r,r')$ by ϕ_n with the expansion coefficients $G_n(r')$ as

$$G(r,r') = \sum_n G_n(r')\phi_n(r),$$

and multiplying $(E-H)$, we get

$$\begin{aligned} (E-H)G(r,r') &= \sum_n G_n(r')(E-H)\phi_n(r) \\ \delta(r-r') &= \sum_n G_n(r')(E-E_n)\phi_n(r) \end{aligned}$$

Multiplying $\phi_m^*(r)$ and the volume integration leads to

$$\begin{aligned} G_n(r') &= \phi^*(r')/(E-E_n), \text{therefore,} \\ G(r,r') &= \sum_n \frac{\phi_n^*(r')\phi_n(r)}{E-E_n} \end{aligned}$$

is obtained. With the identity of

$$\frac{1}{x+i\epsilon} = \mathrm{P.}\frac{1}{x} - i\pi\delta(x),$$

$$\begin{aligned} G(r,r') &= \sum_n \frac{\phi_n^*(r')\phi_n(r)}{E+i\epsilon-E_n} \\ &= \mathrm{P.}\sum_n \frac{\phi_n^*(r')\phi_n(r)}{E-E_n} - i\pi\sum_n \delta(E-E_n)\phi_n^*(r')\phi_n(r) \end{aligned}$$

is obtained. Therefore, we get the expression of the electron density distribution ρ as

$$\begin{aligned} \rho(r,E) &= \sum_n \delta(E-E_n)\phi_n^*(r)\phi_n(r) \\ &= -\frac{1}{\pi}\mathrm{Im}G(r,r) \end{aligned}$$

Consequently, once the Green's function of the crystal is obtained, we get the electron density directly from it.

Next, the crystal Green's function $G(r,r')$ is constructed. $G(r,r')$ satisfies the Schrödinger equation of

$$(\nabla^2 + E - V(r))G(r,r') = \delta(r-r'),$$

and it is found that G is written down as

$$G(r,r') \;=\; g(r,r') + \int g(r,r'')V(r'')G(r'',r')dv''.$$

In the case of the free space Green's function, it is expanded as

$$\begin{aligned} g(r+R_m, r'+R_n) &= \delta_{mn} g(r,r') + \sum_{LL'} J_L(r) g^{mn}_{LL'} J_{L'}(r'), \\ g(r,r') &= -i\sqrt{E}\sum_L J_L(r_<) H_L(r_>), \end{aligned}$$

where,

$$\begin{aligned} J_L(r) &= j_l(\sqrt{E}r) Y_L(r), \\ H_L(r) &= h_l^{(1)}(\sqrt{E}r) Y_L(r). \end{aligned}$$

Expanding $G(r,r')$ as the same manner,

$$\begin{aligned} G(r+R_m, r'+R_n) &= \delta_{mn} G^m_s(r,r') + \sum_{LL'} \mathcal{J}_L(r) G^{mn}_{LL'} \mathcal{J}_{L'}(r') \\ G^m_s(r,r') &= -i\sqrt{E}\sum_L \mathcal{J}_L(r_<) \mathcal{H}_L(r_>) \\ \mathcal{J}_L(r) &= P_l(\sqrt{E}r) Y_L(r) \\ \mathcal{H}_L(r) &= Q_l(\sqrt{E}r) Y_L(r) \end{aligned}$$

and by direct insertion of this formula to the integral equation the expansion coefficients G^{mn}_{LL} is determined as

$$G^{mn}_{LL'} \;=\; g^{mn}_{LL'} + \sum_{L''l} g^{ml}_{LL''} t^l_{L''} G^{ln}_{L''L'}$$

D Some Numerical Techniques

D.1 Contour Integration

Now, the density distribution is calculated from the crystal Green's function. To obtain the density distribution of electrons, it is needed to integrate the Green's function about energy precisely, however, it is difficult because of the complicated structure of the density of states. To overcome this difficulty the contour integration technique is often employed [143]. First, the Green's function is continuated to the complex energy plane.

$$\begin{aligned} G(r,r;z) &= \sum_n \frac{\phi_n^*(r)\phi_n(r)}{z-E} \\ &= \int_{-\infty}^{\infty} \sum_n \delta(E'-E_n)\frac{\phi_n^*(r)\phi_n(r)}{z-E'}dE' \\ &= -\frac{1}{\pi}\int_{-\infty}^{\infty} \mathrm{Im}G(r,r';E')/(z-E')dE' \end{aligned}$$

Here, G(z) is analytical in the whole complex plane except on the real axis. So we can deform the integration path arbitrary in the complex plane.

$$\begin{aligned} \rho(r) &= \sum_n |\phi_n(r)|^2 \\ &= \int_{-\infty}^{E_F} \rho(r,E)dE \\ &= -\frac{1}{\pi}\int_{-\infty}^{E_F} \mathrm{Im}G(r,r;E)dE \\ &= -\frac{1}{\pi}\int_A \mathrm{Im}G(r,r;z)dz \\ &= -\frac{1}{\pi}\int_C \mathrm{Im}G(r,r;z)dz. \end{aligned}$$

The contour integration can be performed precisely, because the complicated structure of the DOS is smeared out. At $z = E + i\Gamma$, G(z) is

$$\begin{aligned} \mathrm{Im}G(r,r;z) &= \mathrm{Im}G(r,r;E+i\Gamma) \\ &= \frac{1}{\pi}\int_{-\infty}^{\infty} \mathrm{Im}G(E')\frac{\Gamma}{(E'-E)^2-\Gamma^2}dE'. \end{aligned}$$

This means the delta function on the real axis is spread into the Lorentzian shape with the half width of Γ (fig. 54).

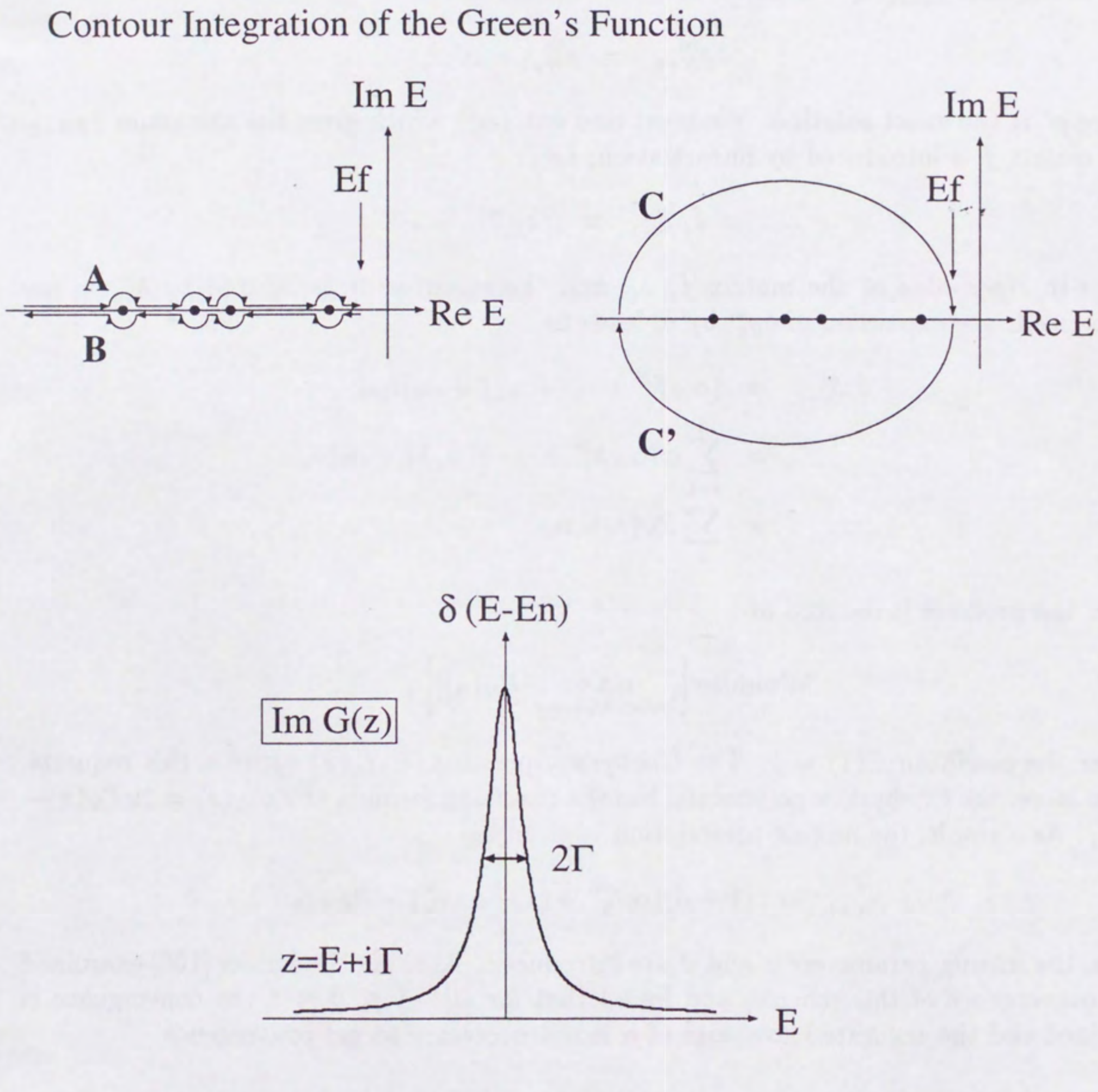

Figure 54: Contour integration of the Green's Function

D.2 Chebyshev Acceleration

The Chebyshev acceleration is a popular technique used in the relaxation method to solve a simultaneous equations [144]. It was applied to solve the present non-linear problem. In this scheme, ρ^{in}_{N+1} is written as a linear combination of the previous outputs, *i.e.*

$$\rho^{in}_{N+1} = \alpha_N \rho^{out}_N + \alpha_{N-1}\rho^{out}_{N-1} + \cdots + \alpha_1 \rho^{out}_1 + \alpha_0 \rho^{out}_0 .$$

It is found that $\sum_{i=1}^{N} \alpha_i = 1$. Here, we write the error as

$$\delta\rho^{in}_{N+1} = \rho^{in}_{N+1} - \rho^*,$$

where ρ^* is the exact solution. We must find out $\{\alpha_i\}$ which gives the minimum $\delta\rho_{N+1}$. The matrix f is introduced by linearization, *i.e.*,

$$\delta\rho^{in}_{N+1} = f\delta\rho^{out}_N .$$

The i-th eigenvalue of the matrix f, λ_i, and the eigenvector associated to λ_i, v_i, are introduced. the expansion of $\delta\rho^{in}_1$ by v_i leads to

$$\begin{aligned}\delta\rho^{in}_{N+1} &= (\alpha_N f^N + \cdots + \alpha_1 f + \alpha_0)\delta\rho_0 \\ &= \sum_{i=1}^{k} c_i(\alpha_N \lambda_i^N + \cdots + \alpha_1\lambda_1 + \alpha_0)v_i \\ &= \sum_i P_N(\lambda_i)c_i v_i .\end{aligned}$$

Here, the problem is reduced as

$$\text{Minimize}\left[\max_{\lambda_{min}\le\lambda\le\lambda_{max}} |P_N(\lambda)|\right],$$

under the condition $P(1) = 1$. The Chebyshev polynomial $T_n(x)$ satisfies this requests. Even more, the Chebyshev polynomial has the recursion formula of $T_{N+1}(x) = 2xT_N(x) - T_{N-1}$. As a result, the mixing prescription is given as

$$\rho^{in}_{N+1} = (1+\beta)(\alpha\rho^{out}_N + (1-\alpha)\rho^{in}_N) - \beta\rho_{N-1}.$$

Here, the mixing parameters α and β are introduced. Akai and Dederices [106] examined the convergence of this scheme, and found that for all $-1 \le \beta \le 1$ the convergence is attained and the accurate knowledge of α is not necessary to get convergence.

E Polycrystal Pattern

In ionic crystals, line spreads of the β-NQR spectrum often become up to several 10 % in FWHM (full width at half maximum) as shown in the β-NQR spectra of ^{19}O in TiO$_2$ (fig. 12) and ^{12}N in hexagonal BN (fig. 1 in ref. [109]). For a precise discussion, it is important to understand the origin of the line width of the spectrum. In particular, it is noticed whether the spread is symmetric or asymmetric about the center of the peak, when we determine the electric quadrupole coupling constant from such spread spectrum. One of factors for the line spread in ionic substances is the EFG from point defects. Ionic crystals contain lattice defects such as vacancy, interstitials and impurities by nature. Besides, in the case of β-NMR experiment, diffracted incident particles, γ-rays and neutrons irradiate a catcher, and of course probe nuclei itself are implanted into the sample. This makes radiation damages in the catcher. Because of the long range nature of the $1/r$ Coulomb potential and the absence of the effective screening by the conduction electron as in metals, such point defects can produce additional EFGs at the probe nucleus and a random distribution of the defects causes a spread of the EFGs at the probe nuclei. In this section, to verify such effect on the NMR spectrum, the EFG produced by a uniform distribution of point defects (point charges) is discussed and the line spread under the high magnetic field limit is estimated.

First, an estimation for the EFGs produced by a point charge. A point charge ne (C) which is placed at a distance r (m) produces the Coulomb potential V (V) at the origin as,

$$V = \frac{ne}{4\pi\epsilon_0 r},$$

where e and ϵ_0 are respectively the elementally electric charge and the dielectric constant of vacuum and $1/4\pi\epsilon_0 = 8.987552 \times 10^9 \sim 9 \times 10^9$ (Vm/C). The second derivative of the Coulomb potential gives the EFG at the origin as,

$$\begin{aligned} q &= \frac{d^2V}{dr^2} = \frac{2ne}{4\pi\epsilon_0 r^3} \\ &\sim 28.8 \times 10^{-10}\frac{n}{r^3}\ (\mathrm{V/m^2}). \end{aligned}$$

We have $q \sim 300 \times 10^{19}$ (V/m^2) for $r = 1$ (Å) and $n = 1$.

The other preliminary knowledge is about a line shape for a powdered sample of an axially symmetric ($\eta = 0$) crystal. As shown in section 2, under the high magnetic field resonance frequency between the magnetic quantum number of m and $m+1$ is given as

$$\nu_{m\leftrightarrow m+1} = \nu_L - \frac{3eqQ}{4I(2I-1)h}\left(\frac{3\cos^2\theta - 1}{2}\right)(2m+1),$$

by the first order perturbation calculation. The powdered sample consists of grains each of which is a single crystal, resulting in a uniform distribution of vector $\boldsymbol{q}$ on a unit sphere as illustrated in fig. 55. In the respective grains, the resonance frequency is calculated by the above expression. The relative NMR intensity for a region of frequency between ν and $\nu + d\nu$ is written as $f(\nu)d\nu$ with a shape function $f(\nu)$. The shaded area on the sphere in fig. 55 contributes to $f(\nu)d\nu$, because ν depends only on θ which is a slope of $\boldsymbol{q}$ relative to the external field. The assumption of the uniform distribution of $\boldsymbol{q}$ leads to

$$f(\nu)d\nu = (\sin\theta)d\theta,$$

with a proper normalization of $f(\nu)$. Assuming $I=1$ for a brevity, we can get the shape function as,

$$\begin{aligned} f_{\pm}(\nu) &= 1/\left(\frac{3\nu_Q\cos\theta}{2}\right) \\ &= 2/\left(3\nu_Q\sqrt{\frac{1}{3}\left[\mp\frac{4}{\nu_Q}(\nu_{\pm}-\nu_L)+1\right]}\right), \end{aligned}$$

where $+,-$ means that $m=0,-1$ respectively and ν_Q is defined as $3eqQ/2I(2I-1)$. This shape function $f_{\pm}(\nu)$ is shown in fig. 55 for positive ν_Q. The NMR spectrum is obtained by superposing f_+ and f_-. Here, notice that at the Larmor frequency ν_L, the NMR intensity is doubled (for $I=1$ case) [95], because f_+ and f_- transition are occurred simultaneously for the same probe nuclei (like the β-NQR situation).

Now, we can derive the shape function of the β-NQR spectrum under the existence of the uniform distribution of point defects. The following points are supposed.

- There is only one defect in a volume v_a around a probe nucleus, *i.e.*, $v_a/v_c\times n=1$ is satisfied with a defect number density of n and a unit cell volume per one atom of v_c.
- In the volume of v_a, a continuous distribution of point defects is assumed, *i.e.*, a lattice structure is ignored in calculating the shape function.
- For a brevity of volume integrations, v_a is approximated by a sphere whose volume is equal to v_a, *i.e.*, $4\pi/3r_a^3=v_c/n$.

Defects on a spherical shell whose radius is r around the probe produce EFGs which have the same magnitude but directions of which are different. This is a similar situation as a powdered sample. So, it is found that the shape function is constructed by superposing the poly crystal patterns with relative weights of each shell surface of $4\pi r^2$. A total EFG at a probe nucleus is a sum of an intrinsic EFG $\boldsymbol{q}$ in a sample and a perturbation by defects EFG $\Delta\boldsymbol{q}(r)$ whose magnitude depends on a distance between the probe and the defects. Assuming that $q\gg\Delta q$ and $\boldsymbol{q}$ is parallel to the external magnetic field, we obtain

$$f_{\pm}(\nu,\Delta\nu_Q) = 2/\left(3\Delta\nu_Q\sqrt{\frac{1}{3}\left[\mp\frac{4}{\Delta\nu_Q}(\nu_{\pm}\pm\frac{\nu_Q}{2}-\nu_L)+1\right]}\right),$$

where ν_Q and $\Delta\nu_Q$ are $3eqQ/2h$ and $3e\Delta qQ/2h$ for $I=1$, respectively. $f_{\pm}$ is illustrated in fig. 56. As shown in the figure, the spread by defects on the smaller shell is wider than by ones on the bigger shell, because of the r dependence of the EFG. To obtain a real β-NQR effect, it is needed to integrate f by ν and $\Delta\nu_Q$.

$$(\text{NMR effect}) = \int d(\Delta\nu_Q)\int d\nu f(\nu,\Delta\nu_Q).$$

The case of ^{12}N in h-BN, which was discussed in [109], is shown in fig. 57 for example. In this case, it is supposed that defects, each of which has charge of $-3e$, distribute with the density of 0.5 ppm. A frequency modulation of ± 11 kHz and $\nu_Q=81$ kHz were employed according to the real experimental condition. The obtained spectrum is slightly

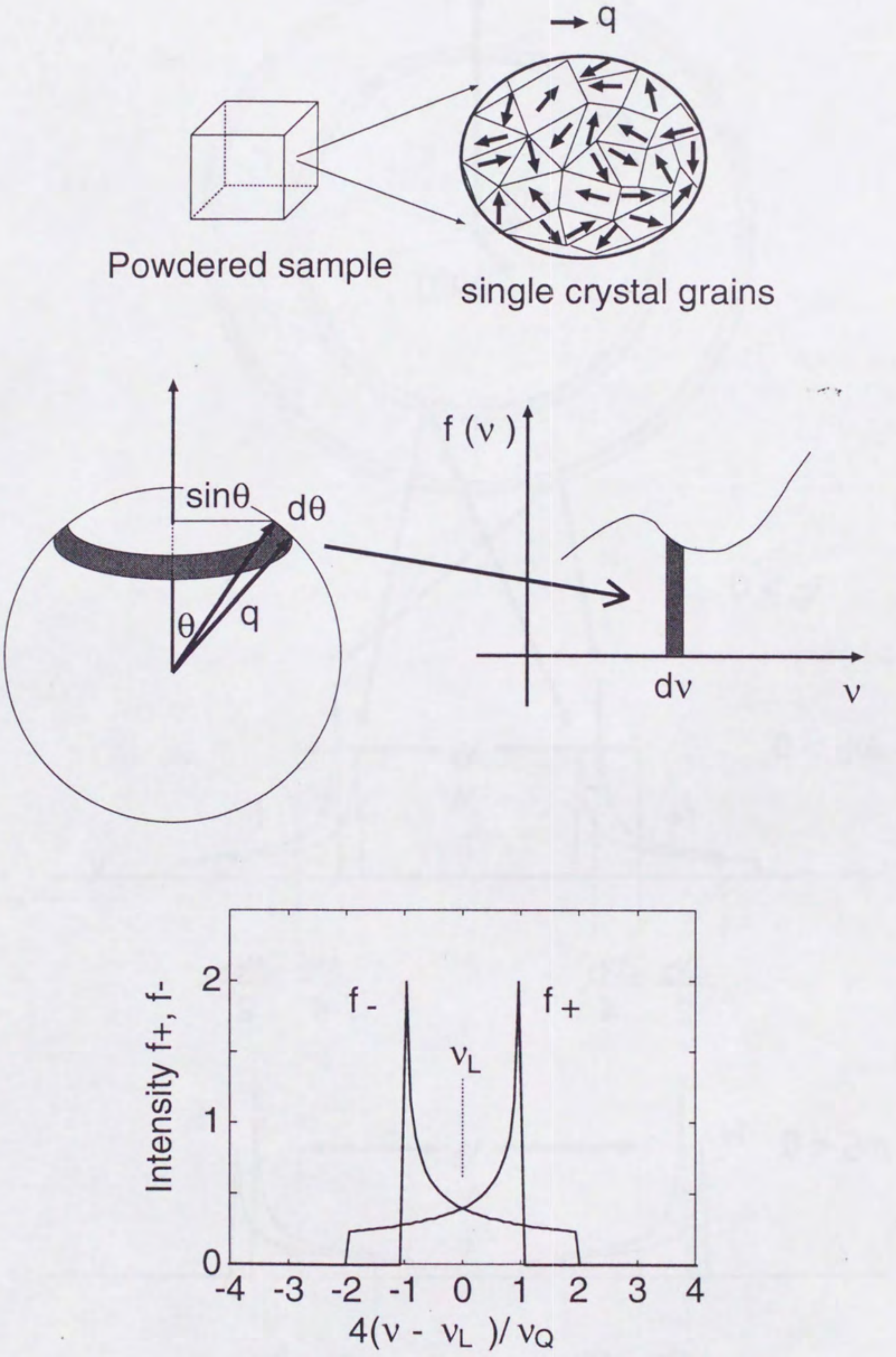

Figure 55: Powder pattern.

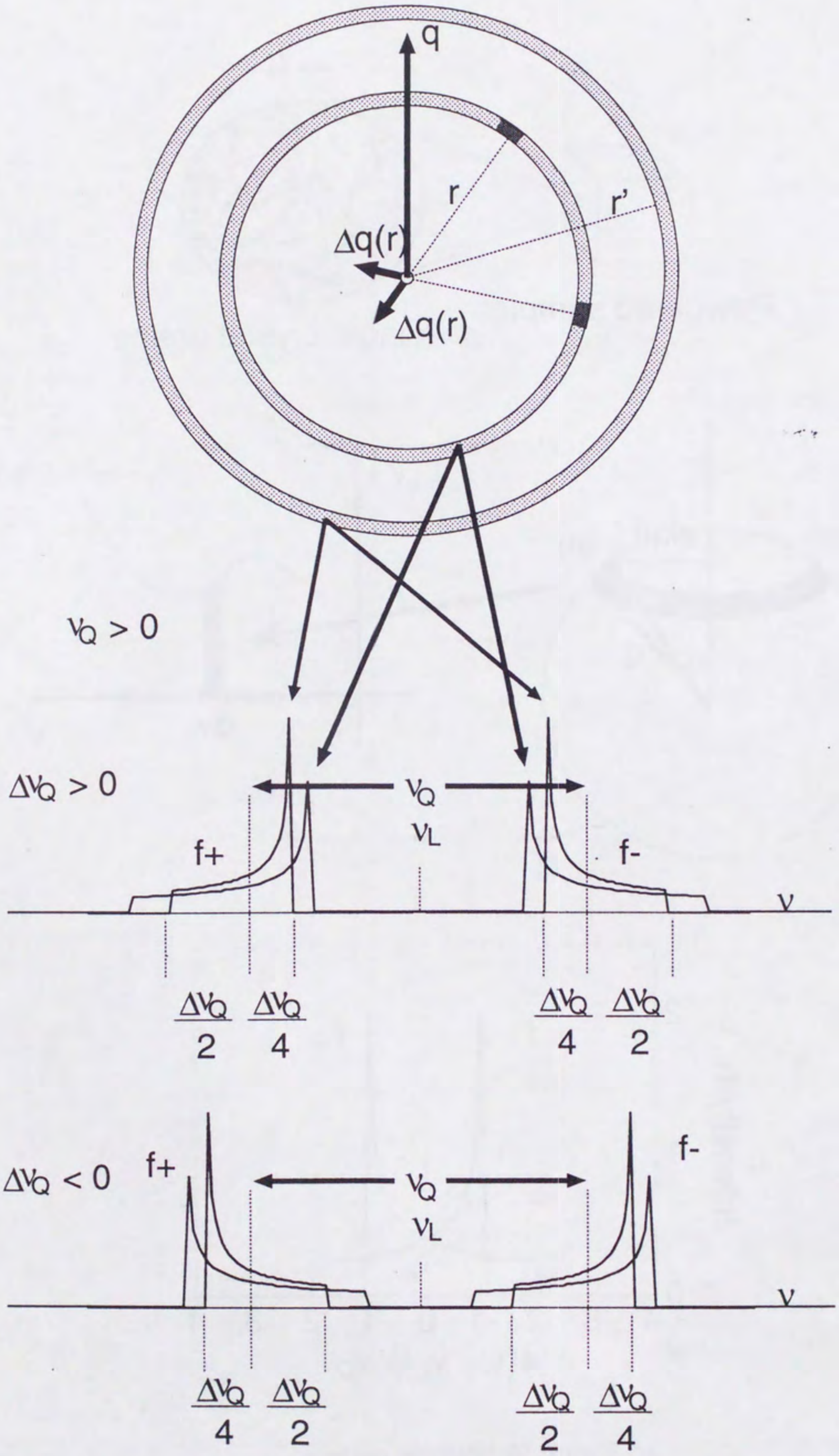

Figure 56: Superposition of the powder pattern.

asymmetric about ν_Q. It is found that ν_{center}, which was derived by fitting a Gaussian to the calculated points, deviates from the ν_Q by less than 17% of the line width. This deviation was taken into account as a systematic error when the quadrupole moment of ^{12}N was derived. However, taking the charge neutral nature of the crystal, it is expected that the opposite charge distributes simultaneously with equal density. In such case, it is found that ν_{center} is equal to ν_Q.

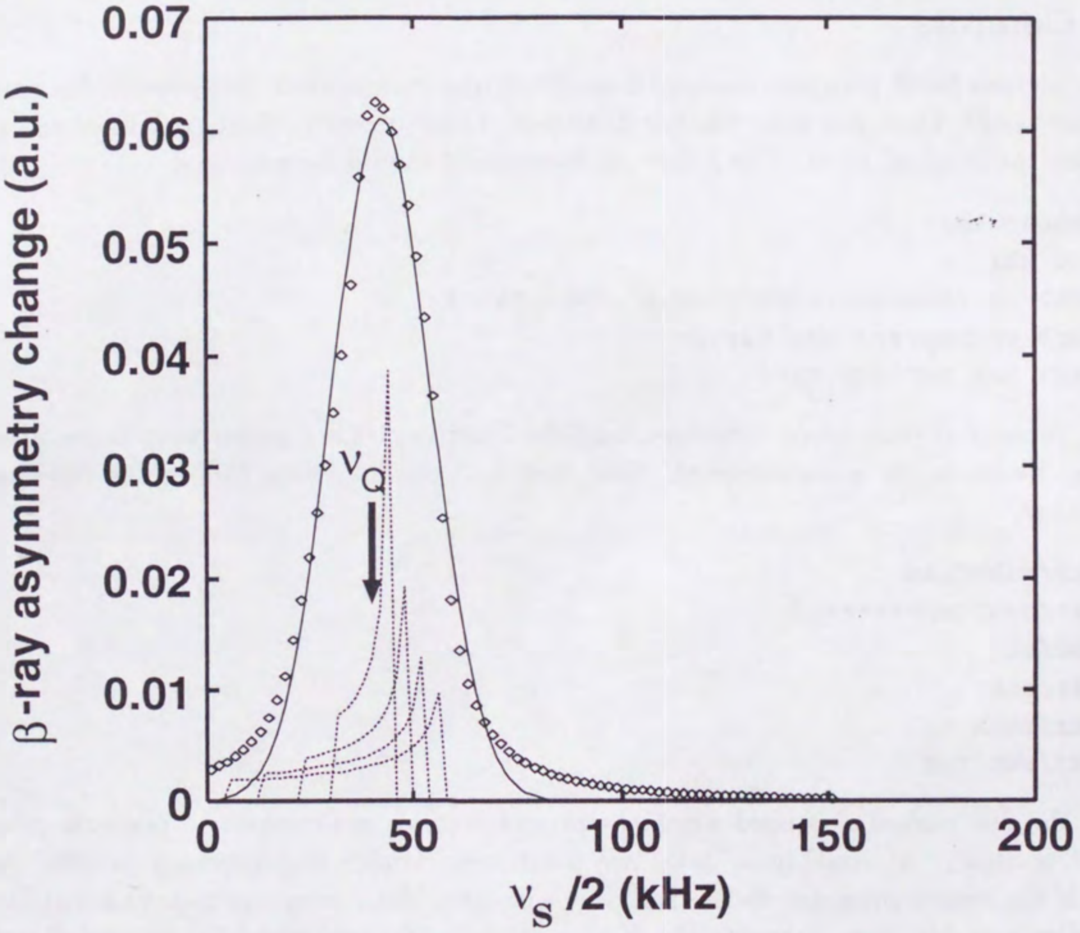

Figure 57: Simulated β-NQR spectrum of ^{12}N in h-BN with the defect density of 0.5 ppm. A uniform distribution of point charge of $-3e$ is assumed.

F How to use the KKR Package

The KKR band structure calculation code has been developed by Prof. Akai since 1979. The KKR package is a set of subroutines written in the FORTRAN. It is not so difficult to perform some calculations with this package even if one is not so familiar to the computational principles and some numerical techniques explained in the text. In this section, directions of the KKR package are given.

F.1 Compile

Usually, a given KKR program package is archived and compressed. Suppose its file name to be 'kkr.tar.Z'. First you take 'kkr.tar.Z' to your home directly. Next, you must restore it and get the original form. The following commands should be executed.

```
home> mkdir kkr
home> cd kkr
home/kkr> cp /somewhere/kkr.tar.Z ./kkr.tar.Z
home/kkr> uncompress kkr.tar.Z
home/kkr> tar xvf kkr.tar .
```

Here, /home/ is your home directory, and the directory /kkr/ under your home directory may be made for a convenience. Now, you find the following files in the directory /home/kkr/.

```
home/kkr/makefile
home/kkr/source/******.f
home/kkr/in
home/kkr/out
home/kkr/data
home/kkr/kkr.tar
```

Here, the file 'makefile' is used when the program codes are compiled. The new directories of 'source', 'in', 'out' and 'data' are produced. Under the directory 'source' you find all of the source program codes, and 'in', 'out' and 'data' may use to save input files, output files and data files, respectively. You can delete 'kkr.tar' which is not needed now.

The package has too many subroutines, so it is convenient to employ the 'make' command. The 'make' command refers to the 'makefile' and compile the files whose names are written in the 'makefile'. Moreover, the 'make' command finds out the changed files, and compiles only them.

```
home/kkr> make
```

Just do it, you get an executable file 'kkr'. To start a calculation, an input file in which lattice parameters and some numerical parameters are written is needed. How to write the input file is explained in the next section. If you want to execute the kkr calculation with your input file named as 'input.in' and save a result in a file named as 'output.out', command as the following.

```
home/kkr> kkr < in/input.in >out/output.out &
```

The last '&' means that this job is carried out as a background job.

F.2 Subroutines

The KKR package consists of more than 100 subroutines. Here, to get a survey of the KKR package a brief flowchart is given in fig. 58. A comment on each subroutine is also given in table 17.

Table 17: Subroutines in the KKR package.

Subroutine	Comment
small.f	Some parameters and arrays are defined and krmain is called.
readin.f	A given input file is read in.
krmain.f	Main routine of the KKR.
chklat.f	Check muffin tin radii and modify them if they conflict.
prmvec.f	The primitive lattice vector and the reciprocal lattice vector are generated.
bzmesh.f	
**bzm.f	k-points in the Brillouin zone are set up.
genlpt.f	Lattice points in the real and reciprocal space are generated.
madlng.f	The madelung constants are calculated.
gtchst.f	The KKR structure constants are calculated.
gsdatp.f	Initial potentials are constructed from the atomic calculations.
atmicv.f	The atomic calculation is performed.
corcnf.f	The configuration of the core states is confirmed.
drvmesh.f	The energy contour is defined.
phasea.f	The atomic t-matrix is calculated.
radial.f	The radial Schrödinger equation is solved.
fczero.f	Single site Green's function.
cstate.f	The radial Schrödinger equation is solved for the core states.
conkkr.f	The crystal Green's function is constructed.
kkrsea.f	The structure constant are interpolated for each energy point.
cinvrs.f	$(1-gt)^{-1}$ is calculated.
bzmsum.f	Integration in k-space.
chrdnc.f	The charge density distribution is calculated.
neutrl.f	The charge neutrality is calculated and ϵ_f is shifted.
potenv.f	The Poisson equation is solved. The exchange-correlation potential is calculated.
banden.f	The energy eigenvalues are summed up.
totalw.f	The total energy of the system is calculated.
erranc.f	The convergence is checked, and new input potential is constructed.
dsenum.f	The results are printed out.
hypera.f	The hyperfine field is calculated.
getefg.f	The electric field gradient is calculated.

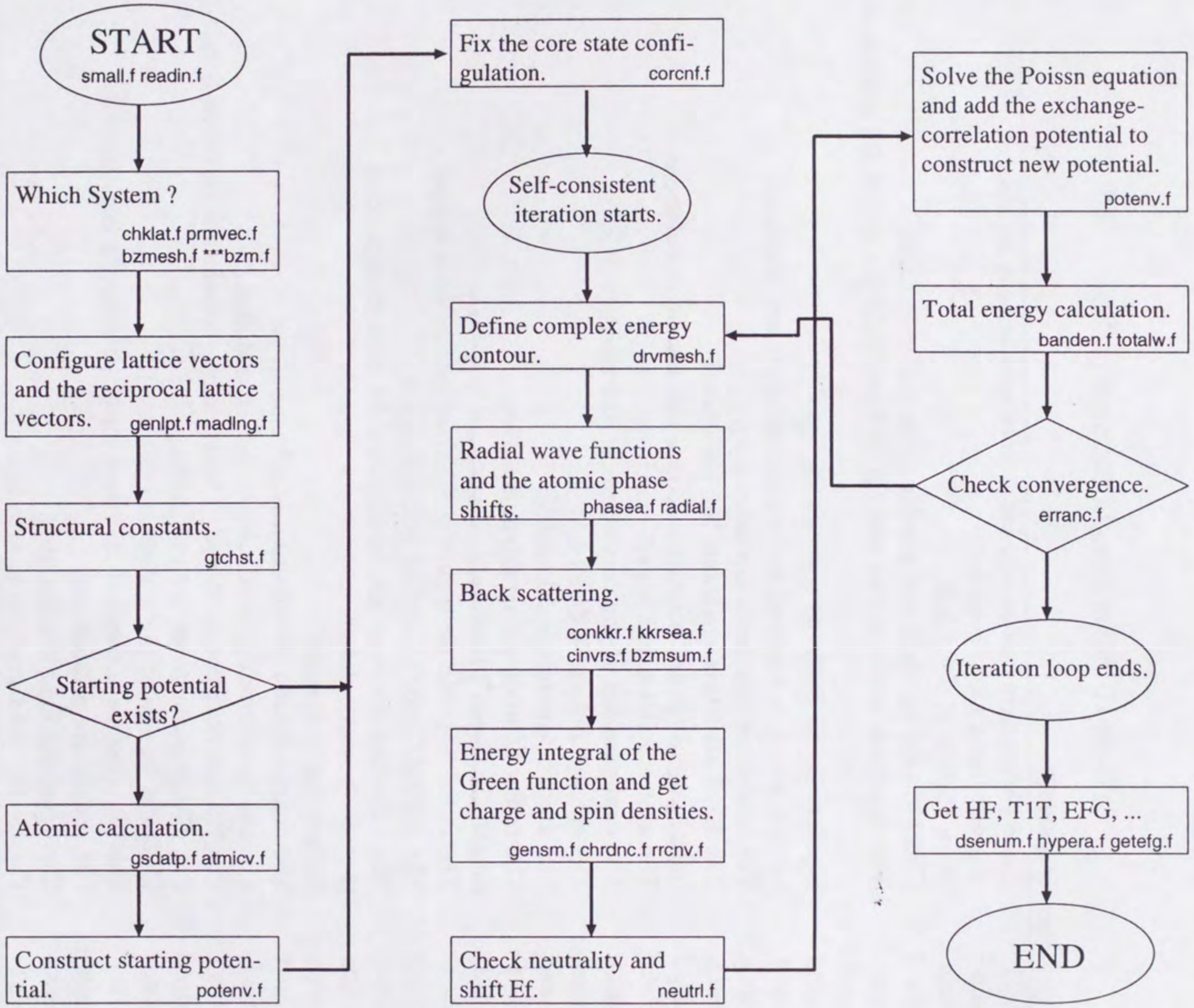

Figure 58: The flow chart of the band structure calculation.

F.3 The Origin of Energy

In the muffin tin approximation, a constant energy is assumed in an interstitial region. Energy at the interstitial region is set equal to zero as shown in fig. 59. A relation between parameters which will be explained in the next section is also shown in the figure.

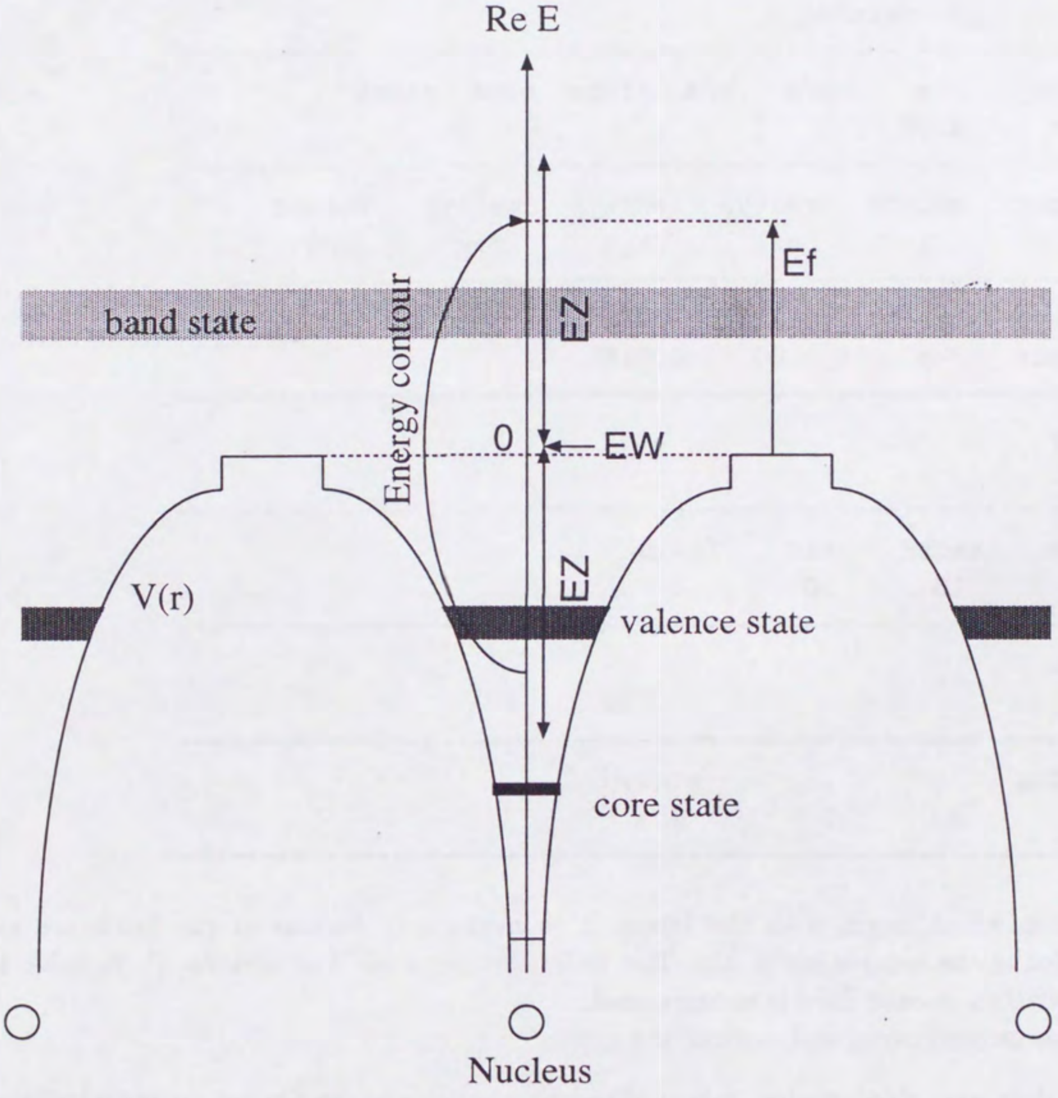

Figure 59: The origin of energy.

F.4 Input File

The lattice parameters, such as the Bravais type, the lattice constants and atomic numbers and so on, are written in an input file and it is transfered to the main program when the kkr is executed. As an example, the input file used in the calculation of fcc Ni is shown.

```
c ---------------------Nickel---------------------------------
            go  data/ni
c ------------------------------------------------------------
c   brvtyp     a     c/a   b/a  alpha  beta  gamma
     fcc     6.60  ,    ,      ,     ,      ,     ,
c ------------------------------------------------------------
c   ecentr   ewidth   reltyp   sdftyp   magtyp   record
      0        1       nrl      mjw      mag      2nd
c ------------------------------------------------------------
c   outtyp   bzqlty   maxitr   pmix
    update     m        80    0.015
c ------------------------------------------------------------
c   ntyp
     1
c ------------------------------------------------------------
c   type    anclr    rmt    field
     Ni      28       0       0
c ------------------------------------------------------------
c   natm
     1
c ------------------------------------------------------------
c   atmicx                   atmtyp
     0       0       0        Ni
c ------------------------------------------------------------
```

The lines which begin with the letter 'c' is neglected. Names of the fields are also commented in the sample input file. The delimiter is spaces ' ' or comma ','. In table 18, what is written in each field is summarized.

Next, some comments and notices are given.

- In '**dsp**' and '**dos**' modes, values of record, outtyp and maxitr are automatically set to be 2nd, quit and 1, respectively.
- You can specify a file name of a potential data by a relative pass name.
- If c/a, b/a, α, β and γ are evident from '**brvtyp**' , you can omit to write them.
- An energy contour to integrate a density of states must be in a region of '**ecentr**'±'**ewidth**'. During iteration cycles the ϵ_f is modified to satisfy the charge neutral condition, so it must be noticed that the contour does not go over the region. It is not possible to predict the ϵ_f, so ecentr and ewidth are determined by trial and error.
- The previous potential data is stored with the presently calculated potential data into the data file not to lose the data by a trouble. '**2nd**' means that the calculation

Table 18: Parameters written in the input file.

Field	Value	Meaning
go	go	perform a band structure calculation.
	dsp	display a previous result.
	dos	calculate a density of states.
file	*file name*	file name in which a potential data is written.
brvtyp	fcc, bcc, hcp, $\cdots$	which type of the Bravais lattices.
a		lattice constant in atomic unit.
c/a, b/a		c/a and b/a ratios of lattice constants.
alpha, beta, gamma		α, β and γ in degrees.
ecentr	-1.0~0.5	center of energy for the chebyshev interpolation.
ewidth	0.5~2.0	enegy window for the chebyshev interpolation.
reltyp	nrl	no relativistic treatment.
	sra	scaler relativistic approximation.
sdftyp	mjw, vbh, $\cdots$	which exchange correlation potential is used.
magtyp	mag, nmag	magnetic or non-magnetic.
record	init	initially start a calculation.
	1st, 2nd	continues a previous calculation.
outtyp	update	potential data is updated.
	quit	potential data is not updated.
bzqlty	0,1,2,$\cdots$	The bigger, the finer mesh in the Brillouin zone.
	t,s,m,l,h,u	see nfqlty.f
maxitr	≥ 1	the maximum number of the iteration loop.
pmix	0.01~0.03	a parameter used in mixing V^{in} and V^{out}.
ntyp		how many types of atom exist in a unit cell.
type	*type name*	names of the respective types of atom.
anclr		atomic number.
rmt		muffin tin radius.
field		external magnetic field at each site.
natm		number of atoms in a unit cell.
atmicx	*coordinates*	where each atom is.
atmtyp	type name	which type of the atom at the lattice point.

starts with the latest data file, and '**1st**' means that the calculation starts with the 2nd latest data file.

- 'anclr'=0 means that a vacancy is put at the lattice point.
- If muffin tin spheres whose radii are given by '**rmt**' conflict each other their radii are automatically modified not to so. If '**rmt**' = 0, muffin tin radii are set so that their ratio is equal to the ratio of the atomic radii.
- The lattice point at which an atom is put is specified with the Cartesian coordinate (*e.g.*, written as 0.5, 0.5, 0.5) or with the primitive vector (*e.g.*, written as 0.5a, 0.5b, 0.5c).
- If some input files are in the same file, they are performed sequentially.

By the way, size of an array used in the KKR program depends on a system to be calculated. According to a system it is necessary to reserve enough area. The size of the arrays in the KKR program is declared in the subroutine 'small.f'. The parameters used in the 'small.f' are summarized in table 19.

Table 19: Parameters used in 'small.f'.

Parameter	Meaning
ntypmx	maximum number of types of atoms in a unit cell.
natmmx	maximum number of atoms in a unit cell.
ndmx	maximum number of irreducible blocks of the Green's function. $\leq$ natm(natm-1)
mxl	$l \geq$mxl are truncated.
ngmx	The chebyshev expansion is performed up to ngmx-th order.
mse	mesh points on the energy contour.
msr	radial mesh points.
lastmx	reserved area to calculate the CG coefficients.
nrpmx	maximum number of lattice points used in the Ewalt's sum.
ngpmx	maximum number of reciprocal lattice points used in the Ewalt's sum.
nkmx	maximum number of k-points in the Brillouin zone.
nwk	size of the work area (for real number).
niwk	size of the work area (for integer number).

If unsuitable parameters are given in the input file or small.f, the program returns error messages. Therefore, you can specify what is wrong.

F.5 Output File

A result of a calculation is shown on a display or is redirected to save into an output file. As an example, the output for the calculation on Ni is shown, for which the input file has already been shown.

```
23-Jun-97
   meshr  mse    ng      mxl
     400     35     13       3


  complex energy mesh
  1( -1.3000, 0.0000)   2( -1.2998, 0.0032)   3( -1.2990, 0.0073)
  4( -1.2969, 0.0127)   5( -1.2926, 0.0196)   6( -1.2843, 0.0284)
  7( -1.2697, 0.0392)   8( -1.2451, 0.0523)   9( -1.2059, 0.0674)
 10( -1.1468, 0.0838)  11( -1.0633, 0.1003)  12( -0.9538, 0.1149)
 13( -0.8213, 0.1254)  14( -0.6747, 0.1299)  15( -0.5269, 0.1276)
 16( -0.3908, 0.1192)  17( -0.2760, 0.1063)  18( -0.1865, 0.0911)
 19( -0.1213, 0.0756)  20( -0.0764, 0.0612)  21( -0.0470, 0.0485)
 22( -0.0283, 0.0379)  23( -0.0168, 0.0293)  24( -0.0098, 0.0225)
 25( -0.0057, 0.0172)  26( -0.0033, 0.0130)  27( -0.0019, 0.0099)
 28( -0.0011, 0.0075)  29( -0.0006, 0.0056)  30( -0.0003, 0.0042)
 31( -0.0002, 0.0032)  32( -0.0001, 0.0024)  33( -0.0001, 0.0018)
 34(  0.0000, 0.0014)  35(  0.0000, 0.0010)

  data read in
  go=go   file=data/ni
  brvtyp=fcc  a=  6.60000  c/a=0.00000  b/a=0.00000  alpha= 0.  beta= 0.  gamma= 0.
  ew=  0.000  ez=  1.000  reltyp=nrl  sdftyp=mjw    magtyp=mag
  record=init  outtyp=update  bzqlty=m   maxitr= 80  pmix=0.02400  ntyp= 1  natm= 1
  file to be accessed=data/ni
  created

  lattice constant
  bravais=fcc   a=  6.60000   c/a=1.0000   b/a=1.0000
  alpha=  90.00    beta=  90.00    gamma=  90.00
  type of atom
  type=Ni         anclr=  28.  rmt=0.35355  field=  0.000

  atoms in unit cell
  atmicp=   0.00000000    0.00000000    0.00000000  atmtyp=Ni

  preta= 0.44780   eta= 0.44780
nrpt=            141
nrpt=            169
  last= 243   np=  6   nt= 169   nrpt=141    nk=  110    nd=    1
  itr=  1       rms error = -1.724
  itr=  2       rms error = -2.239
  itr=  3       rms error = -2.657
  itr=  4       rms error = -2.967
  itr=  5       rms error = -3.645
  itr=  6       rms error = -3.695
  itr=  7       rms error = -4.268
  itr=  8       rms error = -5.061
  itr=  9       rms error = -5.356
  itr= 10       rms error = -5.470
  itr= 11       rms error = -6.321
  itr= 11  cpu time=      0.05 sec

        nl       cnf           energy
   -----------------------------------
        1s      2.000         -595.8142
        2s      2.000          -70.7050
        2p      6.000          -61.8163
        3s      2.000           -7.9863
        3p      6.000           -5.2730
        3d      8.000           -0.7806
        4s      2.000           -0.5252


  record 1 will be overlaid by input and
  record 2 will be replaced by new output.

  core configuration for Z= 28
  state  1s 2s 2p 3s 3p 3d 4s 4p 4d 5s 5p 4f 5d 6s 6p 5f 6d 7s
   up     1  1  3  1  3  0  0  0  0  0  0  0  0  0  0  0  0  0
```

```
   down    1  1  3  1  3  0  0  0  0  0  0  0  0  0  0  0  0

   *****.self-consistent iteration starts *****
      Ni
   itr=  1 neu=  0.6346  moment= -0.1778  te=  -3011.4102699  err= -0.135
   itr=  2 neu= -0.5453  moment=  0.0426  te=  -3011.6353084  err= -1.080
   itr=  3 neu= -1.6592  moment= -0.1689  te=  -3011.8170398  err=  0.060
   itr=  4 neu=  0.3643  moment= -0.1279  te=  -3011.6356415  err= -0.968
   itr=  5 neu=  0.5579  moment= -0.0323  te=  -3011.1891523  err= -0.012
   itr=  6 neu= -1.0928  moment= -0.2517  te=  -3011.6486783  err= -1.134
   itr=  7 neu= -1.1549  moment=  0.0169  te=  -3011.6512342  err= -0.942
   itr=  8 neu= -0.0839  moment= -0.2198  te=  -3011.6325866  err= -0.964
   itr=  9 neu=  0.4699  moment= -0.4589  te=  -3011.6393966  err= -0.964
   itr= 10 neu= -0.1406  moment= -0.4012  te=  -3011.6343622  err= -1.034
   itr= 11 neu= -0.4198  moment= -0.5616  te=  -3011.6382921  err= -1.055
   itr= 12 neu= -0.1871  moment= -0.5999  te=  -3011.6369520  err= -1.197
   itr= 13 neu=  0.0159  moment= -0.5694  te=  -3011.6363347  err= -1.232
   itr= 14 neu=  0.1717  moment= -0.5829  te=  -3011.6368507  err= -1.289
   itr= 15 neu=  0.0819  moment= -0.5847  te=  -3011.6365158  err= -1.343
   itr= 16 neu= -0.0415  moment= -0.5786  te=  -3011.6364937  err= -1.308
   itr= 17 neu= -0.0409  moment= -0.5757  te=  -3011.6364755  err= -1.310
   itr= 18 neu=  0.0207  moment= -0.5723  te=  -3011.6364125  err= -1.356
   itr= 19 neu=  0.0432  moment= -0.5699  te=  -3011.6364215  err= -1.410
   itr= 20 neu= -0.0033  moment= -0.5685  te=  -3011.6364182  err= -1.475
   itr= 21 neu= -0.0336  moment= -0.5702  te=  -3011.6364691  err= -1.630
   itr= 22 neu= -0.0230  moment= -0.5690  te=  -3011.6364654  err= -1.710
   itr= 23 neu=  0.0033  moment= -0.5686  te=  -3011.6364666  err= -1.754
   itr= 24 neu=  0.0120  moment= -0.5692  te=  -3011.6364801  err= -1.791
   itr= 25 neu=  0.0019  moment= -0.5696  te=  -3011.6364875  err= -1.883
   itr= 26 neu= -0.0070  moment= -0.5700  te=  -3011.6364946  err= -1.973
   itr= 27 neu= -0.0056  moment= -0.5700  te=  -3011.6364973  err= -2.015
   itr= 28 neu=  0.0007  moment= -0.5699  te=  -3011.6364977  err= -2.079
   itr= 29 neu=  0.0034  moment= -0.5698  te=  -3011.6364984  err= -2.128
   itr= 30 neu=  0.0009  moment= -0.5698  te=  -3011.6364991  err= -2.164
   itr= 31 neu= -0.0025  moment= -0.5697  te=  -3011.6365005  err= -2.187
   itr= 32 neu= -0.0032  moment= -0.5697  te=  -3011.6365019  err= -2.238
   itr= 33 neu= -0.0016  moment= -0.5697  te=  -3011.6365032  err= -2.315
   itr= 34 neu= -0.0001  moment= -0.5697  te=  -3011.6365046  err= -2.370
   itr= 35 neu= -0.0001  moment= -0.5697  te=  -3011.6365060  err= -2.421
   itr= 36 neu= -0.0007  moment= -0.5697  te=  -3011.6365073  err= -2.483
   itr= 37 neu= -0.0010  moment= -0.5697  te=  -3011.6365083  err= -2.547
   itr= 38 neu= -0.0007  moment= -0.5697  te=  -3011.6365090  err= -2.606
   itr= 39 neu= -0.0002  moment= -0.5697  te=  -3011.6365096  err= -2.662
   itr= 40 neu= -0.0001  moment= -0.5697  te=  -3011.6365102  err= -2.720
   itr= 41 neu= -0.0002  moment= -0.5697  te=  -3011.6365107  err= -2.772
   itr= 42 neu= -0.0004  moment= -0.5697  te=  -3011.6365112  err= -2.820
   itr= 43 neu= -0.0004  moment= -0.5697  te=  -3011.6365116  err= -2.879
   itr= 44 neu= -0.0002  moment= -0.5697  te=  -3011.6365119  err= -2.946
   itr= 45 neu= -0.0001  moment= -0.5697  te=  -3011.6365123  err= -3.005
   itr= 45  cpu time=     41.09 sec
1  sdftyp=mjw     reltyp=nrl   dmpc=0.024
      Ni
   itr= 45  neu -0.0001  chr,spn 10.0000 -0.5697  intc,ints  0.7311  0.0230
   rms err= -3.005 -3.015
   ef=   0.6863115   0.6756310  def=  32.4366705   0.8699492
   total energy= -3011.636512




                              *** type-Ni       Ni (z= 28.0) ***
   core charge in the muffin-tin sphere =17.9926197
   valence charge in the cell (spin up  ) =     0.23393(s)   0.24128(p)   3.86666(d)
   valence charge in the cell (spin down) =     0.23168(s)   0.22498(p)   4.47773(d)
   total charge=  27.26889   valence charge (up/down)=   4.34188   4.93439
   spin moment=  -0.59251

   core level  (spin up  )
```

```
    -594.4095214 ry(1s)      -69.2809468 ry(2s)       -60.3963619 ry(2p)
      -6.5651881 ry(3s)       -3.8585432 ry(3p)
 core level  (spin down)
    -594.4204662 ry(1s)      -69.3217581 ry(2s)       -60.4298725 ry(2p)
      -6.6288458 ry(3s)       -3.9206680 ry(3p)

 hyperfine field of Ni
    75.321 kG (core=   63.695 kG  valence=   11.627 kG )
 core contribution
     7.315 kG(1s)     162.654 kG(2s)    -106.274 kG(3s)

 charge density at the nucleus
   14884.1346 (core=  14878.1463  valence=      5.9883 )
 core contribution
   13447.8312(1s)      1247.9213(2s)       182.3938(3s)



cpu used        42.26 sec
```

First, a date, 'meshr', 'mse', 'ng' and 'mxl' are written. Showing a mesh on an energy contour, the contents of the input file is confirmed. If muffin tin radii are modified, the new radii are shown. Next, it is calculated that how many lattice points (nrpt), reciprocal lattice points (ngpt) and k-points (nk) are needed. When 'record=init', the LDA calculation on each atom is performed and an initial potential is constructed. Then, configurations of core states are listed. The core configurations are set up in subroutine 'corcnf.f'. It is noticed that the core states must not come into the energy contour to avoid double counting of the core electrons.

After these output of initial conditions, a self consistent iteration is carried out. For each iteration loop, charge neutrality, spin moment, total energy and error between input and output potentials are shown to observe a convergence behavior. If the error becomes under a tolerance which is set up in the subroutine 'small.f', the iteration loop is stopped, and a result is printed out. If the number of loops exceeds 'maxitr', the iteration loop also stopped. Lastly, from the obtained electronic structure, the hyperfine field, the EFG and so on are calculated.

G Data Compilations of Experimental EFGs

The experimental EFG values have already been summarized by Vianden [2], Witthuhn *et al.* [3] and Kaufmann *et al.* [1] in their reviews on electric quadrupole interactions in non-cubic metals. However, some of the nuclear quadrupole moments have been revised. Therefore, it is necessary to re-evaluate EFG values according to new quadrupole moments. Here, we show how the experimental EFGs employed in this thesis were derived from gathering of experimental results and which quadrupole moments were used in respective evaluations. Following rules to deal with the experimental data were adopted.

- The quadrupole moments in the table of Raghavan were used [113].
  - If we have some quadrupole moments concerning for an isotope, an averaged value of them was used.
- The electric quadrupole coupling constants in the table of Vianden were used.
  - If we have some coupling constants concerning for a combination of a host and a probe, an averaged value of them was used.
- The electric field gradient can be evaluated by the following relation.

$$\begin{aligned} eqQ/h(\mathrm{MHz}) &= \frac{1.602177\times10^{-19}q(10^{19}\mathrm{V/m^2})\times Q(\mathrm{b})}{6.626076\times10^{-34}} \\ &= 0.2417988\times q(10^{19}\mathrm{V/m^2})\times Q(\mathrm{b}) \end{aligned}$$

- If we have some experimental EFGs of isotopes, an averaged value was used.
  - It is plausible that the final experimental error for the EFG does not exceed to the smallest error of the quadrupole moments of the isotopes. When the final error become too small by the averaging operation, it was set equal to the smallest error of the quadrupole moments.
- If no error is given to an experimental result, it was not used.
  - Only when we had no other data, it was employed.
- We did not concern which experimental technique was used.
- The experiments at low temperature (below 77 K) were differentiated from the others.

Now, the experimental electric quadrupole coupling constants, the nuclear electric quadrupole moments and the derived electric field gradients are tabulated. If the signs of coupling constants, quadrupole moments and EFGs were determined experimentally, they are written explicitly. The abbreviations for the experimental methods are followings,

Abbreviation	Method
ME	Mössbauer effect
NMR	Nuclear magnetic resonance
NQR	Nuclear quadrupole resonance

NO	Nuclear Orientation
TDPAD	Time differential perturbed angular distribution
SOPAD	Stroboscopic observation of perturbed angular distributions following nuclear reactions
IMPAC	Coulomb excitation recoil implantation perturbed angular correlation
IPAC	Integral perturbed angular correlation
TDPAC	Time differential perturbed angular correlation

Table 20: Compilation of the Experimental EFGs in HCP Metals.

Host	nucleus	Probe state	I^π	Q (b)	eqQ/h (MHz)	q (10^{19}V/m^2)	Temp.(K)	Method
Be	^{9}Be	g.s.	$3/2^-$	+0.05288(38)	0.0564(3)	4.41(4)	295	NMR
					0.0618(18)	4.83(14)	77	NMR
Mg	^{25}Mg	g.s.	$5/2^+$	+0.1994(20)	0.324(6)	6.72(14)	4.2	NMR
					0.230(-)	4.77(-)	293	NMR
Sc	^{44}Sc	68	1^+	0.21(2)	1.90(10)	37.4(40)	293	TDPAC
	^{45}Sc	g.s.	$7/2^-$	-0.22(1)	2.02(3)	38.0(20)	293	NMR
						av=38(2)		
Ti	^{43}Ti	3066	$19/2^-$	0.30(7)	8.0(16)	110(34)	293	TDPAD
	^{47}Ti	g.s.	$5/2^+$	+0.303(24)			4	NMR
	^{49}Ti	g.s.	$7/2^+$	+0.24(1)			4	NMR
				av=0.25(1)	7.7(-)	127(-)		
Co	^{59}Co	g.s.	$7/2^+$	+0.35(3)				
				+0.41(1)				
				av=0.40(1)	2.90(7)	30(1)	4.2	NMR
	^{60}Co	g.s.	5^+	+0.44(5)	-3.1(4)	-29(5)	∼0	NO
						av=-30(3)		
Zn	^{65}Zn	g.s.	$5/2^-$	-0.023(2)				
				-0.03(2)				
				av=-0.023(2)	positive	negative	∼0	NO
	^{67}Zn	g.s.	$5/2^-$	+0.150(15)	13.620(83)			NQR
					12.0(4)		4.2	NMR
					+12.34(3)		4.2	ME
					av=+12.485(30)	+344(34)		
		439	$9/2^+$	-0.51(5)	-41.2(21)	+334(37)	∼0	NO
						av= 339(33)		
		605	$9/2^+$	0.60(6)	45.5(4)	+314(31)	300	TDPAD
Zr	^{90}Zr	3589	8^+	-0.51(3)	45.5(4)	369(22)	∼0	TDPAD
	^{91}Zr	g.s.	$5/2^+$	-0.206(10)	18.7(3)	375(19)	4.2	NMR
						av=372(18)		
Tc	^{99}Tc	g.s.	$9/2^+$	-0.129(6)	5.716(-)	183(9)	293	NMR
Ru	^{99}Ru	90	$3/2^+$	+0.231(12)	5.4(3)	97(7)	283	TDPAC

Table 21: Compilation of the Experimental EFGs in HCP Metals. (Continued)

Host		Probe		Q (b)	eqQ/h (MHz)	q (10^{19}V/m^2)	Temp.(K)	Method
	nucleus	state	I^π					
Cd	^{105}Cd	e.s	$21/2^+$	1.17(1)	173(1)	612(6)	483	TDPAD
	^{107}Cd	845	$11/2^-$	0.94(1)	139(1)	612(8)	483	TDPAD
		2679	$21/2^+$	+1.21(6)	180(9)	615(43)	483	TDPAD
	^{109}Cd	463	$11/2^-$	-0.92(-)	136.6(10)	614(-)	483	TDPAD
	^{111}Cd	247	$5/2^+$	+0.77(12)				
				+0.80(10)				
				+0.83(13)				
				av=+0.79(7)	+125(4)		293	TDPAD
					125(1)		293	TDPAD
					126.0(10)		293	TDPAD
					125.0(9)		293	TDPAD
					124.66(48)		293	TDPAD
					av=+124.94(36)	+612(5)		
	^{109}Cd	g.s.	$5/2^+$	+0.69(7)	+89(11)	+533(85)	~0	NO
	^{115}Cd	180	$11/2^-$	-0.54(5)	-50(15)	+382(120)	~0	NO
						av=482(69)		
La	^{133}La	535	$11/2^-$	1.4(2)	50.2(5)	148(21)	293	TDPAC
	^{139}La	g.s.	$7/2^+$	+0.20(1)	7.8(3)	161(10)	2	NMR
					7.25(-)	150(-)	6	NQR
Lu	^{175}Lu	g.s.	$7/2^+$	+3.49(2)				
				3.62(9)				
				av=3.50(2)	429(-)	507(-)	1	SH
	^{176}Lu	g.s.	7^-	+4.92(3)				
				+4.97(3)				
				5.07(7)				
				av=+4.96(2)	613(-)	511(-)	1	SH
		127	1^-	-1.47(1)	-128(16)	+360(45)	~0	NO
	^{177}Lu	g.s.	$7/2^+$	+3.39(2)	+307(12)	+374(15)	~0	NO
		970	$23/2^-$	4.23(67)	+381(42)	373(71)	~0	NO
						av=+373(16)		
Hf	^{175}Hf	g.s.	$5/2^-$	+2.8(4)	+603(75)	+891(169)	~0	NO
	^{176}Hf	88	2^+	-2.10(2)	-435(6)		4.2	ME
					-455(17)		4.2	ME
					av=-437(7)	+861(16)		
	^{178}Hf	g.s.	2^+	-2.02(2)	-444(3)	+909(11)	4.2	ME
	^{180}Hf	93	2^+	-2.00(2)	-354(83)	+732(172)	293	IMPAC
					-434(15)	+897(32)	4.2	ME
		1142	8^-	+4.6(3)	+990(60)	+890(79)	~0	NO
						av$_{l.t.}$=894(9)		

Table 22: Compilation of the Experimental EFGs in HCP Metals. (Continued)

Host	Probe			Q (b)	eqQ/h (MHz)	q ($10^{19}\mathrm{V/m^2}$)	Temp.(K)	Method
	nucleus	state	I^π					
Re	^{182}Re	g.s.	2^+	+1.8(2)	-223(7)	-512(59)	~0	NO
		e.s.	7^+	+4.1(3)	-502(30)	-506(49)	~0	NO
	^{183}Re	g.s.	$5/2^+$	+2.3(2)				
				+2.1(2)				
				av=+2.2(1)	-281(20)	-528(45)	~0	NO
	^{184}Re	g.s.	3^-	+2.8(2)				
				+3.1(3)				
				av=+2.9(2)	-340(22)	-485(46)	~0	NO
	^{185}Re	g.s.	$5/2^+$	+2.18(2)				
				2.21(4)				
				2.19(2)				
				av=2.19(1)	271(23)		4.2	NAR
					269.5(7)		2.0	NAR
					av=269.5(7)	509(3)		
	^{186}Re	g.s.	1^-	+0.618(6)				
				+0.60(6)				
				+0.54(9)				
				av=+0.617(6)	-73(7)	-489(47)	~0	NO
	^{187}Re	g.s.	$5/2^+$	+2.07(2)				
				2.09(4)				
				av=+2.07(2)	255.67(13)		4.2	NAR
					255.2(5)		2.0	NAR
					av=255.6(13)	511(6)		
		206	$9/2^-$	3.04(5)	376(6)	512(12)	293	TDPAC
	^{188}Re	g.s.	1^-	+0.572(6)				
				+0.36(16)				
				av=+0.572(6)	-92	-665(73)	~0	NO
						av$_{l.t.}$=-510(3)		
Os	^{186}Os	137	2^+	-1.63(4)				
				-1.61(5)				
				-1.18(16)				
				av=-1.61(3)	+179(9)		4.2	ME
					136(13)		4.2	IPAC
					av=+165(7)	-424(17)		
	^{191}Os	g.s.	$9/2^+$	+2.53(16)	-278(9)	-454(32)	~0	NO
	^{193}Os	g.s.	$3/2^-$	+0.47(6)	-96(15)	-845(170)	~0	NO
						av=-433(15)		
Tl	^{192}Tl	251	8^-	0.44(7)	24.0(15)	226(39)	~0	TDPAD

Table 23: Compilation of the Experimental EFGs at Impurities in Zn.

Host	Probe			Q (b)	eqQ/h (MHz)	q (10^{19}V/m^2)	Temp.(K)	Method
	nucleus	state	I^π					
Zn	Zn				see the table of EFGs in HCP Metals.			
	^{66}Ga	1464	7^-	0.78(4)	97(6)	514(41)	293	TDPAD
	^{67}Ge	734	$9/2^+$	1.3(3)	86.6(8)	275(64)	633	TDPAD
	^{69}Ge	398	$9/2^+$	1.0(2)	88.24(65)		374	TDPAD
					77.70(23)		576	SOPAD
					av=78.87(22)	326(65)		
	^{71}Ge	175	$5/2^+$	0.23(5)	17(3)	306(86)	633	TDPAD
						av=301(69)		
	^{73}As	428	$9/2^+$		20.2(4)		653	TDPAD
	^{77}Br	293	$5/2^-$	$\sim$0.4	83.0(20)	858(-)	293	TDPAC
	^{79}Kr	147	$5/2^-$	0.45(3)	87.0(6)	800(54)	293	TDPAC
	^{83}Kr	9	$7/2^-$	+0.495(10)	103(5)	861(45)	293	TDPAC
						av=836(56)		
	Rb					$\langle$50		
	^{110}Ag	118	6^+	+1.44	+67.2(20)	+193(15)	$\sim$0	NO
	^{111}Cd	247	$5/2^+$	av=0.79(7)	+132.2(14)		293	TDPAC
					133.9(14)		298	TDPAC
					133.1(10)		293	TDPAC
					av=+133.1(7)	+697(62)		
	^{115}In	829	$3/2^+$	-0.60(2)	-193(13)	+1330(100)	293	TDPAC
	^{117}In	659	$3/2^+$	0.59(1)	181.7(15)	1274(24)	295	TDPAC
						av=+1227(23)		
	^{119}Sn	24	$3/2^+$	-0.083(3)	-36.7(6)	+1829(73)	77	ME
	^{129}I	28	$5/2^+$	-0.685	+245(15)	-1479(-)	293	TDPAC
	^{132}I	278	1^+	0.170(6)	64(32)	1557(780)	293	TDPAC
	^{132}I	49	3^+	0.23(7)	390(110)	7013(2910)	293	IPAC
						av=-1923(753)		

Table 24: Compilation of the Experimental EFGs at Impurities in Cd.

Host		Probe		Q (b)	eqQ/h (MHz)	q (10^{19}V/m^2)	Temp.(K)	Method
	nucleus	state	I^π					
Cd	^{67}Zn	605	$9/2^+$	0.60(6)	39.5(4)	272(27)	310	TDPAD
	^{66}Ga	1230	7^-	0.78(4)	83(4)	440(31)	293	TDPAD
	^{67}Ge	734	$9/2^+$	1.3(3)	56.3(6)	179(41)	383	TDPAD
	^{77}Br	130	$5/2^-$	~0.4	66.5(20)	688(-)	293	TDPAC
	^{79}Kr	147	$5/2^-$	0.45(3)	44.0(8)	404(28)	293	TDPAC
	Rb					⟨60		
	Cd				see the table of EFGs in HCP Metals.			
	^{115}In	829	$3/2^+$	-0.60(2)	-146(5)		293	TDPAC
					149(6)		293	TDPAC
					av=-147(4)	+1013(44)		
	^{117}In	659	$3/2^+$	0.59(1)	132(-)		293	TDPAC
					146(15)		294	TDPAC
					145.03(21)		290	TDPAC
					av=145.03(21)	1016(17)		
	^{119}In	654	$3/2^+$	0.60(2)	147(3)	1013(40)	295	TDPAC
						av=1015(17)		
	^{112}Sn	2552	6^+	0.25(2)				
				0.29(7)	66(3)	1092(100)	293	TDPAD
	^{113}Sn	731	$11/2^-$	0.41(1)	104.8(55)	1057(61)	300	TDPAD
	^{114}Sn	3088	7^-	0.32(6)	65.7(7)		550	TDPAD
					67.4(7)		480	TDPAD
					av=66.6(5)	861(28)		
	^{115}Sn	619	$7/2^+$	0.26(-)	47.7(5)	759(-)	550	TDPAD
	^{116}Sn	2369	5^-	0.26(1)	54.7(5)		480	TDPAD
					51.7(9)		550	TDPAD
					av=54.0(4)	859(33)		
		3548	10^+	0.50(-)	105.8(10)	875(-)	480	TDPAD
	^{118}Sn	2572	7^-	0.32(-)	56.4(8)	729(-)	550	TDPAD
		3112	10^+	0.41(-)	75.3(7)	760(-)	550	TDPAD
	^{119}Sn	24	$3/2^+$	0.094(4)				
				-0.065(5)				
				-0.061(-)				
				av=-0.083(3)	-26.2(15)	+1305(88)	77	ME
						av$_{r.t.}$=+890(21)		
	^{112}Sb	e.s.	8^-	0.71(7)	5.9(2)	34(4)	500	TDPAD
	^{129}I	28	$5/2^+$	-0.685	+259(26)	-1564(-)	293	TDPAD
	^{132}I	278	1^+	0.170(6)	38(23)	924(560)	293	TDPAD
		49	3^+	0.23(7)	430(140)	7732(3446)	293	IPAC
						av=-1099(553)		
	^{123}Xe	181	$7/2^-$	1.33(14)	116(2)	361(38)	278	TDPAD
	^{125}Xe	e.s.	$7/2^+$	1.40(15)	122.1(6)	360(37)	552	TDPAD
						av=360(38)		

Table 25: Compilation of the Experimental EFGs at Cd Probe in HCP Metals. The TDPAC Method is utilized in the respective experiments.

Host	Probe			Q (b)	eqQ/h (MHz)	q (10^{19}V/m^2)	Temp.(K)	Mother
	nucleus	state	I^π					
	^{111}Cd	247	$5/2^+$	+0.79(7)				
Be					17.1(7)		293	^{111}Ag
					-16.0(2)		293	^{111}Ag
					av=-16.1(7)	-84(8)		
					52.5(15)		293	^{111}In
					54.6(5)		293	^{111}In
					55.3(10)		293	^{111}In
					av=54.6(4)	286(25)		
Mg					7.7(2)		298	^{111}In
					-7.0(2)		298	^{111}Ag
					av=-7.4(1)	-39(3)		
Ti					27.8(2)		296	^{111}In
					+27.5(5)		293	^{111}Ag
					av=+27.8(2)	+146(13)		
Co					0.96(6)	5.0(5)	295	^{111}In
Zn					+132.2(14)		293	^{111}Ag
					133.9(14)		298	^{111}In
					133.1(10)		293	^{111}In
					av=+133.1(7)	+697(62)		
Y					14.20(30)	74.3(6.8)	293	^{111}In
Zr					14.1(2)		293	^{111}In
					14.76(7)		293	^{111}In
					+15.4(6)		293	^{111}Ag
					av=+14.70(7)	+77.0(6.8)		
Ru					22.6(3)	118(11)	293	^{111}In
Cd				see the table of EFGs in HCP Metals.				
Lu					14(1)	73(8)	293	^{111}In
Hf					+27.2(5)		293	^{111}Ag
					28.8(5)		295	^{111}In
					av=+28.0(4)	+147(13)		
Re					-29.2(6)		293	^{111}Ag
					29.73(14)		293	^{111}In
					av=-29.70(14)	-155(14)		
Os					33.4(3)	175(16)	300	^{111}In
Tl					7.8(8)	41(6)	293	^{111}In

Table 26: Compilation of the Experimental EFGs in TiO_2.

nucleus	Probe state	I^π	Q (b)	eqQ/h (MHz)	η	q (10^{19}V/m^2)	Remark
^{12}N	g.s.	1^+	0.0098(9)	0.469(5)	0.37(2)	198(18)	β-NMR site 1 $V_{YY}//$c
				2.888(12)	0.038(5)	1219(112)	β-NMR site 2 $V_{YY}//$c
^{17}O	g.s.	$5/2^+$	-0.026(3)	1.497(4)	0.868(5)	-238(27)	NMR $V_{XX}//$c Cr doped
				1.512(4)	0.831(7)	240(28)	NMR $V_{XX}//$c
^{19}O	g.s.	$5/2^+$	0.0037(4)	0.213(2)	0.836(8)	—	β-NMR $V_{XX}//$c substitutioanl site $Q(^{19}$O) was derived.
				0.350(9)	0.760(9)	390(40)	β-NMR $V_{XX}//$c interstitial site
^{41}Sc	g.s.	$7/2^-$	0.178(3)	9.05(8)	—	—	β-NMR
^{45}Sc	g.s.	$7/2^-$	-0.22(1)	11.02(1)	0.983(3)	207(9)	NMR $V_{YY}//$c present
^{47}Ti	g.s.	$5/2^+$	+0.303(24)	16.8(2)	0.19(1)	229(18)	NMR $V_{ZZ}//$c
				16.14(15)	0.303(8)	220(18)	NMR $V_{ZZ}//$c Cr doped
^{49}Ti	g.s.	$7/2^+$	+0.24(1)	13.9(2)	0.19(1)		NMR $V_{ZZ}//$c
				14.00(3)	0.192(8)		NMR $V_{ZZ}//$c present
				av=14.00(3)	av=0.191(6)	241(10)	
				13.09(11)	0.303(8)	226(10)	NMR $V_{ZZ}//$c Cr doped
					av=0.191(5)	av=238(9)	
^{93}Nb	g.s.	$9/2^+$	-0.32(2)				
			-0.366(18)				
			av=-0.34(1)	49.83(13)	0.463(7)	606(18)	NMR $V_{ZZ}//$c present
^{111}Cd	247	$5/2^+$	av= +0.79(7)	105(1)	0.18(1)		TDPAC Poly crystal
				107.1(3)	0.18(1)		TDPAC Poly crystal
				av=107(3)	av=0.18(1)	561(50)	
^{181}Ta	482	$5/2^+$	2.35(6)	not given	0.58(4)	1330(6)	TDPAC Poly crystal